MODELLING SEDIMENT TRANSPORT AND MORPHOLOGY DURING OVERWASH AND BREACHING EVENTS

- MSc THESIS -

P.L.M. (LODEWIJK) DE VET

JULY 28, 2014

Deltares
Enabling Delta Life

TU Delft Delft University of Technology

NUS National University of Singapore

Front cover: Fire Island near Pelican Island, New York (source: Google Earth). The satellite image originates eleven months after Hurricane Sandy caused a breaching event at this location. Due to the tide, the breach width is increased substantially in the months after the storm.

Modelling sediment transport and morphology during overwash and breaching events

by

P.L.M. (Lodewijk) de Vet

in partial fulfillment of the requirements for the degree of

Master of Science
in Civil Engineering

at the Delft University of Technology and the National University of Singapore.
to be presented publicly on Wednesday August 20, 2014 at 09:00 AM (CEST).

Thesis committee:	prof. dr. ir. M.J.F. Stive,	Delft University of Technology
	ir. J.P. den Bieman,	Deltares
	ir. R.T. McCall,	Deltares
	dr. ir. A.M. Talmon,	Delft University of Technology
	dr. ir. P.J. Visser,	Delft University of Technology
	dr. Jing Yuan,	National University of Singapore

An electronic version of this thesis is available at http://repository.tudelft.nl/.

Preface

This thesis concludes the double degree Master of Science programme at Delft University of Technology and National University of Singapore. The thesis work was conducted during eight very enjoyable months at Deltares.

I would like to thank my daily supervisors at Deltares - Joost and Robert - for the time they invested in me, their very constructive feedback and helping me to discover which direction I wanted to go to with this research. Furthermore, many thanks to Paul Visser for the inspiring talks regarding the physics of breaching, Arno Talmon for showing me different viewpoints towards various theories, Jing Yuan for the useful feedback and Marcel Stive for the constructive meetings we had. Further, I am grateful to my friends for making the last years enjoyable and my graduation colleagues at Deltares for the great discussions we had during coffee breaks. Last, but certainly not least, special thanks to my parents, my brothers and Dip for their encouragements, unconditional support and patience.

This thesis is definitely not my last contribution to science.

Lodewijk de Vet
Delft, July 2014

Summary

Executive summary

Currently, morphodynamic models as XBeach show substantial overestimations of the erosion rates during breaching and overwash events at barrier islands. The presently used limitations on the Shields parameter and the sediment concentration do hinder erosion, but have undesirable side effects, e.g. the breaching process is suppressed. By implementing additional physics, e.g. the erosion hindering effect of dilatancy and a proper bed slope effect, substantial improvements are achieved for idealised cases. However, two hurricane case studies showed that these model improvements do not hinder erosion sufficiently to achieve reasonable results. A proper description of bed roughness, which is preferably depth dependent and accounts for vegetation, together with calibration of the wave skewness and asymmetry is found to be very important. If this knowledge is applied on a newly introduced case study of Fire Island (hurricane Sandy, 2012), both breaching and overwash are modelled much more in line with reality. However, the complexity of having various morphodynamic processes within one model domain makes calibration a challenging task, requiring a more advanced bed roughness formulation.

Extended summary

During large storm events, barrier islands are subject to substantial erosion causing retreat of the coastline or even lowering of the dunes by overwash and breaching processes. These storm events can have a devastating effect on local topography and ecology, e.g. if a permanent breach channel is generated. As a result, the safety of the mainland can be affected negatively due to inadequate protection against storm surges and waves. To estimate storm impact and the effectiveness of protective measures, a robust modelling tool is required.

The XBeach model is a numerical $2DH$ morphodynamic model which has a good skill in predicting regular coastal erosion. For overwash and breaching events however, the model needs to be improved as the erosion rates are generally overestimated during these conditions. The main research objective of this thesis is to increase the predictive skill of the XBeach model during overwash and breaching conditions by implementing new model physics. The most important missing processes are implemented and the improved model is validated to several experiments and case studies.

A literature review resulted in an understanding of the morphological processes which are especially important during breaching and overwash events. Dilatancy becomes important at large flow velocities; an inflow of water is required to increase the pore volume which causes an in-bed directed force and consequently an increase of stability of the grains on the bed. Dilatancy can be accounted for by increasing the critical Shields parameter locally. In addition, the fall velocity of suspended sediment is reduced for large concentrations and the quasi-steadiness of the sediment concentration in the sediment-mass balance is reconsidered. Finally, the bed slope effect is improved as it is found to be important for the breaching process during which steep slopes occur. With this study, these physical processes are implemented in the XBeach model.

With the assessment of the XBeach model - on various experiments and field cases - insight is obtained into the importance of various processes. Before the implemented additional physical processes are considered, the sediment transport limitations to the concentration and Shields parameter currently used in the model are researched. A comparison of these results is made to the model with the additional model physics. To test the importance of the individual processes in the improved model, the processes are turned-off, or are modified one-by-one. The model results are compared to measurement data, but it is also verified whether the qualitative description of the dike breach phases by Visser (1998) can be confirmed based on XBeach and how detailed structures like antidunes are modelled.

The models of the considered experiments do show a substantial increase in performance by the improvements, except for the Santa Rosa Island hurricane case study in which still a substantial overestimation of erosion rates is modelled. As the main goal of the XBeach model is to achieve accurate predictions for field cases, this is not satisfying. A new hindcast of an overwash and breaching event by hurricane Sandy on Fire Island is introduced, to get more insight into the overestimations. The Fire Island case is interesting due to the large variety of processes which occurred over a longshore distance of only $2\ km$. Again, strong overestimations of the erosion rates are observed if the XBeach model is used, even with the suggested model improvements. Since the improvements did show substantial increase of skill in the laboratory and other idealised cases, an analysis is made towards possible reasons of the insufficient prediction of overwash and breaching events in field cases with XBeach.

Several additional physical processes are considered to get to more reasonable model results. By analysing the influence of larger sediment grains, ground water flow, a stronger wave asymmetry and skewness, a Manning roughness instead of a Chézy friction coefficient and the increase of bottom friction to account for vegetation, it is tested which of those processes could explain the large overestimation of the morphological changes. Finally, the morphological changes in the most promising model set-up are analysed to get an understanding of which morphological processes take place during which phase of the storm event.

As a general conclusion, it is stated that the proposed adjustments in model physics do increase the predictive skill of the XBeach model substantially. Especially the dilatancy concept and the bed-slope effect are important processes. However, during storm events in field cases, other factors dominate the results of the model. It is found that a good representation of the bottom friction and the wave skewness and asymmetry is very important to achieve proper model predictions.

Contents

Nomenclature

A	Archimedes buoyancy index	$[-]$
A	Geometric parameter in the formulation of Van Rhee	$[-]$
A	Wave action density	$[J \cdot m^{-2} \cdot s^{-1}]$
A_s	Wave asymmetry parameter	$[-]$
A_s	Sediment transport coefficient	$[-]$
C	Chézy parameter	$[m^{0.5} \cdot s^{-1}]$
C	Depth averaged sediment concentration	$[m^3 \cdot m^{-3}]$
c	Propagation velocity	$[m \cdot s^{-1}]$
c	Sediment concentration	$[m^3 \cdot m^{-3}]$
c_b	Near-bed sediment concentration	$[m^3 \cdot m^{-3}]$
c_f	Coefficient of bed roughness	$[-]$
C_{eq}	Depth averaged equilibrium sediment concentration	$[m^3 \cdot m^{-3}]$
D	Determinant	$[-]$
D	Dune height	$[m]$
D	Sediment particle size	$[m]$
D_*	Dimensionless particle size	$[-]$
D_h	Horizontal sediment diffusion coefficient	$[m^2 \cdot s^{-1}]$
D_r	Roller energy dissipation term	$[W \cdot m^{-3}]$
D_w	Wave energy dissipation term	$[W \cdot m^{-3}]$
D_{50}	Median sediment particle size	$[m]$
E	Sediment pickup flux	$[m \cdot s^{-1}]$
F	Wave induced stresses	$[kg \cdot m^{-1} \cdot s^{-2}]$
f	Coriolis coefficent	$[s^{-1}]$

F_G	Gravity force in the balance of Shields	$[N]$
F_i	Dilatancy force in the balance of Shields	$[N]$
F_L	Lift force in the balance of Shields	$[N]$
F_S	Drag force in the balance of Shields	$[N]$
f_{mor}	Morphological acceleration factor	$[-]$
F_{net}	Net force	$[N]$
f_{T_s}	Correction factor in the expression of the adaptation time scale	$[-]$
f_{u_A}	Calibration factor wave asymmetry and skewness	$[-]$
g	Gravitational acceleration	$[m{\cdot}s^{-2}]$
h	Local water depth	$[m]$
h_0	Height of a control volume just below the sheared zone	$[m]$
h_l	Height of a control volume in the sheared zone	$[m]$
i	Hydraulic gradient	$[-]$
k	Permeability	$[m{\cdot}s^{-1}]$
m_{cr}	Critical value of the bed slopes for avalanching	$[-]$
n	Manning roughness coefficient	$[-]$
n	Porosity	$[-]$
n_0	Bed porosity before erosion occurs	$[-]$
n_l	Bed porosity in the sheared zone	$[-]$
q	Sediment transport rate per unit width	$[m^2{\cdot}s^{-1}]$
q_x	Cross shore sediment transport discharge, excluding pores	$[m^2{\cdot}s^{-1}]$
q_y	Longshore sediment transport discharge, excluding pores	$[m^2{\cdot}s^{-1}]$
R	Runup	$[m]$
S	Sedimentation flux	$[m{\cdot}s^{-1}]$
s	Streamwise direction	$[-]$
S_k	Wave skewness parameter	$[-]$
S_r	Roller energy density	$[J{\cdot}m^{-2}{\cdot}s^{-2}]$
S_w	Wave energy density	$[J{\cdot}m^{-2}{\cdot}s^{-2}]$
T	Wave period	$[s]$

t	Time	$[s]$
T_s	Adaptation time scale in advection-diffusion equation for sediment	$[s]$
T_w	Temperature of water	$[^\circ C]$
U	Depth averaged flow velocity	$[m{\cdot}s^{-1}]$
u	Flow velocity	$[m{\cdot}s^{-1}]$
u^E	Eulerian flow velocity in cross shore direction	$[m{\cdot}s^{-1}]$
u^L	Lagrangian flow velocity in cross shore direction	$[m{\cdot}s^{-1}]$
u^S	Stokes drift in cross shore direction	$[m{\cdot}s^{-1}]$
u_*	Bed shear stress velocity	$[m{\cdot}s^{-1}]$
u_A	Sediment advection velocity	$[m{\cdot}s^{-1}]$
U_{crc}	Critical flow velocity related to flow	$[m{\cdot}s^{-1}]$
U_{crw}	Critical flow velocity related to waves	$[m{\cdot}s^{-1}]$
U_{cr}	Critical flow velocity above which sediment transport is enforced	$[m{\cdot}s^{-1}]$
u_{rms}	Root-mean-square velocity	$[m{\cdot}s^{-1}]$
V	Volume	$[m^3]$
v^E	Eulerian flow velocity in longshore direction	$[m{\cdot}s^{-1}]$
v^L	Lagrangian flow velocity in longshore direction	$[m{\cdot}s^{-1}]$
v^S	Stokes drift in longshore direction	$[m{\cdot}s^{-1}]$
v_e	Erosion velocity: $-v_{sed}$	$[m{\cdot}s^{-1}]$
v_{mg}	Velocity magnitude	$[m{\cdot}s^{-1}]$
v_{sed}	Sedimentation velocity: $-v_e$	$[m{\cdot}s^{-1}]$
v_{sup}	Superficial flow velocity of the water entering the bed	$[m{\cdot}s^{-1}]$
w	Fall velocity	$[m{\cdot}s^{-1}]$
w_0	Fall velocity of a single grain	$[m{\cdot}s^{-1}]$
x	Cross shore axis coordinate	$[m]$
y	Longshore axis coordinate	$[m]$
z	Vertical axis coordinate, upward direction is positive	$[m]$
z_b	Bed level elevation	$[m]$
z_s	Surface elevation	$[m]$

α_i	Constant	$[-]$
β	Bed slope angle	$[rad]$
Δ	Difference operator	$[-]$
Δ	Relative density: $(\rho_s - \rho)/\rho$	$[-]$
ϵ	Voidage	$[-]$
ν	Kinematic viscosity	$[m^2 \cdot s^{-1}]$
ν_h	Horizontal eddy viscosity	$[m^2 \cdot s^{-1}]$
ν_T	Vertical eddy viscosity	$[m^2 \cdot s^{-1}]$
ϕ	Angle of internal friction	$[rad]$
Φ_p	Dimensionless pick-up flux	$[-]$
ψ	Direction of the flow, relative to the on-slope directed vector	$[rad]$
ρ_s	Sediment density	$[kg \cdot m^{-3}]$
ρ	Density of water	$[kg \cdot m^{-3}]$
σ	Intrinsic wave frequency	$[s^{-1}]$
$\tau_{b,cr}$	Critical bed shear stress for the initiation of motion	$[kg \cdot m^{-1} \cdot s^{-2}]$
τ_b	Bed shear stress	$[kg \cdot m^{-1} \cdot s^{-2}]$
τ_s	Wind shear stress	$[kg \cdot m^{-1} \cdot s^{-2}]$
$\theta_{cr}^{B\&D}$	Modified critical Shields parameter accounting for bed slope and dilatancy	$[-]$
θ_{cr}	Critical Shields parameter for the initiation of motion	$[-]$
θ	Shields parameter	$[-]$
θ	Wave direction	$[rad]$
$\mathbf{R}$	Reynolds number associated with a falling particle	$[-]$

List of Figures

List of Tables

Chapter 1

Introduction

1.1 Background

Morphodynamics is the mutual adjustment of morphology and hydrodynamic processes involving sediment transport (Bosboom and Stive, 2013). Sediment transport formulae relate the movement of sand particles to parameters like the flow velocity and the sediment particle size. It is common knowledge that these formulae have a restricted predictive skill, even within their validity range. The majority of transport equations are calibrated on rivers and coastal areas with relatively small flow velocities and the performance of these equations at large velocities ($1 - 10\ m/s$) is investigated only to a limited extent (Van Rhee, 2010).

During storm events, water level set-up and large waves can result in large flow velocities and morphological changes can be substantial. Figure 1.1 shows the devastating impact of hurricane Sandy (October 2012) on the morphology of Fire Island, New York. For the modelling of overwash and breaching cases, it is important to investigate what processes are influencing the transport rates and how sediment transport models can be improved with this knowledge. In this way, more realistic predictions of storm impact can be made and the effectiveness of protective measures can be estimated more accurately.

Figure 1.1: Pre- and post-storm oblique aerial photographs of impact by hurricane Sandy (2012). Pictured is Fire Island near Pelican Island (marked with the arrow), New York. The impact of the storm is clearly visible, a new inlet is created by a breaching event. Taken from the U.S. Geological Survey website (http://usgs.gov/).

The XBeach model (Roelvink et al., 2009) is used in this thesis as a tool to solve the morphodynamic equations and investigate the importance of individual processes. XBeach is a numerical, depth averaged, model that solves coupled $2DH$ equations for long wave propagation, short wave energy, flow, sediment transport and bottom changes, for varying wave and flow boundary conditions. Regarding large flow velocities, the sediment transport can be modified by limiting the Shields parameter in the sediment stirring formulations to approximately 1.

The rationale behind limiting the sediment transport by defining a maximum Shields parameter value, is based on the assumption that sediment transport rates vary only linearly with the flow velocity once sheet flow conditions are met and on the expectation that the current transport formulae overestimate sediment transport at high flow velocities. In this method, the equilibrium sediment concentration is set constant for high flow velocities, which is not necessarily correct (McCall et al., 2010). Additional research is required to validate and/or improve the XBeach model for overwash and breaching conditions at which high flow velocities can occur and limit unwanted effects at lower flow velocities.

It is assumed that the overestimation of the erosion rates is caused by sediment transport and not the hydrodynamics. Various studies showed that XBeach is generally capable of predicting hydrodynamics properly (Roelvink et al., 2009; Daly et al., 2012).

1.2 Relevance of the research

Various studies on dune erosion modelling with XBeach mentioned substantial overestimations of the morphodynamic changes during overwash events (McCall, 2008; McCall et al., 2010; Den Bieman, 2012; Terlouw, 2013). Once the Shields number in the sediment stirring equations was limited to approximately one, significantly better predictive skills were obtained. However, this rough limiting method has unexpected side effects (Terlouw, 2013) and in some cases leads to significantly worse predictions than without the limitation. A more solid theoretical foundation of a sediment transport limiter is required to ensure a valid representation of reality.

To illustrate the effect of limiting the Shields parameter, a fictitious dam breach is modelled in XBeach, see Figure 1.2. As visible, the differences between a model run with a Shields parameter value limitation of 1.0 and a run without this limitation are huge. Without the limitation, the dam has almost vanished after the modelling period, and with the limitation the maximum vertical erosion is equal to only $0.4\ m$. It is difficult to state which of the two model runs is the closest to reality since this is a fictitious case. A maximum vertical erosion of $0.4\ m$ over a $4.5\ h$ period is questionable with velocities up to $6\ m/s$. On the other hand, a crest retreat of over $100\ m$ is modelled which is quite substantial.

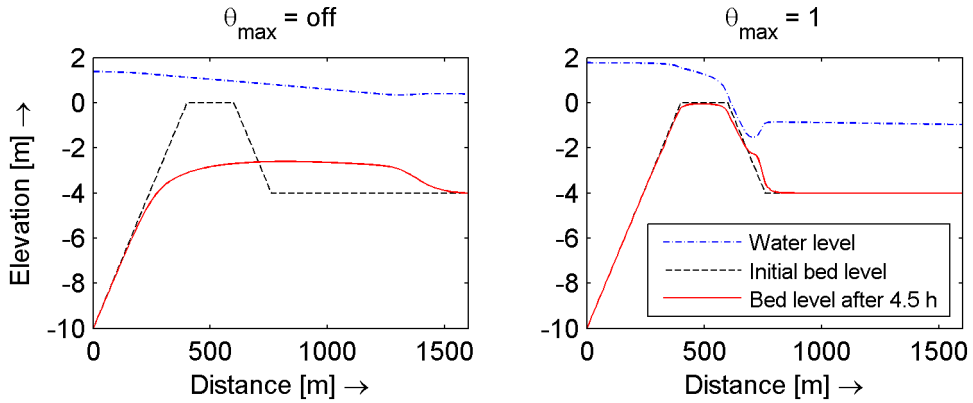

Figure 1.2: XBeach model results for a fictitious dam breach. Constant water level elevation without waves at the boundaries and bed slopes of $1:40$. The figure shows only the domain of interest, the actual modelled domain is much larger to prevent artificial boundary effects. Maximum flow velocities of $6\ m/s$ occurred in the model run. Default model parameters are applied, apart from the θ_{max} parameter in the right plot.

1.3 Research questions

The main research question is defined as:

>> To which extent can the morphodynamic predictions of the XBeach model under overwash and breaching conditions be improved through the implementation of new model physics?

To answer this main question, additional research questions are defined:

1. What physical processes affect the erosion at high flow velocities?
2. What are the limitations of the XBeach model concerning morphodynamic predictions under these conditions?
3. In what way does the predictive skill of the XBeach model improve, if the knowledge concerning sediment transport at high flow velocities is implemented?

1.4 Approach

Five research stages are distinguished:

Phase 1:	literature review of the processes that play a role at high flow velocities
Phase 2:	assessment of the performance of the current version of XBeach
Phase 3:	implementation of the processes obtained from phase 1 into XBeach
Phase 4:	assessment of the modified XBeach model
Phase 5:	application of the modified model on a case study, the hindcasting of hurricane Sandy

The XBeach model is an important element in the research since it is a tool that can be modified relatively easily. However, the focus of the research is valid in general for erosion at high flow velocities.

1.5 Thesis outline

First, a literature study on sediment transport, the processes that can affect the morphodynamics during overwash and breaching events and a description of the XBeach model is presented in Chapter 2. In Chapter 3, an assessment of the current XBeach model is made. Chapter 4 presents the hypotheses defined in this thesis whereafter the XBeach model is improved in Chapter 5 to make it possible to test these hypotheses with the XBeach model. After the performance of the improved model is assessed in Chapter 6, the improved model is used to make a morphodynamic hindcast of the impact by hurricane Sandy on Fire Island in Chapter 7. As the improved model results still in an overestimation of the morphological changes in the Fire Island case study, Chapter 8 studies additional relevant processes. In Chapter 9, the morphological changes of the most promising model set-up are analysed. Finally, a discussion, conclusions and recommendations are provided in Chapters 10 to 12.

The appendices contain information that is not critical for a clear understanding of this thesis, but can be interesting for a reader who is interested in the detailed model settings and validation. In Appendix A, the modification of the initiation of motion by dilatancy is derived and in Appendix B are characteristic bed features analysed which may occur at high flow velocities. Appendix C presents a detailed description of the XBeach model with the morphological formulations used in this model. The general XBeach model parameters are presented in Appendix D. Thereafter, some detailed model tests are provided: Appendix E deals with conceptual model tests, Appendix F tests the improved model for side effects and the improved model is validated for overwash and breaching cases in Appendix G. In Appendix H, the set-up of the Fire Island model is described together with a sensitivity analysis of the model results to the model improvements. Finally, Appendix I provides an analysis on the depth-averaging assumption for breaching cases.

Chapter 2

Theoretical background

2.1 Coastal terminology

In order to get a full understanding of the concepts dealt with in this thesis, it is important to overview the coastal terminology used in these concepts.

2.1.1 Sediment transport

Sedimentation is the settling of sediment particles on the bottom. **Entrainment** is the pick-up of sediment particles from the bottom once a large enough flow velocity is reached. If the sedimentation rate is larger than the pick-up rate of sediment, **accretion** takes place causing the bottom to rise. On the other hand, when the entrainment of sediment dominates, **erosion** causes the bottom level to fall.

2.1.2 Coastal region

Figure 2.1 shows a visualisation of a typical beach profile. The **backshore** extends from the dune foot to the mean high water (MHW) line. The zone between the MHW line and the mean low water (MLW) line is known as the **foreshore**. The **shoreface** is the part of the profile located seaward of the MLW line, which is affected by wave action and typically extends to waterdepths of 10 to $20\ m$. The latter depth is the so-called **depth of closure**, as the most seaward point of interest (Bosboom and Stive, 2013). No precise definition is available for this depth of closure.

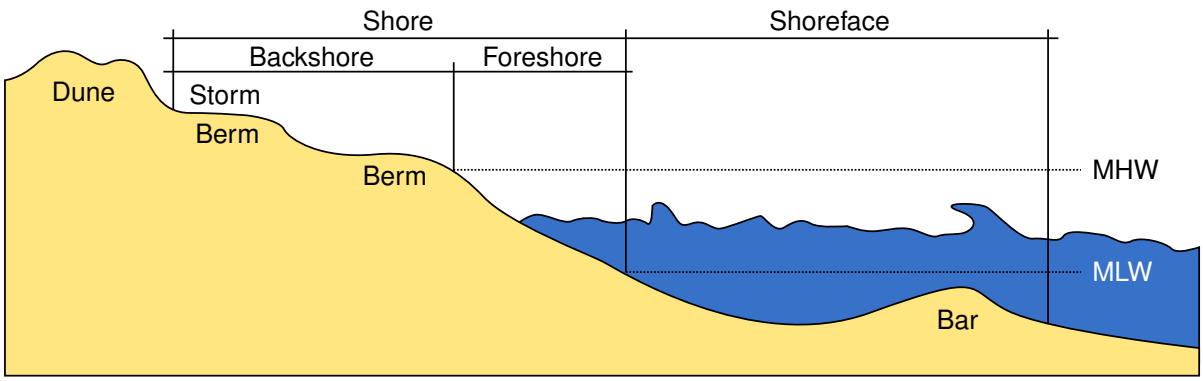

Figure 2.1: Terminology coastal region, adapted from U.S. Army Corps of Engineers (2002).

2.2 Storm regimes

2.2.1 Terminology

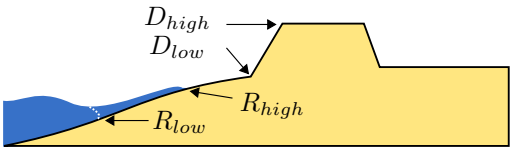

D_{high} = *highest part of the 'first line of defence'*
D_{low} = *elevation of the base of the dune*
R_{high} = *tide + storm surge + wave runup*
R_{low} = *tide + storm surge + wave rundown*

Figure 2.2: Terminology Sallenger (2000).

Sallenger (2000) defines four different storm regimes which can be distinguished based on the dune dimensions and the extremes of the water level elevation (see Figure 2.2):

1. **Swash regime:** $R_{high} < D_{low}$, erosion of the shore; sand is transported offshore. During more quiescent conditions over weeks or months, the offshore deposited sand is transported back to the shore.

2. **Collision regime:** $D_{low} \leq R_{high} < D_{high}$, erosion of the shore and dunes, sand is transported offshore. In contrast to the swash regime, the sand is not readily transported back to reinforce the eroded locations.

3. **Overwash regime:** $R_{high} \geq D_{high}$ & $R_{low} < D_{high}$, water can flow landward and the flow decelerates with distance landward. This gradient in flow leads to erosion of the dune or shores and deposition landward, often resulting in washover fans. The sand is not readily returned seaward after the storm.

4. **Inundation regime:** $R_{low} \geq D_{high}$, the dike/barrier island is completely submerged. Flow and morphology characteristics determine the direction and quantity of sediment transport.

The regimes are visualised in Figure 2.3. During a storm, a number of regimes can be encountered over time. For example, a rising storm surge can result initially in a swash regime followed by a collision regime whereafter overwash takes place. During a mild storm, inundation and overwash might not be observed. Besides variations in time, spatial varying regimes in longshore direction can be observed. Not only the dune height can vary in longshore direction, but also the wave height is not necessarily constant.

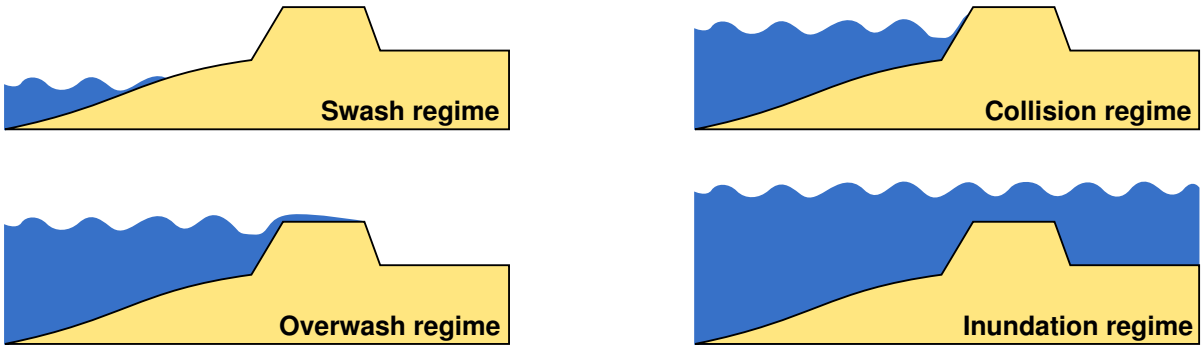

Figure 2.3: Different storm regimes defined by Sallenger (2000).

Donnelly et al. (2006) uses a slightly different terminology in which the inundation regime is called inundation-overwash and the overwash regime is considered as runup-overwash. The focus of this thesis is on the overwash regime containing both the runup-overwash as the inundation-overwash. Overwash can initiate the breaching process during which the crest elevation of the beach profile is lowered and sediment is transported into the bay. The breach channel can remain open after the storm to tidal flows.

2.2.2 Morphological response during overwash conditions

As mentioned in section 2.2.1, all the storm regimes have their own characteristics regarding the morphological response. The response during runup-overwash and inundation-overwash is complicated by the large variety of processes that play a role. Donnelly et al. (2006) mentions that the following processes determine the extent and magnitude of overwash deposits:

1. Tidal phase during storm, storm surge magnitude and storm duration;
2. Wave height, wave period and storm approach angle;
3. Nearshore bathymetry and beach topography, in particular barrier width and elevation;
4. Wind direction and velocity;
5. Presence or absence of dune vegetation.

Typical overwash formations are shown in Figure 2.4. Overwash usually exploits existing gaps or lower areas in the foredune line. The resulting flow transports sediment through the gap, known as a **throat**, and spreads it laterally on the back barrier. Once the flow widens, the flow velocity reduces and entrained sediment is deposited. The process is called **fanning overwash**, refering to the resulting features called **washover fans**. Once the storm reduces in intensity, sand is also deposited in the throats, causing a slight local accretion. If neighboring washover fans interact, a **washover terrace** is formed. **Sheetwash** is evidence of inundation by which the entire barrier is subject to erosion (Donnelly et al., 2006).

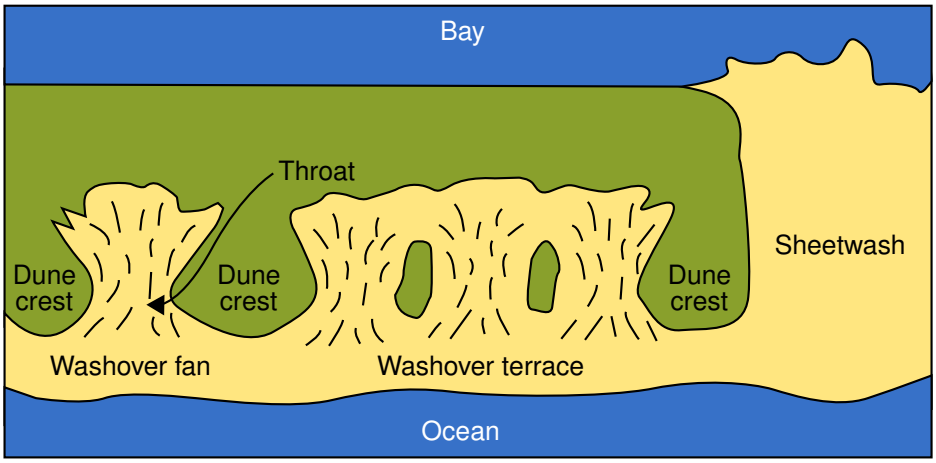

Figure 2.4: Definitions of common morphological deposits occurring during overwash conditions. Adapted from Donnelly et al. (2006).

2.3 Breaching process

There are many failure mechanisms that can initiate a breaching process (Ministerie van Verkeer en Waterstaat, 2007). One of the simplest is the erosion due to a continuous flow caused by a large enough water level elevation, which is called inundation-overwash. Eventually, all failure mechanisms result in a deformation of the dike or dune profile.

Visser (1998) presents in his BRES model a decomposition of the breaching processes in which five distinct phases are recognised:

1. Steepening of the inner slope of the dike in the breach channel up to a critical slope.
2. Retrograde erosion of the inner slope at the constant critical slope, yielding a decrease of the width of the crest of the dike in the breach.
3. Lowering of the top of the dike in the breach, with constant critical breach side slope angles, resulting in an increase of the width of the breach.
4. Critical flow stage in which the breach continues to grow mainly in lateral direction. The vertical growth of the breach depends on the erodability of the base of the dike.
5. Subcritical flow stage in which the breach continues to grow until the flow velocities become so small that sediment transport is not initiated any more. The flow through the breach stops when the hydraulic gradient over the dike reaches zero.

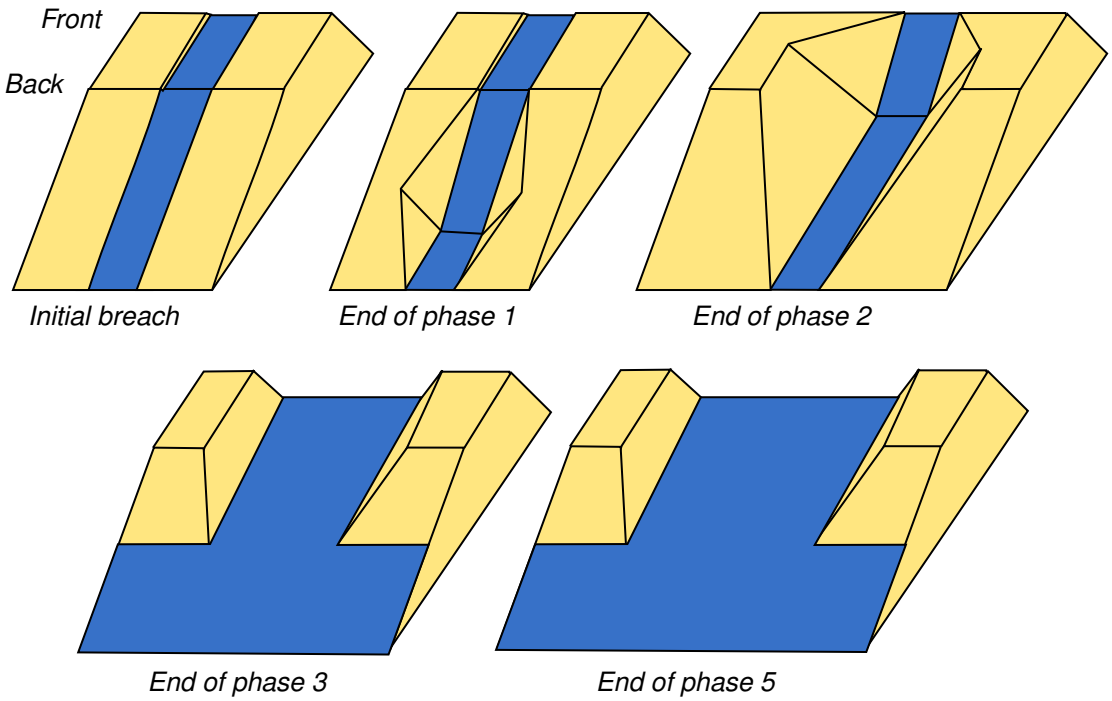

Figure 2.5: Different phases during the breaching process. Adapted from Visser (1998).

2.4 Sediment transport

2.4.1 General introduction

By bed shear stresses, sediment particles on the bed are forced into movement. Gradients in transport rates q result in a change of the bottom level z_b, simply based on continuity considerations (also known as Exner's Law):

$$\frac{\partial z_b}{\partial t} + \frac{1}{1-n}\left(\frac{\partial q_x}{\partial x} + \frac{\partial q_y}{\partial y}\right) = 0 \tag{2.1}$$

In which the parameter n represents the porosity of the bed, which has generally a value in the order of 0.4. Examining this straightforward relation, large flow velocities do not necessarily lead to large bottom level changes. If transport rates are approximately constant in time and space, no substantial bed level change will occur. Especially at locations where a strong change in hydrodynamics occurs, for example a narrowing or a widening of a channel, large gradients in transport rates will arise.

Sediment transport formulae relate the sediment transport rates to the flow velocity, among other parameters. Although transport formulas are based on physical considerations, like the initiation of movement, calibration remains important.

Distinction is made between bed-load and suspended load transport (Bagnold, 1956):

- **Bed-load** transport is the sediment transport mode that consist of the particles that are rolling and making small jumps on the bed.
- **Suspended load** transport is the the part of the sediment transport load consisting of particles that are suspended in the water column and are not in contact with the bed.

At high shear stresses (Shields parameters larger than 0.8-1.0), particles move in multiple layers which is known as **sheet flow transport** (Bosboom and Stive, 2013). Since the particles are in contact with the bed, this transport mode is considered as bed-load transport. The different transport modes are visualised in Figure 2.6.

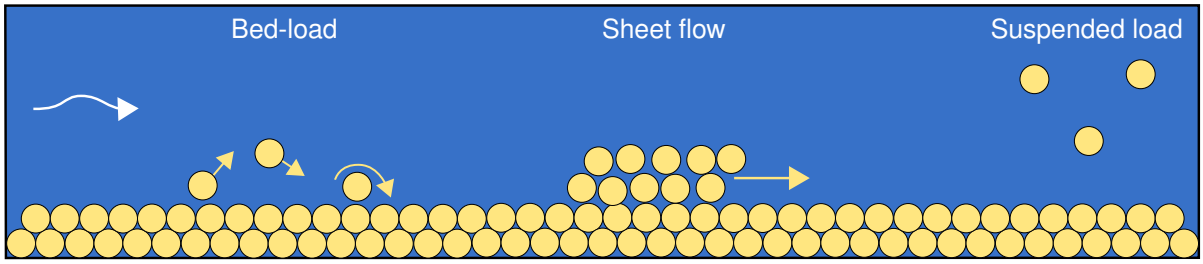

Figure 2.6: Different sediment transport modes.

2.4.2 Calculation of transport rates

The total load is the sum of the bed-load and suspended load modes. Mathematically, it is defined as the product of the flow velocity u and the sediment transport concentration c, integrated over

the flow depth h:

$$q = \int_0^h u(z)\, c(z)\, dz \tag{2.2}$$

For a depth averaged model, this equation is approximated by the product of the depth averaged flow velocity U, the depth averaged sediment transport concentration C and the water depth:

$$q = UCh \tag{2.3}$$

In a depth averaged model, the contributions of the bed-load transport (subscript b) and the suspended load transport (subscript s) to the depth averaged sediment concentration C are superimposable:

$$\left.\begin{array}{l} q = q_b + q_s \\ q_b = U_b C_b h = U C_b h \\ q_s = U_s C_s h = U C_s h \end{array}\right\} q = U\left(C_b + C_s\right) h = UCh \rightarrow C = C_b + C_s \tag{2.4}$$

This formulation is mathematically valid. However, one should keep in mind that C_b and C_s are averaged over the full water depth and are hence *not* the average concentrations in the referred layers. The actual concentrations that occur in these layers can differ substantially since the bed-load layer thickness is rather small (in the order of centimeters).

An empirical equation is required to relate the sediment transport rates to the hydrodynamic conditions. For example, two distinct sediment transport equations are implemented in XBeach. Both calculate the equilibrium concentration C_{eq}, the concentration at which the entrainment of sediment is in equilibrium with the sedimentation, based on the depth averaged velocities:

- Soulsby-Van Rijn: $C_{eq,b} \sim U^{2.4}$ and $C_{eq,s} \sim U^{2.4}$
- Van Thiel-Van Rijn: $C_{eq,b} \sim U^{1.5}$ and $C_{eq,s} \sim U^{2.4}$

Equation 2.3 only accounts for the advection of sediment. In reality, suspended sediment is also transported by dispersion. Therefore, a depth averaged advection-diffusion equation can be used to calculate the actual sediment concentrations (Galappatti and Vreugdenhil, 1985):

$$\frac{\partial hC_s}{\partial t} + \frac{\partial hC_s u^E}{\partial x} + \frac{\partial hC_s v^E}{\partial y} + \frac{\partial}{\partial x}\left(D_h h \frac{\partial C_s}{\partial x}\right) + \frac{\partial}{\partial y}\left(D_h h \frac{\partial C_s}{\partial y}\right) = \frac{hC_{eq,s} - hC_s}{T_s} \tag{2.5}$$

In this equation, D_h is the horizontal dispersion coefficient and the superscript E refers to the Eulerian frame of reference. The right-hand side of this equation can be viewed as the difference between the erosion and the deposition flux $E - D$ which is the forcing in the Galappatti equation. For the suspended load, an adaptation time scale T_s is included to account for the time it takes to get to the equilibrium concentration. In contrast, bed-load sediment is assumed to react instantaneously to velocity changes because turbulent mixing in the bed-load layer is rather small and it therefore influences the motion of sediment particles only slightly (Bosboom and Stive, 2013):

$$C_b = C_{eq,b} \tag{2.6}$$

Appendix C provides a complete overview of the equations used in the morphological computation in the XBeach model.

2.4.3 Initiation of motion as studied by Shields

At small flow velocities, the forcing to bring the sediment particles into motion is not sufficient. Shields (1936) introduced the concept of initiation of motion, the conditions at which the particles just start moving. He considered the stability of an individual particle. Figure 2.7 presents the considered forces that act on a sediment grain (in reality, other forces might be also relevant). The **gravity force** F_G is directly related to the mass of the particle. The contraction of the flow lines around the particles results in a lower local pressure above the particles (Bernoulli law) and therefore in a net upward directed **lift force** F_L. Further, the **drag force** F_S is the result of the skin friction and a pressure difference on the up and downstream sides of the grain by the flow separation at the downstream side of the particle (Bosboom and Stive, 2013).

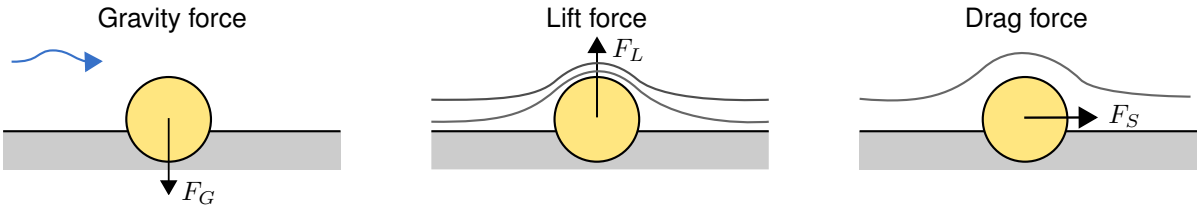

Figure 2.7: Forces that act on an individual sediment grain. Adapted from Bosboom and Stive (2013).

At the conditions of initiation of motion, these forces are in equilibrium. A vertical force balance based on simplifications, for example a spherical geometry, results in what is known as the critical Shields parameter θ_{cr} (Shields, 1936):

$$F_G = F_L \rightarrow c_1 \left(\rho_s - \rho\right) g D^3 = c_2 \rho U_{cr}^2 D^2 \tag{2.7a}$$

$$\theta_{cr} = \frac{c_1}{c_2} = \frac{\rho U_{cr}^2 D^2}{\left(\rho_s - \rho\right) g D^3} = \frac{\tau_{b,cr}}{\left(\rho_s - \rho\right) g D} \tag{2.7b}$$

In these equations, ρ_s represents the sediment density, ρ the density of water, g the gravitational acceleration, D the sediment grain size, U_{cr} the critical depth averaged flow velocity, τ_b the critical bed shear stress and c_i are constants. The critical Shields parameter is a constant which depends on the particle Reynolds number. In reality, there is not always a balance of the forces. The Shields parameter θ, so not the critical one, represents the actual forcing on the particle and is defined as a function of the relative density Δ and the actual bed shear stress τ or the bed shear stress velocity u_*:

$$\theta = \frac{\tau_b}{\left(\rho_s - \rho\right) g D_{50}} = \frac{\tau_b}{\Delta \rho g D_{50}} = \frac{\rho u_*^2}{\Delta \rho g D_{50}} = \frac{u_*^2}{\Delta g D_{50}} \tag{2.8}$$

Many empirical sediment transport formulae calculate the sediment transport rate as a function of the difference between the actual Shields parameter θ and the critical Shields parameter θ_{cr}. If the critical Shields parameter is larger than the actual Shields parameter value, a zero transport rate is calculated.

2.5 The XBeach model

The hurricane seasons, especially those of 2004 and 2005, have pointed at an urgent need to be able to assess the vulnerability of coastal areas and design coastal protection for future events.

In view of this, the Morphos-3D project was initiated by the US Army Corps of Engineers. As part of this initiative, an open-source program, XBeach for eXtreme Beach behaviour, has been developed to model the nearshore response to hurricane impacts (Roelvink et al., 2009).

The model domain is divided into a two-dimensional and depth averaged computational grid. XBeach solves the long waves based on the shallow water equations. Short waves and short wave groupiness are taken into account by means of a non-stationary wave action balance. In this way, the short waves are not phase-resolved, but the wave energy of the short waves varying on the wave-group time scale is taken into account. Sediment transport and morphology is accounted for by means of the sediment transport equation of Van Thiel-Van Rijn (or Soulsby-Van Rijn), the Galappatti equation, the Exner equation and an avalanching algorithm. In the XBeach model, two artificial limiters are implemented to restrict the sediment transport rates that can occur: the sediment concentration magnitude is limited to c_{max} (by default $0.1\ m^3/m^3$) and the Shields parameter can be restricted by θ_{max} to 1 (by default not limited). For a more detailed description of the XBeach model, reference is made to Appendix C.

2.6 Physics under breaching and overwash conditions that are not included in the XBeach model

Under overwash and breaching conditions, large flow velocities can result in large sediment transport rates and concentrations. Sediment transport formulae are calibrated mainly on river and coastal conditions with rather small velocities. Therefore, it is wise to observe the processes that can affect the transport rates at these conditions, to get to more realistic predictions.

2.6.1 Hindered erosion by dilatancy

Van Rhee (2010) assumes that erosion is hindered by dilatancy effects at high flow velocities. The concept of dilatancy is explained in Figure 2.8. Soil with a small porosity requires an increase of pore volume before the grains can be picked-up from the bed. The increase of pore volume requires an inflow of water. Since this inflow of water can be rather slow at certain conditions, under-pressure in the pores hinders the entrainment of sediment particles with an in-bed directed forcing.

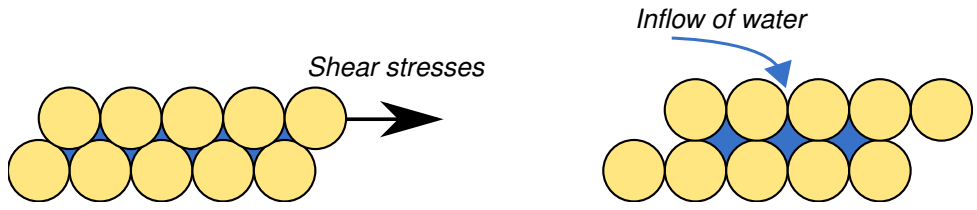

Figure 2.8: The principle of dilatancy explained. Particles in the bed with a small porosity require an increase of the pore volume before they can be picked-up.

This in-bed directed forcing should be included in the concept of initiation of motion, which was introduced in Section 2.4.3. By taking this force into account, it follows that the critical Shields parameter has to be modified by (see Appendix A for the derivation):

$$\theta_{cr}^{D} = \theta_{cr}\left(1 + \frac{v_e}{k_l}\frac{n_l - n_0}{1 - n_l}\frac{A}{\Delta}\right) \tag{2.9}$$

In this formulation, v_e refers to the erosion velocity, k_l is the permeability, n_0 is the porosity prior to erosion, n_l is the porosity in the sheared zone and the parameter A is equal to $3/4$ for single particles and approximately 1.7 for a continuum.

Magnitude of the dilatancy effect

The theory is demonstrated by Van Rhee (2010) using the Van Rijn (1984a) pick-up function Φ_p:

$$\Phi_{p,VanRijn} = \frac{E}{\sqrt{\Delta g D_{50}}} = 0.00033 D_*^{0.3}\left(\frac{\theta - \theta_{cr}}{\theta_{cr}}\right)^{1.5} \tag{2.10}$$

$$\Phi_{p,VanRhee} = \frac{E}{\sqrt{\Delta g D_{50}}} = 0.00033 D_*^{0.3}\left(\frac{\theta - \theta_{cr}^{B\&D}}{\theta_{cr}^{B\&D}}\right)^{1.5} \tag{2.11}$$

In these equations is E the erosion flux and D_* the dimensionless grain size. Van Rhee (2010) translates the dimensionless pick-up flux to the velocity at which the bed is moving upward, known as the sedimentation velocity v_{sed}. The sedimentation flux *S* is in this definition the product of the settling velocity of the particles w_s and the near bed concentration c_b. The sedimentation velocity can be calculated as:

$$v_{sed} = \frac{S - E}{1 - n_0 - c_b} = \frac{w_s c_b - E}{1 - n_0 - c_b} \tag{2.12}$$

Figure 2.9 shows the effectiveness of taking dilatancy into account. The erosion velocity is reduced substantially, but still an overestimation compared to measurement data is made.

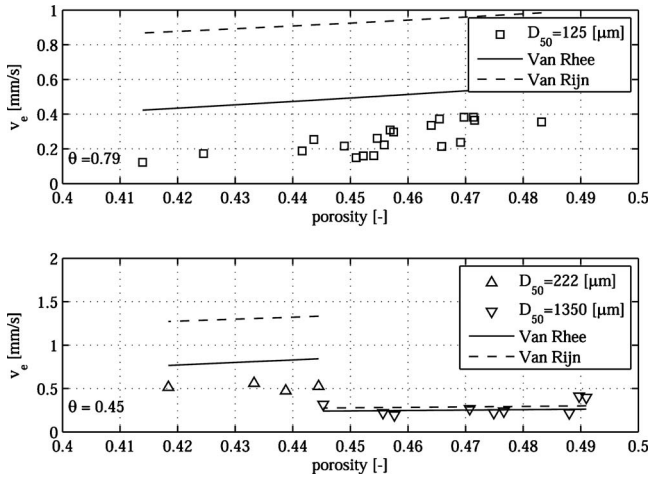

Figure 2.9: Computed and measured erosion velocities as a function of the porosity for different grain sizes. Taken from Van Rhee (2010).

The limitation to the critical Shields parameter θ_{cr} is expected to have a comparable effect on the sediment transport rates as these are related to the the pick-up flux.

2.6.2 Hindered settling

In nature, very large sediment concentrations can be observed, Winterwerp (2006) mentions the concept of hyperconcentrations. For example, in the Yellow River near Sammenxia in China, peak concentrations up to $911\ g/l$ where measured. These concentrations occurred with very fine sediments with a median grain size of $D_{50} = 30\ \mu m$ (Winterwerp, 2006). Large concentrations can also play a role at larger grain sizes, for example in a flow with large velocities in case of overwash or breaching conditions. These large concentrations are likely to be measured close to the bed. See Figure 2.10 for a schematic visualisation of a typical concentration profile.

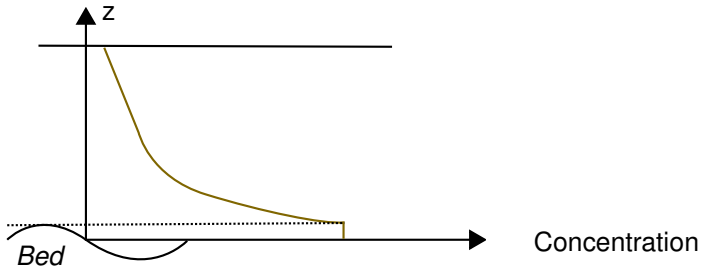

Figure 2.10: A typical sediment concentration profile over depth. Adapted from Van Rijn (2007b).

As a consequence of large flow velocities, the sediment concentration can lead to a reduction of the fall velocity of sediment particles (Richardson and Zaki, 1954):

$$w = \epsilon^{\alpha} = (1 - c)^{\alpha} w_0 \tag{2.13}$$

In this expression is the fall velocity of a single grain noted by w_0, is the reduced fall velocity expressed by w and ϵ refers to the voidage. The value of α is generally within the range of $2.3 - 4.6$, depending on the particle Reynolds number.

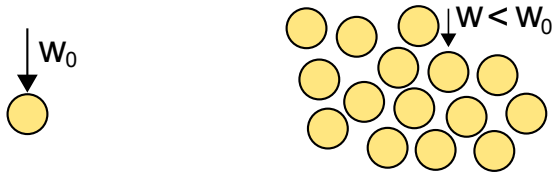

Figure 2.11: Principle fall velocity reduction at high sediment concentrations.

Magnitude of the hindered settling effect

Figure 2.12 shows that the fall velocity should be reduced with $20-40\%$ at sediment concentrations of 10% and $5 - 10\%$ at concentrations of 2%.

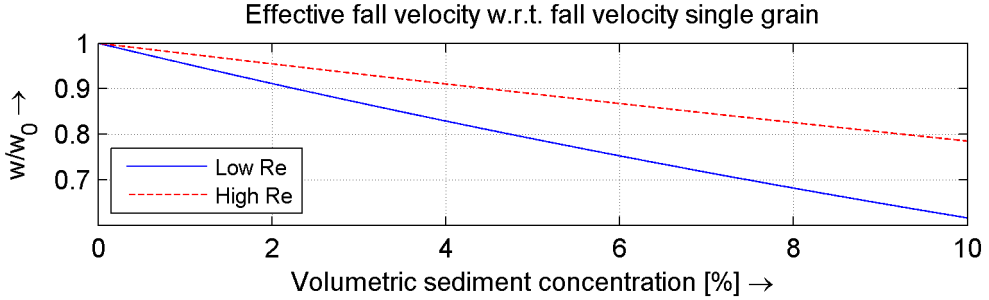

Figure 2.12: Fall velocity reduction as a function of the volumetric sediment concentration. Small Reynolds particle numbers approach zero, large values approach infinity.

It is difficult to state a-priori how substantial the influence of reducing the fall velocity at high concentrations will be on the sediment transport rates. In general, the time scale in the depth averaged advection-diffusion equation, as presented in Equation 2.5, will be affected. The time scale is often a function of the ratio between the water depth and the fall velocity:

$$T_s = f\left(\frac{h}{w}\right) \tag{2.14}$$

A reduction of the fall velocity leads hence to a larger time scale. A short, but large, equilibrium concentration peak is damped out more effectively. Also a low equilibrium concentration peak is subject to more damping. It is case dependent whether a larger time scale results in more or less erosion.

Since bed-load transport is supposed to obtain the equilibrium transport rates instantaneously, the diffusion model is of no importance for bed-load transport. Therefore, the fall velocity that determines the time-scale in the advection-diffusion model is only relevant for the suspended load transport.

2.6.3 Damping of turbulence

For large sediment concentrations, sediment particles have a damping effect on turbulence. As a result, the velocity profile and with that the sediment concentration profile are also affected by the presence of sand in the water column (Van Rijn, 2007b). Winterwerp (2001) showed the importance of taking damping of turbulence into account by analysing experimental data. Figure 2.13 shows the eddy viscosity profile and the concentration profile as calculated by Toorman (2003) which confirms the findings of Winterwerp (2001). As visible, the effects of the presence of sand are substantial.

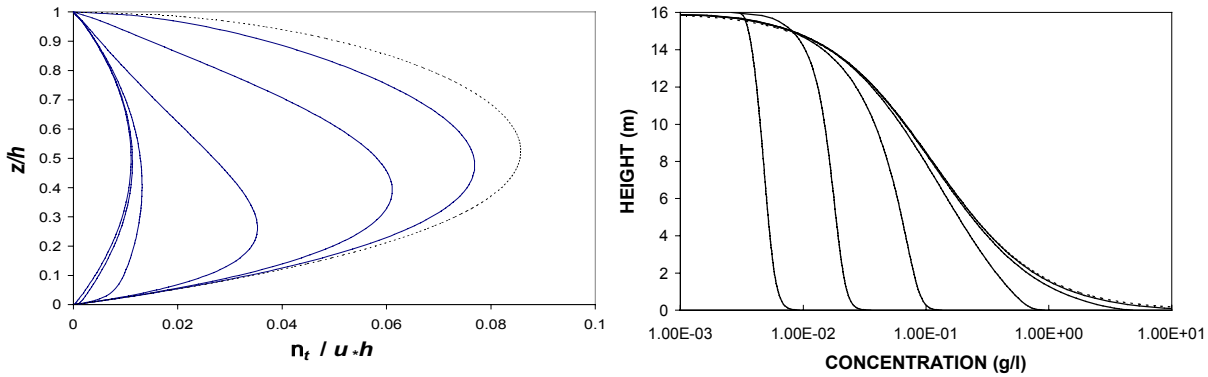

Figure 2.13: Left graph: the effect of sand on the vertical eddy viscosity ν_T profile in steady open-channel flow, increasing concentration from right to left (4.9, 16.3, 49, 163, 326 and 488 mg/l). Right graph: simulated concentration profiles, increasing concentration from left to right. Taken from Toorman (2003).

Magnitude of the damping of turbulence

The results of Winterwerp (2001) and Toorman (2003) are based on an open channel-flow configuration. Under these conditions, an almost perfect parabolic eddy viscosity profile is observed, see Figure 2.13. However, flow velocities are highly variable in coastal areas and the presence

of a logarithmic velocity profile is questionable. Still, turbulence is present which should thus be damped. The magnitude of the turbulence damping is highly dependent on the turbulence model and the case characteristics.

2.7 Limitations of the XBeach model

The XBeach model is a robust, but computationally intensive model. It can take days for the current model to compute the complete morphodynamics of a single storm event, even if a morphological acceleration factor is used on a modern quad-core i7 computer. Therefore, it is justifiable to make simplifications. In this end, it is not the objective of the model to compute everything perfectly, requiring years to calculate a single storm event.

Still, it is very important to be aware of the assumptions made in the model. If a certain process is neglected, one should be aware of other processes being influenced by the assumption as well. XBeach, and morphodynamic models in general, should hence be used as a prediction tool for an engineer and not as a black box that is an exact representation of reality. Therefore, the most important limitations of the XBeach model are identified. In Chapter 5, some of these limitations are solved by improving the model.

2.7.1 Processes which are schematised in XBeach

Depth averaging

The XBeach model consists of a $2DH$ grid: the spatial domain is divided in grid cells, but the vertical dimension is modelled by just one layer of cells. As a consequence, vertical profiles are not computed explicitly. For example, the suspended sediment concentration is often much larger near the bottom than near the surface, see Figure 2.10. All the information of the vertical structures is hence put in one single number for each grid cell. To bring the Stokes drift into account, two velocities are calculated: the Eulerian flow velocity and the Lagrangian flow velocity. By this simplification, spiral flow motions and depth varying flow directions are not taken into account.

Phase-averaged short waves

The wave energy of the short waves is calculated by the wave action balance, see Appendix C.1.2. The exact surface elevation and phases of these short waves are not resolved. This is not a very bad assumption since solving them would require very small grid sizes (in the order of centimeters) to model the shape of these waves smoothly. Most of the XBeach models that are applied on practical storm cases consist of grid sizes that are two orders of magnitude larger. By taking into account the wave-group varying energy of the short waves, the waves are modelled much better already than by other morphodynamic models. Further, the XBeach model is applied on dissipative beaches for which most of the short wave energy is dissipated once the short waves reach the shoreline.

The Exner equation

The Exner equation is not fully mass-conservative since it is derived on a steady-state assumption regarding the sediment concentrations. Hence, a change in sediment concentration in the water column does not result in a change of the bottom level:

$$\frac{\partial z_b}{\partial t} + \frac{f_{mor}}{1-n}\left(\frac{\partial q_x}{\partial x} + \frac{\partial q_y}{\partial y}\right) = 0 \tag{2.15}$$

For small concentrations, this is not expected to be a problem, bottom level changes due to gradients in sediment transport are expected to be much more substantial. However, large inaccuracies could occur once gradients in sediment transport are (almost) zero and a large concentration of sediment is present in the water column.

To illustrate the problem, a water column with a height of $10\ m$, an initial sediment concentration of $0.1\ m^3/m^3$ and a flow velocity of $0\ m/s$ is considered. Due to the zero flow velocity, sediment transport gradients are zero, there are hence no bottom level changes to be expected by the Exner equation. However, the sediment mass in the water column is substantial which will sedimentate fully at the bottom by the gravity force. Assuming a bed porosity of 0.4, the raise of the bed level by the settling of the sediment grains in the water column should equal eventually:

$$\Delta z = \frac{hC}{1-n} = \frac{10 \cdot 0.1}{1-0.4} = 1.67\ m \tag{2.16}$$

Empirical sediment transport equations

Sediment transport rates predicted by empirical formulae can vary up to an order of magnitude, which is quite common for sediment transport predictions (Bosboom and Stive, 2013). Therefore, calibration of the formulae on the location specific conditions is important. Unfortunately, data of the transport rates is scarce and the conditions can vary spatially within a model domain.

Non-cohesive sediments

The focus of the research is on sand. Cohesive forces between the grains, which may occur with clay and fine particles, are not studied. Winterwerp and van Kesteren (2004) explain the physics of cohesive sediment in the marine environment. They state that it is impossible to provide generally applicable rules to predict the transport of cohesive sediments since it varies too much in composition and can occur in many appearances. The theories related to cohesive sediments are generally relevant for particles smaller than $63\ \mu m$. For beaches with course grains in the order of $300\ \mu m$, it is thought to be reasonable to ignore the cohesive forces between grains.

Bed friction

Bed friction is modelled by a constant Chézy value over the whole model domain (generally in the order of $55\ m^{0.5}/s$), which is hence not depth dependent. However, it is possible to vary the Chézy value per user defined region.

2.7.2 Processes modelled incorrectly by XBeach

Rough estimate of bed slope effect

The presently implemented bed slope effect is based on the engineering formula of Soulsby (1997):

$$q_{s,slope} = q_s \left(1 - \alpha \frac{\partial z_b}{\partial s}\right) \tag{2.17}$$

However, there is a slight difference: Soulsby's formulation is only a modification of the magnitude of the transport in the direction of the transport vector. The currently implemented slope effect works slightly different (Deltares, 2014b):

$$q_{x,slope} = q_x - \alpha h C \sqrt{(u^L)^2 + (v^L)^2} \frac{\partial z_b}{\partial x} \tag{2.18a}$$

$$q_{y,slope} = q_y - \alpha h C \sqrt{(u^L)^2 + (v^L)^2} \frac{\partial z_b}{\partial y} \tag{2.18b}$$

The *magnitude* of the Lagrangian velocity is used for the correction. Regardless the direction of the velocity, the transport is modified. For example, if the Lagrangian vector is directed in x-direction, the transport in y-direction is affected too with the same quantity. Using the magnitude of a velocity is hence in contrast to the theory of Soulsby.

Even if the engineering formulation of Soulsby is implemented properly, the considered bed slope effect has it limitations. More physical based expressions are available in literature, an overview of many theories is given by Van Rijn (1993).

2.7.3 Processes not modelled by XBeach

Section 2.6 provided a description of several processes which are relevant for breaching and overwash cases but which are not yet implemented in the XBeach model:

- Hindering of erosion by dilatancy
- Hindered settling
- Turbulence damping

Also aeolian sediment transport and vegetation are not (fully) considered in the XBeach model, a short description of these processes is given below.

Aeolian sediment transport

An important process that can recover the dune profile between storms is aeolian transport. Prior to the overwash regime and during the days and months after the storm, the wind can play an important role in the evolution of the dune profile. Aeolian transport is currently not included in the hydrodynamic models, but the coupling of these models with an aeolian sediment transport model can be an option (Den Bieman, 2012). During overwash conditions, the dunes are largely under water and this process is not relevant. In this thesis, the focus is on the hydrodynamic sediment transport and aeolian transport is not considered.

Vegetation

The presence of vegetation can have substantial influences on the morphological evolution over time. Grass and woody plants can stabilize dunes against windblown sand transport (Kobayashi et al., 2013). The negligence of aeolian sediment transport can hence be a reasonable assumption if such vegetation is present. Also sediment transported by water can be affected by the vegetation. The near-bed velocity will be reduced and vegetation can reduce the erosion and promote the deposition. But there is also a real possibility for in-stream objects, such as vegetation, to promote localized erosion (Rominger et al., 2010).

In the XBeach model, the effect of vegetation on the entrainment and deposition of sediment is not taken into account. However, XBeach can model the influence of vegetation on the flow. This is done with a dissipation term in the wave action balance due to short wave attenuation by vegetation and a drag force in the momentum equation due to the interaction of vegetation with the mean and group vary flow. The drag force due to short wave flow is not yet implemented. The mentioned approach is based on Mendez and Losada (2004).

The flow patterns can hence be adjusted, but data on the vegetation parameters is often scarce and these can vary spatially. Therefore, a simple bed roughness increase at the vegetated location could also be a reasonable option. The influence of vegetation on the erosion and deposition of sediment is not modelled by the complexity of the subject.

Chapter 3

Assessment XBeach performance on overwash and breaching cases

Prior to the improvement of the XBeach model, the performance of the current model will be assessed. For this assessment, the "Groundhog Day" release of the source code is used (Deltares, 2014b). Besides the default settings of the model, the behaviour of the artificial limiters θ_{max} and C_{max} (see Section C.1.5) and the older sediment transport equation of Soulsby-Van Rijn, will be examined.

A variety of laboratory tests and field measurements are used to observe the relevant processes during overwash and breaching cases. First, the behaviour of the θ_{max} limiter is tested based on measurements on sediment transport rates by Voogt et al. (1991). Thereafter, the evolution of a beach is examined both in $1D$ with a laboratory experiment as in $2D$ with data on a full-scale breach at Het Zwin, the Netherlands. Finally, the performance of the model on the morphodynamic evolution by Huricane Ivan on Santa Rosa Island is investigated.

The Brier Skill Score (Murphy and Epstein, 1989) and the bias are used to asses the skill of the model with respect to measurement data, which are defined in this thesis as:

$$BSS = 1 - \frac{MSE\left(computed, measured\right)}{MSE\left(initial, measured\right)} = 1 - \frac{\sum_{i=1}^{N}\left(z_{b,computed,i} - z_{b,measured,i}\right)^2}{\sum_{i=1}^{N}\left(z_{b,initial,i} - z_{b,measured,i}\right)^2} \tag{3.1}$$

$$Bias = \frac{1}{N}\sum_{i=1}^{N}\left(z_{b,computed,i} - z_{b,measured,i}\right) \tag{3.2}$$

3.1 Sediment concentrations measured by Voogt et al.

In this section, the sediment transport equations of XBeach with its limiters are compared to laboratory data. First an introduction to the experiment is given.

3.1.1 Introduction

Voogt et al. (1991) performed a full-scale flume experiment with a water depth of about $1\ m$ and flow velocities in the range of $1.5 - 2.5\ m/s$. Due to a large flow discharge, feeding sediment at the upstream boundary was not an option, therefore a self-eroding flow without an initial sediment load in the flume was used. The $60\ m$ long test section of the flume was not long enough to ensure equilibrium transport at the end of the test section. Therefore, a two-dimensional mathematical model was used to compute, by extrapolation, the equilibrium sediment transport based on measurements of the sediment-concentration and flow-velocity profiles. Figure 3.1 presents the set-up of the experiment, see Voogt et al. (1991) for more details.

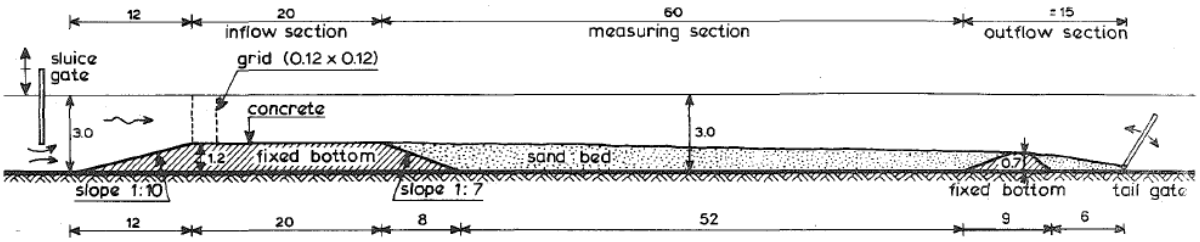

Figure 3.1: Experimental set-up of the experiment. Measures in meters. Taken from: Voogt et al. (1991).

3.1.2 Results

Figure 3.2 shows the results of the flume experiment of Voogt et al. (1991) in combination with the equilibrium sediment concentrations calculated with the formulae of XBeach. As visible, the modelled sediment transport rates increase in the model with Shields parameter restriction only linearly with the flow velocity once the actual Shields parameter is larger than one. The dataset suggests that this limiter results in too small sediment loads. Based on this dataset, the θ_{max} limiter seems to have a very poor predictive skill.

Another observation is that all modelled rates are an overestimation with respect to the data points. On the other hand, the shape of the predicted transport rates is in line with the data. The overestimation can be explained by the inexactness of the sediment transport formulae and the data. The uncertainty in the dataset, which is marked with the boxes in the figure, is quite substantial. Another explanation could be that a limitation to the transport formulae is required to translate the predictions in the graph horizontally. Which of the two explanations is true cannot be determined based on just one dataset.

The last conclusion that can be made based on this figure, is that the Van Thiel-Van Rijn equation results in transport rates similar to the Soulsby-Van Rijn method. There is hence no judgement possible which of the two transport formulae performs better.

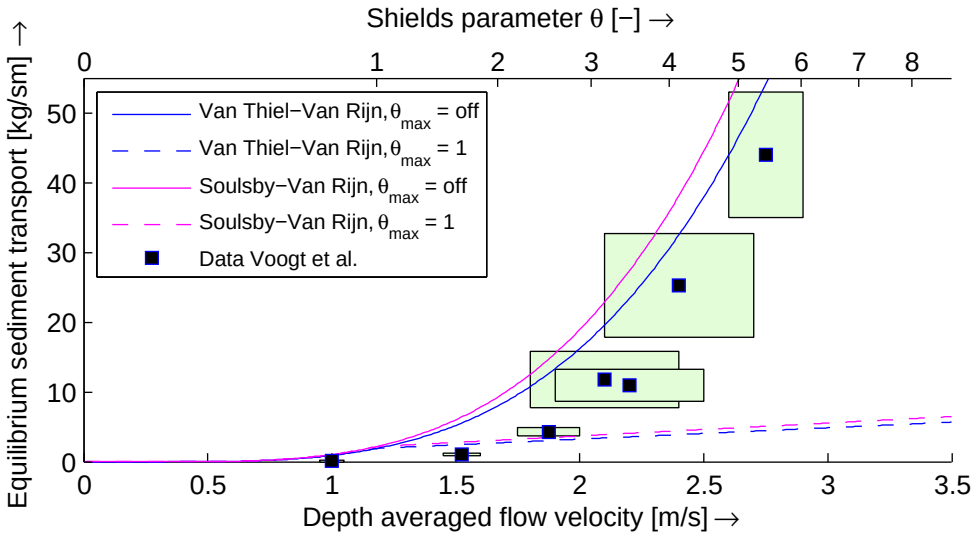

Figure 3.2: Data of Voogt et al. (1991) in combination with plot of the sediment transport function in XBeach with and without a limiter (limiter is set to $U_{max} = 1.2\ m/s$ according to the data of Voogt et al.).

The presented sediment transport rates are the total loads. The ratio between the bed-load transport and the total load is shown in Figure 3.3 for the Van Thiel-Van Rijn transport formulation with a variety of water depths. This graph shows that, for large flow velocities in the order of $1\ m/s$, the bed-load transport is of substantial less importance than the suspended load transport. This conclusion seems to be also valid for small water depths.

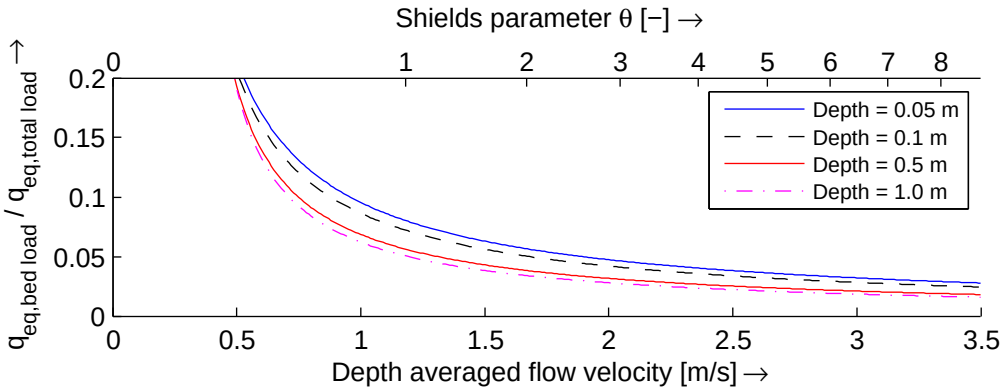

Figure 3.3: Sediment transport formulation of Van Thiel-Van Rijn with parameters based on data of Voogt et al. (1991). Plotted is the bed-load transport as a ratio to the total load for a variety of depths.

The measured equilibrium sediment transport rate of $44\ kg/sm$ at a flow velocity of $2.75\ m/s$ corresponds to a depth averaged sediment concentration of:

$$C = \frac{q}{\rho U h} = \frac{44}{2600 \cdot 2.75 \cdot 1} = 0.0062\ m^3/m^3 = 0.62\% \tag{3.3}$$

This depth averaged concentration is rather small. Unfortunately, the experiment is not performed with a smaller water depth. For example, the Van-Thiel-Van Rijn equation gives comparable sediment transport rates at a ten times smaller water depth of $0.1\ m$, see Figure 3.4. Since the flow velocity and the sediment transport rate are approximately equal to the original case but now the water depth is a factor ten smaller, the *depth averaged* equilibrium concentrations are for this case

now approximately a factor ten larger (up to 7%). It is possible that the dataset would have a different tendency if these larger depth averaged concentrations were met. Analyses based on this data set are hence not directly valid for large flow velocities in general.

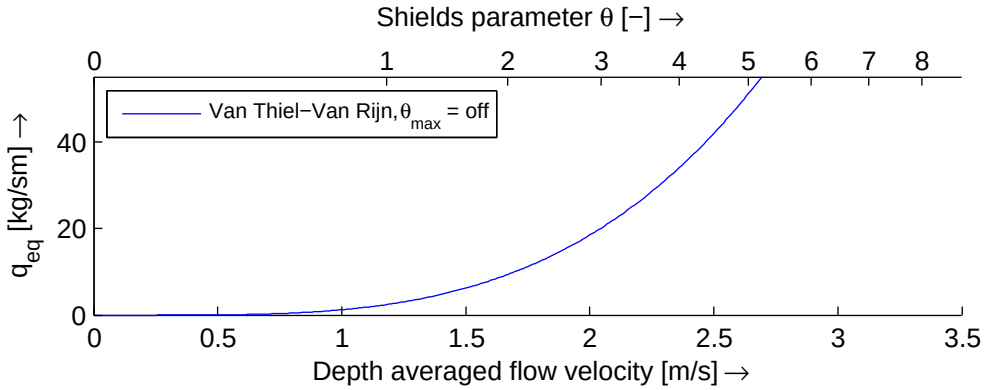

Figure 3.4: Same parameters as in the experiment, now with a ten times smaller water depth.

3.2 2DV Scheldt Flume experiment "Bresgroei"

In 1991, several experiments were performed in the Scheldt Flume of Waterloopkundig Laboratorium "de Voorst", the Netherlands. The purpose of the research was to get an understanding of the relation between the cross-section of a dike and the expected damage by a storm event. The data of the experiments are published in a comprehensive report (Steetzel and Visser, 1992). Figure 3.5 shows a visualisation of the experimental set-up. The applied down-scaling of the dike dimensions is $1 : 10$, the experiment is a representation of a $7\ m$ high dike with a water level located $0.5\ m$ above the top of the dike. At the beginning of the experiment, the element that blocks the water on top of the dike is removed, and the evolution of the dike profile is recorded with a video camera (see Figure 3.6) together with a registration of the water level elevation and flow velocity at several locations. The experiments vary in the type of foreshore, sediment grain size, porosity and in one case waves were involved. As an indication: flow velocities of $2.5 - 3.5\ m/s$ occurred on the inner dike slope (Steetzel and Visser, 1992).

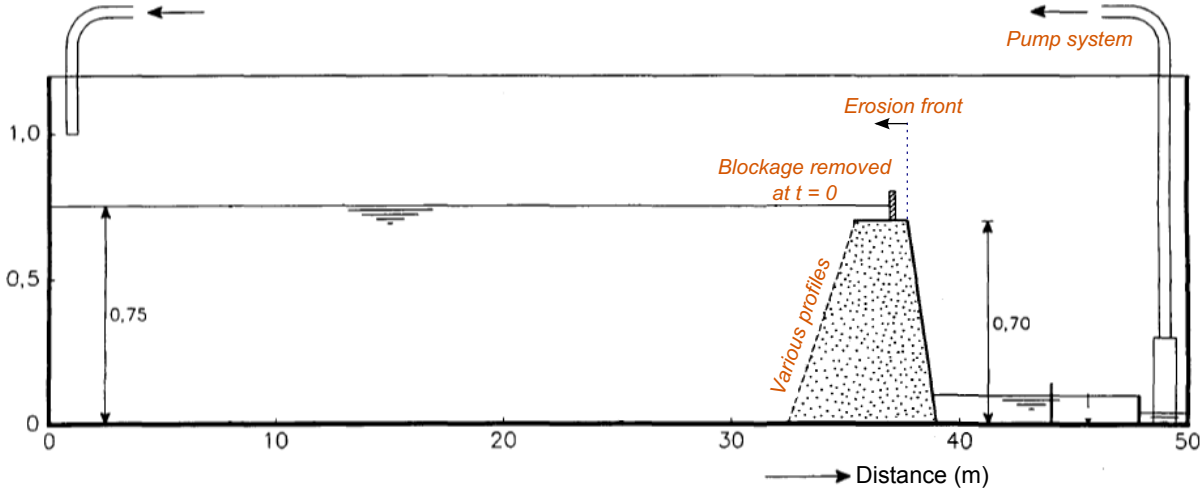

Figure 3.5: Set-up of the experiment. Adapted from Steetzel and Visser (1992).

3.2.1 Description experiment T5

For this assessment, the focus is on experiment T5. The experiment is characterised by a dike profile and no wave forcing is considered. Later, in Chapter 6 where the improved model is assessed, also other settings of this experiment are considered. Experiment T5 is characterized by the following characteristics:

- Bed slope front side: $1:4$
- Bed slope back side: $1:3$
- Length crown of the dike: $1.3\ m$
- Crown height: $0.70\ m$
- Water level: $0.75\ m$
- $D_{50} = 220\ \mu m$ and $D_{90} = 297\ \mu m$
- Porosity: $37.9 - 40.2\%$
- Duration experiment: $7\ min$

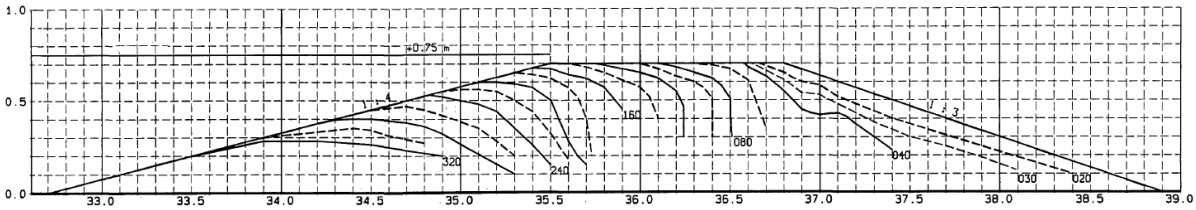

Figure 3.6: Cross-section of the dike in experiment T5 at several times (in seconds) after the beginning of the experiment. Both axis in meters. Taken from: Steetzel and Visser (1992).

3.2.2 Description XBeach model set-up

In XBeach, the experiment is modelled on a $1DH$ grid with grid cells of $0.05\ m$ around the dike, with a smooth increment up to $0.5\ m$ near the boundaries. To reduce the influence of the downstream boundary on the sediment flow, the model domain is extended up to a total length of $70\ m$ in downstream direction.

The model has been run for a small variety of settings. As a base run, the Van Thiel-Van Rijn sediment formulation is used with a maximum sediment concentration of $0.1\ m^3/m^3$. Further, bedload and suspended load transport are calculated separately. Figure 3.7 shows a time stack of the bed level of the base run.

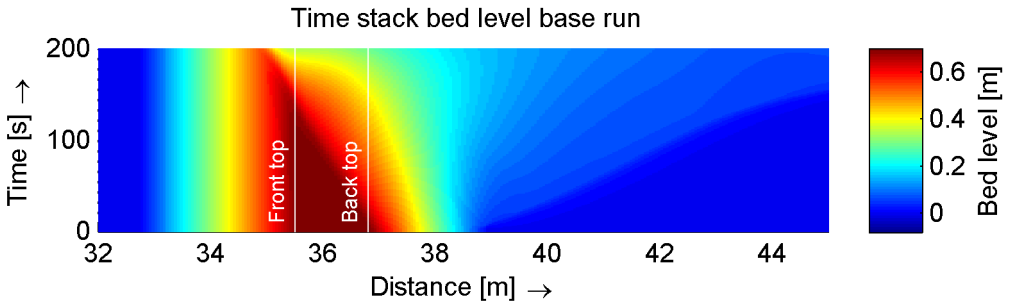

Figure 3.7: Time stack of the first $200\ s$ of the base run, modelled with XBeach.

In addition to this base run, the following modifications are made one by one:

- Using the older Soulsby-Van Rijn transport formulation.
- Limiting the Shields parameter θ_{max} by 1.0.
- Limiting the depth averaged concentration C_{max} to 0.3. Usually, sediment transport concentrations are limited to 0.1. To be precise, the bed-load transport and the suspended load transport are individually limited to half of this value.

For the present stage in the research, interest is drawn to the erosion rates that occur. As a measure, the propagation velocity of the erosion front is observed and compared to the experimental data. Further, also the shape of the eroded dike is examined to detect undesirable side effects of the sediment transport limiters.

3.2.3 Propagation velocity of the erosion front

Once the blockage is removed, water flows over the dike causing erosion of the inner dike face. As a consequence, the location of the inner dike crown line propagates towards the front of the dike, see Figure 3.7. Figure 3.8 shows the distance travelled by the erosion front in time.

Initially, a linear relation is observed between time and the location of the erosion front, both in the measurement data as in the model results. This implies a constant propagation velocity of the erosion front. For flume experiment T5, this propagation velocity equals approximately $0.01\ m/s$. This linear relation is noticed till the erosion front reaches the front dike top, which can be explained by the presence of a constant depth and flow velocity. Once the front dike top is eroded, the water level difference between the front and the back of the dike increases, causing a change in hydrodynamics. The same reasoning yields for the sedimentation front as visible in the time stack of Figure 3.7. Since the velocity downstream of the dike is smaller, but still more or less constant in time, a comparable linear relation is observed but with a smaller propagation velocity.

Figure 3.8 suggests that the Soulsby-Van Rijn formulation results in a serious overestimation of the erosion rates. The other model runs lead to a far more reasonable propagation of the erosion front on top of the dike crown. However, once the front dike top is eroded and the actual breaching takes place, different behaviour is observed. The Shields number restriction in the sediment transport formulas results in a substantial underestimation of the erosion, the limiter is too strict. Once the maximum value of the sediment concentration is increased to 0.3, larger erosion rates are observed. The maximum sediment concentration is hence reached in the base run, and by limiting the sediment concentration artificially to $0.1\ m^3/m^3$, the base run represents the propagation of the erosion front more accurately.

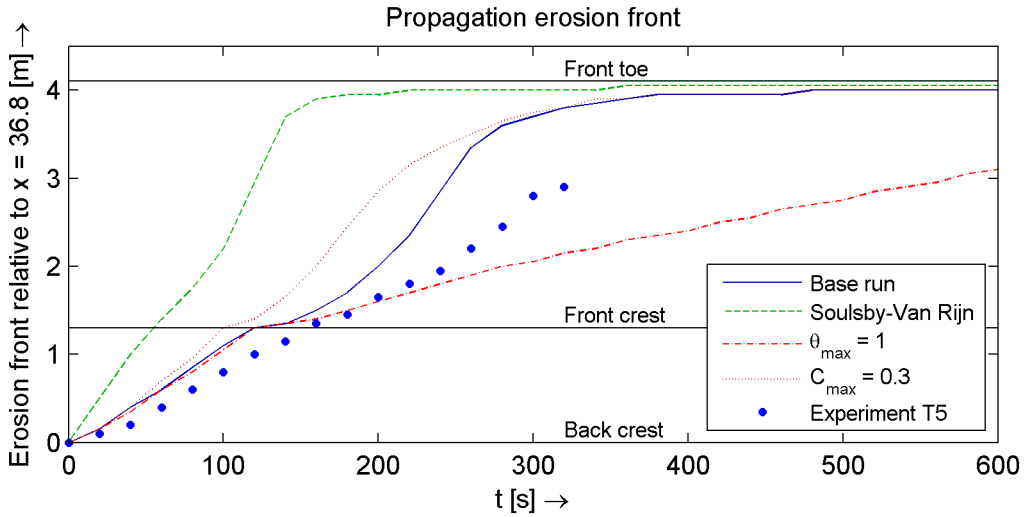

Figure 3.8: Propagation of the erosion front in time. The position of the erosion front is defined as the smallest x coordinate for which at least 1 centimeter erosion occurred. Note that the erosion front is propagating in negative x direction, as visualised in Figure 3.5. The tangent of a curve equals the propagation velocity of the erosion front.

3.2.4 Shape of the bed profile after erosion

Figure 3.9 presents a cross-section of the dike after $120\ s$. Since some of the runs are eroding much faster compared to the experimental data, the results are plotted again in Figure 3.10 at times on which the location of the erosion front corresponds to the experimental data. The focus of the analysis of this section is hence purely on the shape of the eroded profile and not on the times at which these are achieved, the latter has been treated in the previous section.

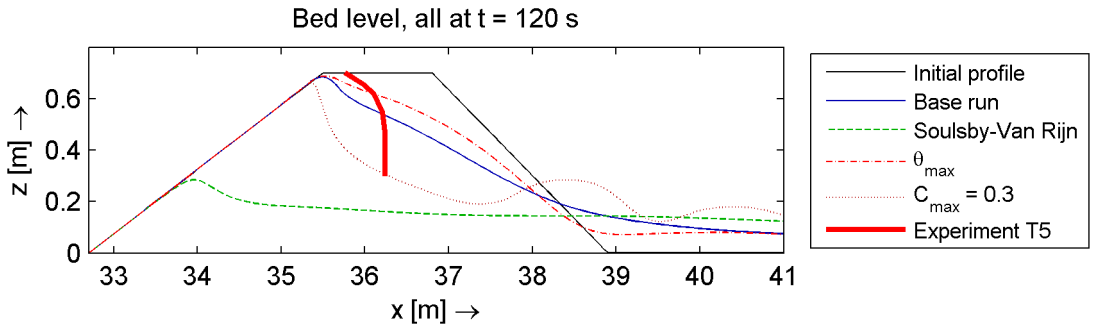

Figure 3.9: Bed profiles for the model runs, all presented after $120\ s$.

Limiting the Shields number shows a significant underestimation of the erosion rates, the bed level at the eroded locations is too high. Also the Soulsby-Van Rijn transport formulations do not lead to the desired results. Important to compare are the base run and the increment of the maximum concentration to $0.3\ m^3/m^3$. The latter shows a more accurate prediction of the bed profile, especially in the cross-section after $240\ s$ from the beginning of the experiment.

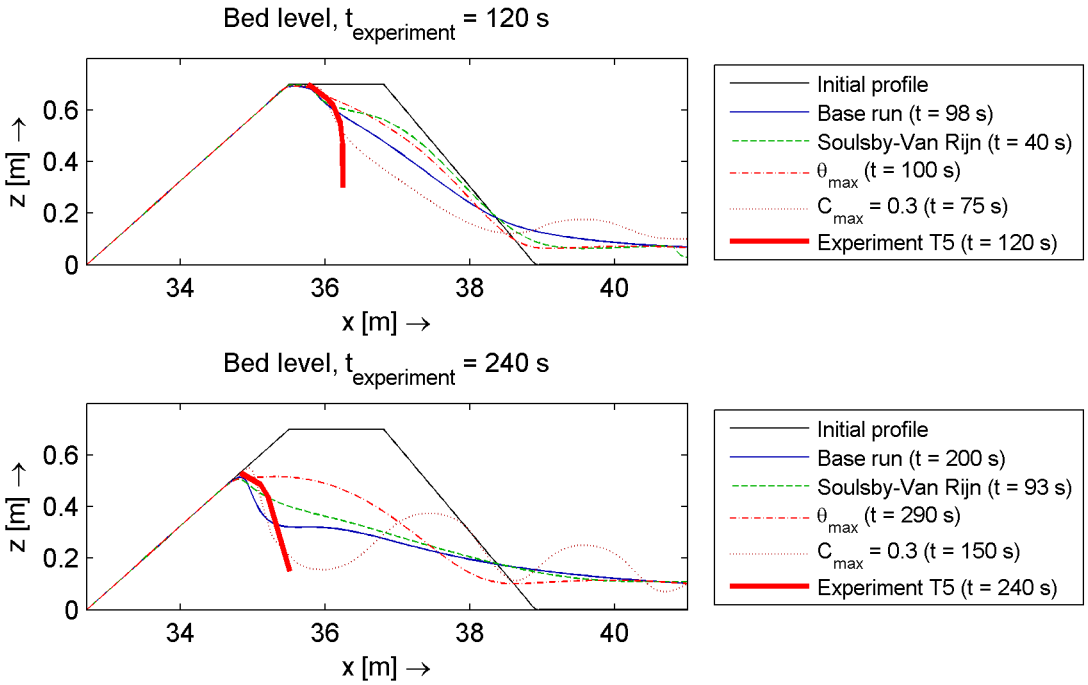

Figure 3.10: Bed profiles after $120\ s$ and $240\ s$ in the experiment. Model runs are presented at a time at which the locations of the erosion fronts correspond to the experimental data.

3.2.5 Validation to the theory of Visser (1998)

Although the experiment is a one-dimensional test, it seems that the theory of Visser (1998), see Section 2.3, is in line with the results of the model runs. As visualised in Figure 2.5, the back slope should first flatten until a stable slope is achieved. Since the back slope has initially a steepness of $1:3$ and the critical wet slope is set as 0.3, some avalanching should take place, which is observed in Figure 3.11.

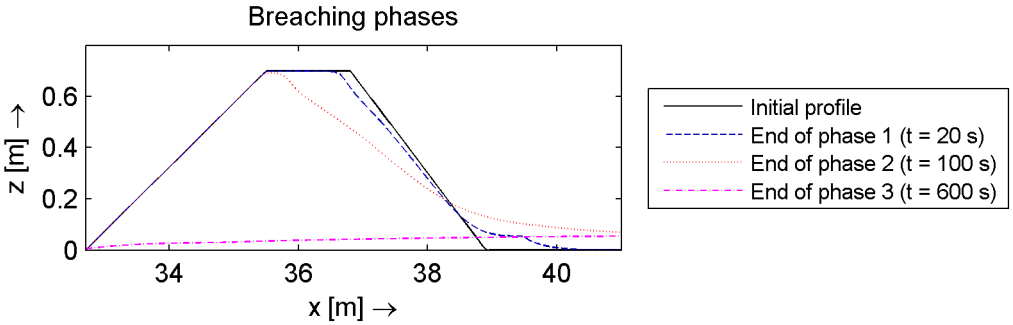

Figure 3.11: XBeach model results of the bed profile after the various phases.

During the second phase, the back side of the dike should erode, causing the back top of the dike to propagate to the front of the dike, see Figure 3.11. The frontward propagation of the back side of the dike occurred without a substantial lowering of the dike crest, as also observed in the experimental results in Figure 3.6. As mentioned earlier, the different model results describe the location of the erosion front similarly. Only the Soulsby-Van Rijn method erodes much faster during this phase.

During the third phase of the breaching process, the crest of the dike lowers. As visible in Figure 3.8, the differences between the model runs are now much larger. The other phases of the dike breach in the theory of Visser, during which the breach width growths, are not modelled since a pure $1D$ simulation is considered.

3.2.6 Conclusion of the flume experiment

Overall, the occurrence of the first three breaching phases of the theory by Visser (1998) are modelled properly. However, the performance of the different model runs is not the same. The Van Thiel-Van Rijn sediment formulation results in far better predictions of the morphology compared to the older Soulsby-Van Rijn model. Limiting the maximum sediment concentration to $0.1\ m^3/m^3$ limits the sediment transport such that the propagation velocity of the erosion front is represented more accurately. However, it has the undesired side effect of a worse prediction of the bed profile shape (especially during the third breaching phase) and it has no physical justification. As expected, the Shields number limitation in the sediment transport formulae leads to less morphological changes but the limitation is too strict and it results in a completely different bed profile.

These conclusions imply that the present sediment transport limiters C_{max} and θ_{max} do result in smaller morphological changes but lead to undesirable artificial side effects at the same time.

3.3 Zwin dam breach

In 1994, a full-scale dam breach experiment (Bakker et al., 1996) was performed in Het Zwin, The Netherlands. Within one hour, the breach has grown to a width of $41\ m$ after an initial disturbance was enforced. The goal of the experiment was to obtain measurement data of the breaching process for calibration and validation of breach models, in particular the BRES model of Visser (1998). Breach models are of importance to assess the safety of dike designs. Figure 3.12 presents the initial profile as measured on the test location.

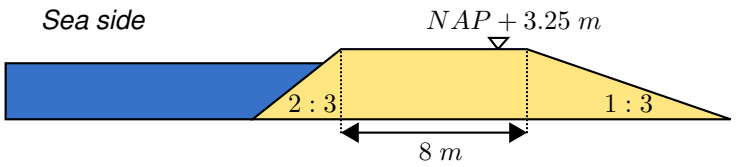

Figure 3.12: Initial profile of the Zwin breach experiment. Adapted from Bakker et al. (1996).

Since the breach width is measured, the two-dimensional behaviour of the breaching process can be investigated. This experiment is hence a good complement to the one-dimensional breaching case of the previous section. Figure 3.13 presents some photos of the experiment.

Figure 3.13: Photos of the breaching experiment, left: initiation of the breach, right: the breach in the final stage of the breaching process. Taken from Bakker et al. (1996).

3.3.1 Description model set-up

The experiment is modelled in XBeach based on the reported characteristics. No waves were enforced since the experiment was performed at calm conditions and the water elevation was the main driver for the breaching process. A grid spacing of $0.5\ m$ is applied near the breach, increasing towards the boundaries. For more information on the model set-up, see Appendix G.2.1.

The same parameter settings as with the Scheldt Flume experiment are observed. In addition, the bed slope effect is turned off in one of the model runs to test the importance of this effect in $2D$.

3.3.2 Comparison model results with experimental data

During the Zwin test, the breach width was measured over time. It is possible to calculate the breach width out of the model results and compare it with the experimental data. In this analysis, the breach width is defined as the smallest width at crest level. As a result, the performance of the XBeach model can be assessed. Figure 3.14 shows the measured and calculated breach widths over time. For several minutes, the breach width remains constant. Thereafter the breach increases substantially in width until the water level in the lagoon equals the sea water level and no more forcing is present to enlarge the breach.

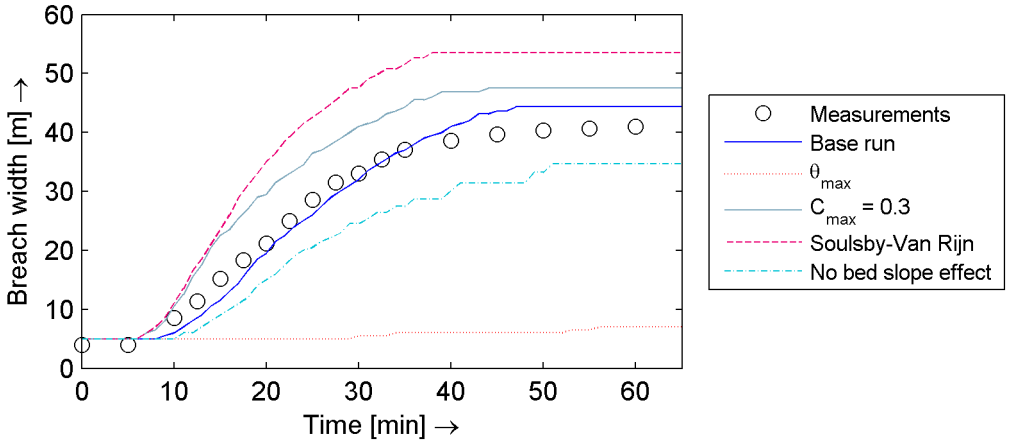

Figure 3.14: Breach width of the Zwin test over time for all model runs with the experimental data.

The differences between the different model runs are large. First, the θ_{max} parameter results in very unrealistic erosion rates, the breach width increases only slightly. The default C_{max} limitation to 0.1 in the base run causes structural less erosion rates compared to the larger limitation to the sediment concentration. Compared to the data, the shape of the function is different, initially there is an underestimation and eventually there is an overestimation, but the magnitude of the breach width is in good accordance. Just like with the Scheldt Flume model, the Soulsby-Van Rijn equation causes substantial more erosion.

An important observation is that the model run without a bed slope effect results in a substantial different trend compared to the base run. As mentioned in Section 2.7.2, the currently implemented bed slope effect is very rough. Since the differences by the bed slope effect are large, it is definitely important to validate the correctness of the implemented effect later on.

3.3.3 Validation to the theory of Visser (1998)

The Scheldt Flume experiment of Section 3.2 has shown that XBeach is capable to model the different phases of a dike breach properly in $1D$. Now, it is checked whether XBeach is also able to do so in $2D$, for which also phases 4 and 5 of the breaching process, the widening of the breach, are relevant.

Figure 3.15 presents some cross-sections of the breach at several moments in time for the base run. The first phase is identified easily, the front and back side of the dam collapse until a stable wet slope is achieved. The critical wet slope is 0.3, which means that both the front slope of $2:3$ as the back slope of $1:3$ should avalanche. The figure confirms this, the front slope avalanches more because of the steeper initial slope. At the end of the first phase, roughly after 1 minute, the front and back side of the dam have achieved the same critical wet slope.

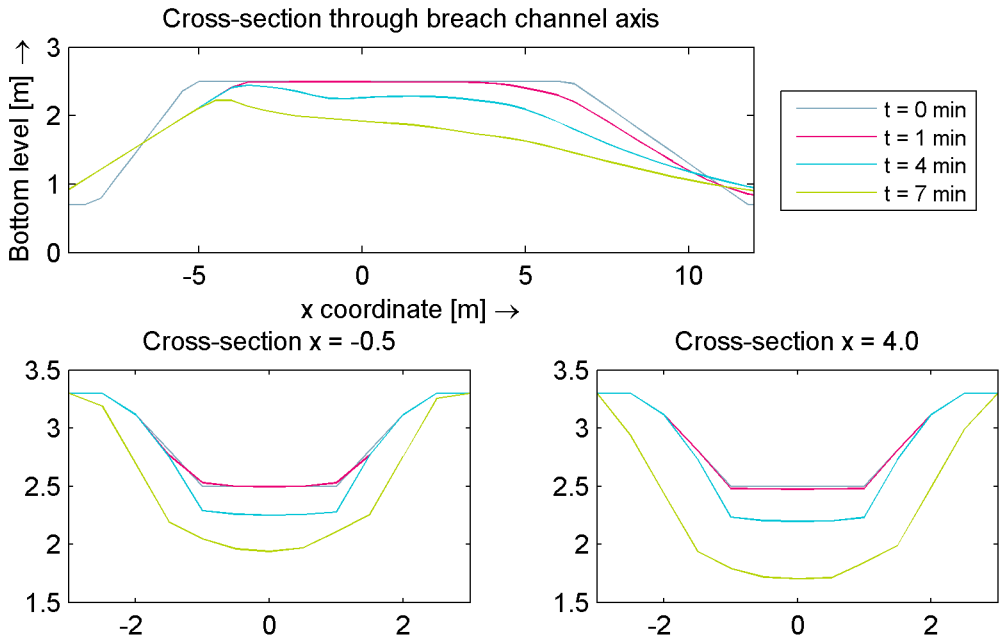

Figure 3.15: Cross-sections at several moments in time. The top plot is a cross-section through the channel axis. The two plots on the bottom are cross-sections perpendicular to the above one at the x-coordinates mentioned. All results are for the base run. The sea side is on the left side of the plots.

After 4 minutes, the second phase, during which the back slope retreated to the front, is completed. During this process, the dune crest did not lower substantially, which is in accordance with the $1D$ Scheldt Flume experiment. As visible from the two cross-sections at the bottom of Figure 3.15, the width of the channel did not increase during this phase. Only some slight lowering of the channel bottom occurred. In the theory of Visser, the bottom channel lowers much more. Whereas the slope behind the dam crest is visualised as the critical wet slope during phase 2 in Figure 2.5, only a very mild slope is modelled in XBeach.

This effect was also observed in the Scheldt Flume model, there it was concluded that the depth-averaged concentration limiter C_{max} is preventing steep slopes to occur during phase 2. This is confirmed in Figure 3.16 in which steeper slopes are observed compared to Figure 3.15. However, there is still a substantial amount of sediment present behind the dam crest. This could suggest that the observed feature is physical or an even larger limit on the sediment concentration is required. No data are available of the cross-sections to test this suggestion.

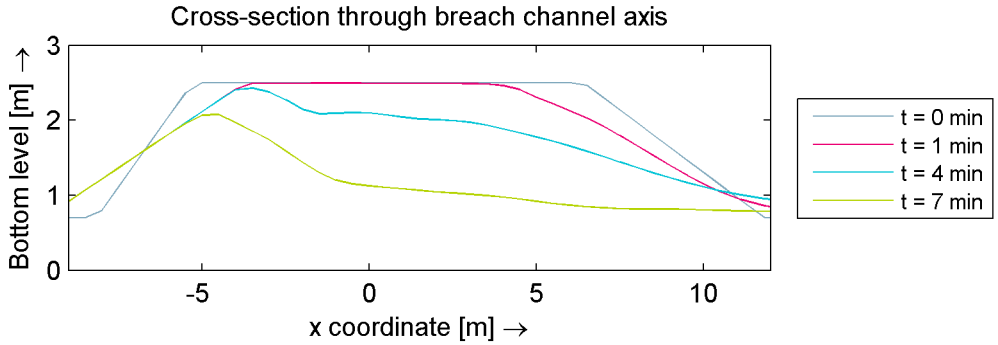

Figure 3.16: Cross-section through the channel axis for $C_{max} = 0.3$ instead of $C_{max} = 0.1$. Results are presented at several moments in time. The sea side is on the left side of the plots.

After 4 minutes, the third phase is started which ends approximately after 19 minutes from the beginning of the experiment. During this phase, the dam crest lowers and the breach width increases at the same time, see Figure 3.17. After this phase, the breach width keeps increasing, as can be seen from Figure 3.14. This increase in width is hence part of phase 4 and 5. Eventually, there is no sufficient hydraulic gradient left to enlarge the breach and phase 5 is finished after approximately $40 - 60$ minutes.

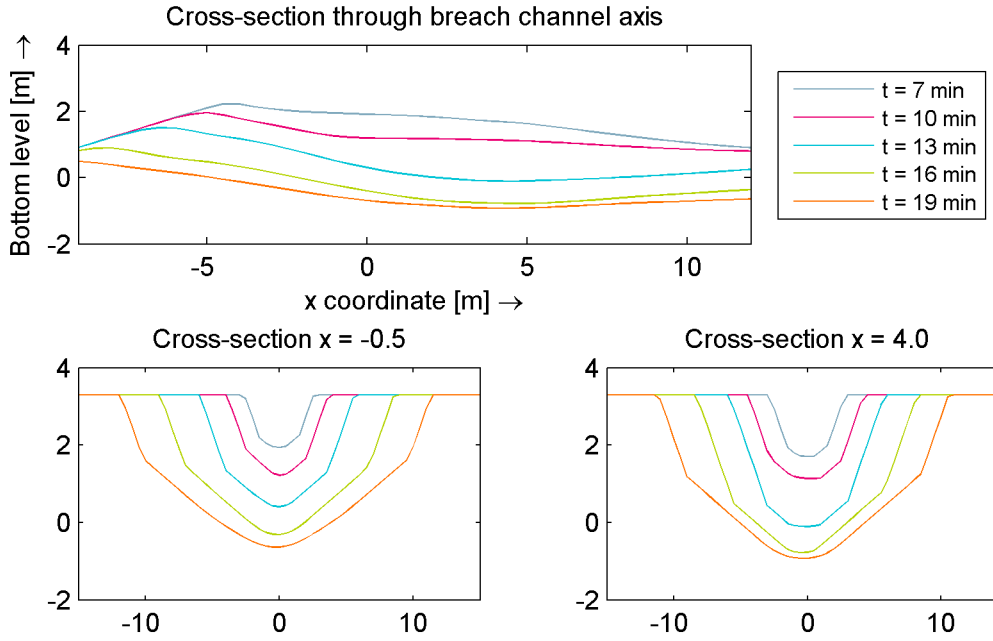

Figure 3.17: The same cross-sections as in Figure 3.15, now at several other moments in time to illustrate the third phase of the breaching process. All results are for the base run. The sea side is on the left side of the plots.

3.3.4 Conclusions of the Zwin experiment

The Zwin model showed the same tendency as observed in the experiment. The different breaching phases are well distinguishable and they elapse more or less in line with the theory of Visser (1998).

The limitation to the Shields parameter results in a very small increase of the breach width, which is an indication for a strong underestimation of the erosion rates. The Soulsby-Van Rijn equation results in larger erosion rates compared to the Van Thiel-Van Rijn sediment equation. Limiting the depth averaged sediment concentration causes less erosion compared to the model run with a larger concentration limit. Further, the concentration limitation causes initially less erosion compared to the measurement data and eventually more erosion. Finally, the profile behind the dam crest is modelled too gentle with this limit.

The bed slope effect has substantial effects on the sediment transport, if included it results in substantial more erosion. It is questionable whether the results of the included bed slope effect are valid.

3.4 Santa Rosa Island

3.4.1 Explanation model

McCall et al. (2010) modelled the erosion of Santa Rosa Island by hurricane Ivan with XBeach. Santa Rosa Island is located between the Gulf of Mexico and Pensacola Bay. The location modelled is a $2000\ m$ long stretch of which LIDAR (LIght Detection And Ranging) survey data are available of 15 May 2004 (pre-storm) and 19 September 2004 (post-storm). One of the conclusions of McCall et al. (2010) is that a limiter to the sediment transport is required to obtain a post-storm profile that is comparable to post-storm LIDAR data. Figure 3.18 gives an impression of the location of the model domain.

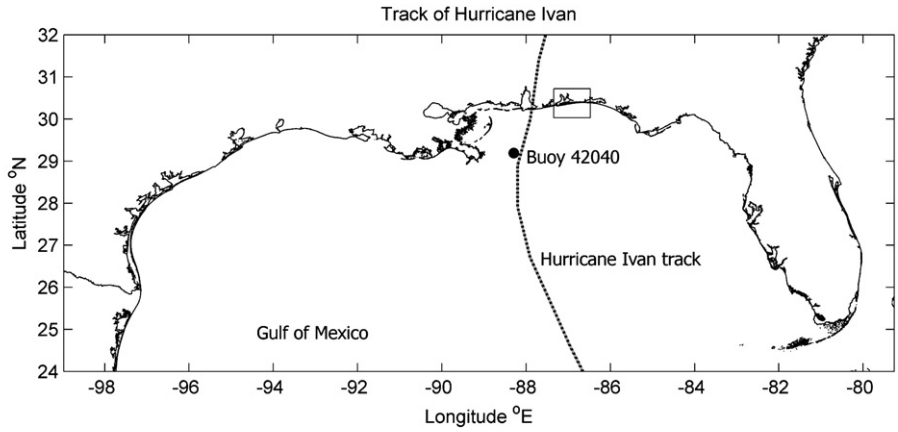

Figure 3.18: Location of the Santa Rosa model, as marked with the gray box. Taken from McCall et al. (2010).

The dike breach experiment of Section 3.2 and the Zwin test of Section 3.3 showed that the Van Thiel-Van Rijn transport formulation performs substantially better compared to the originally implemented Soulsby-Van Rijn equations. Therefore, McCall's case is repeated to check whether it is still required to limit the sediment transport rates to obtain reasonable results in the Santa Rosa Island model.

3.4.2 Model results

Figure 3.19 shows the bed profiles obtained from the LIDAR and the XBeach model for a variation in sediment transport formulae and limiters. To get some more insight into the results, the bed level changes are presented in Figure 3.20 together with some scatter plots of these bed level changes in Figure 3.21. Table 3.1 presents a quantification of the model results in which the Brier Skill Score (Murphy and Epstein, 1989) and the bias were defined in Equations 3.1 and 3.2.

Compared to the XBeach computations as presented in McCall et al. (2010), the model results are definitely not improved. A substantial overestimation of the erosion rates is still observed in the simulations without a Shields parameter limiter. The scatter plot of the Van Thiel-Van Rijn formulations without a sediment transport limiter shows that the erosion is overestimated in almost all grid cells. In contrast, the scatter plot of the model with a limited Shields parameter shows a very good correlation with the LIDAR data. The Shields parameter limiter is not perfect since erosion is limited too much in several points.

Based on the XBeach model results of the previous cases, it is unexpected that the Van Thiel-Van Rijn expression now performs worse compared to the Soulsby-Van Rijn expression. A clear explanation for this observation is not easily found. However, the uncertainty natural of a field case supersede the differences between the sediment transport equations for this case, so the Van Thiel-Van Rijn model does not outperform the Soulsby-Van Rijn expression.

The case with an increased maximum depth averaged sediment concentration (0.3 instead of 0.1) shows no very large differences compared to the main Van Thiel-Van Rijn case. The influence of this sediment transport rate modification on the predicted bed levels is hence not very large for this model.

Since the bed slope effect has been of substantial importance in the Zwin experiment model, it is finally checked whether the bed slope effect has also in this case a substantial influence. Turning off the bed slope effect results in a BSS of only -5.32 and a bias of $-1.79\ m$, which is similar to the model runs with a bed slope effect.

3.4.3 Conclusion of the Santa Rosa case

The overestimation of the erosion rates does still occur in the present version of XBeach for the Santa Rosa model. Only by limiting the Shields parameter to 1.0, a reasonable Brier Skill Score up to 0.68 is obtained. Once the Shields parameter is limited, the results of the two sediment transport models are comparable. No large influence of the implemented bed slope effect is noticed.

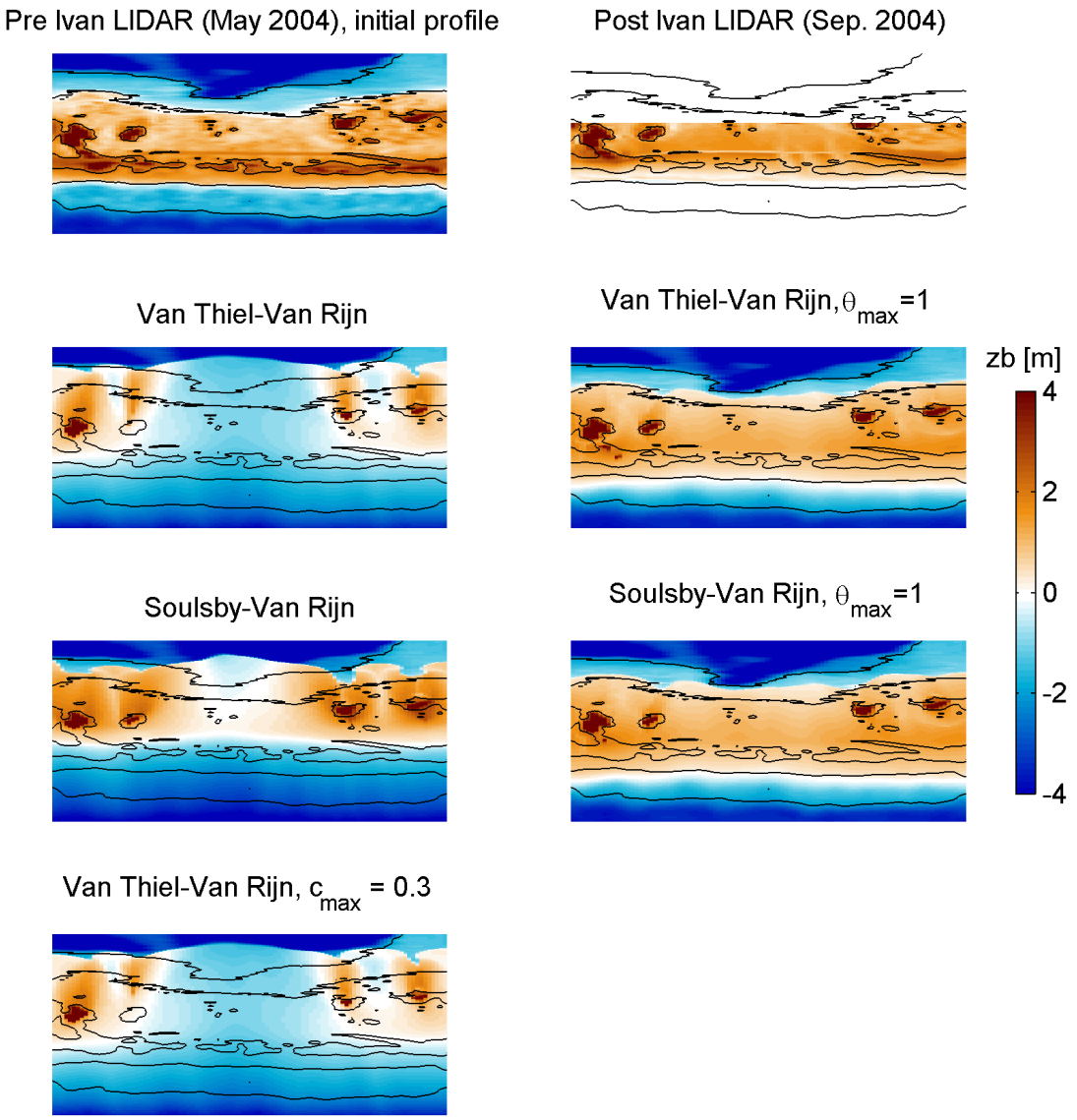

Figure 3.19: Santa Rosa case modelled for a variety of parameters. The black depth contours are provided at an elevation of -2, 0 and 2 m relative to MSL of the initial depth profile. Horizontal axis is 2000 m in longshore direction, vertical axis is 250 m in cross shore direction. The Gulf of Mexico is located at the bottom side of the images, the lagoon at the top side.

Table 3.1: Brier Skill Score and bias as defined in Equations 3.1 and 3.2.

Sediment transport equation	θ_{max}	c_{max}	Skill	Bias (m)
Van Thiel-Van Rijn	off	0.1	-5.78	-1.87
	1.0	0.1	0.75	-0.18
	off	0.3	-5.76	-1.86
Soulsby-Van Rijn	off	0.1	-3.30	-1.26
	1.0	0.1	0.67	-0.22

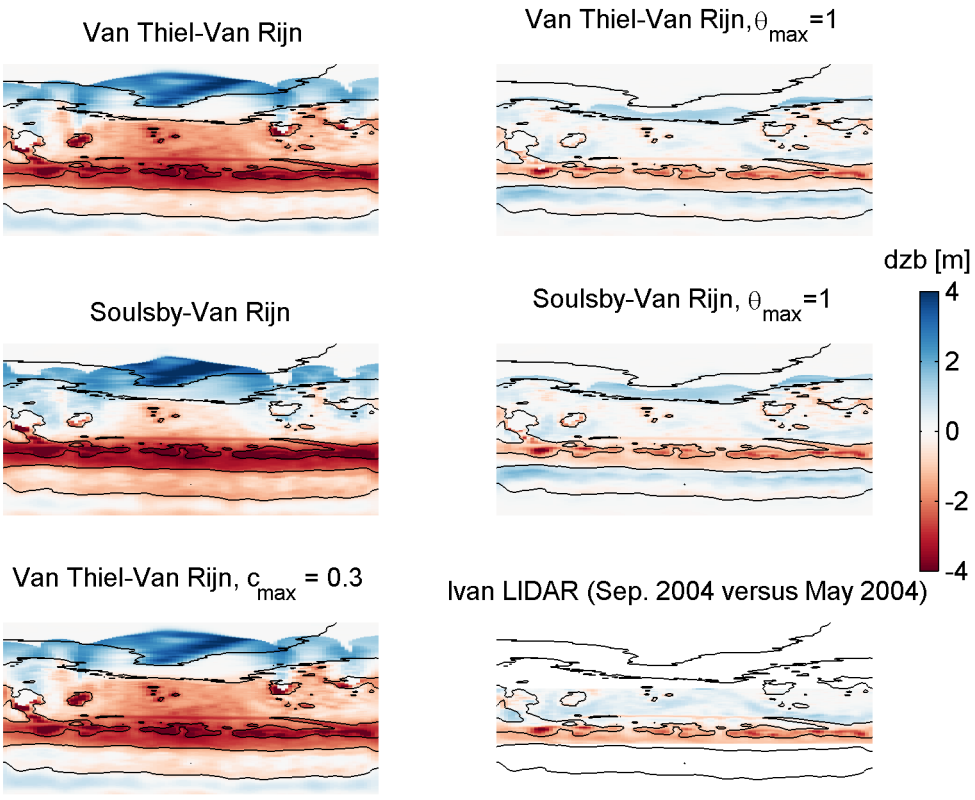

Figure 3.20: Bed level changes, the figures represent net sedimentation/erosion. The black depth contours are provided at an elevation of -2, 0 and 2 m relative to MSL of the initial depth profile. Horizontal axis is 2000 m in longshore direction, vertical axis is 250 m in cross shore direction. The Gulf of Mexico is located at the bottom side of the images, the lagoon at the top side.

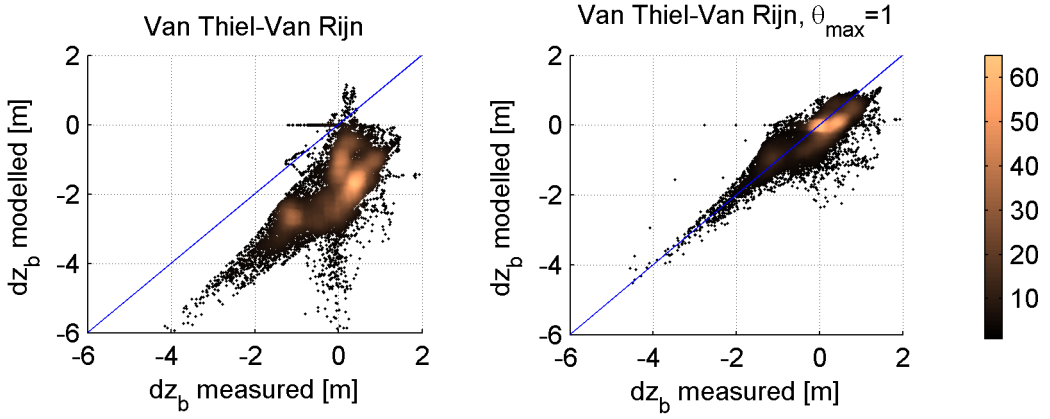

Figure 3.21: Modelled bed level change versus measured bed level change. Only the points are presented for which post-storm data was available. The solid line represents a perfect 1:1 relation. For the data points below the blue line, too much erosion is computed with respect to the LIDAR data.

3.5 General conclusions

Based on the considered cases, it can be concluded that the Soulsby-Van Rijn equation is less applicable to overwash and breaching cases than the more recent Van Thiel-Van Rijn equation. In almost all cases, an overestimation of the erosion rates was observed. Only in the Santa Rosa Island model some slightly better results are achieved. Based on the poor results, the Soulsby-Van Rijn equation will not be considered anymore in this thesis.

Since the erosion rates are overestimated in all cases, the transport limitations are an important subject of this thesis. The limitation of the Shields parameter was introduced with the Santa Rosa Island model in XBeach, where it indeed leads to a good predictive skill. However, the performance of this limiter on the other cases is very bad. In the Scheldt Flume and Zwin breaching cases, serious under predictions of the erosion rates suggest that this limiter should not be used in general. Also the limitation of the sediment transport concentration has unwanted side effects. Although the limiter has the desired effect that the erosion velocity is reduced, the shape of the profile behind the dam crest is affected substantially. The Scheldt Flume experiment showed that the best results regarding the shape of the profile are obtained without a limiter. By the overestimation of the erosion rates there is need for a limiter, but the presently implemented limiters seem not to be the desired solution.

Another important observation is made with the Zwin model, the two-dimensional bed slope effect seems to have a substantial influence on the model results. Since the implemented bed slope effect is some kind of an approximation, further research on the bed slope effect is suggested. This will be done later on in this thesis. For the Santa Rosa case study, the bed slope effect was of substantially less importance, but that case did not involve breaching.

Finally, it is mentioned that the different breaching phases as described by Visser (1998) are relatively well modelled with the XBeach model. Some differences were observed related to the shape of the profile behind the crest. These are partly related to the limitation of the sediment concentration, as shown in the Scheldt Flume experiment.

Chapter 4

Hypotheses

To focus the research on answering the research questions, diverse hypotheses are posited. The main research question is repeated here:

>> To which extent can the morphodynamic predictions of the XBeach model under overwash and breaching conditions be improved through the implementation of new model physics?

The literature review and the assessment of the current XBeach model gave an insight into relevant processes regarding overwash and breaching. Based on this information, presumptions regarding the answer of the research questions can be made. These presumptions will be translated into hypotheses in this chapter which will be tested in the further part of this research.

4.1 Hypotheses on the improvement of the physics

The overestimation of the erosion rates during overwash and breaching conditions results in a bad skill of the XBeach model. The main hypotheses regarding the overestimation of the erosion rates:

1. The overestimation of the erosion rates in the present version of the XBeach model is caused by missing physical processes. Dilatancy plays an important role at the hindering of erosion.

Further hypotheses regarding this topic:

2. Dilatancy is only of importance for a large hydraulic gradient: small grain sizes in combination with a large erosion velocity of the bottom. Therefore, dilatancy does not play a role during the swash and inundation regime.

3. It is possible to obtain good results without the artificial limiters C_{max} and θ_{max}. By not using these artificial limiters, the modelled profiles are expected to have a more realistic shape.

4. The good performance of the θ_{max} limiter in the Santa Rosa case is based on the fact that any limitation on erosion causes better results. This is hence no unique property of the θ_{max} limiter.

5. The reduced fall velocity process results in a larger delay of the actual suspended sediment concentrations to a change in equilibrium concentration which will influence hence the morphology.

6. Improving the bed slope effect will result in more feasible cross-sections of a breach.

   6.a. The present implementation of the engineering formula by Soulsby for the bed slope effect is erroneous. Even if the engineering formula by Soulsby is implemented correctly, the physics are not represented accurately.

   6.b. The magnitude modification due to a bed slope does not change the direction of the transport and with that will not affect the shape of the cross-section of the breach substantially.

   6.c. A change of the bed-load transport direction is required to get to more smooth, and with that more realistic, cross-sections. Without a change of bed-load direction, the cross-sections through the breach channel will show a more angular bed profile.

7. The effect of making the Exner equation mass-conservative, by taking the concentration changes over time into account, is required at locations where variations in flow conditions are substantial.

4.2 Hypotheses related to a morphodynamic hindcast of a storm event

The goal of the XBeach model is not only a proper representation of laboratory experiments, but also a good skill on the hindcast modelling of storm events on beaches and barrier islands. By the larger scale and different model properties, some additional hypotheses are stated.

8. In field cases, often a lot of uncertainties are present. The model results are sensitive to the boundary conditions and the model parameters.

9. The current standard of taking a uniform bed friction over the whole model domain is reasonable. It is not required to increase the bed friction to account for vegetation.

4.3 Approach

To test the hypotheses, the XBeach model will be improved. This is necessary because processes like dilatancy are not yet implemented. The next chapter will deal with the details of these model improvements. Thereafter the improved model is validated based on a variety of cases and the relevant processes are examined. By analysing the model runs, the diverse hypotheses can be tested. Finally, a morphodynamic hindcast of hurricane Sandy is made to test the hypotheses related to a non-idealised field case.

Chapter 5

Model improvements

5.1 Motivation behind the improvements

The XBeach model is an open source project, it is hence possible to modify the source code and investigate the influence of these adjustments. First, it should be determined which improvements will be made. The improvements should be in line with the main research goal: the modelling of sediment transport and morphology during overwash and breaching events. The model improvements are used as a tool to test the hypotheses as presented in Chapter 4.

The processes that play a role at breaching and overwash conditions, as presented in Section 2.6, are not yet implemented in the XBeach model. The concept of **hindered erosion by dilatancy** and the **reduction of the fall velocity for high concentrations** are well described by practical formulations and these will be implemented. The damping of turbulence for high concentrations is a complicated subject and no depth-averaged formulations are available, so more research is required before a proper implementation can be achieved.

Section 2.7 provided the most important limitations of the XBeach model. Some of these are very unsatisfactory and should be improved. An important issue is the **bed slope effect** which is currently not implemented in a valid way and is based on a very rough engineering approach. The bed slope effect can be very important for breaching and overwash cases due to the steep slopes that can occur in these cases. Further, the non-conservatism of the **Exner sediment balance equation** could result in losses of sediment mass if gradients in sediment concentrations are large. The other limitations (depth averaging, phase-averaged short waves, empirical sediment transport equations, non-cohesive sediments, vegetation and the constant Chézy value) are not readily improved.

Table 5.1 presents an overview of which of the limitations will be improved. By implementing/improving these concepts, the XBeach model can be used as a tool to asses under what conditions these processes are important.

Table 5.1: Overview of the limitations of XBeach and which of those are improved.

Processes which are schematised in XBeach	Implemented/improved
Depth averaging	×
Phase-averaged-short waves	×
The Exner equation	✓
Empirical sediment transport equations	×
Non-cohesive sediments	×
Bed friction	×
Processes modelled incorrectly by XBeach	**Implemented/improved**
Rough bed slope effect	✓
Processes not modelled by XBeach	**Implemented/improved**
Hindering of erosion by dilatancy	✓
Hindered settling	✓
Turbulence damping	×
Aeolian sediment transport	×
Vegetation	×

5.2 Hindered erosion by dilatancy

The concept of the dilatancy effect by Van Rhee (2010) is described in Section 2.6.1 and Appendix A. Van Rhee modifies the Shields parameter by a one-dimensional bed slope effect and an inward directed dilatancy force (superscript B refers to the bed slope effect, D to the dilatancy effect):

$$\theta_{cr}^{B\&D} = \theta_{cr}\left(\frac{\sin(\phi-\beta)}{\sin(\phi)} + \frac{v_e}{k_l}\frac{n_l-n_0}{1-n_l}\frac{A}{\Delta}\right) \tag{5.1}$$

Without bed slope effect

For now, the focus is on the pure dilatancy effect. Therefore, the bed slope effect is neglected ($\beta = 0^o$):

$$\theta_{cr}^{D} = \theta_{cr}\left(1 + \frac{v_e}{k_l}\frac{n_l-n_0}{1-n_l}\frac{A}{\Delta}\right) \tag{5.2}$$

The implementation of the bed slope effect on the Shields parameter in combination with the dilatancy effect is dealt with in Section 5.4.5.

Dilatancy effect as a limitation of the sediment transport

The limitation to the Shields parameter can not be implemented directly in XBeach, since the sediment transport formulae are no direct function of the Shields parameter, see Equation C.8. Therefore, the direct relation between the Shields parameter and the flow velocity (Equation C.13) is used:

$$U_{cr} = \sqrt{\frac{\theta_{cr}\Delta g D_{50}}{c_f}} \rightarrow \theta_{cr} = \frac{c_f U_{cr}^2}{\Delta g D_{50}} \tag{5.3}$$

Which result in the required limitation to the critical flow velocity:

$$\frac{c_f \left(U_{cr}^2\right)^D}{\Delta g D_{50}} = \frac{c_f U_{cr}^2}{\Delta g D_{50}} \left(1 + \frac{v_e}{k_l} \frac{n_l - n_0}{1 - n_l} \frac{A}{\Delta}\right) \tag{5.4a}$$

$$U_{cr}^D = U_{cr} \sqrt{1 + \frac{v_e}{k_l} \frac{n_l - n_0}{1 - n_l} \frac{A}{\Delta}} \tag{5.4b}$$

Now, the theory of the dilatancy effect is implemented by replacing U_{cr} in the sediment transport formulae by the above expression for U_{cr}^D. In this expression, there are still non-discussed variables which will be treated in the following sections.

Permeability

The larger the permeability of the bed, the smaller the dilatancy force. Van Rhee (2010) suggests to use the equation proposed by Den Adel (1987):

$$k_l = \frac{g}{160\nu} D_{15}^2 \frac{n_0^3}{(1 - n_0^2)} \tag{5.5}$$

If a constant sediment composition is assumed, the permeability predicted by this formulation is constant over space.

The erosion velocity

The erosion velocity v_e is the velocity at which the bottom level decreases:

$$v_e = \begin{cases} -\frac{dz_b}{dt} & \text{if} \quad \frac{dz_b}{dt} < 0 \\ 0 & \text{else} \end{cases} \tag{5.6}$$

It should be noted that this erosion velocity is required to calculate the morphodynamics based on the critical flow velocity of Equation 5.4b. To get to this erosion velocity, the bed level change at that time step should be known. Since the bed level change is not known on forehand, the set of equations is implicit.

There are three possibilities to deal with this implicitness. First, the erosion velocity could be calculated iteratively. This is very time-consuming since it would require an iteration over the whole morphodynamic module. Another approach, provided by Bisschop et al. (2011), is to simplify the equations into an explicit format by assuming large flow velocities. It is convenient to make such an assumption for situations in which flow velocities are continuously large. However, for a highly dynamic coastal environment, erosion rates at smaller flow velocities are important as well, because the flow velocities are highly variable and the storm surge level is not constant during a storm event. The third approach is to assume that the bed level change of the previous time step is representative for the present time step. For now, this is the most convenient approach since time steps are generally rather small (in the order of $0.01 - 0.1\ s$).

Porosity

The porosity is an important variable in the dilatancy process. A bed porosity prior to erosion in the order of 0.40 is quite common and the exact value should be based on measurement data.

Van Rhee (2010) suggests to estimate the bed porosity n_l by the maximum porosity n_{max} (in this thesis estimated by a value of 0.5). This is reasonable since the porosity will have to be increased to bring the sediment into such a fluid state that it can be picked up, which is the rationale behind the theory of Van Rhee (2010).

Geometric parameter

The parameter A in Equation 5.4b is a coefficient that depends on the geometry of the sediment bed. Van Rhee (2010) mentions that values in the range of $0.75 - 1.7$ are reasonable for this parameter. In case of an inward directed hydraulic gradient, Van Rhee advises a value of 0.75.

5.3 Fall velocity reduction for high concentrations

Section 2.6.2 mentioned the concept of hindered settling for high concentrations. In XBeach, the sediment fall velocity is computed with an expression of Ahrens (2000). No reduction of the fall velocity for high concentrations is implemented yet. See Appendix C.2.2 for more details of the present implementation of the fall velocity.

The implementation of this concept is straight forward. The fall velocity, as calculated with the expression of Ahrens (2000), is modified with the expression of Richardson and Zaki (1954):

$$w = \epsilon^{\alpha} = (1 - c)^{\alpha} w_s \tag{5.7}$$

Rowe (1987) made an estimate of the exponent α by fitting a logarithmic function on a dataset of Richardson and Zaki (1954). The result is a function that purely depends on the Reynolds particle number $\mathbf{R}$:

$$\alpha = 2.35 \frac{2 + 0.175\mathbf{R}^{3/4}}{1 + 0.175\mathbf{R}^{3/4}} \tag{5.8a}$$

$$\mathbf{R} = \frac{w_0 D_{50}}{\nu} \tag{5.8b}$$

The implementation of the fall velocity reduction is purely based on Equations 5.7 and 5.8.

In XBeach, the fall velocity is used to determine the time scale of suspended sediment transport in the advection-diffusion equation.

5.4 Bed slope effect on sediment transport

5.4.1 Types of bed slope effects

The bed slope affects the transport of sediment in a variety of ways, Walstra et al. (2007) distinguish:

1. The bed slope will influence the local near-bed flow velocity.
2. The bed slope may change the transport rate once the sediment is in motion.
3. The bed slope may change the transport direction once the sediment is in motion.

4. The bed slope will change the threshold conditions for initiation of motion.

The influence of the bed slope on the hydrodynamics is not considered here. The other aspects will be dealt with in the following sections. The proper implementation of the engineering formulation of Soulsby (1997), as discussed in Section 2.7.2, is in fact a pure change of the transport magnitude. The improved model is a composition of all the mentioned processes, see Table 5.2.

Table 5.2: Considered processes in the engineering formulation of Soulsby and the improved model.

	Engineering formulation of (Soulsby, 1997)	Improved model
Change transport rate	✓ (total load)	✓ (bed-load)
Change transport direction	×	✓ (bed-load)
Change initiation of motion	×	✓ (total load)

5.4.2 Determination of the bed slope and flow direction in XBeach

In XBeach, the bed slope β is not directly known. Based on the bed level elevations in the grid cells, it is possible to calculate the slopes in x- and y-direction wherafter β can be evaluated.

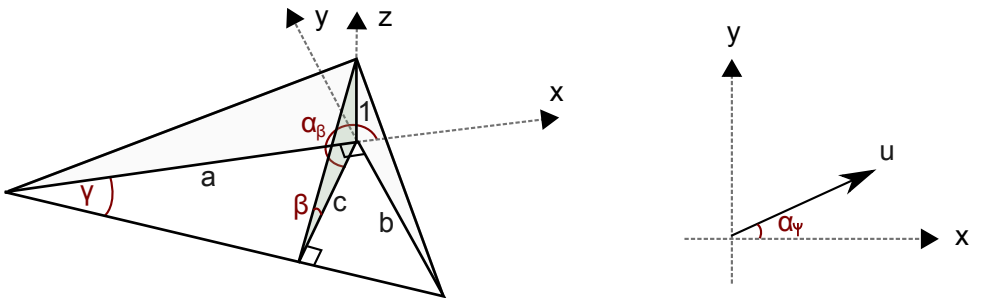

Figure 5.1: Definition sketch of the bed slope angle β and the angle α_ψ between the flow and the x-axis.

In Figure 5.1, the step size in z-direction is set to one, the absolute value of the maximum bed slope $\tan(\beta)$ can be derived based on geometrical considerations:

$$a = \frac{1}{\frac{\partial z_b}{\partial x}}, b = \frac{1}{\frac{\partial z_b}{\partial y}} \tag{5.9}$$

$$\left.\begin{array}{l} \tan(\gamma) = \frac{b}{a} = \frac{\frac{\partial z_b}{\partial x}}{\frac{\partial z_b}{\partial y}} \\ \sin(\gamma) = \frac{c}{a} \rightarrow c = a\sin(\gamma) \\ \tan(\beta) = \frac{1}{c} \end{array}\right\} \tan(\beta) = \left| \frac{\frac{\partial z_b}{\partial x}}{\sin\left(\tan^{-1}\left(\frac{\frac{\partial z_b}{\partial x}}{\frac{\partial z_b}{\partial y}}\right)\right)} \right| \tag{5.10}$$

The angle α_β between the plane of the maximum bed slope and the x-axis equals (see Figure 5.1):

$$\alpha_\beta = \begin{cases} 1.5\pi - \tan^{-1}\left(\frac{\frac{\partial z_b}{\partial x}}{\frac{\partial z_b}{\partial y}}\right) rad & \text{if } \frac{\partial z_b}{\partial y} \geq 0 \\ 0.5\pi - \tan^{-1}\left(\frac{\frac{\partial z_b}{\partial x}}{\frac{\partial z_b}{\partial y}}\right) rad & \text{otherwise} \end{cases} \tag{5.11}$$

The angle α_ψ between the flow direction and the x-axis:

$$\alpha_\psi = \begin{cases} \tan^{-1}\left(\frac{u_y}{u_x}\right) rad & \text{if } u_x \geq 0 \\ \pi + \tan^{-1}\left(\frac{u_y}{u_x}\right) rad & \text{otherwise} \end{cases} \tag{5.12}$$

Finally, the direction of the flow, relative to the on-slope directed vector, is known:

$$\psi = \alpha_\psi - (\alpha_\beta - \pi)\ rad \tag{5.13}$$

5.4.3 Change of transport magnitude once in motion

The change of the transport magnitude is generally done with the use of the longitudinal slope effect (Walstra et al., 2007):

$$q_{slope} = q\left(1 - \alpha\frac{\partial z_b}{\partial s}\right) \tag{5.14}$$

Soulsby (1997) suggests to take a value of 1.6 for the parameter α in his engineering formula and to apply it on the total sediment load. If this method is combined with the other bed slope effects, a smaller value of 0.15 is taken and it is applied on the bed-load only. The latter value is in line with Talmon (1992) who used this parameter in various comparisons with experiments and took values in the range of 0.15 to 0.3 (Walstra et al., 2007).

The bed slope in the direction of sediment transport is approached by (Van Rijn, 2006):

$$\frac{dz_b}{ds} = \frac{dz_b}{dx}\frac{q_x}{|q|} + \frac{dz_b}{dy}\frac{q_y}{|q|} \tag{5.15}$$

5.4.4 Change of transport direction once in motion

For the change of direction of the bed-load transport vector, the expression of Van Bendegom (1947) is used:

$$\tan(\alpha_{\psi,new}) = \frac{q_{b,n}}{q_{b,s}} = \frac{\sin(\alpha_\psi) - f(\theta)\frac{dz_b}{dy}}{cos(\alpha_\psi) - f(\theta)\frac{dz_b}{dx}} \tag{5.16}$$

Walstra et al. (2007) suggest to use the empirical formulation of Talmon et al. (1995):

$$f(\theta) = \frac{1}{9(D_{50}/h)^{0.3}\theta^{0.5}} \tag{5.17}$$

Once the sediment transport angle is modified with Equation 5.16, the sediment transport rates are affect as follows to account for this change in direction:

$$q_{b,x} = |q_b|\cos(\alpha_{\psi,new}) \tag{5.18a}$$

$$q_{b,y} = |q_b|\sin(\alpha_{\psi,new}) \tag{5.18b}$$

With this implementation, there can be sediment transport perpendicular to the flow direction.

5.4.5 Threshold condition for initiation of motion in two dimensions

If sediment is located on a sloping bed, the stability of the grains is affected. Therefore, the threshold condition for the initiation of motion should be modified. Soulsby (1997) considered the derivation of the critical Shields parameter with a two-dimensional sloping bottom, the resulting modified Shields parameter is:

$$\theta_{cr}^B = \theta_{cr}\frac{\cos(\psi)\sin(\beta) + \sqrt{\cos^2(\beta)\tan^2(\phi_i) - \sin^2(\psi)\sin^2(\beta)}}{\tan(\phi_i)} \tag{5.19}$$

The modification factor is hence purely a function of the angle of internal friction, the bed slope and the direction of the flow, see also Figure 5.2.

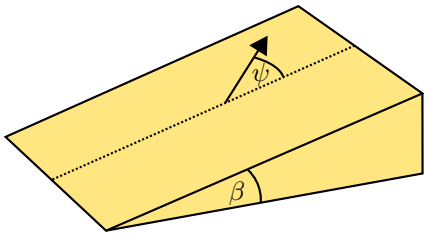

Figure 5.2: Schematic representation of the bed slope effect. The bed slope is equal to $\tan\beta$ and the angle between the on-slope directed vector and the direction of the flow velocity equals ψ. Adapted from: Soulsby (1997).

Figure 5.3 shows the value of the modification factor for a variety of bed slopes and flow angles. As visible, the critical Shields parameter is changed ranging from zero to twice the original critical Shields parameter value.

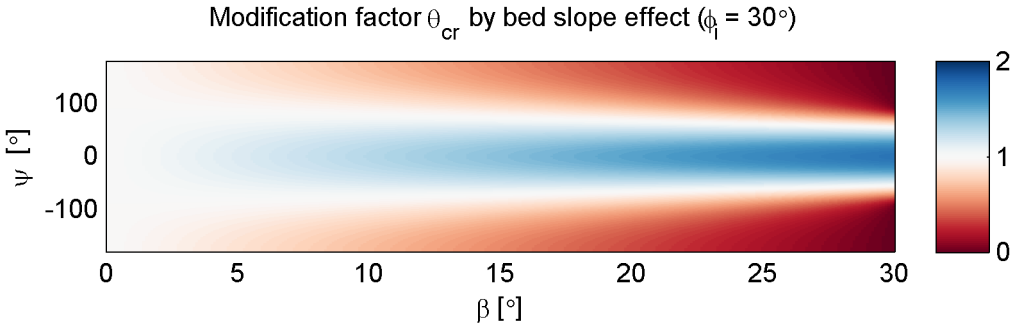

Figure 5.3: Plot of the bed slope effect factor with Equation 5.2.

Combination with dilatancy

The theory of Van Rhee (2010) also affects the critical Shields parameter. In this section, it is derived how the critical Shields parameter should be affected if both dilatancy as the two-dimensional bed slope effect are taken into account.

If the bed slope effect in two dimensions needs to be implemented, one could think that the one-dimensional bed slope effect in Equation 5.1 can simply be replaced by the two-dimensional expression found by Soulsby (Equation 5.19). However, this is not valid. The derivation of Van Rhee (2010), by observing the stability of a particle, should be repeated in two dimensions.

By the two-dimensionality, the vector of the bed slope is not necessarily in line with the direction of the flow velocity. Figure 5.4 shows the relevant forces that are included in the derivation.

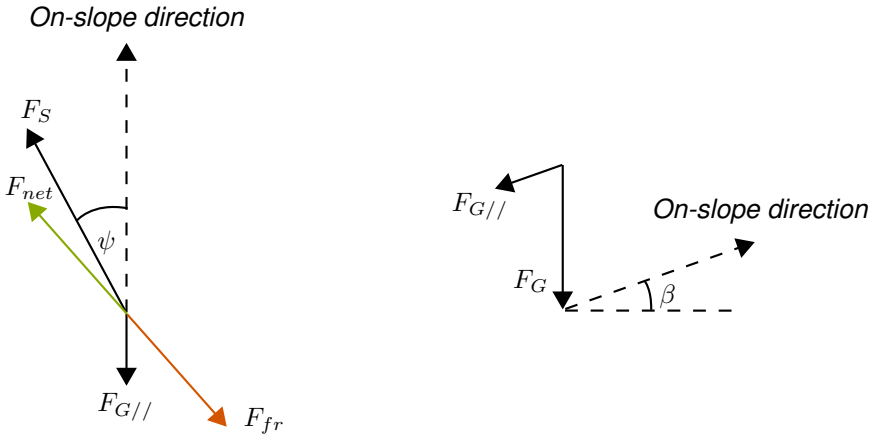

Figure 5.4: Definition of forces, left: top-view, right: cross-section through the plane of the bed slope.

Table 5.3: Magnitude of the forces of Figure 5.4.

Force	Variable	Value
Flow	F_S	F_S
Gravity	$F_{G//}$	$\sin(\beta)F_G$
Net	F_{net}	$\sqrt{\left(\sin\left(\psi\right)F_S\right)^2+\left(\cos\left(\psi\right)F_S-\sin\left(\beta\right)F_G\right)^2}$
Friction	F_{fr}	$\left(F_i+\cos\left(\beta\right)F_G\right)\tan\left(\phi\right)$

Since the value of the critical Shields parameter is to be derived, the net force F_{net} equals the friction force F_{fr} (it is convenient to divide all forces by the gravity force F_G):

$$\sqrt{\left(\frac{F_S}{F_G}\sin\left(\psi\right)\right)^2+\left(\frac{F_S}{F_G}\cos\left(\psi\right)-\sin\left(\beta\right)\right)^2}=\left(\frac{F_i}{F_G}+\cos\left(\beta\right)\right)\tan\left(\phi\right) \tag{5.20}$$

$$\left(\frac{F_S}{F_G}\right)^2-2\frac{F_S}{F_G}\cos\left(\psi\right)\sin\left(\beta\right)+\sin^2\left(\beta\right)=\left(\left(\frac{F_i}{F_G}\right)^2+2\frac{F_i}{F_G}\cos\left(\beta\right)+\cos^2\left(\beta\right)\right)\tan^2\left(\phi\right) \tag{5.21}$$

The determinant of this quadratic equation (with F_S/F_G as the variable) equals:

$$\mathrm{D}=4\left(\left(\tfrac{F_i}{F_G}\right)^2+2\tfrac{F_i}{F_G}\cos\left(\beta\right)+\cos^2\left(\beta\right)\right)\tan^2\left(\phi\right)-4\sin^2\left(\psi\right)\sin^2\left(\beta\right) \tag{5.22}$$

Now, the root of Equation 5.21 can be written as (only the positive root makes physical sense):

$$\frac{F_S}{F_G}=\cos\left(\psi\right)\sin\left(\beta\right)+\sqrt{\left(\left(\frac{F_i}{F_G}\right)^2+2\frac{F_i}{F_G}\cos\left(\beta\right)+\cos^2\left(\beta\right)\right)\tan^2\left(\phi\right)-\sin^2\left(\psi\right)\sin^2\left(\beta\right)} \tag{5.23}$$

Sediment is brought into motion by the original derivation of Shields (1936) if:

$$\theta=\frac{F_s}{F_G}>\tan\left(\phi\right)=\theta_{cr} \tag{5.24}$$

Therefore, the modification factor on the critical Shield factor becomes:

$$\theta_{cr}^{B\&D}=\theta_{cr}\frac{\cos\left(\psi\right)\sin\left(\beta\right)+\sqrt{\left(\left(\frac{F_i}{F_G}\right)^2+2\frac{F_i}{F_G}\cos\left(\beta\right)+\cos^2\left(\beta\right)\right)\tan^2\left(\phi\right)-\sin^2\left(\psi\right)\sin^2\left(\beta\right)}}{\tan\left(\phi\right)} \tag{5.25}$$

One can easily check that this equation equals Equation 5.19 if dilatancy is not taken into account ($F_i=0$) and it is equal to Equation 5.2 if the bed slope effect is neglected ($\psi=0$ and $\beta=0$).

5.5 Volume conservative Exner equation

The Exner equation is not fully mass-conservative. See Equation 5.26, a change in sediment concentration in the water column does not result in a change of the bottom level.

$$\frac{\partial z_b}{\partial t} + \frac{f_{mor}}{1-n}\left(\frac{\partial q_x}{\partial x} + \frac{\partial q_y}{\partial y}\right) = 0 \tag{5.26}$$

This equation can be made volume conservative by taking the changes of the concentrations into account. Therefore, the volume-balance of sediment in the water column is considered. Figure 5.5 presents an overview of all the fluxes.

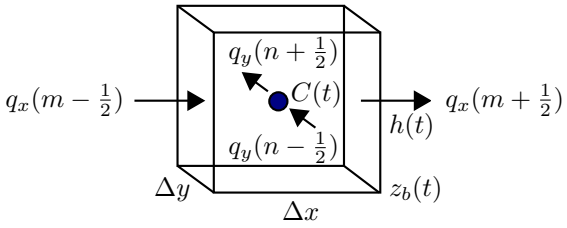

Figure 5.5: Balance of sediment mass in a grid cell.

The volume of the sediment in the water column can change due to two processes:

$$\frac{\partial V_{in\ concentration}}{\partial t} = \Delta x \Delta y \frac{1}{1-n}\frac{\partial Ch}{\partial t} \tag{5.27a}$$

$$\frac{\partial V_{in\ transport}}{\partial t} = \Delta x \Delta y \frac{f_{mor}}{1-n}\left(\frac{\partial q_x}{\partial x} + \frac{\partial q_x}{\partial x}\right) \tag{5.27b}$$

The net change in volume should balance with a change of the bottom level over time. A decrease of sediment volume in the water column corresponds to a rise of the bottom level:

$$\frac{\partial V}{\partial t} = \frac{\partial V_{in\ concentration}}{\partial t} + \frac{\partial V_{in\ transport}}{\partial t} = -\Delta x \Delta y \frac{\partial z_b}{\partial t} \tag{5.28}$$

This results in a volume-conservative Exner equation:

$$\frac{\partial z_b}{\partial t} + \frac{f_{mor}}{1-n}\left(\frac{\partial q_x}{\partial x} + \frac{\partial q_y}{\partial y}\right) + \frac{1}{1-n}\frac{\partial Ch}{\partial t} = 0 \tag{5.29}$$

Chapter 6

Performance of the improved model

6.1 Approach

This chapter assesses the performance of the improved XBeach model. Firstly, it is verified whether the implementation is correct and if the model behaves as expected. Thereafter, the performance of the full morphodynamic model is assessed on overwash and breaching cases.

Appendix D.3 presents an overview of the exact parameter settings of the considered model runs. No calibration of the model runs is performed in this chapter, as intended. It is the tendency of the improvements that is important.

6.2 Verification: conceptual model tests and side effects

Before the focus is on the overwash and breaching cases, it is tested whether the implementation is correct. First, some fictitious models runs are considered to have a detailed look at certain processes. Thereafter two wave flume experiments are modelled to test whether the improved model affects the swash and collision regimes unexpectedly.

6.2.1 Conceptual model tests

Appendix E presents several conceptual model tests. For these cases, the XBeach model is modified to enforce certain hydraulic conditions, e.g. a constant flow velocity. In this chapter, a summary of the most important observations will be given, see the relevant appendices for a more detailed analysis.

Bed slope test case (Appendix E.1)

In this model, a flow is enforced under a certain angle over a sloping bed. The hypothesis which states that the present implementation of the engineering formula of Soulsby is erroneous, can be confirmed based on this model test. The method is intended as a pure magnitude modification of the transport rates, whereas a change of direction was observed using this method.

The order of magnitude of the bed slope effect in the improved model is substantially smaller than the properly implemented engineering formula of Soulsby. This is related to a much smaller coefficient of the magnitude modification of the transport rates (0.15 instead of 1.6).

Eroding bed test case (Appendix E.2)

By enforcing a certain erosion velocity of the bottom level, the influence of dilatancy on the sediment transport rates can be tested. Based on this model test, the method of Van Rhee (2010) seems to be implemented correctly. A larger hindering of the sediment transport rates is observed once a larger erosion velocity is enforced. If the bottom level rises, dilatancy plays no role. Dilatancy causes a horizontal translation of the sediment transport rates in the $q - U$ graph which seems to be rather small. However, this can still result in substantial hindering of erosion since the gradients in transport rates are of importance, not the actual magnitude of the rates.

Accretion of a bed (Appendix E.3)

A flow with a large concentration of sediment is brought suddenly to a zero flow velocity. As a result, the sediment in the water column settles and the bottom level rises. This conceptual model test showed that the latter process, i.e. the rise of the bottom, is not modelled by the default XBeach model at all since no spatial gradients in sediment transport occur. Making the Exner equation volume-conservative solves this problem. When a morphological acceleration factor is applied, the equation is still mass conservative but the adaptation time scale is slightly modified.

6.2.2 Influence modified model on the swash and collision regime

The improvements considered in this thesis are focused on overwash and breaching conditions for which the bed level changes rapidly. It is important to check whether the improvements also have an influence on other processes. Therefore, two swash and collision cases are examined. Appendix F deals with two flume experiments. The most important conclusions are stated here.

Delta Flume 2006 experiments (Appendix F.1)

Various experiments in the Delta Flume with dune profiles are considered. By the limited water level, no overwash is observed and the experiments focus hence on the swash and collision regime. By erosion due to the waves, the dune foot propagates in onshore direction. The hindcast of the bed profile modelled with XBeach is in quite good accordance with the experimental data. If the sediment transport rates are limited by the θ_{max} limiter, some of the runs are affected positively and some negatively. The improved model shows very similar results to the default XBeach settings, no substantial side effects are observed.

Delta Flume H298 experiments (Appendix F.2)

The Delta Flume H298 experiments contain comparable dune profiles to the Delta Flume 2006 experiments. Now, hard dune (foot) revetments with a variation in height are placed in the flume, see Figure 6.1. By the presence of the hard structures, erosion is hindered locally and an erosion hole is generated in front of the structure. The depth of the erosion holes depends on the height of the structures: a low structure has more erosion above the structure and the eroded sand can be trapped in the erosion hole. Comparable conclusions to the Delta Flume 2006 experiment are made: no evidence of side effects by the model improvements are found. Further, θ_{max} is shown to hinder the erosion to a too large extent.

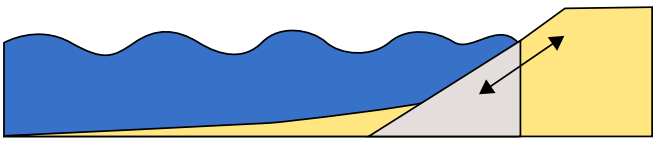

Figure 6.1: Schematic visualisation of the structures in the H298 experiments with a variable height.

6.3 Breaching and overwash models

Now it has been shown that the model improvements seem to work as expected and no substantial side effects are found, the improved model is applied on the breaching and overwash cases of Chapter 3. The improved model is compared to the default XBeach settings (now with $C_{max} = 0.3$, which is also used in the improved model) and the sensitivity of the model improvements is tested.

6.3.1 Improved model compared to the data of Voogt et al.

In Section 3.1, a comparison of the modelled sediment transport rates of XBeach was made to the experimental data of Voogt et al. (1991). Now, the improved model is presented with this dataset in Figure 6.2. As visible, smaller equilibrium sediment transport rates are achieved compared to the default Van Thiel-Van Rijn equation. The larger the erosion velocity, the larger the hindering of the equilibrium sediment transport rate. As mentioned earlier, the dilatancy effect is responsible for this horizontal translation of the equilibrium sediment transport rates by the increase of the critical depth averaged flow velocity U_{cr}.

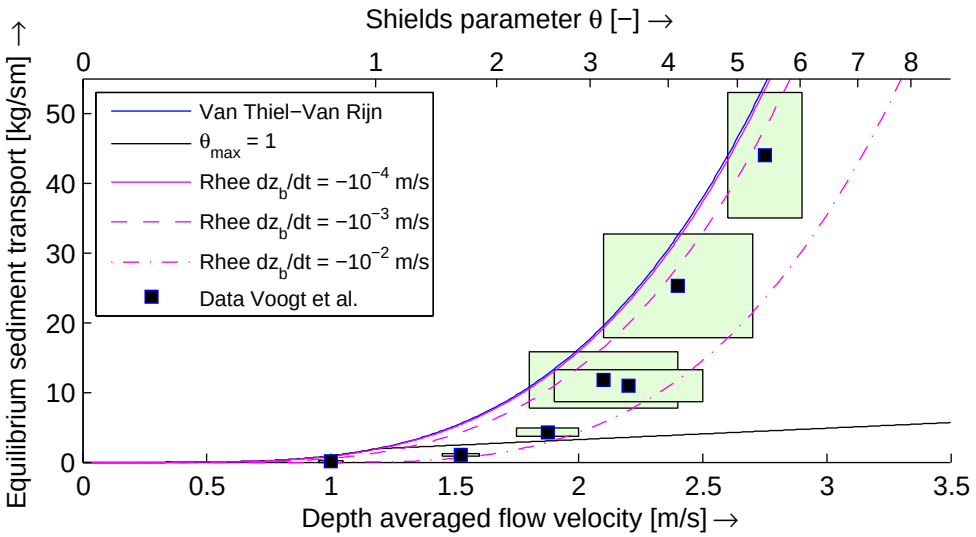

Figure 6.2: Data of Voogt et al. (1991) in combination with plot of the improved sediment transport function in XBeach with and without a limiter to the Shields parameter (limiter is set to $U_{max} = 1.2\ m/s$ according to the data of Voogt et al.). For the dilatancy method, various values of the bed level rates are taken, which are in reality dependent on the transport rates.

It seems that the XBeach results are better in correspondence to the dataset if dilatancy is taken into account. It is not possible to make a strong conclusion based on just this dataset as the uncertainties in the model parameters are substantial.

6.3.2 2DV Scheldt Flume experiment "Bresgroei"

Section 3.2 introduced the one-dimensional breaching experiment by Steetzel and Visser (1992). In this section, the same experiment is used to assess the performance of the improved model. Also variations to the dike profile are observed, since more measurement data are available.

First, the earlier presented experiment T5, containing a dike profile and a median grain size of $220\ \mu m$, is treated. Thereafter, experiment T6 is assessed which uses a dune profile. In experiment T3, the same profile is observed, but now with half the grain size. Finally, experiment T4 deals with waves, which are applied on the dune profile with the fine grain size. See Appendix G.1 for more details.

Dike profile (experiment T5)

Experiment T5 was used to assess the performance of the present XBeach model. Figure 3.8 showed that the location of the erosion front was not yet described correctly. Figure 6.3 presents the prediction of the erosion front with the improved model. Again, the location of the erosion front is defined as the smallest x-value for which more than $1\ cm$ erosion occurred.

Compared to Figure 3.8, the XBeach default performs worse now with respect to the measurement data, this is due to the larger C_{max} value of 0.3 used in all the model runs in this chapter. As visible, the improved model matches the measurement data almost perfectly. The results are also substantially better if compared to the default model runs with the lower concentration limit of 0.1.

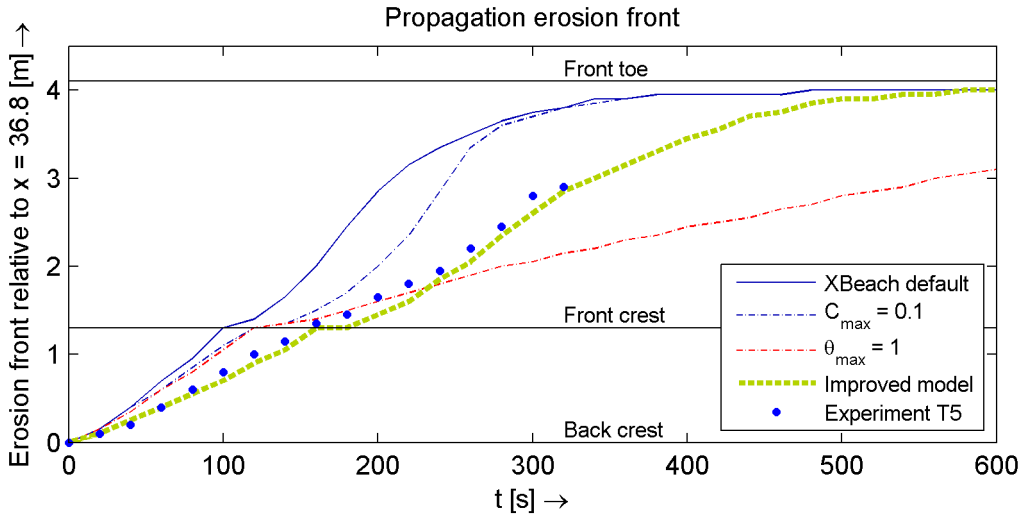

Figure 6.3: Propagation of the erosion front in time for experiment T5. The position of the erosion front is defined as the smallest x coordinate for which at least 1 centimeter erosion occurred.

The fact that a perfect fit to the data is achieved, both in the second as third phase of the breaching process, is not the most important thing as no calibration is applied. More important is the tendency of the improved model and the importance of the different processes used in the improved model. As intended, the improved model results in substantial hindering of the erosion.

In Appendix G.1, a more detailed analysis on the improved model is presented. This analysis confirms the increase in skill of the XBeach model with the introduced improvements. Dilatancy is proven to be the main cause of the erosion hindering in the results. Further, the bed slope effect has also an important influence on the results, required to prevent too much hindering of erosion. The fall velocity reduction and the conservative Exner equation do not substantially change the results.

Dune profile (experiment T6)

If a less steep foreshore is used in the model, the results are slightly different. As expected, the second phase of the breaching event is modelled with similar results compared to the previous experiment, as visible in Figure 6.4. This confirms the suggestion of the breach model by Visser (1998), the backside of the dune/dike determines the progress of the second phase. The skill of the improved model during the second phase is still very good.

During the third phase of the breaching process, once the top of the dune is lowering, some discrepancies between the improved model and the experimental data are observed. Still, the improved model performs better than the XBeach default. Appendix G.1 shows that, although a slight bias is modelled, the skill of

the improvements is very good. Again, dilatancy and the bed slope effect are the main modifiers in the improved model. The slight underestimation of the erosion, could be caused by a too small bed slope effect which would result in a faster propagating erosion front.

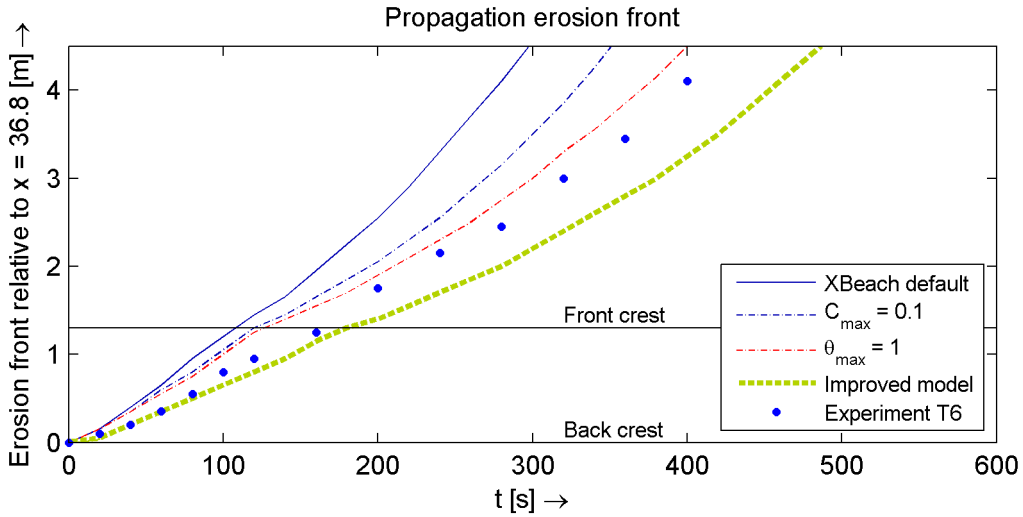

Figure 6.4: Propagation of the erosion front in time for experiment T6. The position of the erosion front is defined as the smallest x coordinate for which at least 1 centimeter erosion occurred.

Dune profile with smaller grains (experiment T3)

If a smaller grain size is applied, dilatancy should be more important in the theory of Van Rhee (2010). At the same time, the sediment transport equations are also affected. Figure 6.5 shows that the XBeach default settings result in more erosion with respect to the larger grain size. Although the improved model overestimates the erosion rates for now, it results still in less erosion compared to the XBeach default. Appendix G.1 notes that it is more effective to increase the dilatancy effect by a larger value for the coefficient A than to neglect the bed slope effect, if one would achieve results closer to the measurement data. Modifying the parameter A is reasonable as it is essentially a calibration parameter.

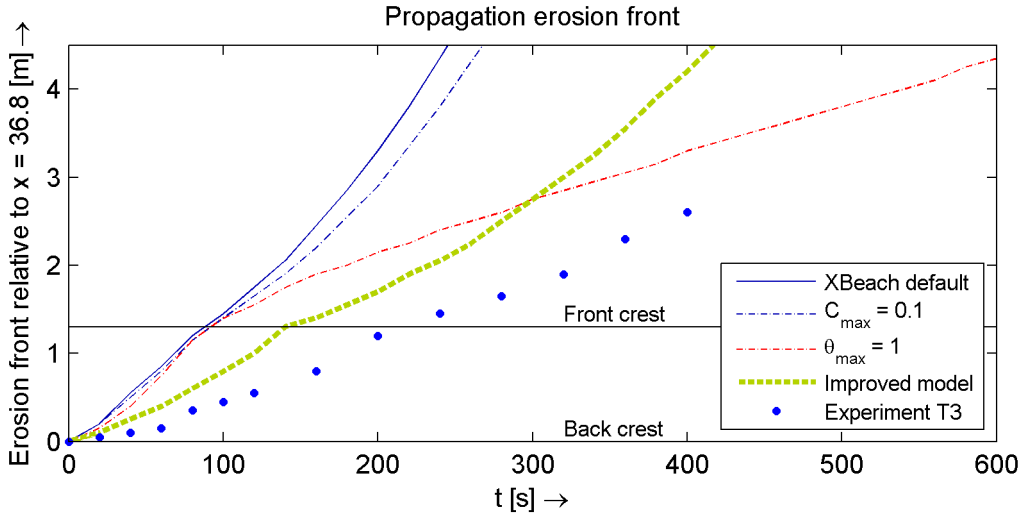

Figure 6.5: Propagation of the erosion front in time for experiment T3. The position of the erosion front is defined as the smallest x coordinate for which at least 1 centimeter erosion occurred.

Dune profile with smaller grains and waves (experiment T4)

Since waves cause the dune crest to lower during phase 2 of the breaching process, a clear figure of the erosion front cannot be made. This lowering of the dune crest is not only a feature observed in the model results, but it is also seen in the experimental data. To get some impression of the results of the improved model, a time stack of the model results is presented in Figure 6.6.

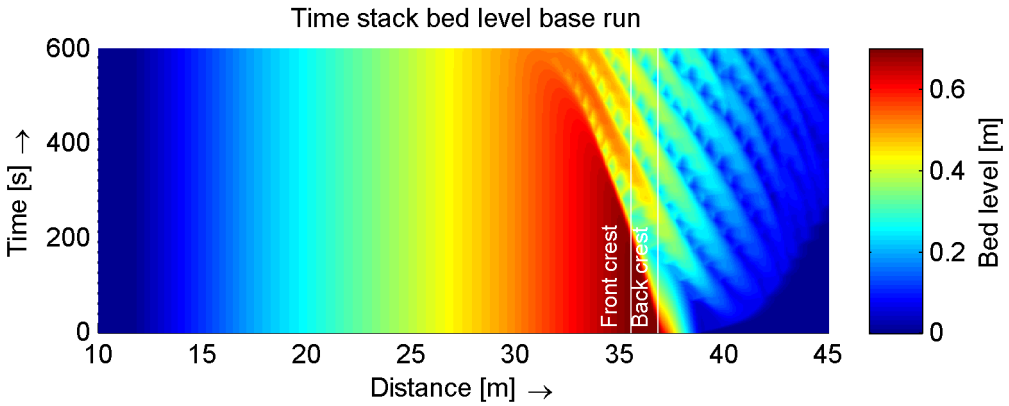

Figure 6.6: Time stack of the improved model for experiment T4.

From Appendix G.1 it can be learned that waves increase the erosion velocity substantially, the back slope retreats hence faster, what is also observed in the measurement data. Just like with the previous experiment with fine grains, the results of the improved model are not perfect but the improved model performs substantially better with respect to the XBeach default. Again, a better approximation is made if a larger value is chosen for the parameter A.

The presence of antidunes and chutes-and-pools

One of the hypotheses is that the artificial limiters C_{max} and θ_{max} result in less realistic shapes of the bottom profiles. This hypothesis will be tested in this section. For now, the focus is on experiment T5 which showed a good performance with respect to the measurement data.

Various types of bottom profiles are observed if C_{max} is set to 0.3. For example, antidunes are noticed after $120\ s$ in Figure 6.7. This profile contains all properties of antidunes as described in Appendix B. Firstly, the water level is in phase with the bed level. Secondly, the profile propagates in upstream direction. In the same figure, the measured bottom profile is presented. Note that the very steep measured profile is not possible in the XBeach model by the limitation of the underwater slopes to 0.3. Besides this difference, the measured profile is in accordance to the modelled profile.

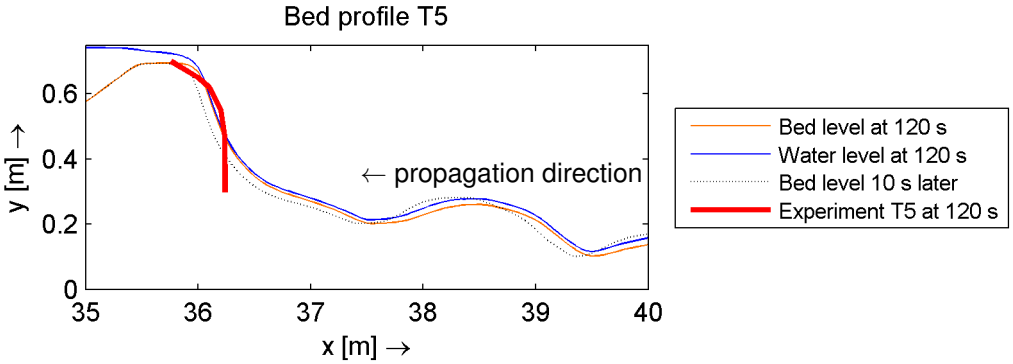

Figure 6.7: Presence of antidunes during the model runs. Presented is the improved model.

Some time later, chute-and-pool features are noticed in Figure 6.8. Also the characteristics of these features are nicely in line with the qualitative theoretical description of Appendix B. The flow accelerates in the chute whereas it slows down in the pool. Thereafter, the next chute-and-pool feature is observed. From this figure, it is clear that also these features propagate in upstream direction. The measurement data confirms the correctness of the steep slope at the back side of the dike crown.

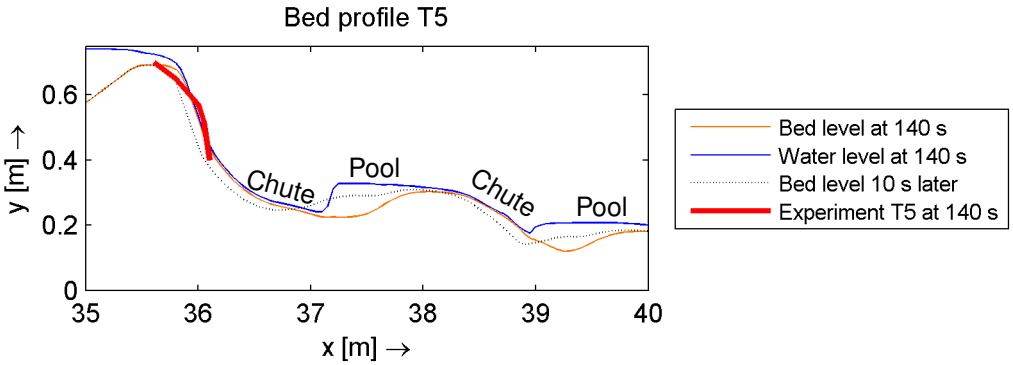

Figure 6.8: Presence of chutes-and-pools during the model runs. Presented is the improved model.

Now it is tested how the profile would look like if the improved model is combined with a C_{max} value of 0.1. Figure 6.9 shows that the bed profile looks much smoother now and no substantial bed features are observed. Also, the back side of the dike profile is much wider and under a less steep angle, which is not in line with the measurement data.

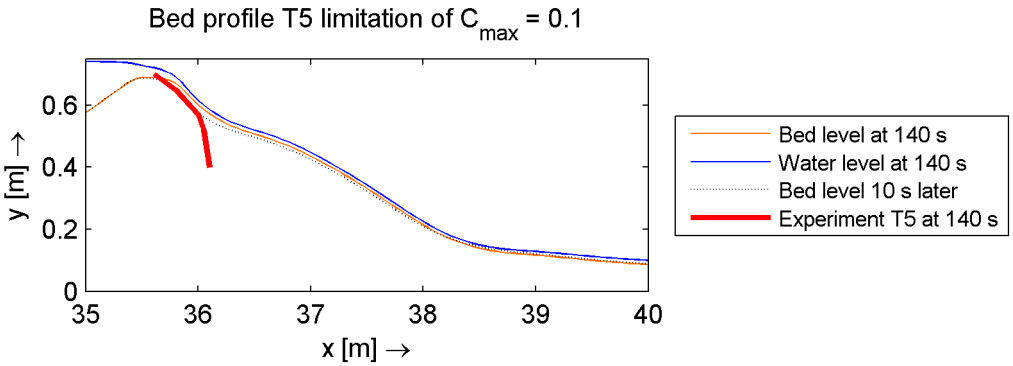

Figure 6.9: Bed features are damped out substantially in the Scheldt Flume model runs if C_{max} is reduced. Presented is the improved model with C_{max} set to 0.1 instead of 0.3.

Finally, the question arises whether the observed bed features are also noticed in the experiment. This is difficult as the profile below a depth of roughly $0.3\ m$ is not reported in the experimental data, as visible in Figure 6.10. However, based on the steepness of the profiles, the large flow velocities and Froude numbers, it is likely that the modelled features will occur in reality. The question remains if these features occur in the same quantity and with the same magnitude as modelled with the XBeach model. Since a strong interaction is present between hydraulics and morphology with these features, it is well possible that discrepancies arise.

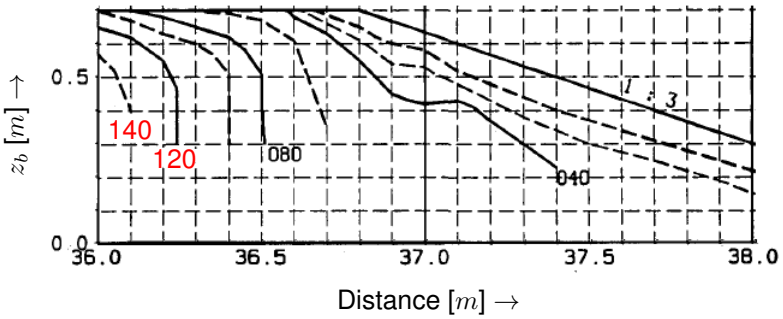

Figure 6.10: Measured bed profiles of experiment T5.

Conclusion of the experiments

To conclude, the improved model has shown substantial improvements with respect to the XBeach default settings. In the T5 experiment, a very good fit to the measurement data was found. In the other experiments some deviations arose, but an exact fit was not the main focus of the analysis. The largest deviations were observed if a smaller grain size was used in the experiment, a stronger dilatancy effect could solve this discrepancy. Once waves were included, the results got a little bit worse, but still the hindering of erosion by dilatancy did modify the obtained profiles substantially in the correct direction.

More important than an exact fit on the measurement data is the importance of the individual improvements in the improved model. Based on this experiment, the conclusion is drawn that dilatancy is the main driver of erosion hindering in the improved model. Further, the bed slope effect has also a substantial influence in the realised results, it increases the erosion slightly for a down-slope directed flow. The fall velocity reduction and the conservative Exner equation did only slightly modify the results.

The hypothesis that the artificial C_{max} limiter hinders the presence of bottom profile features is confirmed. If the limiter is set to the quite large value of 0.3, antidunes and chutes-and-pools are observed which behave qualitatively in line with theory. These features are not observed for a limiter value of 0.1. The question remains whether the observed features are modelled in the right quantity and magnitude.

6.3.3 Zwin dam breach

In Section 3.3, the data of the controlled Zwin dam breach was used to assess the performance of the present XBeach model on a two-dimensional breaching case. Now, the model improvements are applied on this model case.

This section deals with the most important observed processes and is based on Appendix G.2.

Breach width growth

The Zwin model shows a substantial sensitivity to the type of implemented bed slope effect. This is mainly due to the steep slopes in the breaching channel for which the on-slope directed vector is perpendicular to the flow direction. If one observes the performance of the XBeach default settings on the breach width prediction, a much wider breach is predicted with respect to the properly implemented engineering approach of Soulsby, see Figure 6.11.

An overall underestimation of the breach width in the order of 20% is modelled by the improved model. This could suggest that the processes are well described by the improvements and that only a calibration of the sediment transport rates, which are generally uncertain, is required to result in a proper fit on the data. In contrast, the improved engineering approach of Soulsby results in an overestimation of the transport rates during the first half of the run and an underestimation during the second half of the

experiment. This latter observation suggests that there is more hindering of erosion required during the first phases of the experiment in the Soulsby slope effect model run. If the depth averaged sediment concentration is restricted to 0.1, the opposite is observed: first an underestimation of the erosion rates followed by an overestimation. The sediment concentration limiter can hence also be qualified as non-proper model physics. Finally, the limitation to the Shields parameter leads to a very unrealistic breach width of only $7\ m$.

Based on these observations, the improved model seems to be the best estimate of the experiment results if calibrated properly.

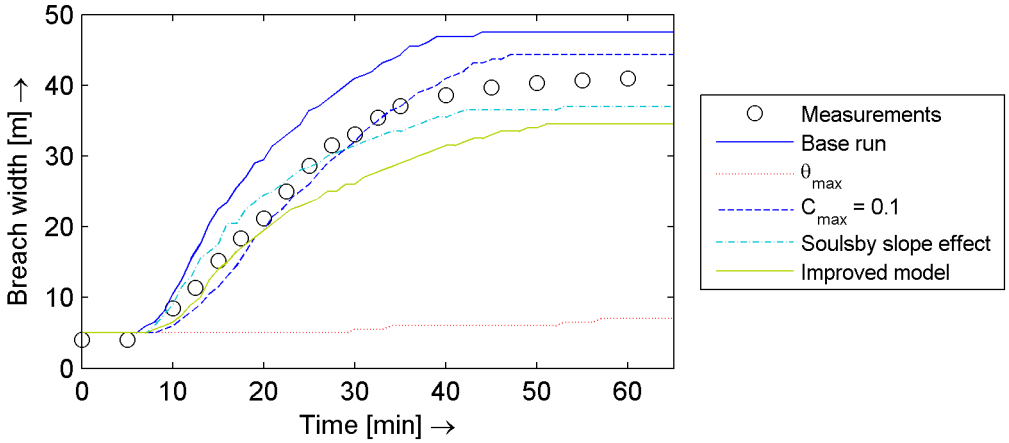

Figure 6.11: Evolution of the gap width over time for a maximum sediment concentration of 0.3.

Appendix G.2 provides an analysis on the sensitivity of the improved model to the different processes in the improved model regarding the breach width prediction. This analysis shows that dilatancy influences the breach width estimate roughly with $2.5\ m$, the bed slope effect has an influence in the order of $0.5\ m$ and the fall velocity reduction in the order of $0.4\ m$. The conservatism of the Exner equation is of no real importance for this case.

Bed profiles

Appendix G.2 showed that the cross-sections of the model results with the improved engineering bed slope effect by Soulsby are very angular. The improved model includes a slight change of transport direction which causes a smoother profile.

A close look to the cross-sections is made to verify if there are bed-forms present in the results modelled with the improvements. Figure 6.12 presents several cross-sections through the breach channel during the first phases of the breaching process. These cross-sections show that the first phase of the breaching process is completed within the first minute. The second phase is finished after roughly four minutes. During this second phase, the breach channel is deepened but no widening is modelled, which is in line with the experimental data as visible in Figure 6.11. Once the third phase is initiated, the breach channel increases both in width as in depth.

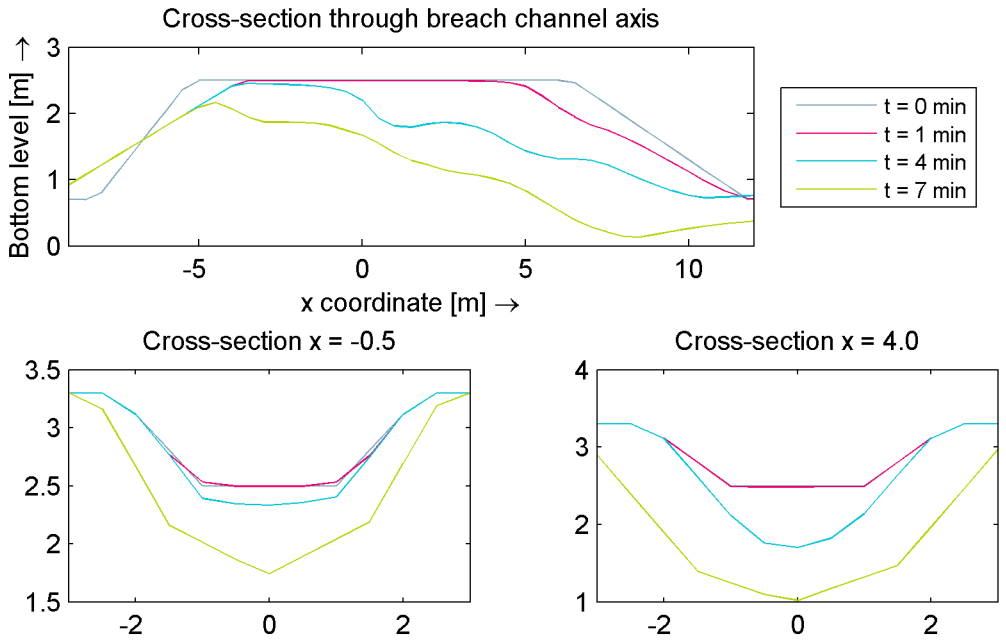

Figure 6.12: Cross-sections at several moments in time with the improved model. The top plot is a cross-section through the channel axis. The two plots on the bottom are cross-sections perpendicular to the above one at the x-coordinates mentioned. All results are for the base run. The sea side is on the left side of the plots.

Figure 6.12, shows some oscillating bed forms. In Figure 6.13, the cross-section through the channel axis after four minutes together with the water level elevation is given. Clear evidence of antidunes is visible: the bed level is in phase with the water level with a wave length of roughly $6\ m$. It is questionable if these features were present in the experiment in the same order. Unfortunately, there is no data available on the bed profiles, only the breach width evolution over time can be used to assess the performance of the model. In Section 3.3, it was already shown that a limitation to the depth averaged sediment concentration causes damping of the bed profiles.

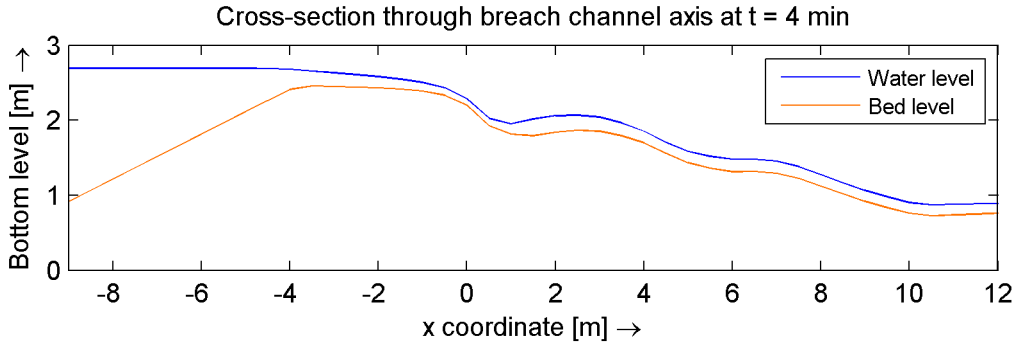

Figure 6.13: Presence of antidunes during the model runs. Presented is the improved model.

Figure 6.14 presents the cross-sections during the third breaching phase. As visible, the width increases now substantially and the depth keeps increasing consequentially. At the sides of the channel, a $1:1$ slope is observed, which equals the critical dry slope and is steeper than the critical wet slope. Once the channel deepens, the width of the channel increases by avalanching. The third phase is finished after approximately 20 minutes whereafter the breach width keeps increasing during the last two breaching phases without substantial depth increases, see Appendix G.2.

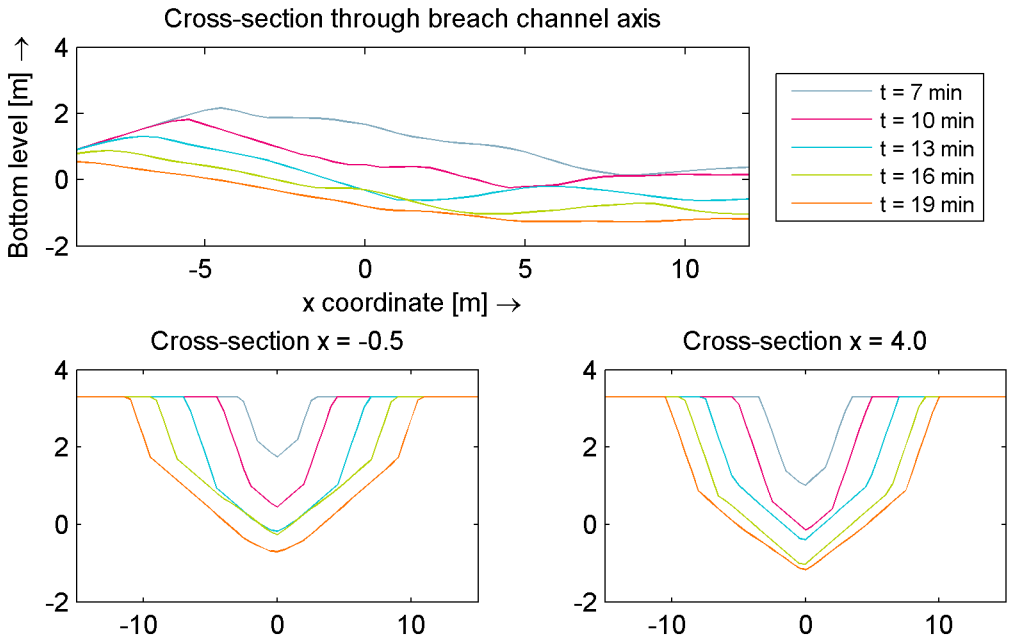

Figure 6.14: Cross-sections at several moments in time with the improved model. The top plot is a cross-section through the channel axis. The two plots on the bottom are cross-sections perpendicular to the above one at the x-coordinates mentioned. All results are for the base run. The sea side is on the left side of the plots.

Conclusion of the Zwin experiment modelling with the improved model

The Zwin experiments showed that the presently implemented bed slope effect differs substantially from the engineering bed slope approach of Soulsby. If the properly implemented engineering bed slope approach of Soulsby is considered, erosion is overestimated during the first half of the experiment and underestimated during the second half. This suggests that some processes are not modelled properly yet.

If the improved model is considered, for which dilatancy is the most important additional process, much better results are observed. Although no perfect fit on the data is achieved, the shape of the breach width evolution function over time is similar to the measurement data. The roughly 20% underestimation of the breach width suggests that some calibration could result in a proper description of the experiment. Besides dilatancy, also the bed slope effect and the fall velocity reduction are of substantial importance. If the depth averaged concentration is limited to only 0.3, bed forms like antidunes are observed.

6.3.4 Santa Rosa Island

In Section 3.4, the XBeach model of McCall et al. (2010) was used to assess the performance of the present XBeach model on a real storm event. Very large overestimations of the erosion rates were modelled, now it is checked if the improved model solve these problems or if other model parameters dominate the model performance.

Performance of the improved model

Even with the hindering of erosion by dilatancy, the improved model does result in only in a small reduction of the erosion volumes. Figure 6.15 shows the final profile computed by the improved model. As visible, still a large breaching channel is modelled. In reality, only an average erosion of $0.09\ m$ was

measured with the LIDAR data. The sensitivity analysis of Appendix G.3 shows that dilatancy has an influence on the bed level changes in the order of only $10\ cm$. The influence of the other processes in the improved model is negligible with respect to the large erosion rates predicted by the model.

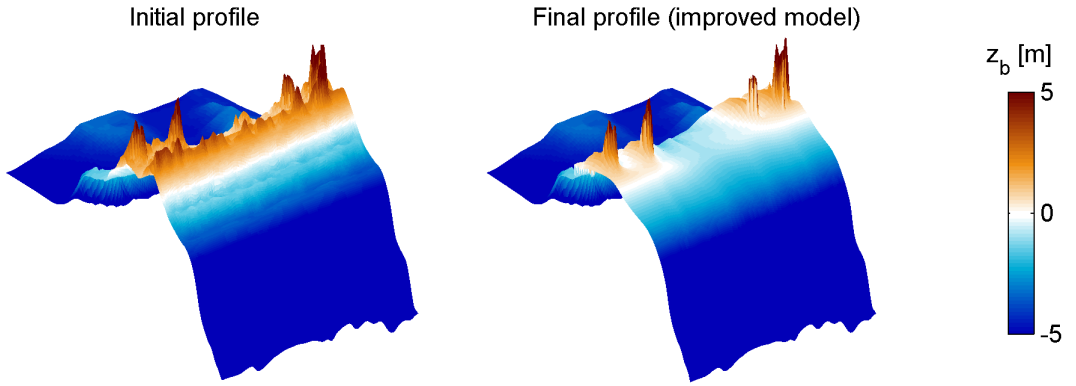

Figure 6.15: Initial and modelled profile of the Santa Rosa model.

Sensitivity to model parameters

Appendix G.3 presents also a sensitivity analysis to other parameters. If the surge level is decreased, substantial better results are achieved, especially if the surge level is reduced at the sea side only. Increasing the grain sizes and decreasing the permeability causes less erosion, as expected (groundwater flow is not considered by the relatively small grain sizes). Still, for all these cases has the model a negative skill.

A large sensitivity to the model is found for the Chézy value. If the Chézy value is decreased substantially, to a value of $20 - 35\ m^{0.5}/s$, a positive skill is achieved. A smaller Chézy value could be reasonable to account for the presence of vegetation and rough structures on top of the barrier island.

Conclusion of the Santa Rosa case

The improvements do not solve the large overestimation of the erosion rates by the XBeach model. It is shown that the overestimation is so large, that the improvements are not significant at all. If the surge level is lowered, the grain sizes are increased or the permeability is reduced; substantial better results are achieved. Only with a reduction of the Chézy value to $35\ m^{0.5}/s$ or less, a positive skill is achieved.

The found increments of the XBeach skill with the presented modifications, lead to the conclusion that any modification improves the predictive skill if the erosion is hindered. This does not mean that the process behind the modification is physical. With this, it can be explained why the θ_{max} limitation results in good results for this case, whereas it performs poorly on the other cases.

6.4 General conclusions

Based on the conceptual model tests, the improvements made in this thesis are validated. A bed slope test case confirmed that the present implementation of the engineering formula of Soulsby is erroneous and that the related improvements behave as expected. An eroding bed test case demonstrated the behaviour of the implemented dilatancy model, which is in line with theory. Finally, the accretion of a bed is observed in a conceptual model which confirms the mass-conservatism of the improved model by the Exner equation improvement.

Two experiments, which were performed in the Delta Flume, confirm that no substantial side effects are introduced in the swash and collision regime of a storm event by the improved model. Side effects were observed if the θ_{max} limiter was applied.

Although the uncertainty in the data of Voogt et al. (1991) is substantial, it places the tendency of the improved model in a good perspective. The larger the modelled erosion rates, the larger the modelled hindering of the transport rates, which is in line with Van Rhee (2010).

The improved model has shown very substantial improvements with respect to the XBeach default in both the Scheldt flume experiment as in the Zwin experiment. The focus was not so much on an exact representation of the data sets since that would require calibration steps. The tendency of the improvements seems to be valid. Mainly a reduction of the erosion rates is achieved by taking dilatancy into account.

Also the bed slope effect is of importance for both experiments. It is shown that the erroneous implementation of the Soulsby bed slope effect causes a substantial overestimation of the breach width in the Zwin test. If the Soulsby bed slope effect is implemented as Soulsby (1997) intended, the erosion during the first half of the experiment is overestimated and underestimated during the second half of the experiment which shows that the model result has a different tendency compared to the experimental data. The improved model does show the correct tendency and calibration could solve the structural underestimation of the breach width evolution over time of roughly 20%. The fall velocity reduction is only of importance in the Zwin experiment and the conservatism of the Exner equation is not important at all.

The hypothesis that the artificial C_{max} limiter hinders the presence of bottom profile features is confirmed. Without a strong limitation, antidunes and chutes-and-pools are observed in the improved model results of the Scheldt Flume test. These features are not modelled for a limiter value of 0.1. Bottom profile features are less substantial in the Zwin model, possibly caused by the much larger grid sizes.

If the improved model is applied on the Santa Rosa model, much less substantial improvements are observed. Dilatancy does not explain the huge overestimation of the erosion rates at the barrier island, which are roughly $1.6\ m$ on average in the model and $0.09\ m$ in the LIDAR data. A surge level lowering, a grain size increase and a reduction of the permeability reduce the erosion rates substantially. Only with a reduction of the Chézy value to $35\ m^{0.5}/s$ or less, a positive skill is achieved. Although the θ_{max} limitation leads to good results for this case, it is not likely to involve proper physics as it has not been proven to work properly in the other cases.

Chapter 7

Modelling Fire Island hurricane event with the improved model

The Santa Rosa case study, as treated in Sections 3.4 and 6.3.4, showed a substantial overestimation of the erosion rates by the XBeach model. A disadvantage of the Santa Rosa case study is that no breaching occurred in the measurement data and that large uncertainties are present regarding the boundary conditions. To get a better understanding of the performance of the XBeach model on an overwash and breaching field case, a new case study is introduced in this chapter. The impact of hurricane Sandy on Fire Island near Pelican Island is selected as a suitable case for this research, based on the morphological processes that occurred during the storm and the quantity of data available.

7.1 Introduction

Hurricane Sandy was a late-season hurricane, as defined from the beginning of June until the end of November, Sandy made landfall on the 29th of November. It is the second costliest hurricane since 1900 by a U.S. damage estimate of $50 billion (it ranks sixth if corrected for inflation, population and wealth normalization) and there are at least 147 deaths recorded, directly related to Sandy (Blake et al., 2013).

The left picture of Figure 7.1 shows the track of the hurricane. Above Jamaica, Sandy reached a 100-kt category 3 status on the Saffir-Simpson Hurricane Wind Scale. It made landfall near Brigantine, New Jersey as ”only” a post-tropical cyclone with 70-kt maximum sustained winds. The tremendous size of Sandy, the largest in diameter measured since 1988, caused a huge storm surge on the New Jersey and New York coastlines (Blake et al., 2013). The distance between the location where Sandy made landfall and the project location is approximately $180\ km$.

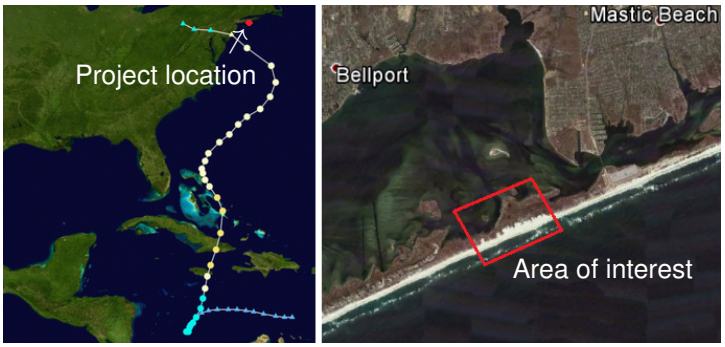

Figure 7.1: Left figure: hurricane track, increasing intensity from blue triangles to yellow circles, taken from Collins (2012). Right: detailed location of the project (source: Google Earth).

The area of interest of this study is located on Fire Island, a barrier island in front of Long Island, New York. See Figure 7.1 for a detailed visualisation. Hurricane Sandy made landfall near the project location on October 29th, 2012. Substantial morphological changes took place due to the large waves and storm surge. In Figure 7.2, pre- and post-Sandy aerial photography is presented. The satellite data shows clear evidence of breaching and overwash by Sandy.

Figure 7.2: Aerial photography of the project location, source: Google Earth. Left: pre-Sandy at July 3rd, 2012; right: post-Sandy at November 4th, 2012.

7.2 Data analysis

Storm regimes

Figure 7.3 presents the available LIDAR (LIght Detection And Ranging) data (USGS, 2012). The data shows the same tendency as visible in the presented satellite pictures. The LIDAR data are present at the 20th of January and the 5th of November with a high density: more than one million points cover the area of interest. For this study, processed and gridded data on a resolution of $1\text{x}1\ m$ is used. Pelican Island is not visible in the post Sandy data, this is not really a problem as the focus is on Fire Island.

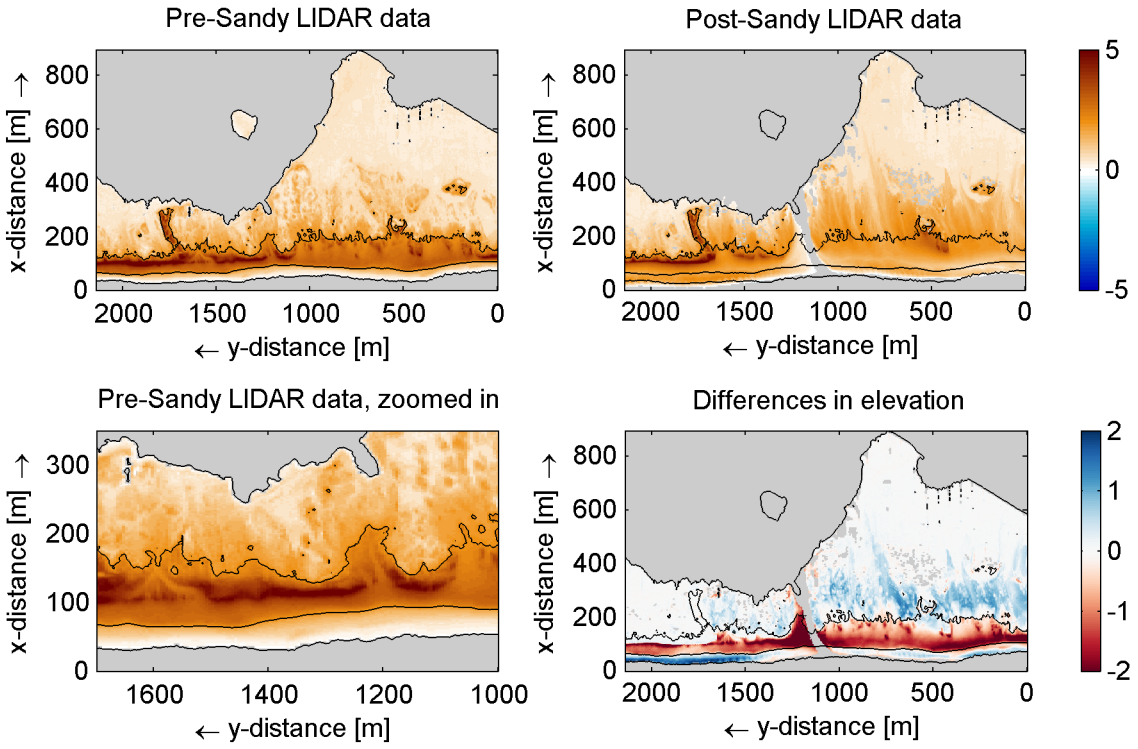

Figure 7.3: Pre and post Sandy LIDAR data, top view. The black depth contours are provided at an elevation of 0 and 2 m relative to NAVD88 of the initial depth profile. Spots without data are marked gray.

Based on these LIDAR data sets and the theory of Chapter 2, a more detailed analysis can be made on what happened during hurricane Sandy. For this analysis, the local axis coordinates of Figure 7.3 are used. In addition to the top view of the LIDAR data, several cross-sections are provided in Figure 7.4.

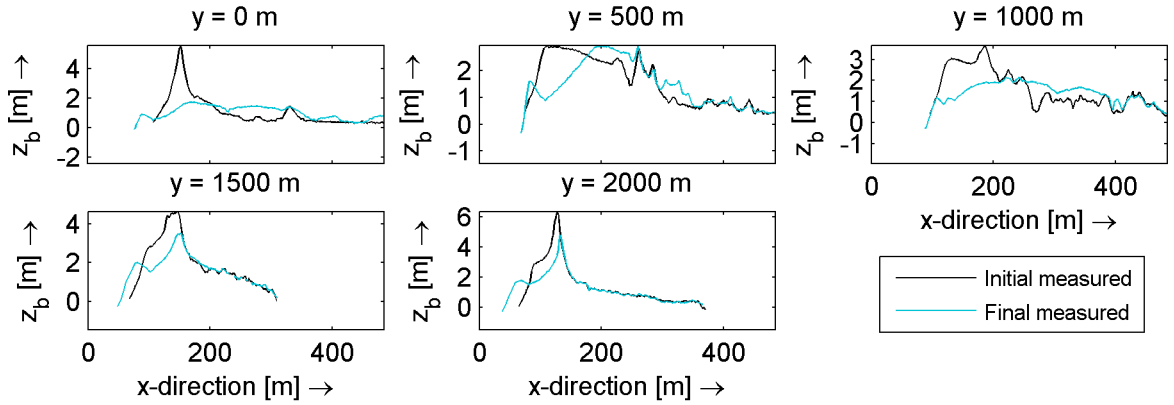

Figure 7.4: Cross-sections of the pre and post Sandy LIDAR data.

- At the right side of the project location (from $y = 0\ m$ to $y = 1100\ m$), clear evidence of **sheetwash** is visible. The relatively low initial dune height results in substantial flow rates across the island causing a wide-spread overwash terrace in which the sand of the dunes is deposited behind the original dunes.
- Around a y value of approximately $1100\ m$, **breaching** caused substantial local lowering of the bottom level. It is not clear why the breach is initiated at exactly this location. An examination of the pre-Sandy LIDAR data shows that the island breached at a location with a relatively large dune height. Just next to it, a lower dune elevation is found. One could also expect a breach around $y = 1550\ m$ in the area of the lower dune height. It is likely that the exact breaching location depends on many complex factors, like the three-dimensional geometry and local soil composition. Figure 7.5 shows evidence for the presence of a breach channel at the project location around the year 1815 Deitz (2013). It is well possible that composition of the soil in the old inlet is different with respect to the rest of the barrier island, causing a local weak spot.
- Around $y = 1600\ m$, an **overwash fan** is observed. The deposits are clearly visible in the satellite photos of Figure 7.2.
- In the region from $y = 1400\ m$ to the left side of the model at $y = 2150\ m$, **collision** occurred resulting in dune erosion without sufficient dune lowering to cause overwash (apart from the overwash spot at $y = 1600\ m$). As a result, the coastline retreated and eroded sand is deposited on the foreshore.
- Substantial **deposition of sand on the foreshore** is observed in the cross-section. This is possibly caused by the recovery of the shore, as the LIDAR data are collected days after the storm.

This case study is interesting due to the large variety of processes which occurred over a longshore distance of only $2000\ m$.

Figure 7.5: Historical map by William Damerum published in 1815. Taken from Deitz (2013).

Breach dimensions

The LIDAR dataset does not provide precise dimensions of the breach generated by Sandy. Therefore, another dataset provided by the USGS (personal communication, 2014) is consulted, see Figure 7.6.

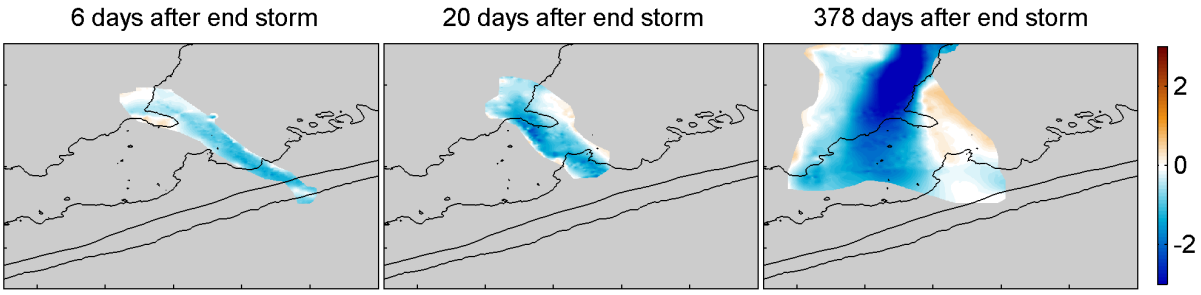

Figure 7.6: Evolution of the breach channel over time. Data by the USGS, days relative to the end of the storm (roughly 31-10-2012). Black lines are the 0 m and 2 m bottom level contours of the pre-storm LIDAR data. Spots without data are marked gray.

As visible, the breach channel is morphologically active during the year after Sandy. The channel shows a very interesting shift in position and increase in width and depth on the long-term. The channel seeks a straight geometry without a bend at the in- and outflow sides. The final geometry is not necessarily the same as directly after the storm as the hydraulic forcing by the storm is different from that by just the tide, but this is not the focus of this thesis.

What is relevant, is the position and the dimensions directly after Sandy. Based on the trend in the data measured 6 days and 20 days after the storm, one can conclude that the channel is already shifting actively during the first days after the storm. After the storm, the width of the channel is increased by the tidal flows. As a result, the actual post Sandy breach might be slightly smaller than the profile measured 6 days after the storm. Resulting in a bed level of roughly $1\ m$ below NAVD88 and a maximum width of approximately $50\ m$.

7.3 Model setup

To study the morphological evolution of the barrier island over time, an XBeach model is set up. Appendix H provides a detailed description on the decisions made and the steps taken to achieve a robust set of boundary conditions, model grid and bathymetry. An overview of the imposed boundary conditions is given in Figure 7.7. The surge level in the bay is based on measurement data and the other hydraulic boundary conditions are obtained from a large Delft3D model. At a distance of approximately $80\ km$ from the project location, the Delft3D predictions are compared to a wave buoy. At this location, the wave conditions are slightly inaccurate by a maximum of $1\ m$ deviation in wave height, $1\ s$ in peak period and 10 degrees in direction during the storm peak, but the model is the best data provider currently available.

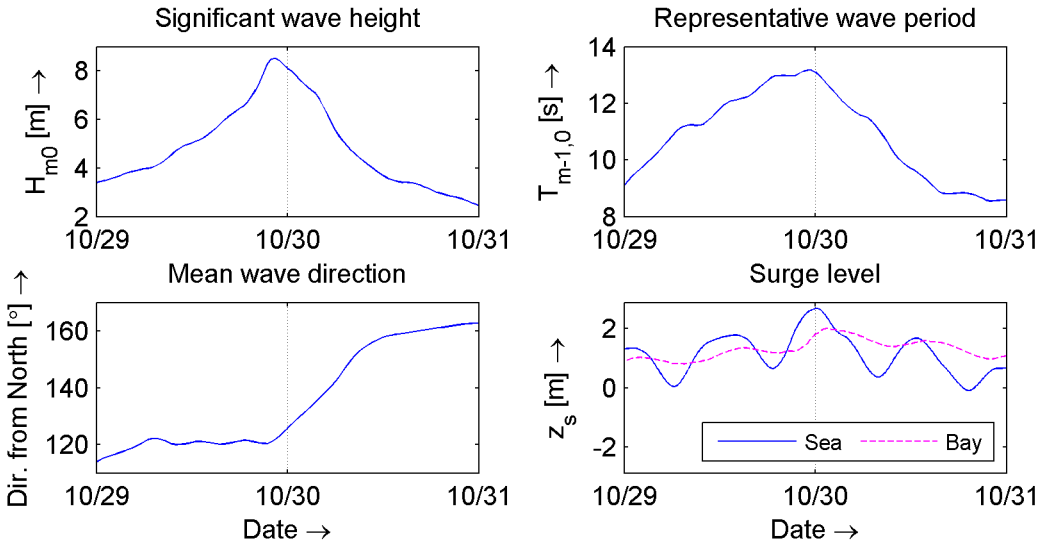

Figure 7.7: Imposed hydrodynamic boundary conditions based on a Delft3D hindcast and a measurement station, details are provided in Appendix H.

Regarding the bathymetry, several datasets - LIDAR (USGS, 2012), Coastal Relief Model (NOAA, 2014) and LARC (personal communication, 2014) - are merged with smooth transitions. Only in the bay no reliable data are available. A uniform bottom level of $1\ m$ below NAVD88 is assumed which will be varied in the sensitivity analysis. Figure 7.8 presents the pre-Sandy bathymetry applied in the model, which includes a synthetic breaker bar as observed in Figure 7.2. In longshore direction, constant grid sizes of $5\ m$ are applied, in cross-shore direction grid sizes vary spatially with a minimum of $2\ m$ near the barrier island and gradually increasing to the offshore boundary. The result is a grid containing 357738 grid cells including a shadow zone of 45 degrees to cover oblique waves at the project location. Finally, a sediment distribution described by a D_{15} of $290\ \mu m$, a D_{50} of $400\ \mu m$, and a D_{90} of $600\ \mu m$ is taken as representative based on three measurements provided by the USGS (personal communication, 2014).

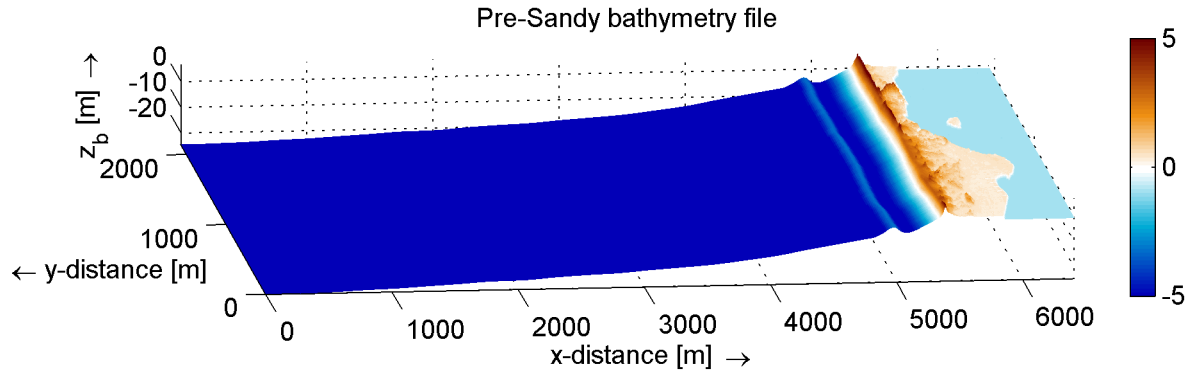

Figure 7.8: Pre-Sandy model bathymetry.

7.4 Results

7.4.1 Default XBeach model

Using the default XBeach model settings to calculate the morphological impact by hurricane Sandy on the 29th to the 30th of August, the model results of Figure 7.9 are retrieved. As visible, the island vanished after the largest surge peak. It is obvious that these results are not in line with reality as the island is still present in the current coastline.

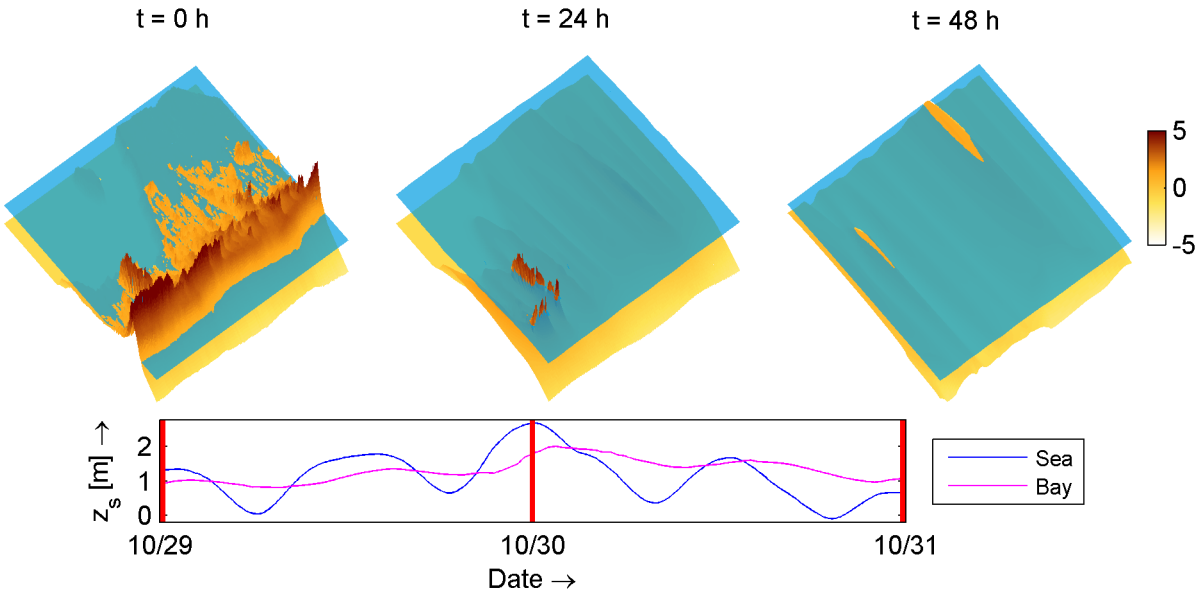

Figure 7.9: A $3D$ view of the model results of the XBeach default settings at some characteristic times (initial situation, at the peak of the storm and the final situation). The bay is located at the top-left of the figures and the sea at the bottom-right.

7.4.2 Shields parameter restriction and the improved model

As the morphological changes are significantly overestimated, it is likely that one or more processes are missing in the model. Two methods are considered which are likely to hinder erosion. First, the Shields parameter is limited in the sediment transport formulae to a value of 1. This method is found to be inappropriate for the many experiments considered in this thesis. However, it did show good skill in the Santa Rosa case study. Second, the model improvements of this thesis are applied to verify whether the additional physics explain the overestimation of the morphological changes.

Figure 7.10 presents a visual comparison of the XBeach default model settings to the model run with the Shields parameter limitation, the improved model and the measurement data. A very bad skill at almost every spot on the barrier island is achieved in the default XBeach model and the model with the improvements.

If the Shields parameter restriction is applied, much better results are achieved. There are many zones which are modelled with a Brier Skill Score of $0.8 - 1$, based on the classification of Van Rijn et al. (2003) such scores could be considered as ”excellent”. However, no breaching is predicted if the limiter is applied. This observation was also noted in the Zwin model of this thesis. As breaching is an important process, the Shields parameter restriction is thought to be inappropriate for this case study.

The model improvements of this thesis do not explain the large overestimation of the morphological changes. Substantial differences compared to the XBeach default are observed, but still a negative skill is achieved at almost all grid cells. Compared to the XBeach default, the breach channels seem to be much narrower, which can be explained by the different bed slope effect.

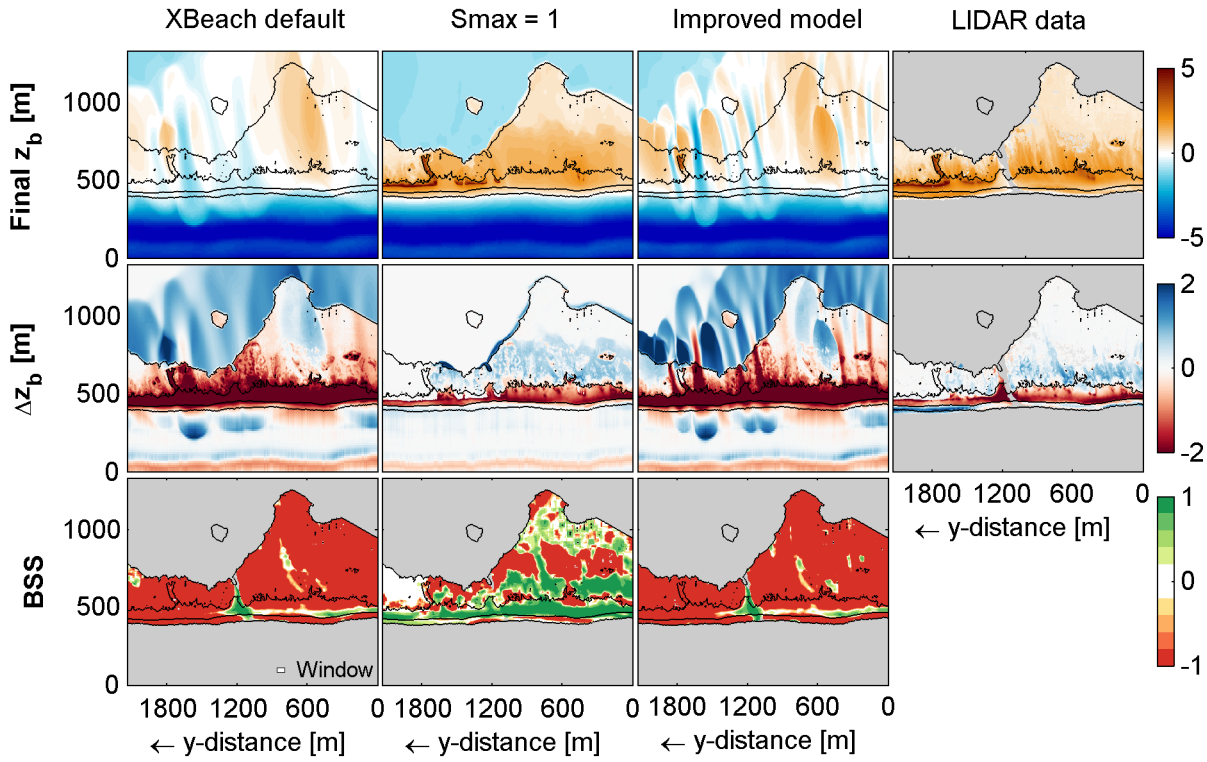

Figure 7.10: Performance comparison between XBeach default, limited Shields parameter and the improved model. Shown are the final bed level, the bed level changes by the storm event and the Brier Skill Score with a moving window of 10x10 cells. The black depth contours are provided at an elevation of 0 and 2 m relative to NAVD88 of the initial depth profile. Spots without data are marked gray.

The results are quantified to take a closer look at the model results. First, four zones are identified based on the initial geometry. In zone A, high dunes are present (up to $\approx 6.5\ m$) which were mainly subject to the collision regime during the storm. Zone B contains also high dunes, but a local weak spot resulted in an overwash fan. In zone C, mainly overwash took place by the lower initial dune height which is relatively uniform in longshore direction. Zone D is defined behind zone C, which is the large low-lying back barrier. The zones are visualised in Figure 7.11.

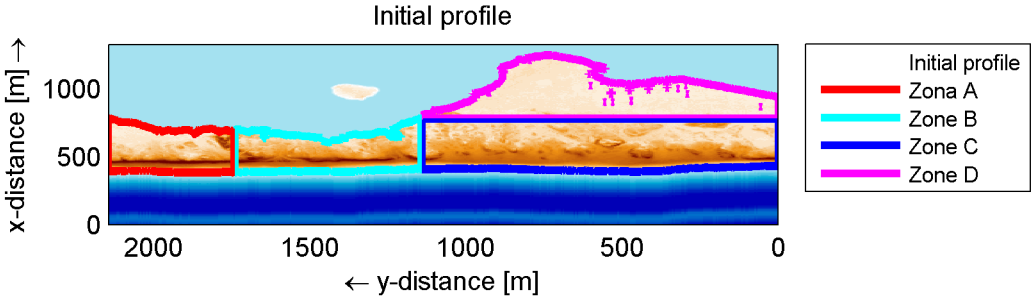

Figure 7.11: Various zones to classify the different parts of the model domain on top of the barrier island.

Table 7.1 presents the Brier Skill Scores and the bias for these zones. The model skill is very poor in all the zones for both the XBeach default as the improved model. An overall bias reduction by the model improvements of $12\ cm$ is achieved, the bias reduction is the largest in zone A. The Brier Skill Score of the model with the Shields parameter restriction is 0.61 for the full barrier island and even 0.71 in the overwash region, zone C. Zone D is modelled with a negative skill if the Shields parameter is applied. As only small morphological changes take place, the Brier Skill Score is not a good estimator for the skill in this region. The mean bottom rise is much more relevant than the profile shape.

As the Brier Skill Score and the bias have a restricted meaning, these numbers are incapable of accounting for specific features, other indicators are introduced. Table 7.2 presents these indicators. The occurrence of breaches is an important point. As breaching is found to be a very sensitive process and it is not obvious why only one breach occurred and it originated at the location it did, it is thought that a slight overestimation of the amount of breaches is better if compared to the situation with no breaches at all. The Shields limitation is unsatisfying as no breaching takes place, the other model runs are also not satisfying as too many breaches are predicted.

If one looks to the dune retreat in the collision regime and the change of the center of gravity in zone C (measure for barrier island roll over), only the Shields parameter restriction results in reasonable numbers as it is the only case in which the barrier island is not washed away. The dune retreat modelled with the Shields parameter restriction is in the same order as observed in the measurement data, although a substantial deviation, in the order of 50%, is measured. The center of gravity change in the overwash zone C is roughly double the measured one.

Table 7.1: BSS and bias for the XBeach default, the limited Shields parameter and the improved model. Zones as defined in Figure 7.11.

Model run	BSS					Bias [m]				
Zone:	A	B	C	D	**Total**	A	B	C	D	**Total**
XBeach default	-9.84	-4.06	-2.76	-16.43	**-3.92**	-1.36	-1.98	-1.36	-0.05	**-1.17**
Smax = 1	0.59	0.52	0.71	-3.45	**0.61**	-0.07	0.08	-0.10	0.10	**-0.02**
Improved model	-8.85	-3.73	-2.71	-23.16	**-3.73**	-0.95	-1.83	-1.32	0.03	**-1.05**

Table 7.2: Model performance indicators for the XBeach default, the limited Shields parameter and the improved model. A star ($*$) indicates that the indicator cannot be calculated for the specific model run, e.g. if too much dune lowering took place to be able to calculate the average dune retreat.

Model run	Number of breaches	Dune retreat at $z_b = 4m$ [m]		Δx_{cg} [m]
		$y = 1800\ m$	$y = 2000\ m$	zone C
LIDAR data	1	8.0	14.0	26.7
XBeach default	$>> 1$	*	*	*
Smax = 1	0	12.0	8.0	44.2
Improved model	$>> 1$	*	*	*

Finally, interest is drawn to the cross-sections to better examine the model results. Figure 7.12 shows the maximum crest height in longshore direction. Both the XBeach default as the improved model result in an average crest-height on the barrier island in the order of $1\ m$, which is much smaller than the actual average crest-height after the storm in the overwash zone of $2\ m$. The Shields parameter restriction causes many more dunes to remain intact, the lowering of the dunes is even underestimated at several spots.

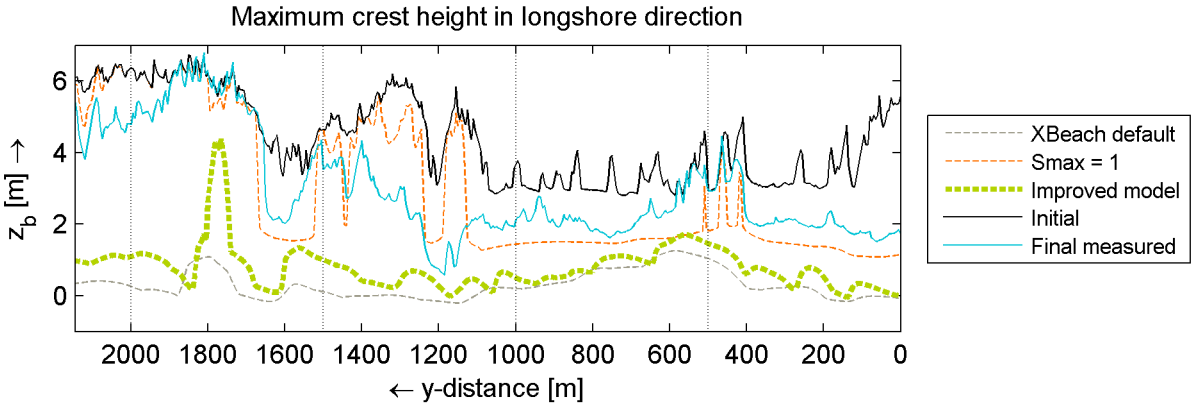

Figure 7.12: Maximum crest height in longshore direction XBeach default, limited Shields parameter and the improved model.

Figure 7.13 presents the cross-sections across the barrier island at intervals of $500\ m$. The earlier observed overestimations in XBeach are also noticed in these plots. It is interesting to see the increase of the bed level at the dune foot, which is only visible in the measurement data. As mentioned in the data analysis, this is probably caused by the recovery of the shore.

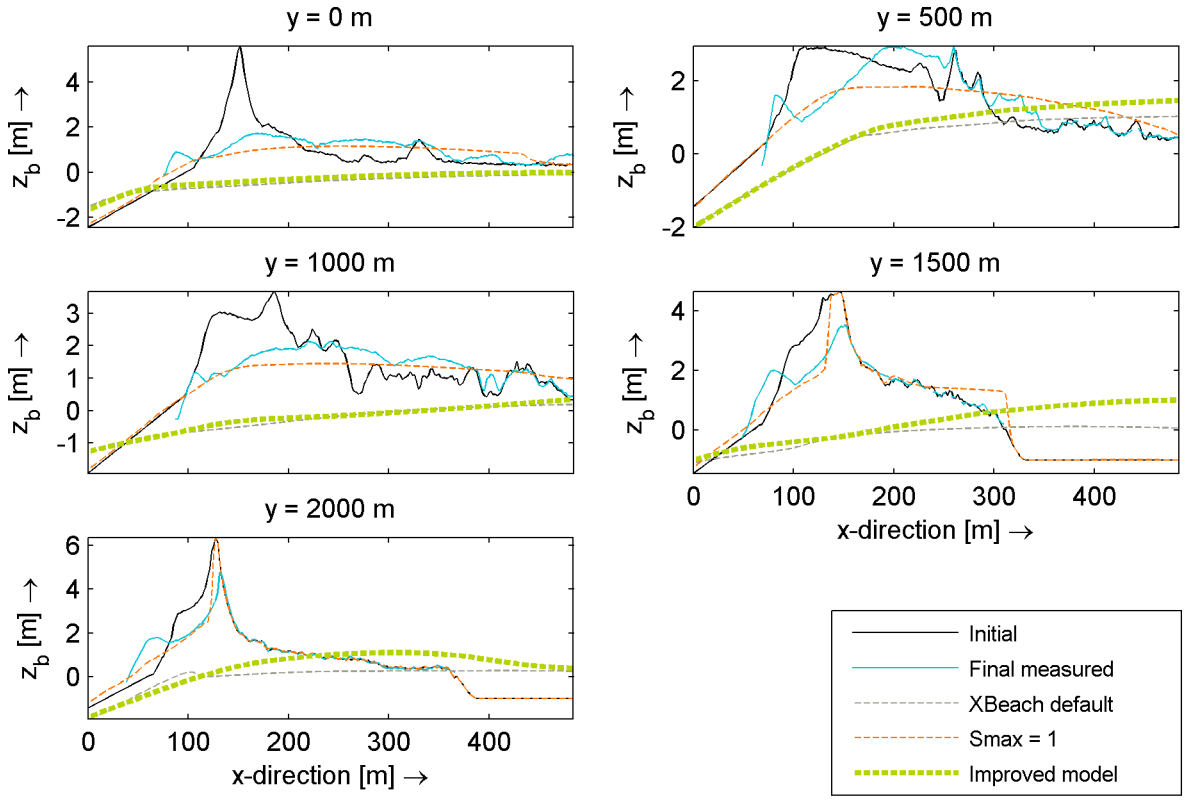

Figure 7.13: Cross-sections XBeach default, limited Shields parameter and the improved model. The cross-sections are provided at certain y-coordinates corresponding to Figure 7.12.

Appendix H shows the results of the improved model if the improvements are modified or turned off one-by-one. Based on this analysis, it can be concluded that none of the additional physics can hinder the erosion sufficiently in this case, even if the most important parameters are varied within a reasonable range. The most influential additional physics in the improved model are the dilatancy effect and the bed slope effect. Still, the influence of the additional physics is an order of magnitude less than the magnitude of the overestimations.

7.5 Conclusions

A new case study is successfully set-up in which much more certainty regarding the boundary conditions is achieved, compared to the Santa Rosa case study discussed earlier. This case study is another example of a field case in which the morphological changes are substantially overestimated by the default XBeach model and the model improvements do not solve this issue. The proposed model improvements are only a secondary effect. Reasonable results are achieved, only by using the Shields parameter restriction. However, with the Shields parameter restriction are several processes hindered of which breaching is the most important one. This unexpected hindering is in line with earlier findings in this thesis.

The fact that the improvements do not solve the issue in this case study does not prove that these additional physics are irrelevant under these conditions. Possibly other, more important, physics are missing or modelled in the wrong way. Therefore, the next chapter will provide an analysis to discover whether other adjustments provide a solution for the problem.

Chapter 8

Modelling Fire Island hurricane event with additional physics

In the previous chapter, the Fire Island model was set-up, which showed reasonable performance with the Shields parameter restriction. However, with this restriction no breach channels are formed. As this is thought to be an important disadvantage, it is tested whether other modifications to the XBeach model can result in more realistic model predictions. The improved model is taken as a base run for this chapter. It is investigated whether a better description of certain processes, e.g. bed friction, could solve the overestimation of the morphological changes. Achieving the exact final solution is not the purpose of this chapter as there will always be uncertainties. More important is that the excessive overestimations are reduced and that the right processes are present at more or less the correct location.

8.1 Introduction of additional physics

Even with the model improvements, Chapter 7 showed substantial overestimations at morphological changes. It is unexpected that even in the collision regime (around $y = 2000\ m$) the results are not sufficient as XBeach is generally capable of properly modelling the collision regime (Roelvink et al., 2009; Daly et al., 2012; Deltares, 2014a).

Several processes are thought to be important for the Fire Island model conditions. These will be examined in more detail.

Larger grain size in the swash zone

One of the measurements on the sediment distribution shows evidence for substantial larger grains in the swash zone (see Appendix H.1.2). These larger grain sizes could result in less erosion. It will be investigated what the influence is of using a D_{50} value of $600\ \mu m$ instead of a value of $400\ \mu m$. If the influence is substantial, multiple sediment fractions should be considered.

Groundwater flow

As grain sizes are substantial ($D50$ in the order of $400\ \mu m$), groundwater flow could be important. The XBeach groundwater module, as described by McCall et al. (2012), is used for this purpose. In the computation, the Darcy-flow permeability coefficient is set as $3.5e^{-4}\ m/s$ (based on Equation 5.5). Further, the initial groundwater level is taken equal to the initial water level in the bay (roughly $NAVD88 + 0.5\ m$) and the level of the uniform aquifer bottom is presumed to be equal to $NAVD88 - 2\ m$. Reference is made to McCall et al. (2012) for further details on the used equations in this module.

Wave asymmetry and skewness

As the short waves are averaged over their period, the shape of the waves is not solved. To account for wave asymmetry and skewness in the morphodynamics, the sediment advection velocity is increased with a wave-averaged velocity due to wave skewness and asymmetry (Van Thiel de Vries, 2009). The sediment advection velocity is estimated as the product of the difference between a skewness parameter S_k and an asymmetry parameter A_s, the root mean square velocity u_{rms} and a calibration factor f_{u_A}:

$$u_A = f_{u_A} \cdot (S_k - A_s)\, u_{rms} \tag{8.1}$$

In XBeach, a default value of 0.1 is used for this calibration factor. Various studies suggested that a larger value could be reasonable (Voukouvalas, 2012; Bugajny et al., 2013). In this thesis, the results with a value of 0.2 are examined.

Manning roughness

Currently, a uniform distribution of the Chézy roughness is used in the XBeach model. As water depths are highly variable across the barrier island, a Manning roughness could be more appropriate. The Manning roughness coefficient n is related to the Chézy parameter C as in Equation 8.2 (Chow, 1959).

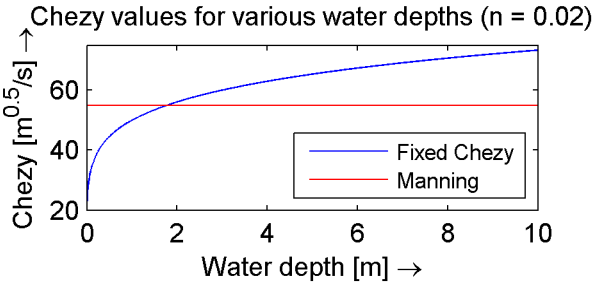

Figure 8.1: Imposed Chézy value as a function of the water depth for a Manning value of 0.02.

$$C = \frac{1}{n} h^{1/6} \tag{8.2}$$

$$c_f = \sqrt{\frac{g}{C^2}} = \sqrt{\frac{gn^2}{h^{1/12}}} \tag{8.3}$$

Note that the factor 1 in this expression is not dimensionless, it has the dimension of $m^{1/3}/s$. A Manning roughness of 0.02 is used in the model domain. Figure 8.1 compares it to the fixed Chézy value, used in the previous model runs.

Vegetation

On the aerial imagery, some vegetation is present behind the dunes. Especially in the overwash region, this could hinder the flow substantially. Figure 8.2 gives an impression of the type of vegetation; grasses with some weeds are present. The National Research Council (1983) suggests the increase of the bottom roughness on top of the barrier island to account for vegetation. Since an overall increase of the bottom roughness would also affect the locations which are not vegetated, the roughness is only increased at vegetated locations by defining a polygon, see Figure 8.2.

Figure 8.2: Left: photo at the project location from Google Earth/Panoramio (by belial666), center: Google Earth picture with vegetation mask (3th of July, 2012), right: vegetation mask interpolated on the computational grid.

Chow (1959) provides several tables to get to reasonable Manning values for floodplains based on visual observations. For high grasses, values in the range of 0.03 - 0.05 are thought to be applicable. For light brush and trees, values in the range of 0.035 - 0.06 are indicated. Various Manning values in the vegetated zone will be examined.

8.2 Results with the additional/modified physics

Now, the additional modifications are applied to the improved model to check whether the suggested processes could explain (part of) the overestimations in the results of the improved model in the last chapter. Table 8.1 presents the Brier Skill Scores and the bias whereas Table 8.2 notes the other model performance indicators.

Table 8.1: BSS and bias for the runs with additional/modified physics. Zones as defined in Figure 7.11.

Model run	BSS					Bias [m]				
Zone:	A	B	C	D	**Total**	A	B	C	D	**Total**
Improved model	-8.85	-3.73	-2.71	-23.16	**-3.73**	-0.95	-1.83	-1.32	0.03	**-1.05**
Larger sediment grains	-3.09	-2.65	-1.61	-18.11	**-2.18**	-0.24	-1.46	-1.04	0.19	**-0.72**
Groundwater flow	-7.92	-3.78	-2.80	-23.70	**-3.71**	-0.83	-1.82	-1.33	0.01	**-1.04**
Asymmetry and skewness	-1.05	-3.51	-2.51	-28.74	**-2.86**	-0.13	-1.58	-1.22	0.18	**-0.81**
Manning roughness	-7.13	-3.04	-1.77	-21.69	**-2.79**	-0.61	-1.61	-1.08	0.17	**-0.82**
Manning vegetation: 0.03	-3.61	-2.14	-0.15	-15.92	**-1.22**	-0.12	-1.16	-0.44	0.32	**-0.35**
Manning vegetation: 0.04	-2.22	-0.80	0.44	-8.05	**-0.27**	-0.08	-0.52	-0.09	0.15	**-0.10**
Manning vegetation: 0.06	-0.95	0.36	0.64	-0.74	**0.39**	-0.13	0.06	0.08	-0.03	**0.02**

Table 8.2: Model performance indicators for the runs with additional/modified physics. A star ($*$) indicates that the indicator cannot be calculated for the specific model run, e.g. if too much dune lowering took place to be able to calculate the average dune retreat.

Model run	Number of breaches	Dune retreat at $z_b = 4m$ [m]		Δx_{cg} [m]
		$y = 1800\ m$	$y = 2000\ m$	zone C
LIDAR data	1	8.0	14.0	26.7
Improved model	$>> 1$	*	*	*
Larger sediment grains	3	*	16.0	*
Groundwater flow	$>> 1$	*	*	*
Asymmetry and skewness	3	35.2	12.0	*
Manning roughness	4	*	*	134.6
Manning vegetation: 0.03	3	*	*	75.3
Manning vegetation: 0.04	2	*	*	60.0
Manning vegetation: 0.06	0	*	*	41.3

By applying larger sediment grains, erosion is hindered as one would expect. As the increment of the skill is not very substantial, even with these larger grain sizes on the full model domain, it is only considered a secondary effect.

Taking the groundwater flow into account has only a very minor influence on the model results. Apparently, the grain sizes are too fine to make this process important. This is in line with the findings of McCall et al. (2012) as they found significant affection of the overwash volumes for hydraulic conductivity values greater than $0.01\ m/s$, which is much larger than the value used in this computation.

Although the modification of the asymmetry and skewness calibration parameter affects the overall skill of the model only a little, the collision regime (around $y = 2000\ m$) is modelled much better. With this modification, the skill in zone A is substantially increased and the dunes are still intact at $y = 1800\ m$ and $y = 2000\ m$.

Applying the Manning roughness, instead of Chézy, shows visible differences but a negative skill is still found. The Manning roughness does not show very different results which can be expected as the Manning roughness was chosen to be more or less in line with the Chézy one.

By modifying the Manning values locally in the vegetated zone within a reasonable range, large improvements are achieved. It is clear that an increase in friction results in an increase of skill. However, if a too large bottom roughness is applied, e.g. a Manning value of 0.06, breaching is hindered. In reality, vegetation is not present any more if substantial erosion has taken place. Therefore, one could argue for a large initial Manning coefficient which decreases with the erosion depth. It is not hard to implement such a process in the XBeach code. However, data are required to calibrate such method. For now, the Manning value of 0.04 in the vegetated zone is thought to be the most appropriate one as breaching is still modelled.

8.3 Combining adjustments towards the most promising set-up

In the previous section, it is found that the bottom roughness increase in the vegetated zone results in much better morphological changes. However, the erosion of the dunes in region A, the collision regime, is still overestimated. To this end the increase in bottom roughness in the vegetated zone, to a Manning value of 0.04, will be combined with the increase of the calibration parameter related to asymmetry and skewness of the waves. Tables 8.3 and 8.4 present the Brier Skill Score, the bias and other model performance indicators of the combined adjustments with respect to the improved model and the individual adjustments.

Table 8.3: BSS and bias for the combined adjustments. Zones as defined in Figure 7.11.

Model run	BSS					Bias [m]				
Zone:	A	B	C	D	Total	A	B	C	D	Total
Improved model	-8.85	-3.73	-2.71	-23.16	**-3.73**	-0.95	-1.83	-1.32	0.03	**-1.05**
Asymmetry and skewness	-1.05	-3.51	-2.51	-28.74	**-2.86**	-0.13	-1.58	-1.22	0.18	**-0.81**
Manning vegetation: 0.04	-2.22	-0.80	0.44	-8.05	**-0.27**	-0.08	-0.52	-0.09	0.15	**-0.10**
Combined adjustments	0.44	0.10	0.36	-8.21	**0.23**	-0.05	0.03	0.18	0.14	**0.11**

Table 8.4: Model performance indicators for the combined adjustments. A star ($*$) indicates that the indicator cannot be calculated for the specific model run, f.e. if too much dune lowering took place to be able to calculate the average dune retreat.

Model run	Number of breaches	Dune retreat at $z_b = 4m$ [m]		Δx_{cg} [m]
		$y = 1800\ m$	$y = 2000\ m$	zone C
LIDAR data	1	8.0	14.0	26.7
Improved model	$>> 1$	*	*	*
Asymmetry and skewness	3	35.2	12.0	*
Manning vegetation: 0.04	2	*	*	60.0
Combined adjustments	1	14.0	12.0	57.2

It is clear that the combination of these two adjustments leads to much better results. First, the skill in the zones A, B and C is now positive and the bias is substantially reduced to a maximum of $0.18\ m$ in zone C. As mentioned in the previous chapter, the Brier Skill Score is not useful to describe the skill in zone D as only minor bottom level changes take place there.

In the improved model with the combined adjustments, breaching is still modelled. Further, the dune retreat is very well in line with the measurement data. The change of the center of gravity in the overwash region (zone C) is still double the measured one, which explains also part of the negative skill in zone D. If a larger bottom friction is used, the change of the center of gravity is much more reduced, as observed in Table 8.2. This larger bottom friction was not thought to be feasible for now as that would hinder the occurrence of a breach and be physically unrealistic.

Figure 8.3 shows the final bottom level, the cumulative sedimentation/erosion and a visual presentation of the Brier Skill Score with a moving window of 10x10 cells. Based on these plots, the good performance of the improved model with the combined adjustments is confirmed. The too large translation of the center of gravity in the overwash zone is visible by the much larger overwash fan length. The latter could be caused by the fact that vegetation in reality not only increases the bottom roughness, but also captures the suspended sediment particles. It is noticed that the breach is modelled at the wrong location. This is not thought to be a problem as the location of the breach is discussed to be a very sensitive process. If one looks to the spatial distribution of the Brier Skill Score, the skill is especially high in the initially high elevated locations ($z_b > 2m$) where scores in the range of $0.6 - 1.0$ are found and much erosion took place.

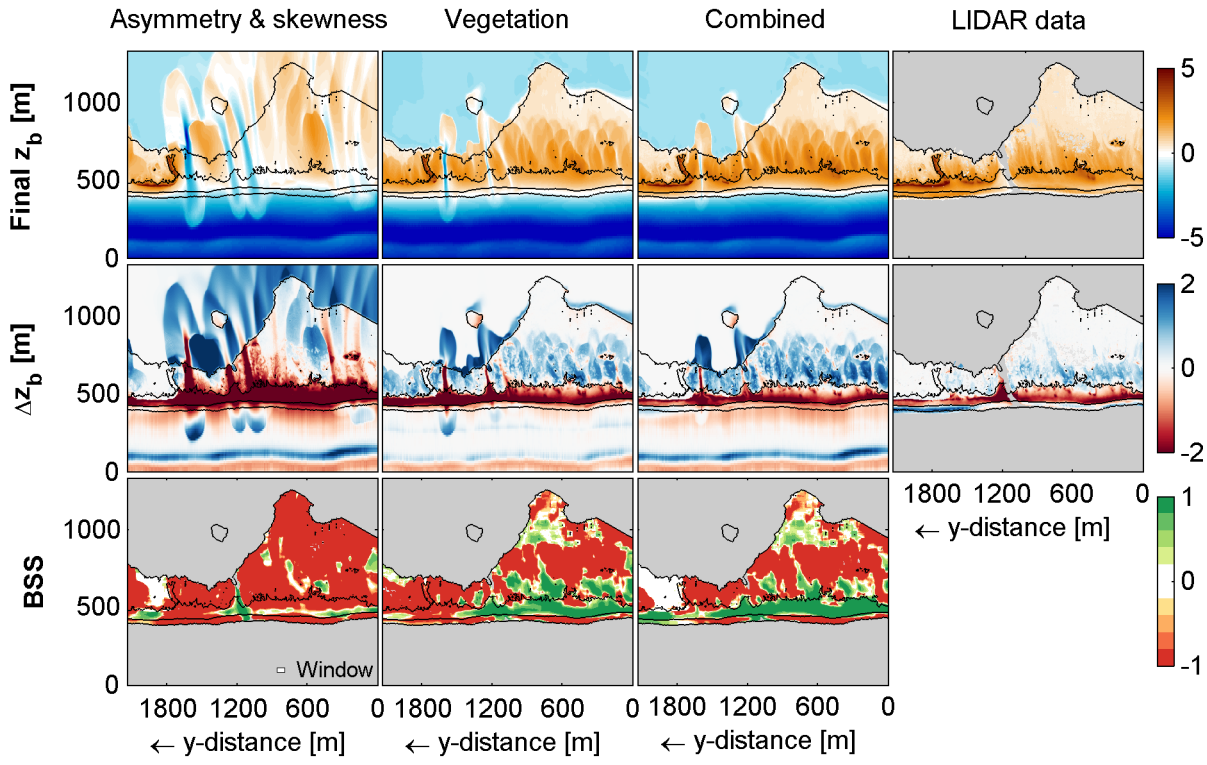

Figure 8.3: Performance comparison between the asymmetry and skewness parameter adjustment, the vegetation adjustment and the combined adjustments. Shown are the final bed level, the bed level changes by the storm event and the Brier Skill Score with a moving window of 10x10 cells. The black depth contours are provided at an elevation of 0 and 2 m relative to NAVD88 of the initial depth profile. Spots without data are marked gray.

Finally, Figures 8.4 and 8.5 present several cross-sections. In the collision regime, a very good fit to the measurement data is found. The dune recovery is not modelled as this happens during the days after the storm; this could explain why the sand bar around $NAVD88 + 1\ m$ is not visible in the model. The largest inaccuracies are found near the breach and at the boundary of the model, where the dune collapsed in the model whereas it did not in reality. In the overwash zone, mainly visible in the cross-sections of $y = 500\ m$ and $y = 1000\ m$, it is visible that a reasonable fit is achieved. The fit on the measurement data of the foreshore is fine and it is confirmed that the negative skill of the region behind the dunes in the overwash region (zone D) is not representative for the actual performance, as the general tendency is fine.

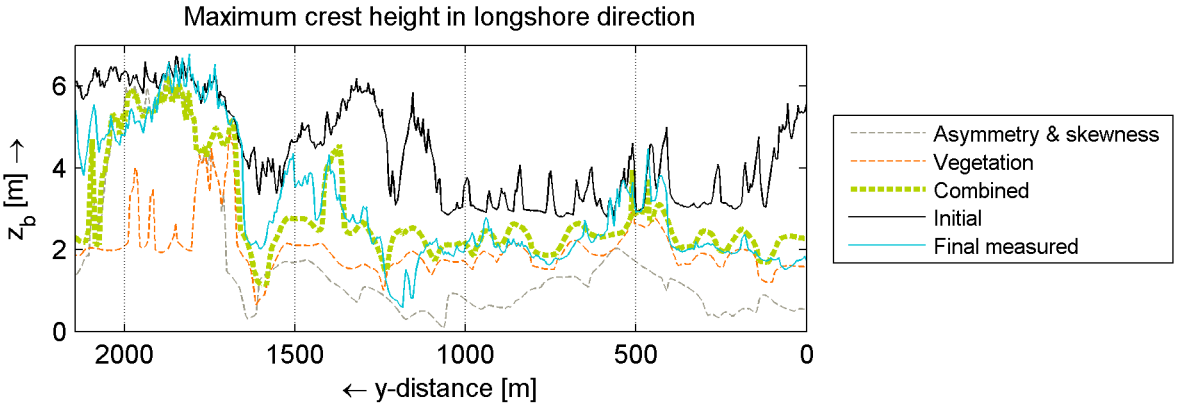

Figure 8.4: Maximum crest height in longshore direction of the asymmetry and skewness parameter adjustment, the vegetation adjustment and the combined adjustments.

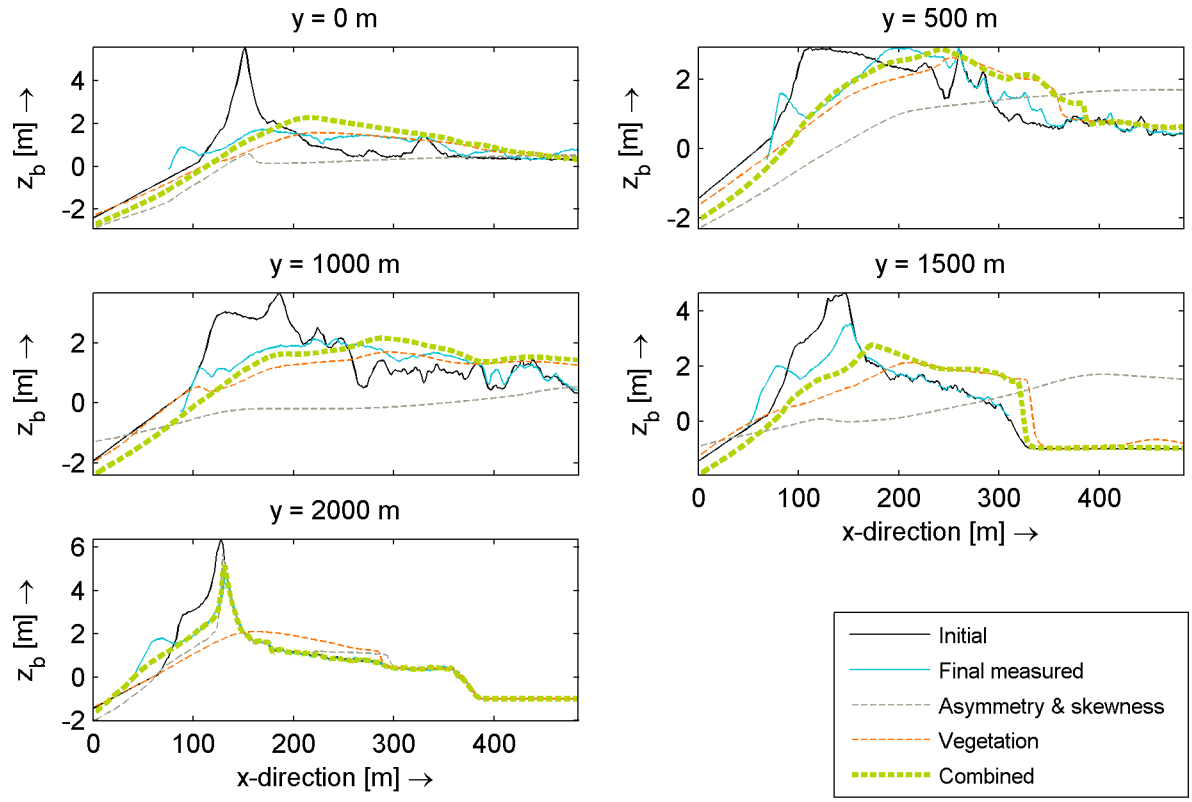

Figure 8.5: Cross-sections of the asymmetry and skewness parameter adjustment, the vegetation adjustment and the combined adjustments. The cross-sections are provided at certain y-coordinates corresponding to the earlier presented figures.

Now, it is checked how important the individual improvements are in the adjusted version of the improved model. Appendix H present the performance of the various improvements. As visible, the model results are not very sensitive to the improvements. The bed slope effect and the dilatancy effect are again the most influential, although the variation in skill and bias is limited. Also the sensitivity of the model skill to the bottom level in the bay, which was marked as the most important unknown, is not found to be very substantial, see Section H.4. However, the depth in the breach channel does show a substantial dependency on the bed level in the bay and if the depth in the bay is lowered too much, no more breaching is modelled.

8.4 Conclusions

Several additional processes are investigated to test whether a better description could explain the overestimation of the morphological changes. It is found that a larger grain size hinders the bottom changes. However, even with an increase of grain size over the whole model domain, which is not realistic, results are insufficient. Taking groundwater flow into account is found to be of no relevance for this case study, presumably by the relatively small permeability. Adjusting the wave asymmetry and skewness parameter is more successful. By this adjustment, the collision regime is much better approximated where many more dunes are found to be intact in the model. The description of the bed roughness by the Manning formula causes slight improvements, but the best results are found if the Manning coefficient is increased locally in the vegetated zone.

By adjusting the improved model with both a modified wave asymmetry and skewness parameter and an increased Manning coefficient in the vegetated zone, a positive skill (0.44 in the collision regime and 0.36 in the overwash zone) is achieved with which breaching is still modelled. It is shown that the improvements introduced in this thesis, i.e. dilatancy, bed slope effect, conservatism of the Exner equation and the reduced fall velocity, are not of substantial influence in this case study.

A further increase of the model skill is possible, but certain model parameters should be increased, e.g. an increased bed roughness in the vegetated zone which decreases with the erosion depth. The difficulty with the calibration is that the different processes, i.e. breaching, overwash and collision, require different parameter settings. This further calibration is not part of this thesis. The results of the improved model with the combined adjustments will be analysed in the next chapter in more detail.

Chapter 9

Analysis of the morphological changes in the Fire Island model

In the previous chapter, reasonable results were obtained in the Fire Island model by using the improved model in combination with an adjustment for the asymmetry & skewness of the waves and by the increase of the bed friction in the vegetated zone. This optimized model will be analysed in this chapter.

Firstly, the various storm phases are analysed. The total modelled duration of 48 hours is split up into several characteristic phases, based on the morphological changes that occurred (see the Sallenger regimes as presented in Chapter 2). In this way, it is possible to get a feeling during which phase of the storm which processes took place. Thereafter, the evolution of the breach over time will be analysed.

9.1 Analysis per storm phase

9.1.1 Collision regime (0-14 h)

During the first hours of the storm, collision of waves is modelled over the whole coastline and no overwash occurred. In Figure 9.1, several cross-sections are presented showing the morphological changes at the shore during this period. Substantial erosion of the back shore is caused by the waves with a significant wave height of $4 - 5\ m$ and a peak period of $10 - 12\ s$, leading to retreat of the dunes. In all the cross-sections, the dune foot is modelled at approximately $NAVD88 + 2\ m$, which retreated $10\ m$ on average during this period. The eroded sand accreted between the $NAVD88 + 0\ m$ and $NAVD88 + 1\ m$ contour lines. Hence sand stays mainly on the foreshore. Further, the shoreface is also subject to some erosion.

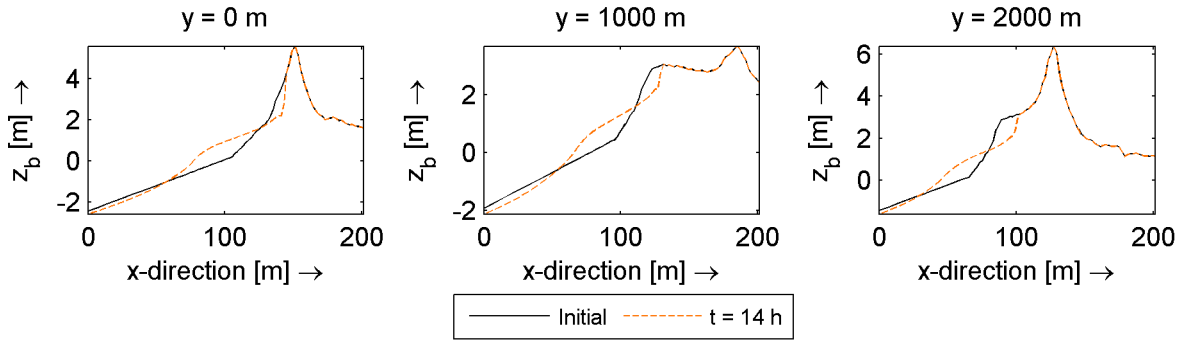

Figure 9.1: Several cross-sections showing the erosion of the shore during the first 14 hours of the model. Bottom level with respect to NAVD88.

Figure 9.2 provides a spatial overview of the area of interest together with the hydrodynamics. In longshore direction, not much variation is visible in the erosion and accretion volume. Also the breaker bar is affected during this phase. By the erosion and deposition, a storm profile is generated which is more dissipative compared to the initial profile.

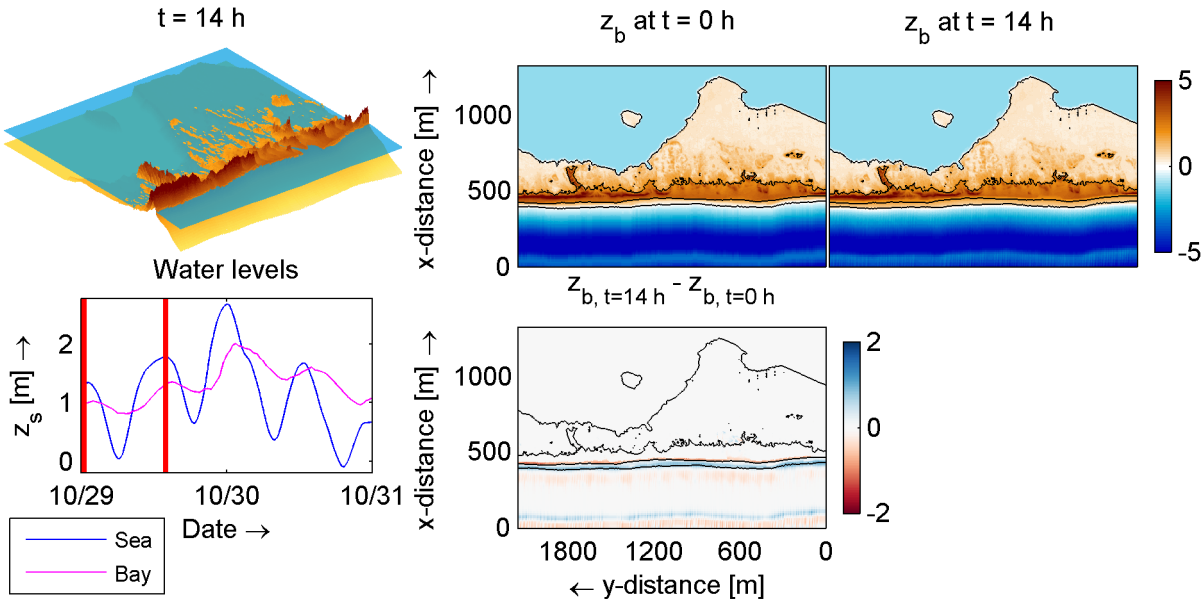

Figure 9.2: Morphological evolution during the swash and collision regime. Top-left: water level and bottom level at the end of this period, bottom-left: water levels at the beginning and the end of this period (red lines), other ones: bottom levels and cumulative sedimentation/erosion. The black depth contours are provided at an elevation of 0 and 2 m relative to NAVD88 of the initial depth profile.

9.1.2 First overwash period (14-17 h)

At high tide, $14 - 17$ hours from the beginning of the computation, overwash of water is observed causing erosion of the top of the dunes and deposition behind these dunes. Figure 9.4 presents the morphological changes during this period.

In the model domain, two washover fans (at $y = 1200\ m$ and $y = 1600\ m$) and two washover terraces (in the region of $y = 100\ m$ to $y = 1100\ m$) are observed. A closer look at the morphological changes during this period, as provided in Figure 9.3, shows clear evidence of these features.

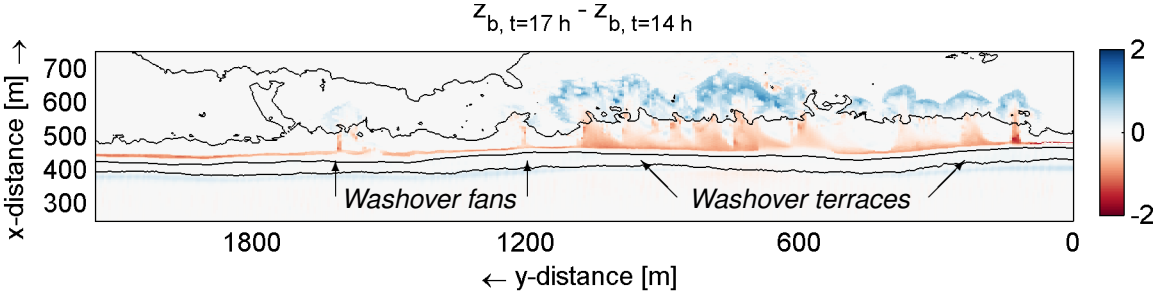

Figure 9.3: Morphological processes during the first overwash period, detailed view on barrier island. The black depth contours are provided at an elevation of 0 and 2 m relative to NAVD88 of the initial depth profile.

Further, erosion of the dunes is observed. The magnitude of this erosion ($10 - 15\ m$ dune retreat) is comparable to the first 14 hours of the storm ($10\ m$ retreat). Note that the mean dune retreat rate of this phase is larger by the shorter duration.

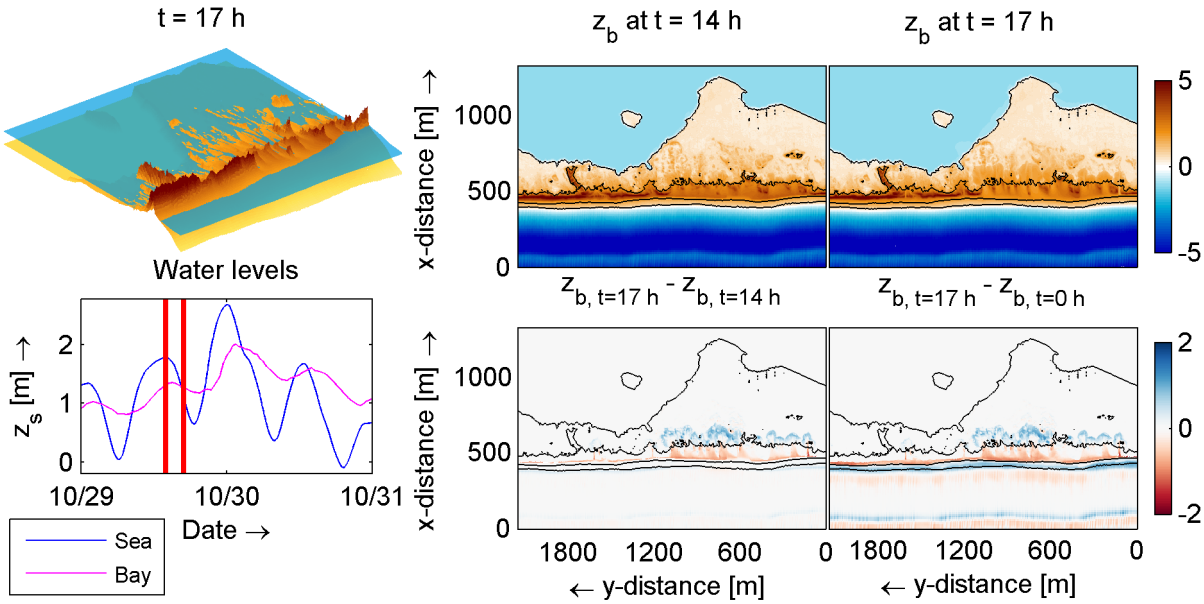

Figure 9.4: Morphological evolution during the first overwash period. Top-left: water level and bottom level at the end of this period, bottom-left: water levels at the beginning and the end of this period (red lines), other ones: bottom levels and cumulative sedimentation/erosion. The black depth contours are provided at an elevation of 0 and 2 m relative to NAVD88 of the initial depth profile.

9.1.3 Second collision period, low tide (17-21 h)

At low tide, little morphological change is modelled as the storm profile was already generated during the first period. By the relatively low surge level, no overwash is observed, see Figure 9.5. During this phase, almost no dune retreat is measured in the model results.

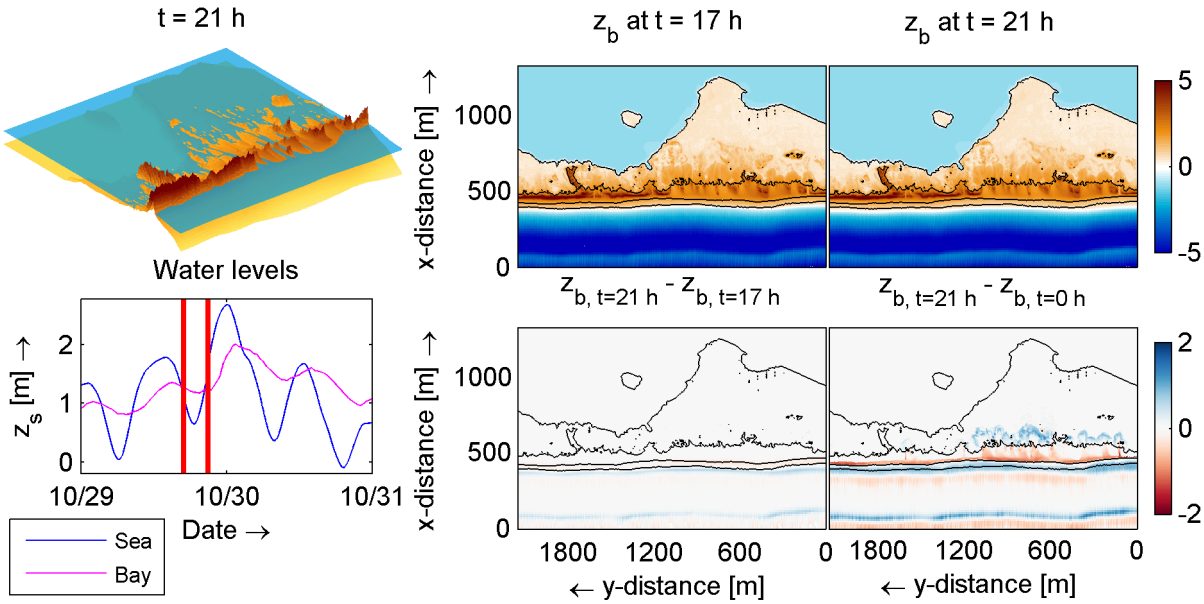

Figure 9.5: Morphological evolution during the second collision period (low tide). Top-left: water level and bottom level at the end of this period, bottom-left: water levels at the beginning and the end of this period (red lines), other ones: bottom levels and cumulative sedimentation/erosion. The black depth contours are provided at an elevation of 0 and 2 m relative to NAVD88 of the initial depth profile.

9.1.4 Second overwash period (21-31 h)

The second overwash period is morphologically the most active one of all considered storm phases. An overview of the morphological changes is presented in Figure 9.6.

During this phase, the overwash fan at $y = 1600\ m$ evolved into a breach channel. At the end of this phase, after 31 hours from the beginning of the model, this breach channel is still fully submerged. This in contrast to the location of the actual breach, which occurred around $y = 1200\ m$. Both at the location of the successfully modelled breach, as the unsuccessfully modelled breach, large amounts of deposits are visible in the bay.

In the region of $y = 0\ m$ to $y = 1100\ m$, a lot of inundation-overwash occurred, causing a substantial reshape of the island. By the large flow velocities, the barrier island is substantially smoothed. The major part of the eroded dune material is deposited at the lower region behind the dunes over a distance of approximately $400\ m$.

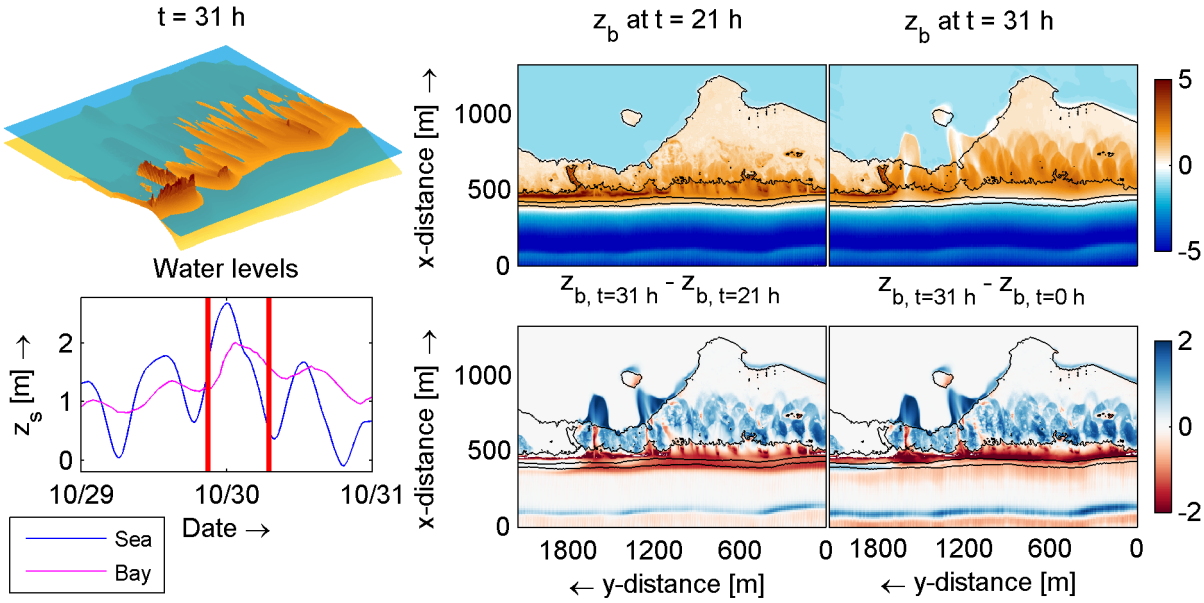

Figure 9.6: Morphological evolution during the second overwash period. Top-left: water level and bottom level at the end of this period, bottom-left: water levels at the beginning and the end of this period (red lines), other ones: bottom levels and cumulative sedimentation/erosion. The black depth contours are provided at an elevation of 0 and 2 m relative to NAVD88 of the initial depth profile.

Finally, substantial morphological activity is observed in the collision zone (around $y = 2000\ m$). As visible in Figure 9.7, the dune retreat of approximately $10\ m$ caused lowering of the dunes locally. Further, the dune foot is located now at a level of $NAVD88 + 3\ m$ instead of $NAVD88 + 2\ m$. The latter was observed during the earlier stages with a lower surge level.

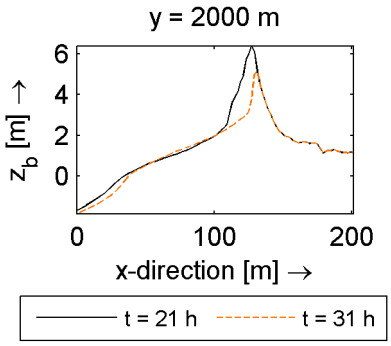

Figure 9.7: Dune retreat second overwash phase.

9.1.5 Last 17 hours of the model run

During the last 17 hours of the computation, not much morphological activity is observed even though a small overwash event is part of this period at high tide.

The only noticeable morphological change is related to the breach channel. By the tidal flows, the channel is further deepened. In contrast to the earlier observations, sediment is also deposited at the sea side of the breach channel. This is evidence for seaward directed flows through the breach which can be explained by the temporarily higher water level in the bay compared to the sea, see the water level graph.

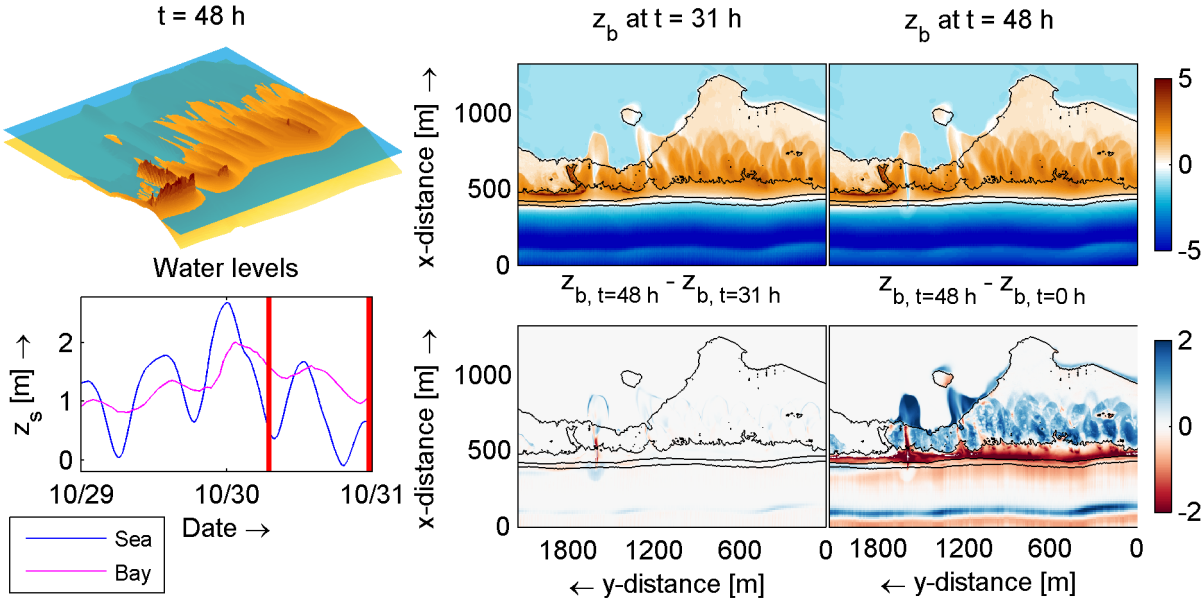

Figure 9.8: Morphological evolution in the last 17 hours of the storm. Top-left: water level and bottom level at the end of this period, bottom-left: water levels at the beginning and the end of this period (red lines), other ones: bottom levels and cumulative sedimentation/erosion. The black depth contours are provided at an elevation of 0 and 2 m relative to NAVD88 of the initial depth profile.

9.2 Analysis of the breach evolution over time

An important focus of this thesis is on the breaching process. With the Fire Island model, it can be studied during which phase of the storm the breach is initiated and what the importance is of the tide in this process. This analysis will be presented in this section.

Figure 9.9 presents the bottom level changes at several characteristic points of both the successful as the non-successful breach. The latter is positioned at the location of the breach which occurred in reality but where the model did not show sufficient bottom level lowering. Further, the water level gradients over the points are presented in this figure to give an estimate of the forcing.

In point C, initially an increase in bottom level is observed. This is caused by the overwash deposits originating from the points A and B. It is clear that the breach channel is generated during the largest surge peak. With the tide, the depth evolution took place further. No equilibrium state has been reached, by the last day of the storm. This means that the dimensions of the breach are still changing during the days after the storm as substantial oscillations of the bottom level are still observed. The fact that no equilibrium is formed was also noticed in the measurement data, as presented in Figure 7.6. It is not the focus of this study to understand the breach channel evolution on the long term precisely.

As the water level gradient also becomes negative, by a larger water level in the bay compared to the sea, the direction of the flow is directed partly towards the sea explaining the deposits at the sea side of the breach channel, as observed in Section 9.1.5.

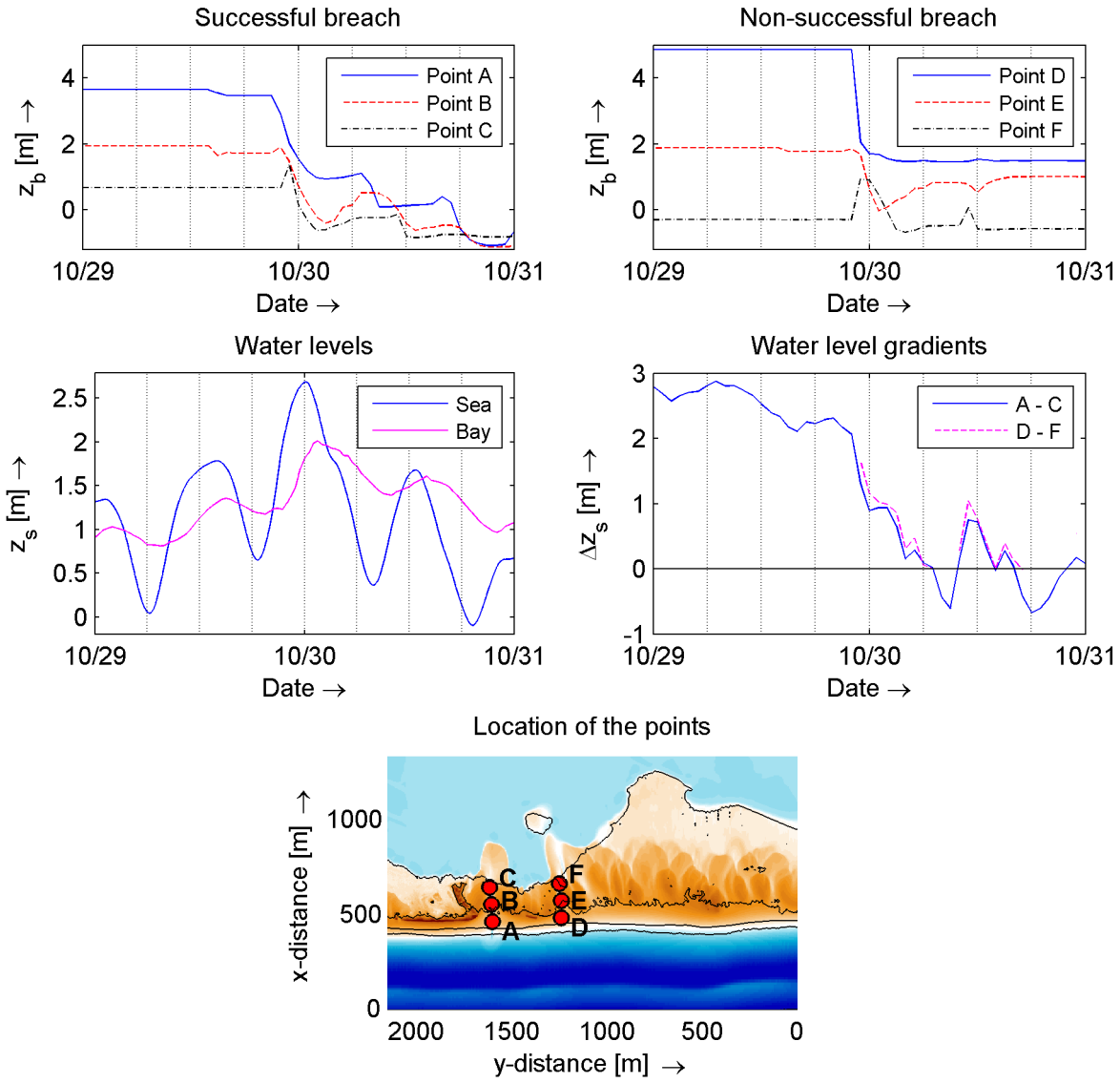

Figure 9.9: Bottom level elevation in the breaches over time at several characteristic locations. The water level gradients are provided over the two outward points.

9.3 Conclusions

This chapter presented an overview of the morphological processes which occurred at Fire Island during hurricane Sandy, as modelled with XBeach.

It is concluded that the major morphological changes happened during the largest surge peak, which had a duration of 10 hours. Before this large surge peak took place, substantial dune retreat occurred and a storm profile (mild beach slope) was formed. Several overwash fans and terraces are modelled, one of the overwash fans evolved into a breach. The breach was formed during the largest surge peak, but still a lot of morphological activity in the breach channel is observed during the tidal periods after the storm. The tide is probably the forcing which withholds the breach channel to close after the storm.

Chapter 10

Discussion

In this chapter, a critical reflection is made regarding several important issues relevant for this thesis.

Model improvements do not result in a perfect fit with measurement data

The implemented additional model physics did result in substantial improvements. However, no perfect fit with measurement data is achieved. It is possible that still some essential physics are missing in the model. Further, simplifications are made with implementations which are simply part of the numerical modelling practice. For example, one could argue that the equilibrium concentration C_{eq} could increase if the fall velocity is reduced. More exact model formulations describing more details would require a very thorough description of the local conditions of which often no detailed data are available.

Dilatancy is proven to be one of the most important erosion hindering processes implemented in this thesis, but the sensitivity to the corresponding model parameters is substantial. Van Rhee (2010) did not suggest that his schematizations should result in a perfect fit, which was observed in the validation of his method with model data in Figure 2.9. Based on these considerations, a perfect fit was not the intention of this thesis. More important was to check if the right processes were modelled with the correct tendency, which is shown to be the case.

The impact of the model improvements on the considered hurricane cases is substantially less if compared to the idealized experiments. As the overestimation of the erosion rates is reduced if more appropriate friction formulations and wave skewness and asymmetry parameters are used, the default XBeach settings do not really lead to a fair base case of the XBeach model. In fact, the better description of the bottom roughness and wave skewness and asymmetry is also a model improvement. In the end, uncertainties and the natural local variations which are part of nature make a perfect representation of reality in the highly complex and dynamic storm events a very challenging task.

Reconsidering the depth-averaged assumption

In the breaching process, depth-averaging might result in unreasonable errors in the sediment transport rates as the direction of the flow can vary strongly over depth. Appendix I deals with this issue. Based on the Zwin case, it is tested with the Delft3D model if depth-averaging is reasonable for that case. A difference in magnitude and gradients is found, which is likely to be a calibration issue. Further, differences in the direction of the sediment transport are observed. However, these are not very substantial at the locations with the largest gradients in the sediment transport rates. One could adjust the directions in the depth-averaged model as a clear increase of the deviation with an increase in distance from the channel axis is observed. For now, it is just noted that depth-averaging introduces some deviations but that depth-averaging seems to be reasonable for breaching cases.

Implications of the morphological acceleration factor

Section H.5 analyses the errors induced by using a morphological acceleration factor. The morphological acceleration factor is used to achieve workable model run durations (1 day instead of 10 days). The general tendency of the model predictions by using the morphological acceleration factor of 10 is the same as the one without applying morphological acceleration. However, a little less erosion is modelled without the acceleration factor, causing no breach channel to be formed. As it is shown that the formation of the breach channel is very sensitive to various parameters (the depth in the breach channel among others), some slightly different parameter settings could result in comparable results without the morphological acceleration. For this research, these deviations are no problem as it is not the exact solution which is important, but the general tendency.

Uncertainty in field measurements

The problem with the field cases containing hurricane events is the large amount of data required. Inaccuracies in the data cause uncertainties in the model results. For example, the deviations in the wave boundary conditions of the Fire Island case are substantial, but this dataset is the best available at the moment. One could think of simply adjusting the wave data with this knowledge, but that is very difficult as it is not simply increasing the spectrum with a certain amount of energy as that would also affect the high and low frequency tail of the spectrum. The question remains if there will ever be a complete and accurate dataset available for comparable locations. In the end, hurricanes can be very unpredictable and it is hence hard to place measurement devices at the right location. Therefore, the model results should not be considered as the truth, even if the modelling tool itself has a very good predictive skill. However, the models are still very useful to analyse the weak spots of a barrier island and to compare various scenarios.

Sensitivity of the location of a breach

This study showed that the exact location of a breach is not readily determined based on the geometry of the initial profile. The Fire Island case contained several breaches in the model, whereas only one breach developed in reality. Several aspects could play a role in the precise location of a breach, e.g. vegetation, structures, spatially varying sediment and roughness characteristics, spatially varying storm surge and initial weaknesses present in the soil, which are not captured in the model. More extensive research is required to fully understand why a breach occurs at a certain location. The problem with this, is that most times no pre-storm measurements are available as the occurrence of the breach was not expected.

Parameter variability in space and time

It is assumed that the sediment characteristics and bottom roughness, except for vegetation, are uniform in space and time. This is not a model requirement, it is possible to initiate the models with a non-uniform distribution. However, the main problem with this is that one has to propose a better distribution which requires data. These spatially varying data are often not available. Further, one could suggest that the initial profile on top of the barrier island is rougher compared to the profile smoothed by water flow. In line with this, a larger bottom friction factor could be used on top of the barrier island, as also demonstrated in this thesis. However, once some erosion takes place, the bed is smoothed and it is likely that the roughness is reduced in the breach channel after some bed lowering took place. This is a difficult process, and experimental data are required to verify this suggestion and to get to a robust formulation.

Chapter 11

Conclusions

The objective of this research was to test to what extent the morphodynamic predictions of the XBeach model under overwash and breaching conditions can be improved through the implementation of new model physics. In this chapter, the conclusions are presented in which reference is made to the hypotheses of Chapter 4.

Many physical processes affect erosion at high flow velocities, which are relevant for breaching and overwash conditions. It is hypothesised that especially the hindering of erosion by dilatancy, as described by Van Rhee (2010), is likely to have a substantial influence on the model results of breaching and overwash events. Further, the reduction of the fall velocity at high sediment concentrations might be a relevant process during these conditions.

As numerical modelling requires simplifications, the XBeach model has its limitations. Many of these limitations are argued to be justifiable and simply necessary to get to a time-efficient model, e.g. depth-averaging, phase averaging of short waves, neglecting of aeolian transport and the restriction to empirical sediment transport equations with only non-cohesive sediments. Other limitations are thought to be dissatisfying during overwash and breaching conditions, namely the highly schematic and improper bed slope effect, the quasi-steadiness of the sediment concentration in the sediment mass-balance and the usage of a uniform Chézy friction coefficient over the whole model domain.

It is found that the hindering of erosion by the artificial sediment concentration restriction and the limitation of the Shields parameter have major side effects. As expected, erosion rates are reduced with these limiters. At the same time, bed features like anti-dunes and chutes-and-pools are suppressed, these features are visible if the concentration is not limited (hypothesis 3). More importantly, the breaching process is hindered far too much by the Shields parameter restriction. Using the Shields parameter restriction is hence considered as bad modelling practice if breaching could occur in the model domain.

The physical processes relevant for breaching and overwash cases which were not included in the XBeach model, i.e. dilatancy and reduced fall velocity at high concentrations, are implemented in the model together with some implementations to overcome the unnecessary limitations of the model regarding overwash and breaching processes, i.e. the improper bed slope effect and the quasi-steadiness of the sediment concentration in the sediment mass balance. Various conceptual model and experimental model tests confirmed the correct trend of the implemented physics. The formulations used show no unexpected behaviour. As expected, dilatancy plays no role in the swash and collision regime (hypothesis 2). No perfect fit is found with measurement data with the improved model, but this is likely to be a calibration issue.

The currently implemented bed slope effect is erroneous as it changes the direction of the sediment transport, even if the flow direction is fully in on-slope direction. By implementing a proper bed slope effect, smooth and with that feasible cross-sections of breach channels are achieved. It is shown that the bed slope effect is a very important process during breaching conditions (hypothesis 6).

Dilatancy is proven to result in substantial hindering of erosion in the models of the Scheldt Flume experiment and the Zwin dam breach which was hence an important missing process in the XBeach model (hypothesis 1). It is only important during rapid changes of the bottom level elevation which is the trigger of the hindering of erosion (hypothesis 2). The method, as proposed by Van Rhee (2010), is sensitive to the parameters used in the formulations. Calibration of the method on case-specific conditions is hence a requirement for correct usage. In the field cases, i.e. the Santa Rosa model and the Fire Island model, dilatancy is found to be of much less importance. Erosion is probably hindered by dilatancy but it does not prevent the overestimation of erosion on the long time scale of a hurricane event.

In contrast, the reduction of the fall velocity at high sediment concentrations is found to be only a minor process regarding the morphological changes. Apparently, sediment concentrations did not affect the morphodynamics in the various cases substantially (in contrast to hypothesis 5). Further, the quasi-steadiness assumption of the sediment concentration in the sediment mass balance is not found to lead to erroneous results. This assumption is made in various other numerical models, based on this research it seems to be a feasible approach (hypothesis 7 is rejected).

The Santa Rose case study showed that the Shields parameter restriction results in a positive skill, but that this could also be achieved by increasing the bottom friction (hypothesis 4). The model results are found to be sensitive to the boundary conditions and model parameters (hypothesis 8), making the Santa Rosa case difficult to interpret by the large uncertainties in the boundary conditions.

In the model describing the morphological changes of Fire Island by hurricane Sandy, as introduced in this thesis, it is found that the model improvements of this thesis do not reduce the overestimation of the erosion rates sufficiently. The Shields parameter restriction does result in a reasonably good skill in these cases, but again breaching is suppressed. A large sensitivity to the bottom friction is found and it is suggested that this could explain an important part of the overestimation of the erosion rates. By implementing the roughness formulation of Manning instead of using the default Chézy formulation, together with a slight increase of the friction on top of the barrier island to account for the rougher profile, as well as a better description of the wave asymmetry and skewness, much better results are achieved while breaching is still observed (in contrast to hypothesis 9). The model sensitivity to the grain sizes and ground water flow is found to be significantly smaller compared to the effect of bed friction.

By analysing the model results of the Fire Island model, it is concluded that the major morphological changes occurred during the 10 hour storm peak. During this period, a breach channel is generated. The tidal currents during the days after the storm peak are important for the further deepening of the breach channel.

To conclude, the morphological predictions of the XBeach model are substantially improved by the implementation of the hindering of erosion by dilatancy and a proper bed slope effect. For the hurricane field cases, it is found that other processes dominate the model results. Especially bed friction and wave skewness and asymmetry are found to be important. In the end, a positive predictive skill is achieved in all the considered cases.

Chapter 12

Recommendations

By applying the XBeach model on several cases, insight is obtained which can be useful for future research. These recommendations are written with the objective to contribute to the improvement of XBeach model predictions and to future modelling studies. The presented recommendations are meant to be constructive and feasible.

Calibration of a field case on an additional case

Both the Santa Rosa model and the Fire Island model exposed a substantial sensitivity of the model results to the bottom roughness coefficients. With that, a careful calibration on the local characteristics, e.g. dune retreat and overwash volume, is required. However, calibration of a model can be dangerous in an academic sense as the post-storm bathymetry is the only dataset one can calibrate on. To improve the quality of the results, one could create a second model, preferably close to the project location. This additional model is purely made for calibration purposes and provides the parameters for the main model.

Use LIDAR data as a supplier for bed roughness data on top of the barrier island

The bed roughness on top of the barrier island is an important unknown. In the Fire Island case study, vegetation was present making an increase in bed roughness reasonable. The Santa Rosa case study shows less evidence for vegetation, but still an increase in bed roughness caused a substantial increase in model skill. There is a need for a better description of the bed roughness on top of the barrier island to get to more reliable model predictions.

Tables with default Manning coefficients are available, but by taking a uniform roughness coefficient one assumes that no substantial spatial gradients in bed roughness are present. If present, these spatial gradients may cause gradients in flow and with that gradients in sediment transport. If high resolution predictions are required, high resolution input data on the roughness coefficients should be available. One approach is to obtain Manning coefficients from LIDAR data, as demonstrated by Smith et al. (2004). This knowledge could be implemented in a XBeach case study in which the uncertainties of the roughness estimates on the morphodynamic results should be an important point of discussion.

Experimental data to improve overwash and breaching predictions

To extensively validate and improve the morphological predictions by the XBeach model, bottom level profiles at several moments in time are very valuable. For example, the Scheldt Flume experiment took an important role in this thesis as it exposed the rate at which the erosion process took place. If a new experiment could be set-up, a three dimensional breaching experiment like the one performed in Het

Zwin is suggested. In the Zwin experiment, only the breach width evolution over time was measured. Intended was to measure also the cross-section of the bed level through the channel axis, but the vibration probes were broken during the experiment. If this experiment is repeated with more high-tech measurement equipments and insight is gained on the evolution of the cross-sections through the breach over time, more accurate model calibration can be performed. Preferably, the experiment is performed in a laboratory at an as large scale as possible such that the conditions are controllable and the uncertainties limited. Performing the experiment various times with different wave conditions will give insight in the importance of waves relative to the flow induced by the water level gradient. This unique dataset is of great value for models like XBeach but may result also in a more fundamental understanding of breaching in general.

Improving effectiveness of model computations

If waves are not fully perpendicular incident to the coast, shadow zones should be prevented by introducing additional computational grid cells as explained in this thesis. In the Fire Island model, the shadow zones increased the amount of grid cells with 50%. To speed up the time consuming field case studies, a more effective alternative on covering all the incident waves should be found.

Make a comparison with other numerical models

In the discussion, the Delft3D model is used to test whether depth-averaging is reasonable for breaching cases. For a new study, it can be interesting to use the robust Delft3D model to make model comparisons with XBeach. Differences in results can be tracked back to differences in model assumptions or differences in implementation of the physical processes. Solid test cases should be defined, e.g. the cases as introduced in this thesis could be used for this purpose. Also the modelling of field cases could be interesting to include in this research, e.g. the Fire Island case study could be repeated relatively easily in Delft3D as boundary conditions and bathymetry files are already available. If comparing to Delft3D, processes like avalanching and short wave groupiness should be turned off in XBeach to obtain a comparable model set-up.

Approach of implementing additional missing processes in the XBeach model

As a basis of additional improvements in the future, a structured validation study should be set-up. All the possible weaknesses of the model should be listed and based on some conceptual model runs, directions of improvements should be prioritized. In this study, the focus was purely on the morphodynamics, but by the interaction of all modules a comprehensive analysis should be made. The improvements should be based on theories which are valid in a broad range of conditions. If substantial changes are made to the XBeach model, the default model parameters should be recalibrated as the model behaviour might be affected. With this, a more reliable and powerful tool is achieved which is suitable for use in a broad range of engineering projects.

The role of sediment limiters in future projects

Based on all the side effects observed related to the concentration limiter and the limitation of the Shields parameter, it is not wise to use these limitations in future projects without a thorough analysis of the validity. Especially, it should be researched what causes the hindering of breaching if the Shields parameter restriction for sediment transport is applied. In fact, only two of the presented cases showed a substantial increase in skill if the Shields parameter was limited. These were the field cases involving a hurricane event, i.e. the Santa Rosa and the Fire Island case studies. As the uncertainties in these models are substantial, these field cases are not necessarily proof of the validity of the Shields parameter restriction. It is proven that also other aspects could explain the mismatch, e.g. bed friction.

References

Ahrens, J. (2000). A fall-velocity equation. *Journal of Waterway, Port, Coastal, and Ocean Engineering*, 126(2):99–102.

Andreotti, B., Claudin, P., Devauchelle, O., Durán, O., and Fourrière, A. (2012). Bedforms in a turbulent stream: ripples, chevrons and antidunes. *Journal of Fluid Mechanics*, 690:94–128.

Bagnold, R. A. (1956). The flow of cohesionless grains in fluids. *Philosophical Transactions of the Royal Society of London. Series A, Mathematical and Physical Sciences*, 249(964):pp. 235–297.

Bakker, W. T., van de Graaff, J., Kraak, A. W., Smit, M. J., Snip, D. W., Steetzel, H. J. ., and Visser, P. J. (1996). Het Zwin, successen en lessen. Technical report, Technische Adviescommissie voor de Waterkeringen.

Bisschop, F., Visser, P., van Rhee, C., and Verhagen, H. (2011). Erosion due to high flow velocities: A description of relevant processes. *Coastal Engineering Proceedings*, 1:32.

Blake, E. S., Kimberlain, T. B., Berg, R. J., Cangialosi, J. P., and II, J. L. B. (2013). Tropical cyclone report, hurricane sandy. Technical report, National Hurricane Center.

Bosboom, J. and Stive, M. J. F. (2013). *Coastal Dynamics 1, Lecture notes CIE4305*. VSSD. ISBN 97890 6562 286 0.

Bugajny, N., Furmańczyk, K., Dudzińska-Nowak, J., and Paplińska-Swerpel, B. (2013). Modelling morphological changes of beach and dune induced by storm on the southern baltic coast using xbeach (case study: Dziwnow spit). *Journal of Coastal Research*, 65:672–677.

Chow, V. (1959). *Open-channel hydraulics*. McGraw-Hill Book Company.

Collins, C. (2012). Hurricane sandy. http://www.erh.noaa.gov/mhx/EventReviews/20121029/20121029.php.

Daly, C., Roelvink, D., van Dongeren, A., van Thiel de Vries, J., and McCall, R. (2012). Validation of an advective-deterministic approach to short wave breaking in a surf-beat model. *Coastal Engineering*, 60(0):69 – 83.

Deitz, J. (2013). Brookhaven & south haven hamlets, historical maps. http://brookhavensouthhaven.org/.

Deltares (2014a). Skillbed report. http://oss.deltares.nl/web/xbeach/skillbed.

Deltares (2014b). XBeach source code, revision 3709. Subversion repository. http://svn.oss.deltares.nl/repos/xbeach/trunk.

den Adel, H. (1987). Heranalyse doorlatendheidsmetingen door middel van de forchheimer relatie.". Technical Report M 1795/H 195, CO 272550/56, Grondmechanica Delft, Waterloopkundig Laboratorium. Dutch.

den Bieman, J. P. (2012). Simulating barrier island evolution. Master's thesis, Delft University of Technology.

Donnelly, C., Kraus, N., and Larson, M. (2006). State of knowledge on measurement and modeling of coastal overwash. *Journal of Coastal Research*, pages 965–991.

Galappatti, G. and Vreugdenhil, C. B. (1985). A depth-integrated model for suspended sediment transport. *Journal of Hydraulic Research*, 23(4):359–377.

Hallermeier, R. J. (1981). Terminal settling velocity of commonly occurring sand grains. *Sedimentology*, 28:859–865.

Kobayashi, N., Gralher, C., and Do, K. (2013). Effects of woody plants on dune erosion and overwash. *Journal of Waterway, Port, Coastal, and Ocean Engineering*, 139(6):466–472.

Komar, P. D. and Miller, M. C. (1975). On the comparison between the threshold of sediment motion under waves and unidirectional currents with a discussion of the practical evaluation of the threshold; reply. *Journal of Sedimentary Research*, 45(1):362–367.

Lang, J. and Winsemann, J. (2013). Lateral and vertical facies relationships of bedforms deposited by aggrading supercritical flows: From cyclic steps to humpback dunes. *Sedimentary Geology*, 296(0):36 – 54.

McCall, R., Masselink, G., Roelvink, D., Russell, P., Davidson, M., and Poate, T. (2012). Modelling overwash and infiltration on gravel barriers. *Coastal Engineering Proceedings*, 1(33).

McCall, R. T. (2008). The longshore dimension in dune overwash modelling. Master's thesis, Delft University of Technology.

McCall, R. T., van Thiel de Vries, J. S. M., Plant, N. G., van Dongeren, A. R., Roelvink, J. A., Thompson, D. M., and Reniers, A. J. H. M. (2010). Two-dimensional time dependent hurricane overwash and erosion modeling at santa rosa island. *Coastal Engineering*, 57:668–683.

Mendez, F. J. and Losada, I. J. (2004). An empirical model to estimate the propagation of random breaking and nonbreaking waves over vegetation fields. *Coastal Engineering*, 51(2):103 – 118.

Ministerie van Verkeer en Waterstaat (2007). Voorschrift toetsen op veiligheid primaire waterkeringen. Technical report. Dutch.

Murphy, A. H. and Epstein, E. S. (1989). Skill scores and correlation coefficients in model verification. *Monthly Weather Review*, 117:572–581.

National Research Council (1983). *Evaluation of the FEMA Model for Estimating Potential Coastal Flooding from Hurricanes and Its Application to Lee County, Florida*. National Academy Press.

NOAA (2014). National Geophysical Data Center, U.S. Coastal Relief Model, Volume 1. http://www.ngdc.noaa.gov/mgg/coastal/crm.html.

Richardson, J. and Zaki, W. (1954). Sedimentation and fluidisation: Part i. *Trans. Inst. Chem. Eng.*, 32(0):35–53.

Roelvink, J. A., Reniers, A. J. H. M., van Dongeren, A. R., van Thiel de Vries, J. S. M., McCall, R. T., and Lescinski, J. (2009). Modelling storm impacts on beaches, dunes and barrier islands. *Coastal Engineering*, 56(11–12):1133 – 1152.

Rominger, J., Lightbody, A., and Nepf, H. (2010). Effects of added vegetation on sand bar stability and stream hydrodynamics. *Journal of Hydraulic Engineering*, 136(12):994–1002.

Rowe, P. N. (1987). A convenient empirical equation for estimation of the richardson-zaki exponent. *Chemical Engineering Science*, 42(11):2795 – 2796.

Sallenger, A. H. (2000). Storm impact scale for barrier islands. *Journal of Coastal Research*, 16(3):890–895.

Shields, A. (1936). Anwendung der ähnlichkeits-Mechanik und der Turbulenz-forschung auf die Geschiebebewegung. *Preussische Versuchsanstalt für Wasserbau und Schiffbau*, 26:524–526.

Simons, D. B. and Richardson, E. V. (1962). The Effect of Bed Roughness on Depth-Discharge Relations in Alluvial Channels. *Geological Survey Water-Supply Paper*, 1498-E.

Simons, D. B. and Richardson, E. V. (1966). Resistance to Flow in Alluvial Channels. *Geological Survey Professional Paper*, 422-J.

Smith, M. J., Asal, F. F. F., and Priestnall, G. (2004). The use of photogrammetry and lidar for landscape roughness estimation in hydrodynamic studies. *ISPRS Congress*, 10:714–719.

Soulsby, R. (1997). *Dynamics of Marine Sands*. Thomas Telford Publications, London. ISBN 0 7277 2584 X.

Steetzel, H. J. and Visser, P. J. (1992). Bresgroei: 2 DV-ontwikkeling initiële bres, verslag onderzoek scheldegoot. TAW report Part II-A, Waterloopkundig laboratorium. Dutch.

Stelling, G. S. and Duinmeijer, S. P. A. (2003). A staggered conservative scheme for every froude number in rapidly varied shallow water flows. *International Journal for Numerical Methods in Fluids*, 43(12):1329–1354.

Talmon, A. M. (1992). *Bed topography of river bends with suspended sediment transport*. PhD thesis, Delft University of Technology.

Talmon, A. M., van Mierlo, M. C. L. M., and Struiksma, N. (1995). Laboratory measurements of the direction of sediment transport on transverse alluvial-bed slopes. *Journal of Hydraulic Research*, 33(4):495–517.

Terlouw, A. (2013). Predicting morpological storm impact on coastal dunes at ameland. Master's thesis, University of Twente.

Toorman, E. A. (2003). Validation of macroscopic modelling of particle-laden turbulent flows. *Belgian National Congress on Theoretical and Applied Mechanics*, 6.

U.S. Army Corps of Engineers (2002). *Coastal Engineering Manual*.

USGS (2012). Topographic lidar: Northeast atlantic coast. NOAA's Ocean Service, Coastal Services Center (CSC).

van Bendegom, L. (1947). Enige beschouwingen over riviermorphologie en rivierverbetering. Technical report, Ministerie van Verkeer en Waterstaat. Dutch.

van Rhee, C. (2010). Sediment entrainment at high flow velocity. *Journal of Hydraulic Engineering*, 136:572–582.

van Rhee, C. and Bezuijen, A. (1992). Influence of seepage on stability of sandy slope. *Journal of Geotechnical Engineering*, 118(8):1236–1240.

van Rijn, L. C. (1984a). Sediment pick-up functions. *Journal of Hydraulic Engineering*, 110(10):1494–1502.

van Rijn, L. C. (1984b). Sediment transport, part iii: Bed forms and alluvial roughness. *Journal of Hydraulic Engineering*, 110(12):1733–1754.

van Rijn, L. C. (1993). *Principles of Sediment Transport in Rivers, Estuaries and Coastal Seas, Part 1*. Aqua Publications.

van Rijn, L. C. (2006). *Principles of Sediment Transport in Rivers, Estuaries and Coastal Seas, Part 2*. Aqua Publications.

van Rijn, L. C. (2007a). Unified view of sediment transport by currents and waves. i: Initiation of motion, bed roughness, and bed-load transport. *Journal of Hydraulic Engineering*, 133(6):649–667.

van Rijn, L. C. (2007b). Unified view of sediment transport by currents and waves. ii: Suspended transport. *Journal of Hydraulic Engineering*, 133(6):668–689.

van Rijn, L. C., Walstra, D. J. R., Grasmeijer, B., Sutherland, J., Pan, S., and Sierra, J. P. (2003). The predictability of cross-shore bed evolution of sandy beaches at the time scale of storms and seasons using process-based profile models. *Coastal Engineering*, 47(3):295 – 327.

van Thiel de Vries, J. S. M. (2009). *Dune erosion during storm surges*. PhD thesis, Delft University of Technology.

Visser, P. J. (1998). *Breach growth in sand-dikes*. PhD thesis, Delft University of Technology.

Voogt, L., van Rijn, L., and Berg, J. (1991). Sediment transport of fine sands at high velocities. *Journal of Hydraulic Engineering*, 117(7):869–890.

Voukouvalas, E. (2012). Modelling and analysis of the dune erosion during the 1976 storm surge. Master's thesis, Delft University of Technology.

Walstra, D. J. R., van Rijn, L. C., van Ormondt, M., Brière, C., and Talmon, A. M. (2007). *The Effects of Bed Slope and Wave Skewness on Sediment Transport and Morphology*, chapter 11, pages 137–150.

Winterwerp, J. C. (2001). Stratification effects by cohesive and noncohesive sediment. *Journal of Geophysical Research: Oceans*, 106(C10):22559–22574.

Winterwerp, J. C. (2006). Stratification effects by fine suspended sediment at low, medium, and very high concentrations. *Journal of Geophysical Research: Oceans*, 111(C5).

Winterwerp, J. C. and van Kesteren, W. G. (2004). *Introduction to the Physics of Cohesive Sediment in the Marine Environment*, volume 56 of *Developments in Sedimentology*. Elsevier.

Appendices

Appendix A

Derivation modification initiation of motion by dilatancy

The derivation of Van Rhee (2010) on the effect of dilatancy on the initiation of motion at high flow velocities is presented in this appendix.

A.1 Derivation hydraulic gradient

A sediment balance can be set-up for the bed consisting of two control volumes: one which is densely packed and one which is dilated. In time, the layer separating both zones is propagating once erosion takes place. Volume conservation (see Figure A.1 for a visualisation) requires:

$$(1 - n_0)h_0 = (1 - n_l)h_l \tag{A.1}$$

The subscript 0 refers to the situation prior to erosion and the subscript l refers to the sheared zone. Over a certain time interval, the height h_0 is increased to h_l.

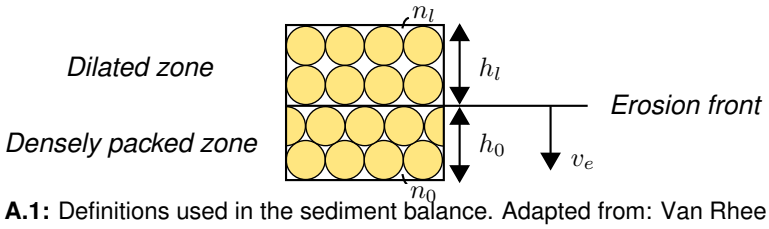

Figure A.1: Definitions used in the sediment balance. Adapted from: Van Rhee (2010).

The corresponding volume increase ΔV over an interval Δt (by definition: $h_0 = v_e \Delta t$, with v_e the erosion velocity):

$$\Delta V = n_l h_l - n_0 h_0 = n_l h_0 \frac{1 - n_0}{1 - n_l} - n_0 h_0 = \frac{n_l - n_0}{1 - n_l} h_0 = \frac{n_l - n_0}{1 - n_l} v_e \Delta t \tag{A.2}$$

The volume increase is the result of water flowing into the pores with the superficial flow v_{sup} velocity of the water entering the bed:

$$\Delta V = v_{sup} \Delta t \tag{A.3}$$

Combining these equations with Darcy's law ($v_{sup} = -k \cdot i$) results in the hydraulic gradient i that will be present during erosion:

$$i = -\frac{v_e}{k_l} \frac{n_1 - n_0}{1 - n_l} \tag{A.4}$$

The hydraulic gradient is hence only of importance if the erosion velocity v_e is large and the permeability k_l low.

A.2 Modification condition for initiation of motion

Shields (1936) derived his expression for the initiation of motion of sediment particles, based on a balance of forces on an individual particle, see Section 2.4.3. Since the hydraulic gradient is a force directed towards the bed, the stability of the particle improves with the presence of this hydraulic gradient. Therefore, the force balance should be reconsidered including this force (F_i in Figure A.2). To illustrate that the dilatancy force is not necessarily pointed in the same direction as the gravity force, a sloping bed is considered.

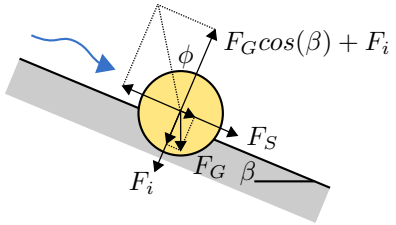

Figure A.2: Force balance for a single particle, adapted from Van Rhee (2010).

The balance of the forces decomposed in the direction of the bed slope, with a slope angle of β and an angle of internal friction of ϕ, reads (Van Rhee, 2010):

$$F_S + F_G \sin(\beta) = (F_G \cos(\beta) + F_i) \tan(\phi) \tag{A.5a}$$

$$\frac{F_S}{F_G} = \left(\cos(\beta) - \frac{\sin(\beta)}{\tan(\phi)} + \frac{F_i}{F_G}\right) \tan(\phi) \tag{A.5b}$$

$$\frac{F_S}{F_G} = \left(\frac{\sin(\phi - \beta)}{\sin(\phi)} + \frac{F_i}{F_G}\right) \tan(\phi) \tag{A.5c}$$

Sediment is brought into motion, as discussed by Shields (1936), if:

$$\theta = \frac{F_S}{F_G} > \tan(\phi) = \theta_{cr} \tag{A.6}$$

If the hydraulic gradient is included and the bed slope is taken into account, a new criterion for the initiation of motion is obtained (the superscript $B\&D$ notes that it accounts for the bed slope and dilatancy):

$$\theta > \frac{F_S}{F_G} = \left(\frac{\sin(\phi - \beta)}{\sin(\phi)} + \frac{F_i}{F_G}\right) \tan(\phi) = \left(\frac{\sin(\phi - \beta)}{\sin(\phi)} + \frac{F_i}{F_G}\right) \theta_{cr} = \theta_{cr}^{B\&D} \tag{A.7}$$

Van Rhee (2010) distinguishes a single particle mode and the continuum mode (in which a small block of soil is considered) for stability as studied by Van Rhee and Bezuijen (1992):

- Single particle: $F_i = \frac{1}{8}\pi D^3 \rho_w g i$ and $G = \frac{1}{6}\pi D^3 (\rho_s - \rho_w) g$
- Continuum: $F_i = \rho_w g i$ and $G = (1 - n_0)(\rho_s - \rho_w) g$

Combining these formulations with Equations A.4 and A.7 results into the following expression. In this formulation, the parameter A is equal to $3/4$ for single particles and approximately 1.7 for a continuum.

$$\theta_{cr}^{B\&D} = \theta_{cr} \left(\frac{\sin(\phi - \beta)}{\sin(\phi)} + \frac{v_e}{k_l} \frac{n_l - n_0}{1 - n_l} \frac{A}{\Delta}\right) \tag{A.8}$$

One can easily achieve the pure dilatancy effect by considering a non-sloping bottom ($\beta = 0$):

$$\theta_{cr}^{B\&D} = \theta_{cr} \left(1 + \frac{v_e}{k_l} \frac{n_l - n_0}{1 - n_l} \frac{A}{\Delta}\right) \tag{A.9}$$

With this equation, the initiation of motion is modified to account for dilatancy.

Appendix B

Characteristic bed features at high flow velocities

At high flow velocities, some characteristic features can be observed. One can think of a hydraulic jump as a transition between super-critical and sub-critical flow causing large gradients in flow velocities and therefore also large gradients in sediment transport rates. Another important feature are antidunes, as visualised in Figure B.1.

Figure B.1: Schematic visualisation of antidunes.

Antidunes are generally deposited as in-phase wave trains at Froude numbers between 0.8 and 1.8 (Lang and Winsemann, 2013). They look similar to regular dunes but have some very important distinct features. In contrast to regular dunes, antidunes propagate in upstream direction, as visualised in Figure B.2. Regular dunes propagate in downstream direction since the flow converges in front of the dune and diverges behind the dune, resulting in erosion of the front and accretion of the back side. By the different flow behaviour of supercritical flow, antidunes propagate upstream by lee side erosion and stoss side accretion; this is caused by the fact that the flow decelerates at the stoss side to achieve a flow velocity which is minimum on top of the crest. A delay in the sediment transport has hence a destabilizing effect on the presence of antidunes (Andreotti et al., 2012). Fully developed antidunes have a length scale of about ten times the water depth and are in phase with the surface waves (Van Rijn, 1993).

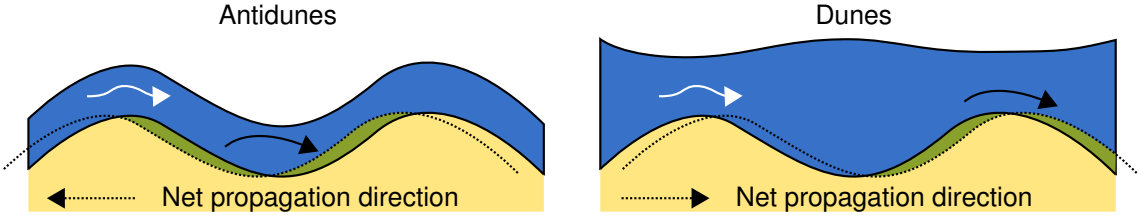

Figure B.2: Different propagation direction antidunes and regular dunes. Adapted from Van Rijn (1993).

At steep slopes and large Froude numbers in the order of $1.6 - 2.1$, chutes-and-pools can be observed which are also known as cyclic steps if repeated several times in downstream direction. These features are formed upstream of hydraulic jumps. The flow accelerates rapidly in the chute and it slows down in the hydraulic jump at the end of the chute whereafter a long pool is observed (Simons and Richardson, 1966; Van Rijn, 1993).

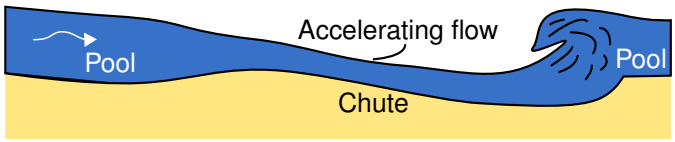

Figure B.3: Schematic visualisation of chutes-and-pools. Adapted from Simons and Richardson (1962, 1966).

There is a strong interaction present between the hydraulics and morphology for all those features.

Appendix C

The XBeach model

This appendix gives an overview of the most important aspects of the XBeach model, based on Roelvink et al. (2009). Thereafter, a more in detail analysis on the morphological formulations is provided.

C.1 General model description

C.1.1 Coordinate system and grid

Figure C.1 shows the grid conventions used in the XBeach model. The x-axis is oriented towards the coast and the y-axis is directed alongshore. The grid is positioned relative to the world coordinates through the origin of the grid and the rotation angle.

A rectilinear or curvi-linear, staggered, non-equidistant grid is applied. Water levels, bed levels, concentrations, wave energy and more are defined in the grid centers. Velocities and sediment transports are defined at the cell interfaces. The bottom level is directed upward as positive, in contrast to some other numerical models (as Delft3D) which define the bottom level in the opposite direction.

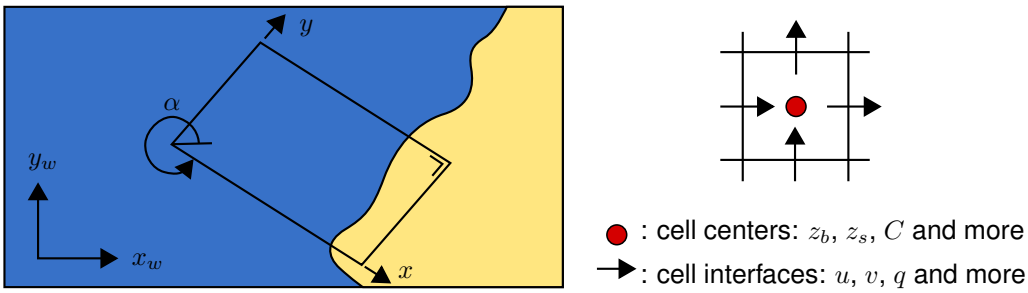

Figure C.1: Coordinate system and grid definition, adapted from Roelvink et al. (2009).

C.1.2 Hydrodynamics

XBeach solves the long waves based on the shallow water equations. Short waves are taken into account by means of the wave action balance. In this way, the precise features of short waves are not phase-resolved (averaged over wave period), but the wave energy of the short waves is taken into account. Gradients in the wave energy of the short waves is a forcing term in the shallow water equations.

Shallow water equations

The shallow water equations form the basis of the hydrodynamic calculations which are based on the GLM (Generalised Lagrangian Mean) approach:

$$\frac{\partial u^L}{\partial t} + u^L \frac{\partial u^L}{\partial x} + v^L \frac{\partial u^L}{\partial y} - f v^L - \nu_h \left(\frac{\partial^2 u^L}{\partial x^2} + \frac{\partial^2 u^L}{\partial y^2} \right) = \frac{\tau_{sx} - \tau_{bx}^E}{\rho h} - g \frac{\partial z_s}{\partial x} + \frac{F_x}{\rho h} \tag{C.1a}$$

$$\frac{\partial v^L}{\partial t} + u^L \frac{\partial v^L}{\partial x} + v^L \frac{\partial v^L}{\partial y} - f u^L - \nu_h \left(\frac{\partial^2 v^L}{\partial x^2} + \frac{\partial^2 v^L}{\partial y^2} \right) = \frac{\tau_{sy} - \tau_{by}^E}{\rho h} - g \frac{\partial z_s}{\partial y} + \frac{F_y}{\rho h} \tag{C.1b}$$

$$\frac{\partial z_s}{\partial t} + \frac{\partial h u^L}{\partial x} + \frac{\partial h v^L}{\partial y} = 0 \tag{C.1c}$$

In these equations is f the Coriolis coefficient, ν_h the horizontal eddy viscosity coefficient, are τ_s the wind shear stresses, τ_b the bed shear stresses, are F the wave-induced stresses and is z_s the surface elevation. All the velocities are in a Lagrangian frame of reference (noted with the L superscript), only the bed shear stresses are calculated with the Eulerian velocities as experienced by the bed (noted with the E superscript):

$$u^E = u^L - u^S \quad and \quad v^E = v^L - v^S \tag{C.2}$$

The Stokes drift (noted with the S superscript) is hence the difference between the Lagrangian velocity and the Eulerian velocity.

The wave-action balance and the roller energy balance

The wave induced-shear stresses (the source term in the shallow water equations) consist of two contributions: the roller induced radiation stress and the wave induced radiation stress (the radiation stress is the depth-averaged spatial flux of momentum). Wave action A is introduced as the quotient of the wave energy density in each directional bin S_w divided by the intrinsic wave frequency σ:

$$A\left(x, y, t, \theta\right) = \frac{S_w\left(x, y, t, \theta\right)}{\sigma\left(x, y, t\right)} \tag{C.3}$$

The wave action is balanced is defined as follows:

$$\frac{\partial A}{\partial t} + \frac{\partial c_x A}{\partial x} + \frac{\partial c_y A}{\partial y} + \frac{\partial c_\theta A}{\partial \theta} = -\frac{D_w}{\sigma} \tag{C.4}$$

where c is the propagation velocity of the wave action in the direction of the subscript and D_w is the wave energy dissipation term. The wave energy dissipation term acts as a source in the roller energy balance equation:

$$\frac{\partial S_r}{\partial t} + \frac{\partial c_x S_r}{\partial x} + \frac{\partial c_y S_r}{\partial y} + \frac{\partial c_\theta S_r}{\partial \theta} = -D_r + D_w \tag{C.5}$$

Here is S_r the roller energy in each bin, c represents the propagation velocity of the roller energy and D_r is a roller energy dissipation term.

Numerical approximations

For the calculation of the flow, a first-order upwind explicit scheme with an automatic time step is applied. The momentum-conserving discretization is similar to the one used by Stelling and Duinmeijer (2003). This scheme is very suitable for overwash and breaching conditions since it describes a combination of sub- and supercritical flows and it can be applied on flooding and drying cases.

C.1.3 Morphology

A detailed description of the morphology module of the XBeach model is given in Section C.2. In this section only a brief description is presented, required to understand the theoretical principles dealt with in this thesis.

The bed level is modified based on morphological formulations as explained in Section 2.4. Gradients in sediment transport rates result in a change of the bed level based on the Exner equation. In XBeach, a morphological factor f_{mor} is included to speed up the calculation:

$$\frac{\partial z_b}{\partial t} + \frac{f_{mor}}{1-n}\left(\frac{\partial q_x}{\partial x} + \frac{\partial q_y}{\partial y}\right) = 0 \tag{C.6}$$

The sediment transport rates are calculated based on the advection and dispersion flux:

$$q_x = hCu^E + D_h h\frac{\partial C}{\partial x} \tag{C.7a}$$

$$q_y = hCv^E + D_h h\frac{\partial C}{\partial y} \tag{C.7b}$$

Sediment concentrations

By default, the formulation of Van Rijn with modifications by Van Thiel-de Vries is used to calculate the equilibrium sediment concentrations (Van Rijn, 2007a,b; Van Thiel de Vries, 2009):

$$C_{eq} = \frac{A_{sb}}{h}\left(\sqrt{v_{mg}^2 + 0.64u_{rms}^2} - U_{cr}\right)^{1.5} + \frac{A_{ss}}{h}\left(\sqrt{v_{mg}^2 + 0.64u_{rms}^2} - U_{cr}\right)^{2.4} \tag{C.8}$$

Here are A_{sb} and A_{ss} sediment transport coefficients for respectively bed-load and suspended load transport, v_{mg} is the velocity magnitude, u_{rms} represents the root-mean-square velocity and U_{cr} is the critical flow velocity for initiation of motion which is related to the critical Shields parameter by Equation C.13. Based on the advection-diffusion equation of (Galappatti and Vreugdenhil, 1985), as presented in Equation 2.5, the actual suspended sediment concentration is calculated. The bed-load transport concentration is assumed to be equal to the equilibrium bed-load concentration.

Bed slope effect

Sediment is transported more easily in down-slope direction than in on-slope direction. To account for this effect, an engineering approach mentioned by Soulsby (1997), is used:

$$q_{s,slope} = q_s\left(1 - \alpha\frac{\partial z_b}{\partial s}\right) \tag{C.9}$$

In this equation is s the streamwise direction and is the constant α by default equal to 1.6. One can easily see that an increase in bed level results in a reduction of the transport rates. The actual implementation of this method in XBeach differs slightly, see Section 2.7.2.

Avalanching

During dune erosion, sandy slopes will avalanche when a certain critical bed slope is exceeded:

$$\left|\frac{\partial z_b}{\partial x}\right| > m_{cr} \quad or \quad \left|\frac{\partial z_b}{\partial y}\right| > m_{cr} \tag{C.10}$$

A distinction is made between wet and dry cells. A grid cell is considered as wet when the depth in that cell is more than a certain threshold depth. By default, the critical slopes m_{cr} for dry and wet points are set to 1 and 0.3 respectively. Once the avalanching algorithm is triggered, sediment is exchanged between the cells to bring the slope back to the critical slope.

C.1.4 Boundary conditions

At the boundaries of the computational grid, certain conditions should be stated to enforce certain hydrodynamics. Otherwise, too many degrees of freedom are present which will not result in a proper calculation.

Wave boundary conditions

At the offshore boundary, the wave energy density is prescribed as a function of y, θ and time. This function can be described based on spectral parameters. At the lateral boundaries, the alongshore gradient is fixed as zero.

Flow boundary conditions

At the seaward and bay side of the computational grid, radiating boundary conditions are enforced, accounting for the incoming bound long waves. At the lateral boundaries, Neumann conditions are used such that the water level gradient equals zero.

C.1.5 Sediment transport limiters in XBeach

Two artificial limiters are included to prevent the occurrence of unrealistic large sediment concentrations.

Restriction of the sediment concentration magnitude by c_{max}

The equilibrium sediment concentrations are both (bed-load and suspended load) limited by half of the user-defined parameter *cmax* (by default $0.1\ m^3/m^3$).

Restriction of the Shields parameter by θ_{max}

The flow velocity that *forces* the sediment into motion, is limited in the equilibrium sediment concentration equations to a flow velocity that corresponds to a Shields parameter value at which sheet flow occurs. The latter is defined by the user-defined parameter *smax* (usually a value around 1.0). The velocity that *transports* the sediment (U in Equation 2.3) can still increase, which results in a linear relation between the flow velocity and the sediment transport rate.

The Shields parameter restriction can be rewritten into a restriction to the flow velocity in the sediment transport equation. The Shields parameter is a function of the shear stress velocity:

$$\theta = \frac{u_*^2}{\Delta g D_{50}} \tag{C.11}$$

It is assumed that the depth averaged flow velocity is related to the bed shear stress velocity through the constant coefficient of bed roughness c_f:

$$U = \frac{u_*}{\sqrt{c_f}} \tag{C.12}$$

By combining Equations C.11 and C.12, a direct relation between the maximum flow velocity and the value of the maximum Shields parameter is obtained:

$$U_{max} = \sqrt{\frac{\theta_{max} \Delta g D_{50}}{c_f}} \tag{C.13}$$

Note that the actual velocities can be larger than this maximum velocity, velocities are restricted to this value only in the calculation of the equilibrium sediment concentration. To get an indication at what flow

velocities the equilibrium concentration is fixed, some characteristic values are filled into the derived expression:

$$U_{max} = \sqrt{\frac{\theta_{max} \Delta g D_{50}}{c_f}} = \sqrt{\frac{1.0 \cdot 1.65 \cdot 9.81 \cdot 0.0002}{0.0032}} = 1.0 m/s \tag{C.14}$$

The sediment transport concentration is for this set of parameters hence constant once velocities are larger than $1\ m/s$.

C.2 Sediment transport in XBeach

Since the XBeach model is still in development, no high-detail manual is available. This section has the purpose of indexing all the relevant equations that are implemented in the source code of XBeach and verifying these equations with literature.

XBeach is a 2DH model which consists of *m* grid cells in *x*-direction and *n* grid cells in *y*-direction. For each time step, a system of equations is solved numerically for each box. The calculations are based on a set of initial conditions and the boundary conditions. In the following sections, the equations of the morphological calculation will be treated.

C.2.1 Morphological change

The evolution of the bottom level elevation in time is the result of gradients in the sediment transport. It is described by Exner's Law (sediment volume conservation) as defined in Equation 2.1. In XBeach a morphological factor is included to speed up the calculation:

$$\frac{\partial z_b}{\partial t} + \frac{f_{mor}}{1-n}\left(\frac{\partial q_x}{\partial x} + \frac{\partial q_y}{\partial y}\right) = 0 \tag{C.15}$$

The sediment transport rates q_x and q_y are the volume of sediment, excluding pores, flowing per second through a cross-section perpendicular to the axis indicated in the subscript. These rates can be expressed in terms of the depth averaged flow velocity and concentration:

$$q_x = U_x C h \tag{C.16a}$$

$$q_y = U_y C h \tag{C.16b}$$

The water depth and flow velocities are calculated based on a large set of hydrodynamic equations. A depth averaged advection-diffusion equation is used to calculate the concentrations (Galappatti and Vreugdenhil, 1985):

$$\frac{\partial hC}{\partial t} + \frac{\partial hCu^E}{\partial x} + \frac{\partial hCv^E}{\partial y} + \frac{\partial}{\partial x}\left(D_h h \frac{\partial C}{\partial x}\right) + \frac{\partial}{\partial y}\left(D_h h \frac{\partial C}{\partial y}\right) = \frac{hC_{eq} - hC}{T_s} \tag{C.17}$$

The time scale T_s is defined as:

$$T_s = \max\left(f_{T_s}\frac{h}{w_s}, T_{s,\min}\right) \tag{C.18}$$

The factor f_{T_s} (default value of 0.1) is a correction factor to account for the fact that w_s is calculated based on depth averaged data. The minimum adaptation time T_s is by default 0.5 seconds.

The sediment transport rates in XBeach are not calculated by Equations C.16, but by a set of equations which are derived from the advection-diffusion equation:

$$q_x = hCu^E + D_h h \frac{\partial C}{\partial x} \tag{C.19a}$$

$$q_y = hCv^E + D_h h \frac{\partial C}{\partial y} \tag{C.19b}$$

C.2.2 Sediment transport equations

General parameters

The kinematic viscosity is calculated based on an expression of Van Rijn which is a function of the water temperature:

$$\nu = \frac{4}{20 + T_w} 10^{-5} \tag{C.20}$$

XBeach asumes a constant temperature of 20 degree Celsius, which results in a constant kinematic viscosity of $10^{-6}\ m^2/s$.

The dimensionless sediment particle size is defined as:

$$D_* = \left(\frac{\Delta g}{\nu^2} \right)^{1/3} D_{50} \tag{C.21}$$

Bed shear stresses play a key role in the initiation of sediment transport. It is convenient to express this shear stress in the dimensions of a velocity, the bed shear stress velocity:

$$u_* = \sqrt{\frac{\tau_b}{\rho}} \tag{C.22}$$

Fall velocity

Ahrens (2000) derives a formulation for the fall velocity based on a relationship suggested by Hallermeier (1981):

$$\mathbf{R} = \alpha_1 \sqrt{A} + \alpha_2 A \tag{C.23}$$

The Reynolds number associated with a falling particle and the Archimedes buoyancy index in this equation are defined as:

$$\mathbf{R} = \frac{w D_{50}}{\nu} \tag{C.24}$$

$$A = \frac{\Delta g D_{50}^3}{\nu^2} \tag{C.25}$$

Based on data of Hallermeier, Ahrens derived the following empirical formulations for the constants in Equation C.23:

$$\alpha_1 = 1.06 \tanh \left(0.016 A^{0.50} \exp \left(-120/A \right) \right) \tag{C.26}$$

$$\alpha_2 = 0.055 \tanh \left(12 A^{-0.59} \exp \left(-0.0004 A \right) \right) \tag{C.27}$$

The fall velocity can now be derived out of the preceding equations:

$$w_s = \alpha_1 \sqrt{\Delta g D_{50}} + \alpha_2 \frac{\Delta g D_{50}^2}{\nu} \tag{C.28}$$

XBeach uses a rewritten form of the equations in which a comparable dimensionless parameter S_* is defined as:

$$S_* = \sqrt{A}/4 \tag{C.29}$$

Wave stirring

If long wave stirring is turned on, the velocity magnitude is equal to the magnitude of the Eulerian velocity:

$$v_{mg} = \sqrt{\left(u^E\right)^2 + \left(v^E\right)^2} \tag{C.30}$$

If wave stirring is turned off:

$$v_{mg} = \left(1 - \frac{dt}{f_{cats} \cdot T_{rep}}\right) v_{mg} + \frac{dt}{f_{cats} \cdot T_{rep}} \sqrt{\left(u^E\right)^2 + \left(v^E\right)^2} \tag{C.31}$$

In this equation is f_{cats} a factor on T_{rep}, the representative wave period, to obtain the current averaging time scale.

Root-mean-squared velocity

For the root-mean-squared velocity, the following expression is used:

$$u_{rms} = \frac{\pi H_{rms}}{T_{rep}\sqrt{2}\sinh\left(k(h + \delta H_{rms})\right)} \tag{C.32}$$

where k represents the wave number, h the local water depth and δ states what fraction of the wave height should be added to the water depth.

To account for the wave breaking induced turbulence due short waves, the root mean-squared velocity is adjusted (constant of 1.45 estimated in the Thesis of Van Thiel de Vries (2009)):

$$u_{rms}^2 = u_{rms}^2 + 1.45 k_b \tag{C.33}$$

where k_b is the turbulence variance in the bed, approximated with empirical formulations in XBeach.

Equilibrium concentration

In the present version of XBeach, two sediment transport formulations are available. The formulae of the two formulations are presented in the next sections. For both methods, the total equilibrium sediment concentration is calculated as:

$$C_{eq} = \max\left(\min\left(C_{eq,b}, \tfrac{1}{2}C_{\max}\right) + \min\left(C_{eq,s}, \tfrac{1}{2}C_{\max}\right), 0\right) \tag{C.34}$$

Soulsby-Van Rijn

The Soulsby-Van Rijn transport equations are known as (Soulsby, 1997; van Rijn, 1984b) :

$$C_{eq,b} = \frac{A_{sb}}{h}\left(\sqrt{v_{mg}^2 + 0.018\frac{u_{rms}^2}{C_d}} - U_{cr}\right)^{2.4} \tag{C.35a}$$

$$C_{eq,s} = \frac{A_{ss}}{h}\left(\sqrt{v_{mg}^2 + 0.018\frac{u_{rms}^2}{C_d}} - U_{cr}\right)^{2.4} \tag{C.35b}$$

The bed-load and suspended load coefficients are calculated with:

$$A_{sb} = 0.005h\left(\frac{D_{50}}{h\Delta g D_{50}}\right)^{1.2} \tag{C.36a}$$

$$A_{ss} = 0.012 D_{50} \frac{D_*^{-0.6}}{\left(\Delta g D_{50}\right)^{1.2}} \tag{C.36b}$$

The threshold velocity defines at which depth averaged velocity sediment motion is initiated (which is hence related to the critical Shields parameter θ_{cr}):

$$U_{cr} = \begin{cases} 0.19 D_{50}^{0.1} \log 10 \left(\frac{4h}{D_{90}}\right) for D_{50} < 0.0005 \\ 8.5 D_{50}^{0.6} \log 10 \left(\frac{4h}{D_{90}}\right) for D_{50} < 0.05 \end{cases} \tag{C.37}$$

Finally, the drag coefficient:

$$C_d = \left(\frac{0.40}{\ln\left(\frac{\max(h, 10 z_0)}{z_0}\right) - 1} \right)^2 \tag{C.38}$$

If the θ_{max} limiter is applied, Equations C.35 are replaced by:

$$C_{eq,b} = \frac{A_{sb}}{h} \left(\sqrt{\min\left(v_{mg}^2 + 0.018 \frac{u_{rms}^2}{C_d}, \frac{\theta_{\max} g D_{50} \Delta}{c_f} \right)} - U_{cr} \right)^{2.4} \tag{C.39a}$$

$$C_{eq,s} = \frac{A_{ss}}{h} \left(\sqrt{\min\left(v_{mg}^2 + 0.018 \frac{u_{rms}^2}{C_d}, \frac{\theta_{\max} g D_{50} \Delta}{c_f} \right)} - U_{cr} \right)^{2.4} \tag{C.39b}$$

Van Thiel-Van Rijn

The equilibrium sediment concentration is calculated with the Van Thiel-Van Rijn formulations as follows (Van Rijn, 2007a,b; Van Thiel de Vries, 2009):

$$C_{eq,b} = \frac{A_{sb}}{h} \left(\sqrt{v_{mg}^2 + 0.64 u_{rms}^2} - U_{cr} \right)^{1.5} \tag{C.40a}$$

$$C_{eq,s} = \frac{A_{ss}}{h} \left(\sqrt{v_{mg}^2 + 0.64 u_{rms}^2} - U_{cr} \right)^{2.4} \tag{C.40b}$$

In these equations are the bed-load coefficient and suspended load coefficient defined as (note that Equation C.41b is equal to C.36b):

$$A_{sb} = 0.015 h \frac{\left(D_{50}/h\right)^{1.2}}{\left(\Delta g D_{50}\right)^{0.75}} \tag{C.41a}$$

$$A_{ss} = 0.012 D_{50} \frac{D_*^{-0.6}}{\left(\Delta g D_{50}\right)^{1.2}} \tag{C.41b}$$

The critical velocity is computed as a weighted summation of the separate contributions by currents and waves (van Rijn, 2007a):

$$U_{cr} = \beta \cdot U_{crc} + (1 - \beta) \cdot U_{crw} \tag{C.42a}$$

$$\beta = \frac{v_{mg}}{v_{mg} + U_{rms}} \tag{C.42b}$$

The critical velocity for currents is based on Shields (1936):

$$U_{crc} = \begin{cases} 0.19 D_{50}^{0.1} \log 10 \left(\frac{4h}{D_{90}} \right) for D_{50} <= 0.0005 \\ 8.5 D_{50}^{0.6} \log 10 \left(\frac{4h}{D_{90}} \right) for D_{50} <= 0.002 \\ 1.3 \sqrt{\Delta g D_{50}} \left(\frac{h}{D_{50}} \right)^{1/6} for D_{50} > 0.002 \end{cases} \tag{C.43}$$

The critical velocity for waves is based on Komar and Miller (1975):

$$U_{crw} = \begin{cases} 0.24 (\Delta g)^{2/3} (D_{50} T_{rep})^{1/3} for D_{50} <= 0.0005 \\ 0.95 (\Delta g)^{0.57} (D_{50})^{0.43} (T_{rep})^{0.14} for D_{50} > 0.0005 \end{cases} \tag{C.44}$$

If a Shields parameter limitation is enforced, Equations C.40 are rewritten into:

$$C_{eq,b} = \frac{A_{sb}}{h} \left(\sqrt{\min \left(v_{mg}^2 + 0.64 u_{rms}^2, \frac{\theta_{\max} g D_{50} \Delta}{c_f} \right)} - U_{cr} \right)^{1.5} \tag{C.45a}$$

$$C_{eq,s} = \frac{A_{ss}}{h} \left(\sqrt{\min \left(v_{mg}^2 + 0.64 u_{rms}^2, \frac{\theta_{\max} g D_{50} \Delta}{c_f} \right)} - U_{cr} \right)^{2.4} \tag{C.45b}$$

Appendix D

General XBeach model parameters

D.1 Default parameters

This chapter provides the relevant parameter settings of the XBeach model runs. Some of these settings differ intentionally from the default XBeach values.

Table D.1: General parameters used in the XBeach model runs. If a parameter value is taken differently from the XBeach default settings, the XBeach default value is given between brackets.

Parameter	Value	Unit	Meaning
C	55	$m^{0.5}/s^1$	Chézy coefficient.
rho	1025	kg/m^3	Density of water.
D_{50}	200	μm	Median sediment grain size.
D_{90}	300	μm	90% percentile sediment grain size.
por	0.4	–	Porosity of sediment in the bed.
CFL	0.7	–	Maximum Courant number on which the actual time step of the hydrodynamic simulation is based.
swave	0 (1)	–	Short waves module turned off for model runs without waves, in other cases a value of 1 is used.
morphology	1	–	Bed update module is turned on.
avalanching	1	–	Avalanching module is turned on.
wetslp	0.3	–	Critical avalanching slope under water (dz/dx and dz/dy).
dryslp	1.0	–	Critical avalanching slope above water (dz/dx and dz/dy).
sedtrans	1	–	Sediment transport module is turned on.
form	2	–	Sediment transport formulation: Van Thiel-Van Rijn.
bed	1	–	Bed-load transport is calculated.
sus	1	–	Suspended load transport is calculated.
bulk	0 (1)	–	By defining bulk as 0, bed-load and suspended load sediment rates are calculated separately. Otherwise, all transport is calculated as suspended sediment load.
cmax	0.3 (0.1)	m^3/m^3	Maximum depth-averaged sediment concentration. Both the bed-load as the suspended load are limited to half of this value.

The presented list is far from complete, `http://oss.deltares.nl/web/xbeach/reference` provides the default values of other parameters involved in the XBeach model.

D.2 Default parameters improved model

The model improvements considered in Chapter 5 require certain additional parameters to be introduced. These are presented in Table D.2.

Table D.2: Parameters of the improved XBeach model. The majority of these parameters are introduced with the model improvements made in this research. If a parameter value is taken differently from the default settings, the default value is given between brackets.

Parameter	Value	Unit	Meaning
highflowdilatancy	1	$-$	Dilatancy effect at high flow velocities (Van Rhee method).
RheeA	0.75	$-$	Constant A in the expression of Van Rhee (2010), see Equation A.8.
D_{15}	150	μm	15% percentile sediment grain size (required for Van Rhee method).
bdslpeffmag	4	$-$	Adjust the sediment transport magnitude for bed slopes.
facsl	0.15 (1.6)	$-$	Factor used in the adjustment of the transport magnitude for bed slopes.
bdslpeffini	1	$-$	Adjustment of the critical Shields parameter for bed slopes (initiation of motion).
bdslpeffdir	1	$-$	Adjustment of sediment transport direction based on the theory of Talmon et al. (1995).
tunedir1	1	$-$	Factor on the angle of the adjustment of the sediment direction.
angleinternalfric	30	deg	Angle of internal friction.
fallvelred	1	$-$	Reduction of the fall velocity of sediment at high concentrations.
sourcesink	0	$-$	If a value of 0 is applied, the default Exner equation is used. With a value of 1 are the fluxes in the advection-diffusion equation accounted for in the bed level updated. By using a value of 2, gradients of the concentration over time are included in the Exner equation.

Most of these parameters are straightforward. A value of 1 means that the specific module is turned on. The parameters related to the bed slope effects have some additional options:

Parameter *bdslpeffmag*:

0. Do nothing
1. Originally implemented factor $(1 - facsl \cdot \tan(\beta))$ on **total** sediment transport rates
2. Originally implemented $(1 - facsl \cdot \tan(\beta))$ on **bed-load** transport rates
3. Factor $(1 - facsl \cdot \tan(\beta))$ in flow direction on **total** sediment transport rates
4. Factor $(1 - facsl \cdot \tan(\beta))$ in flow direction on **bed-load** transport rates

Parameter *bdslpeffini*:

0. Do nothing
1. Modification critical Shields parameter **total** sediment load
2. Modification critical Shields parameter **bed-load**

Parameter *bdslpeffdir*:

0. Do nothing
1. Bed-load direction modification theory by Talmon et al. (1995)

For more information on the theory behind the bed slope effects, see Section 5.4.

D.3 Model runs

A large variety of parameter settings is used for the cases presented in this report. The case-depending parameters are mentioned in the relevant sections. Further, there is a set of standard model runs which are used in all the cases. These standard settings make a comparison of certain improvements over different cases possible.

Table D.3: Parameters of the model runs which are used in addition to the case-depending parameters and the default parameters as presented in Table D.1.

Model run	Base parameters	Modifications
XBeach default	Table D.1	–
Smax	Table D.1	*smax* $= 1$
Soulsby slope effect	Table D.1	*bdslpeffmag* $= 3$
Improved model	Tables D.1 & D.2	–
No dilatancy effect	Tables D.1 & D.2	*highflowdilatancy* $= 0$
With A = 1.75 (dilatancy)	Tables D.1 & D.2	*rheeA* $= 1.75$ (instead of 0.75)
No bed slope effect	Tables D.1 & D.2	*bdslpeffmag* $= 0$
		bdslpeffini $= 0$
		bdslpeffdir $= 0$
Double direction change	Tables D.1 & D.2	*tunedir1* $= 2$
With 20° internal friction	Tables D.1 & D.2	*angleinternalfric* $= 20$
No fall velocity reduction	Tables D.1 & D.2	*fallvelred* $= 0$
With conservative Exner	Tables D.1 & D.2	*sourcesink* $= 2$

Appendix E

Conceptual model tests

This appendix presents cases to test whether certain improvements made in the XBeach model are implemented correctly and to check the behaviour of these improvements on a detailed scale. Table E.1 presents a short description of these tests:

Table E.1: Overview of the modelled experiments to investigate the presence of side effects.

Appendix	Page	Name	Description
E.1	E.2	Sloping bed test case	A sloping bed with a flow under certain angles is considered. The performance of the different bed slope effects is considered.
E.2	E.6	Eroding bed test case	The performance of the Van Rhee method to account for dilatancy is validated by enforcing a certain rising/falling velocity of the bed.
E.3	E.8	Accretion of a bed	The time scale in the advection-diffusion equation for sediment is explored. An accreting bed is considered by enforcing a zero flow velocity while there is still sediment in the water column.

E.1 Sloping bed test case

E.1.1 Model description

To test how properly the different bed slope effects are working, a fictitious case is considered which focuses on the bed slope effects. The morphology module is turned off, this means that the sediment transport rates are still calculated but the bed level is not updated.

Table E.2: Adjustments to the default parameter settings of Table D.1

Parameter	Value	Unit	Meaning
morphology	0	–	Turn off the morphology module. The bed is not updated but sediment transport rates are still calculated.

The XBeach source code is modified to enforce a velocity vector under a certain (user defined) angle with respect to the x-axis and a constant (user defined) depth of $0.1\ m$ over the whole grid. As a result, the sediment transport rates are not varying spatially. Interest is drawn to the sediment transport rates and not to the sediment transport concentrations. The majority of the bed slope effects are only visible in the transport rates.

Since the bed level is not updated, dilatancy, θ_{max} and the conservatism of the Exner equation are of no importance for this case. Further, the focus is on bed-load transport, the fall velocity reduction is hence also not considered.

The XBeach source code is modified for this test case such that the magnitude of the velocity is equal to the time. As a result, the value of the time is proportional to the flow velocity:

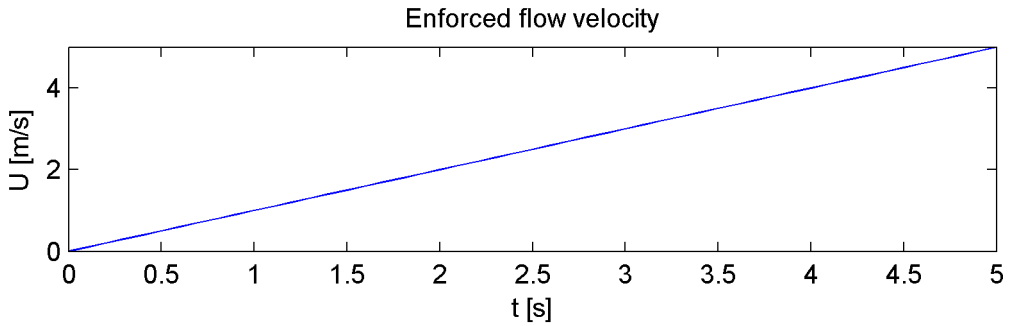

Figure E.1: Flow velocity varies linearly with time. As a result, the relation between the sediment transport rates and the flow velocity is easily made.

Seven cases are considered. First, a test is performed without a bed slope, the sediment transport rates should be equal for all the model runs. Thereafter, a sloping bed is introduced with an angle of $30°$, the direction of the flow and the direction of the bed is varied over six cases as visualised in Figure E.2.

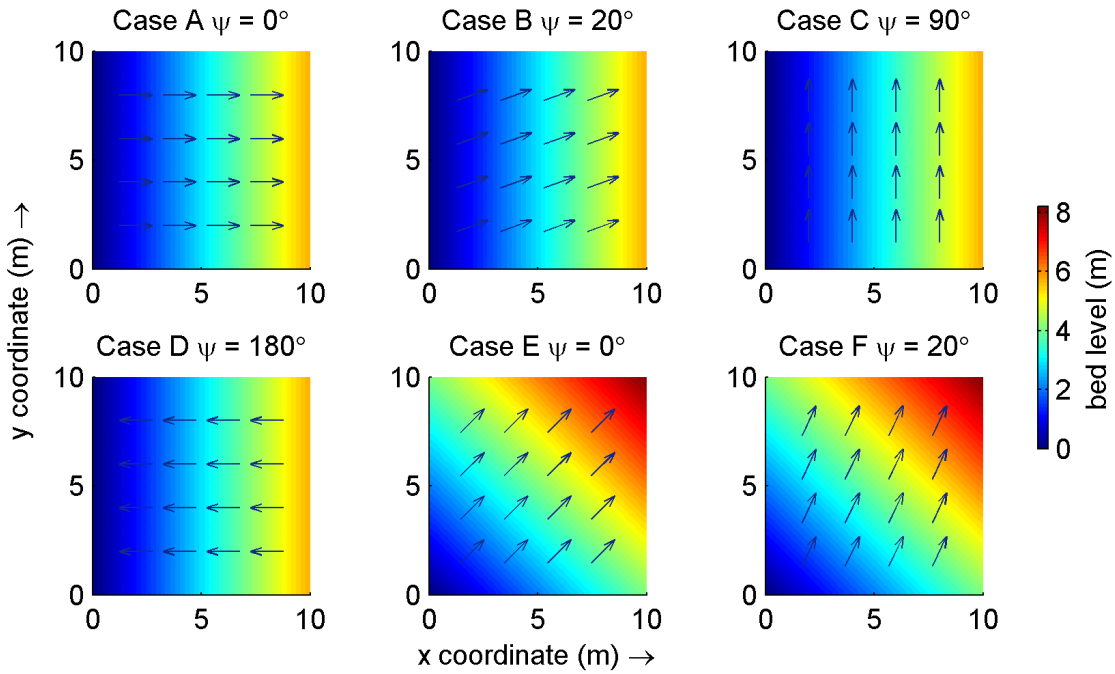

Figure E.2: Considered cases, all with a bed slope of $30°$.

E.1.2 Results

Check of the calculated sediment transport rates

To validate the calculated bed-load transport rates, the transport rates are calculated manually for the used parameter configuration (equations as presented in Appendix C):

$$\Delta = \frac{\rho_s - \rho_w}{\rho_w} = \frac{2650 - 1025}{1025} = 1.5854 \tag{E.1}$$

$$U_{cr} = U_{crc} = 0.19 D_{50}^{0.1} \log 10 \left(\frac{4h}{D_{90}} \right) = 0.19 \cdot 0.0002^{0.1} \log 10 \left(\frac{4 \cdot 0.1}{0.0003} \right) = 0.2533 m/s \tag{E.2}$$

$$A_{sb} = 0.015 h \frac{(D_{50}/h)^{1.2}}{(\Delta g D_{50})^{0.75}} = 0.015 \cdot 0.1 \frac{(0.0002/0.1)^{1.2}}{(1.5854 \cdot 9.81 \cdot 0.0002)^{0.75}} = 6.5720 \cdot 10^{-5} \tag{E.3}$$

$$C_{eq,b} = \frac{A_{sb}}{h} \left(\sqrt{v_{mg}^2 + 0.64 u_{rms}^2} - U_{cr} \right)^{1.5} = \frac{6.5720 \cdot 10^{-5}}{0.1} \left(\sqrt{5^2 + 0} - 0.2533 \right)^{1.5} = 6.7965 \cdot 10^{-3} \tag{E.4}$$

Since the bed-load transport is assumed to respond instantaneously to a variation in forcing, the actual bed-load concentration equals this equilibrium concentration. Now, the transport rate is easily evaluated as:

$$S_{bed} = U C_b h = 5 \cdot 6.7965 \cdot 10^{-3} \cdot 0.1 = 3.40 \cdot 10^{-3} m^2/s \tag{E.5}$$

The exact same rate is observed in the model runs without a slope effect, see Table E.3 which is presented later on.

Decomposition of the transport rates over x- and y-direction

Figure E.3 shows the sediment transport rates divided over the grid directions. No bed slope effect is considered in this figure. Since the magnitude of the flow velocity is equal in all cases, the magnitude of the transport rates should also correspond. The figure shows that this is indeed the case. Only the transport rates decomposed in x- and y-direction vary as expected.

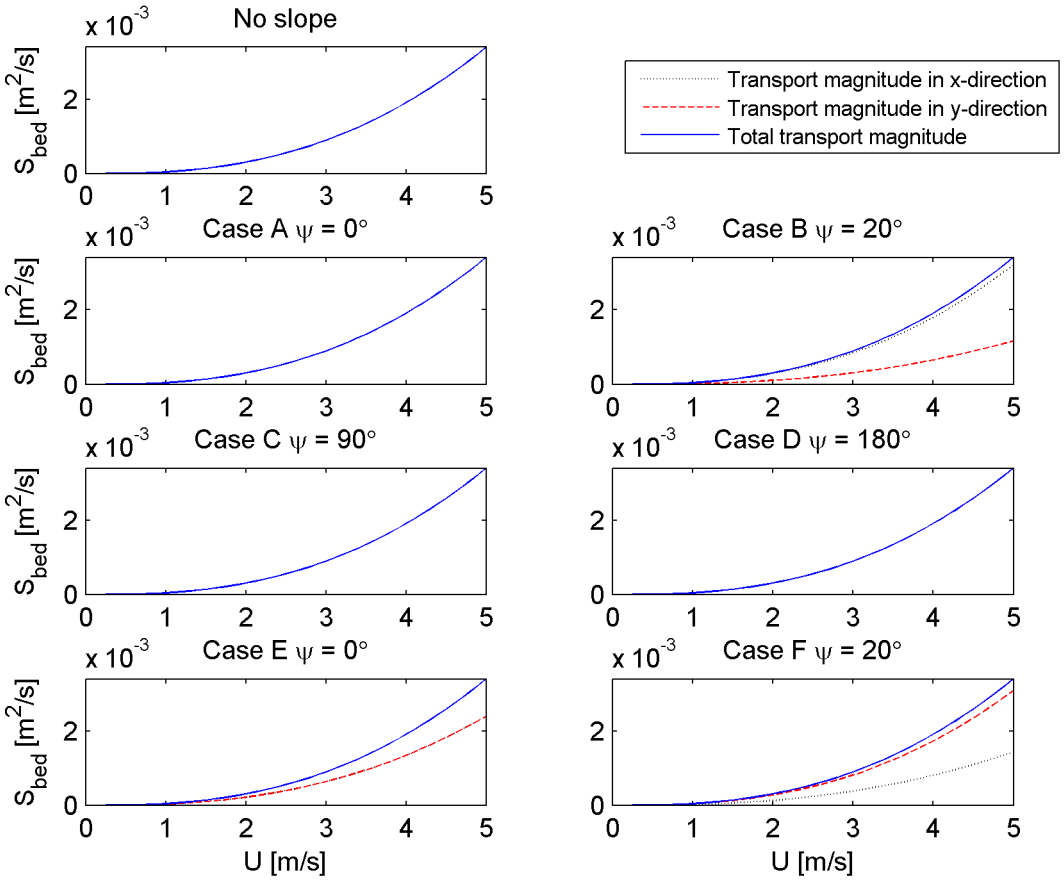

Figure E.3: Bed-load transport rates as a function of the flow velocity for the different cases. These rates are without a bed slope effect.

Comparison between the different bed slope effects

Tables E.3 and E.4 present the absolute respectively the relative bed-load transport rates for the different cases. As visible, the transport reduces if the flow acts perpendicular to the bed slope and increases if the flow is in down-slope direction and a bed slope effect is applied.

As expected, the transport rates are equal for all cases if no bed slope effect is modelled. Further, the transport rates of Case E should equal the rates of Case A and the result of Case F should equal the result of Case B since only a rotation of the grid is applied. This is indeed true, so there seems to be no numerical grid-related errors involved.

An important observation is that the Soulsby slope effect results in substantial different results compared to the XBeach default model settings. This confirms that the presently implemented bed slope effect is not in line with the engineering formula of Soulsby (1997), as suggested in Section 2.7.2. Another

observation is that the XBeach default settings result in a change of direction of the transport, what can be learned from Case C. In this case is the flow direction perpendicular to the on-slope directed vector, still a change of transport direction is modelled. The presently default XBeach model contains hence no pure magnitude modification of the transport rates.

Finally, the improved model contains both a modification of the transport magnitude as the direction. This is in line with the implemented theory. It seems that the change of direction of the transport is of less importance compared to the change of magnitude. However, the change of direction is clearly visible in Case C for which the flow direction is perpendicular to the on-slope directed vector.

Table E.3: Absolute bed-load transport rates of the sloping bed test case. Case names as introduced in Figure E.2.

Model run	No slope	Case A	Case B	Case C	Case D	Case E	Case F
XBeach default	3.40e-03	2.59e-04	1.16e-03	4.63e-03	6.54e-03	2.59e-04	1.16e-03
Soulsby slope effect	3.40e-03	2.59e-04	4.48e-04	3.40e-03	6.54e-03	2.59e-04	4.48e-04
Improved model	3.40e-03	3.03e-03	3.05e-03	3.67e-03	3.99e-03	3.03e-03	3.05e-03
No bed slope effect	3.40e-03	3.40e-03	3.40e-03	3.40e-03	3.40e-03	3.40e-03	3.40e-03
With 20° internal friction	3.40e-03	3.01e-03	3.04e-03	3.67e-03	3.99e-03	3.01e-03	3.04e-03
Double direction change	3.40e-03	3.03e-03	3.05e-03	3.67e-03	3.99e-03	3.03e-03	3.05e-03

Table E.4: Bed-load transport rates of the sloping bed test case relative to the no-slope transport rates. Case names as introduced in Figure E.2.

Model run	No slope	Case A	Case B	Case C	Case D	Case E	Case F
XBeach default	1.00	0.08	0.34	1.36	1.92	0.08	0.34
Soulsby slope effect	1.00	0.08	0.13	1.00	1.92	0.08	0.13
Improved model	1.00	0.89	0.90	1.08	1.17	0.89	0.90
No bed slope effect	1.00	1.00	1.00	1.00	1.00	1.00	1.00
With 20° internal friction	1.00	0.89	0.89	1.08	1.17	0.89	0.89
Double direction change	1.00	0.89	0.90	1.08	1.17	0.89	0.90

E.1.3 Conclusions

Hence, it can be concluded that the default XBeach slope effect results in substantial different results compared to the Soulsby engineering formula which is a pure magnitude modification. Further, there are no numerical grid-related errors present and the improved model seems to behave as one could expect.

E.2 Eroding bed test case

E.2.1 Model description

To test the effect of dilatancy on the sediment transport rates, a conceptual model test is created. In this test, the bed level is enforced to rise or fall with a certain vertical velocity. To achieve this enforced bed rising/falling velocity, the morphology is turned off and the sediment transport rates are still calculated, similar to the sloping bed test case. By modifying the XBeach source code, the rising velocity of the bed is set to a fixed user defined value.

Table E.5: Adjustments to the default parameter settings of Table D.1

Parameter	Value	Unit	Meaning
morphology	0	–	Turn off the morphology module. The bed is not updated but sediment transport rates are still calculated.

The velocity is enforced to rise with time, as visualised in Figure E.1, to obtain a clear relation between the sediment transport rates and the velocity.

E.2.2 Results

In the Van Rhee (2010) method, it is expected to see an influence of dilatancy only if the bed is eroding, so no modification when there is accretion. Further, a larger fall velocity of the bottom should result in a smaller sediment transport rate since the hindering of erosion is more substantial:

$$U_{cr}^{D} = U_{cr}\sqrt{1 + \frac{v_e}{k_l}\frac{n_l - n_0}{1 - n_l}\frac{A}{\Delta}} \tag{E.6}$$

Figure E.4 present the sediment transport rates as a function of the flow velocity for the improved model, as extracted from the XBeach model runs. The same parameters are used as in the sloping bed test case. Hence, for a zero bed rise velocity are the transport rates exactly the same as in the sloping bed test case.

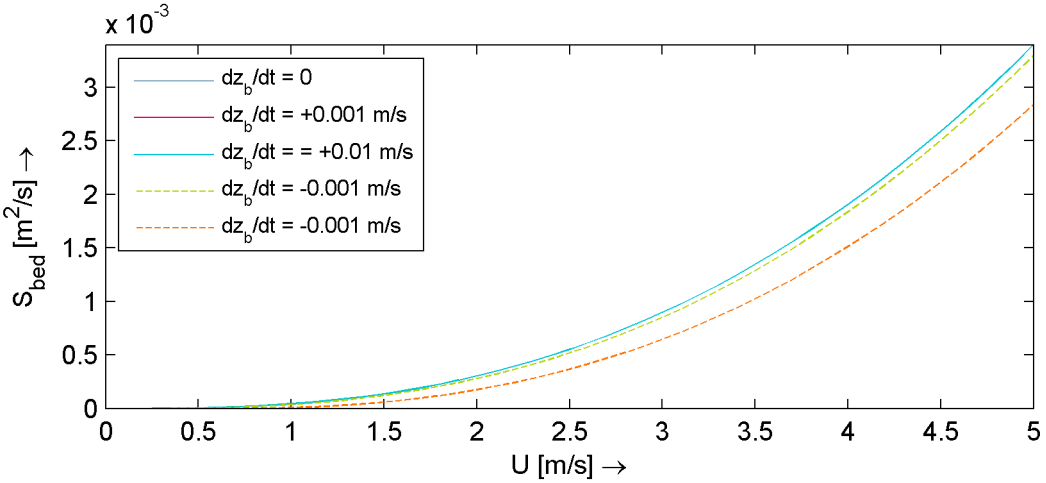

Figure E.4: Bed-load transport rates as a function of the flow velocity for a variety of bed level rates.

Indeed, there is no influence by dilatancy on the sediment transport rates if no net erosion takes place. Further, it is confirmed that the magnitude of the modification of the transport rates by dilatancy increases with a larger erosion rate.

Influence of the other parameters

The results presented in this appendix are just for one parameter set (the default one of XBeach). As mentioned in Tables D.1 and D.2 is the $D50$ by default equal to $200\ \mu m$ and the $D15$ equal to $150\ \mu m$. In the method of Van Rhee, the $D15$ is an important parameter in the determination of the permeability:

$$k = \frac{g}{160\nu} D_{15}^2 \frac{n_0^3}{(1-n_0^2)} \tag{E.7}$$

If the $D15$ is halved to $75\ \mu$, the permeability is reduced to one-quarter of the original permeability. Based on Equation E.6, one can see that halving the sediment grains size has hence the same effect as a four times larger erosion velocity of the bed. In a similar fashion, the influence of the other parameters can be compared to the influence of modification of the erosion velocity as presented in Figure E.4. Since this comparison is possible, the other parameters are not varied in this test case since it is already proven that the dilatancy implementation has the correct tendency.

E.2.3 Conclusions

To conclude, the Van Rhee method is approved to be implemented correctly. The correct tendency of the method is observed. Accretion of the bed does not result in dilatancy and the larger the erosion velocity the larger the hindering of erosion. Dilatancy results in a horizontal translation of the sediment transport rates if it is visualised as a function of the flow velocity.

E.3 Accretion of a bed

E.3.1 Model description

To observe the behaviour of the time-scale in the advection-diffusion equation and to test the performance of the mass-conservative Exner equation, an accretion test case is made. The flow velocity is enforced as zero over the whole model run time and an initial concentration of $0.10\ m^3/m^3$ is enforced over the full initial $10\ m$ depth. By settling, the concentration in the water column will decrease to zero and the bed level should rise.

E.3.2 Results

Figure E.5 presents the evolution of the bed level over time. Indeed, the default XBeach model is not fully conservative; all sediment mass is lost. The improved model does converge smoothly to the exact final solution and is hence mass-conservative.

In XBeach, there is also another option available to make the Exner equation mass conservative: fluxes in the advection-diffusion equation are accounted for in the bed level update. This option is used by setting the *sourcesink* parameter to 1. The method presented in this thesis is considered by setting the *sourcesink* to 2. Both methods give exactly the same evolution of the bed level, differences occur if a morphological acceleration factor is used, see the next section.

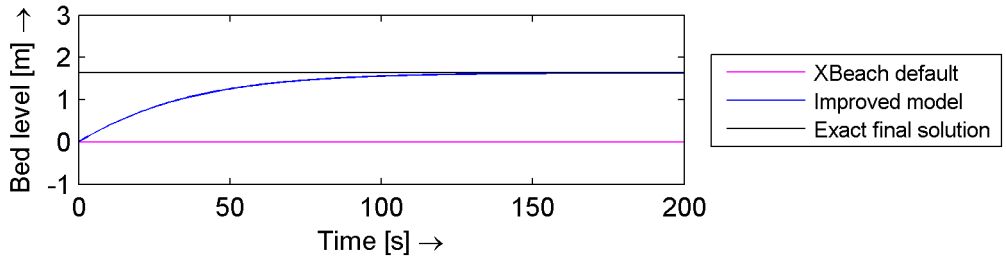

Figure E.5: Bed level over time for the volume conservative Exner equation. The flow velocity is fixed to zero while there is sediment mass in the water column.

Figure E.6 shows the evolution of the sediment concentration in the water column over time. As expected, it decreases smoothly with time. Note that the evolution of the bed level over time is not a direct indicator for the evolution of the depth averaged concentration over time, this because also the water depth is varying.

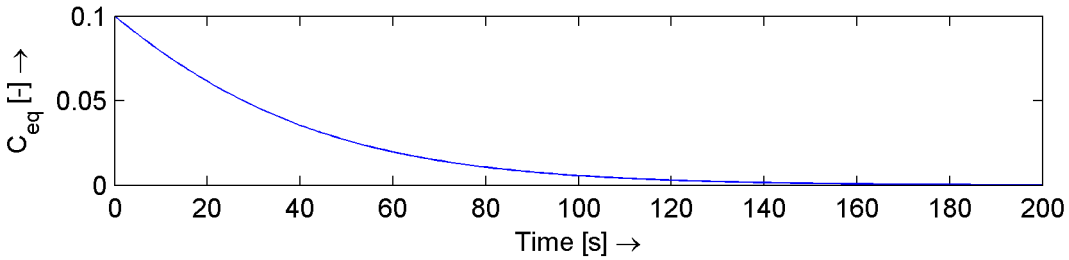

Figure E.6: Depth averaged sediment concentration over time for the volume conservative Exner equation. The flow velocity is fixed to zero while there is sediment mass in the water column.

E.3.3 Morphological acceleration factor

As mentioned, the current XBeach method to make the Exner equation mass-conservative (*sourcesink* $= 1$) does lead to different results compared to the method of this thesis (*sourcesink* $= 2$) if a morphological

acceleration factor is considered. This is visible in Figure E.7. Although even the method presented in this thesis is not perfectly, the time-scale is slightly adjusted by the morphological factor, it does lead to the exact final solution. This is certainly not the case for the present mass-conservative Exner equation approach in XBeach, which leads to substantial overestimations of the bed level change.

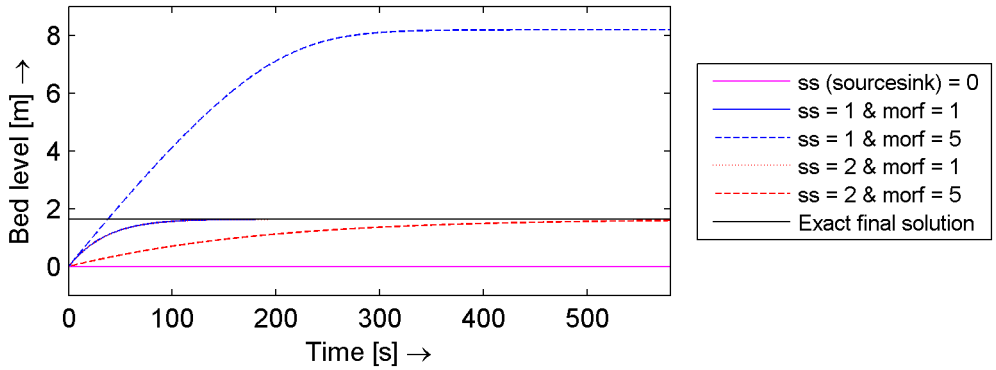

Figure E.7: The same situation as in Figure E.5, now with an alternative method to obtain mass-conservatism and with a morphological acceleration factor.

E.3.4 Conclusions

The presented method of making the Exner equation mass-conservative does indeed not result in mass-losses. Once a morphological acceleration factor is introduced, the results are less accurate but still mass-conservative. This is not the case for the present mass-conservative Exner equation approach in XBeach.

Appendix F

Side effects of the improvements

This appendix presents cases to test whether certain improvements made in the XBeach model source code have undesired side effects. Table F.1 gives a short description of the considered model cases. The focus of this analysis is on the swash and collision regime, which shouldn't be affected substantially by the implementations made with this thesis.

Table F.1: Overview of the modelled experiments to investigate the presence of side effects.

Appendix	Page	Name	Dimensions	Waves	Description
F.1	F.2	Delta Flume 2006	1D	Yes	Erosion of dunes. Data are available for various boundary conditions and profiles.
F.2	F.6	Delta Flume H298	1D	Yes	Due to the presence of a hard structure, an erosion hole is generated. Various heights of the hard structure are examined.

F.1 Delta Flume 2006

F.1.1 Model description

The grid file and boundary conditions used for this model are based on the model published in the XBeach skillbed (Deltares, 2014a). The Delta Flume 2006 experiments were performed for a variety of wave periods. At certain moments in time, the bed level profile was measured. Figure F.1 shows the initial profiles of the four considered experiments. Only experiment T04 has some substantial differences; two dune rows are present in the initial profile.

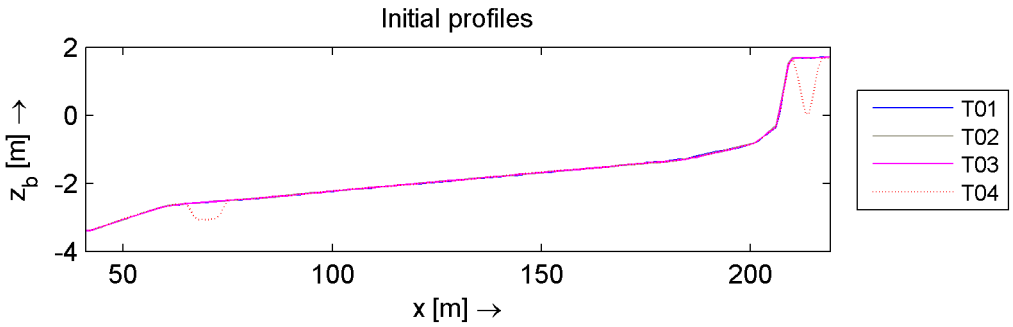

Figure F.1: Initial profiles. As visible, the bathymetries of the model runs are comparable. The only noticeable differences are visible in model run T04 which consists of two separate dunes.

Table F.2 presents the wave characteristics, in all runs is a Pierson-Moskowitz spectrum enforced. Further, Table F.3 mentions the modifications to the default XBeach parameters.

Table F.2: Overview of the characteristics of the experiments. Last three variables are the wave dissipation parameters.

Experiment	H_{rms} $[m]$	T_p $[s]$	$T_{m-1.0}$ $[s]$	α	γ	n
T01	1.02	4.90	4.45	1.0	0.50	10
T02	1.07	6.12	5.56	1.0	0.48	10
T03	1.10	7.35	6.68	1.0	0.45	10
T04	1.10	7.35	6.68	1.0	0.45	10

Table F.3: Adjustments to the default parameter settings of Table D.1

Parameter	Value	Unit	Meaning
C	65	$m^{0.5}/s^1$	Chézy coefficient.
rho	1000	kg/m^3	Density of water.
CFL	0.9	–	Maximum Courant number on which the actual time step of the hydrodynamic simulation is based.
Tsmin	1	s	Minimum adaptation time scale in advection diffusion equation for sediment.
dzmax	0.003	μm	Maximum bedlevel change due to avalanching.
wetslp	0.1	–	Critical avalanching slope under water (dz/dx and dz/dy).

F.1.2 Results

Figures F.2 to F.5 show both the modelled as the measured bed level at certain moments in time. By the waves, the dunes erode and the dune foot propagates in onshore direction. In general, the tendency of the model predictions is in good accordance to the measurement data, although some overprediction of the erosion rates is observed. There are some strong differences between the model predictions observed for the front dune of experiment T04 regarding the θ_{max} parameter. In general, the improved model has the same tendency and order of erosion as the XBeach default. So no side effects are mentioned visually.

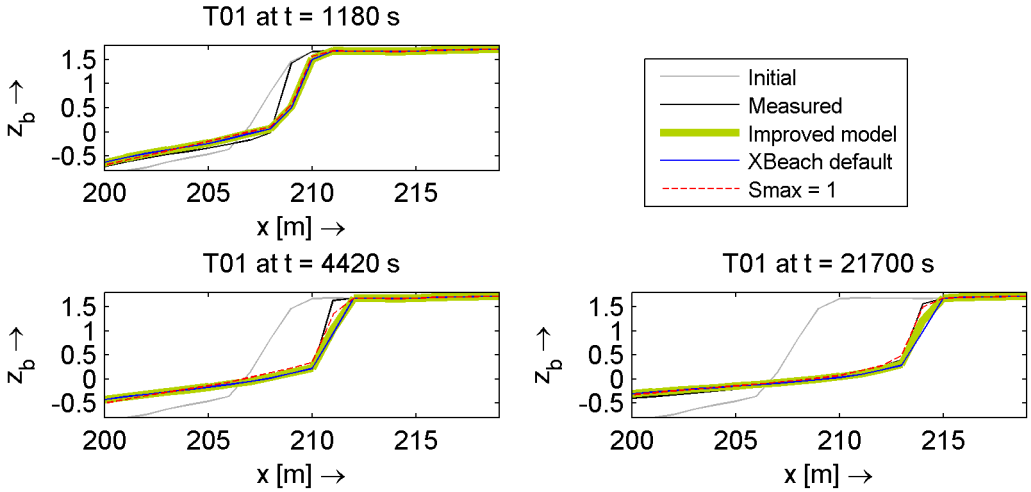

Figure F.2: Model results for T01.

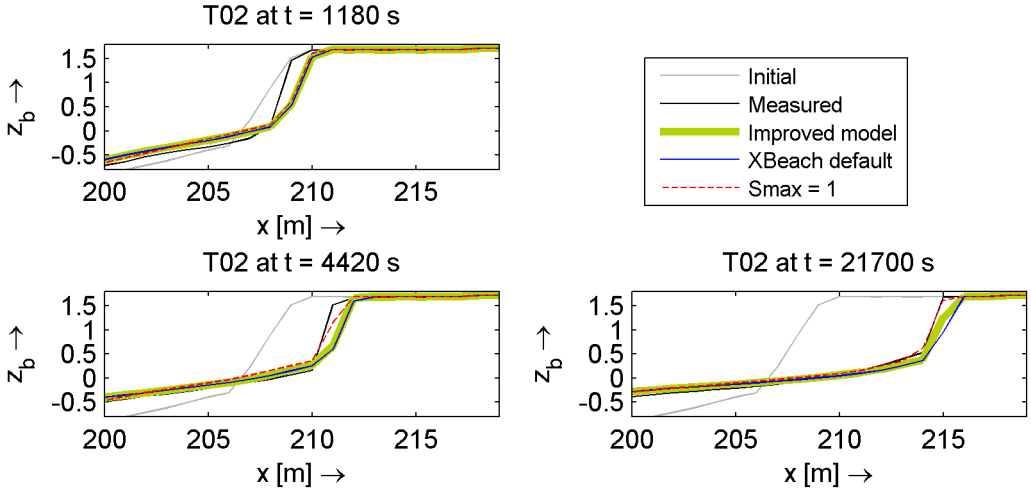

Figure F.3: Model results for T02.

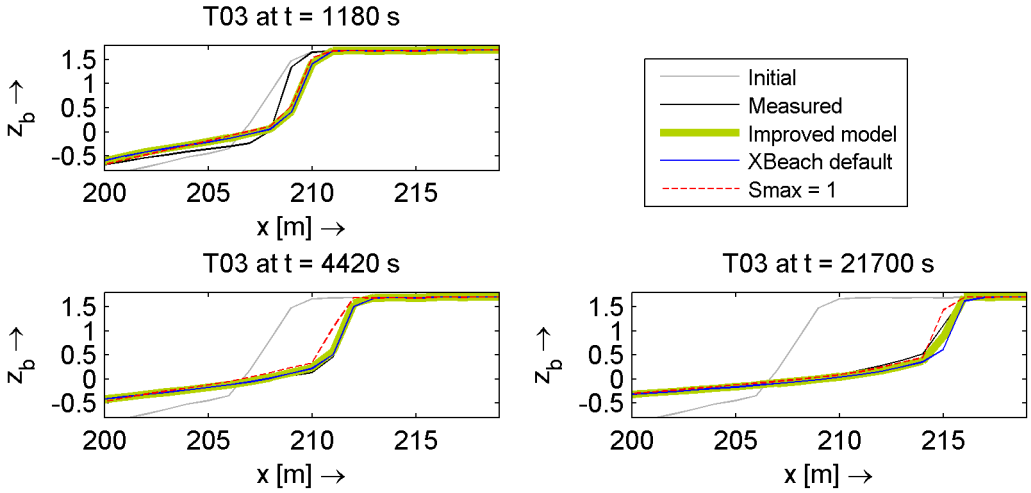

Figure F.4: Model results for T03.

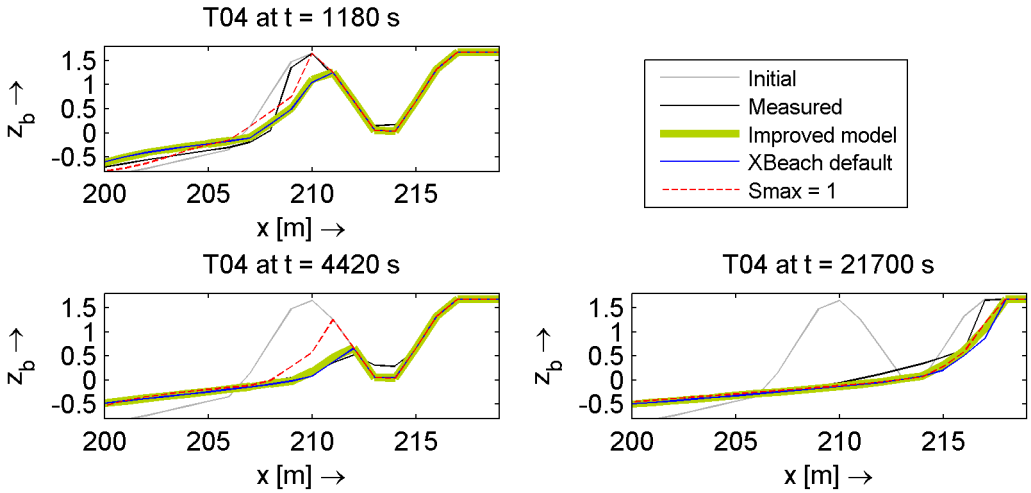

Figure F.5: Model results for T04.

F.1.3 Sensitivity

F.4 presents the Brier Skill Scores for all the model runs regarding the improved model. The only substantial differences between the model runs are related to the θ_{max} parameter. For some of the experiments this parameter results in an improvement and in other runs this parameter results in a decrease of skill. This dataset confirms what was found in the visual analysis; the improved model does not change the model results substantially. The data shows that also the modifications to the improved model do not introduce substantial side effects.

Note that although the Brier Skill Scores are high for the base run, not all features are modelled perfectly. For example, in test T04 is the erosion of the first dune modelled too fast, even though the final profile is modelled fine.

Table F.4: Brier Skill Score calculated for the domain from x = 200 m till x = 219 m at two moments in time. Improvements compared to the base run of more than 0.05 are marked green, decreases in score of more than 0.05 are marked red.

	T01		T02		T03		T04	
Model run	4420 s	21700 s	4420 s	21700 s	4420 s	21700 s	4420 s	21700 s
XBeach default	0.91	0.97	0.85	0.95	1.00	0.98	0.98	0.91
Smax = 1	**0.96**	1.00	**0.95**	0.99	**0.93**	0.99	**0.82**	0.95
Soulsby slope effect	0.91	0.97	0.84	0.95	1.00	0.97	0.98	0.88
Improved model	0.93	0.99	0.86	0.98	1.00	0.99	0.98	0.94
No dilatancy effect	0.93	0.98	0.86	0.98	1.00	0.99	0.98	0.93
With A = 1.75 (dilatancy)	0.94	0.99	0.87	0.98	1.00	0.99	0.97	**0.96**
No bed slope effect	0.94	0.99	0.87	0.99	1.00	0.99	0.97	**0.97**
With 20° internal friction	0.93	0.98	0.86	0.98	1.00	0.99	0.98	0.92
No fall velocity reduction	0.93	0.99	0.86	0.98	1.00	0.99	0.98	0.94
With conservative Exner	0.93	0.99	0.87	0.98	1.00	0.99	0.98	0.94

F.1.4 Conclusions

Limiting the Shields parameter by θ_{max} affects some of the model runs positively and some negatively, what could be classified as a side effect of the θ_{max} parameter. Based on the analysis of this appendix, it seems that no substantial side effects are introduced with the improvements introduced in this thesis.

F.2 Delta Flume H298

F.2.1 Model description

The grid file and boundary conditions used for this model are based on the model published in the XBeach skillbed (Deltares, 2014a). The initial profiles of the model runs are based on the measured initial profiles in the experiment which are for the three model runs almost identical, see Figure F.6.

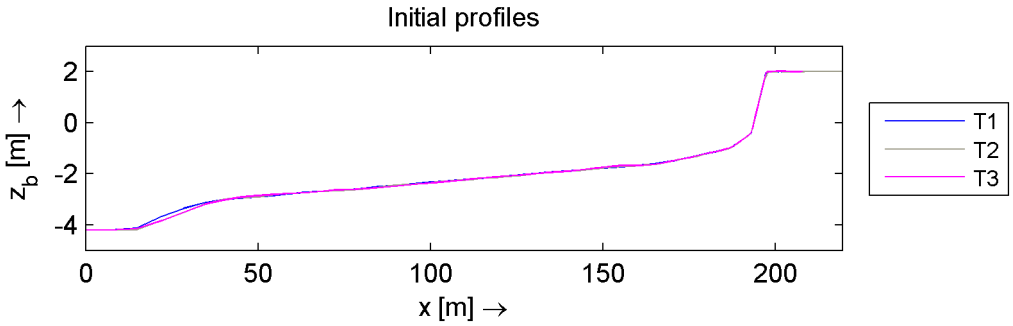

Figure F.6: Initial profiles. As visible, the bathymetries of the model runs are comparable.

In these experiments are hard structures involved which reach from the dune toe to a certain height on the dune slope. The three experiments differ in the height to which these structures reach, the structures are visualised in Figure F.7.

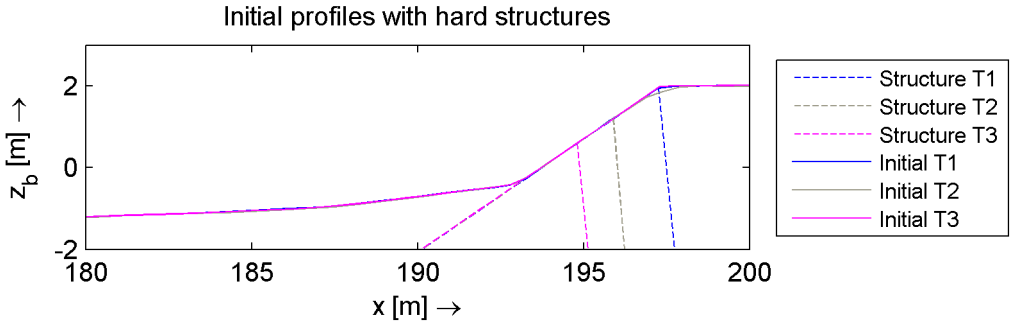

Figure F.7: The model runs differ in the height of the hard structures.

A Pierson-Moskowitz spectrum is enforced. Table F.5 presents the adjustments made to the default XBeach parameter settings.

Table F.5: Adjustments to the default parameter settings of Table D.1

Parameter	Value	Unit	Meaning
depthscale	0.833333	–	Depth scale of (lab)test simulated.
struct	1	–	Hard structure module is turned on.
D_{50}	225	μm	Median sediment grain size.
D_{90}	338	μm	90% percentile sediment grain size.
H_{m0}	1.5	m	Significant wave height.
fp	0.185	$1/s$	Peak frequency of the wave spectrum.

F.2.2 Results

Figures F.8 to F.10 show the final profiles modelled by XBeach together with the measurement data. By the presence of the hard structures, an erosion hole is generated. The depth of the erosion hole

depends on the height of the structure. Above a low structure, there will be still some substantial erosion be present. The eroded sand is transported shoreward and can be trapped in the generated erosion hole. If a large structure is applied, there is less erosion above the structure and the erosion hole before the structure will therefore grow more substantially.

This tendency is visual in both the measurement data as in all the model runs. The predictions by the improved model are almost exactly the same as the XBeach default. However, the θ_{max} limitation results definitely in a way too small erosion hole, which is certainly an undesired side effect.

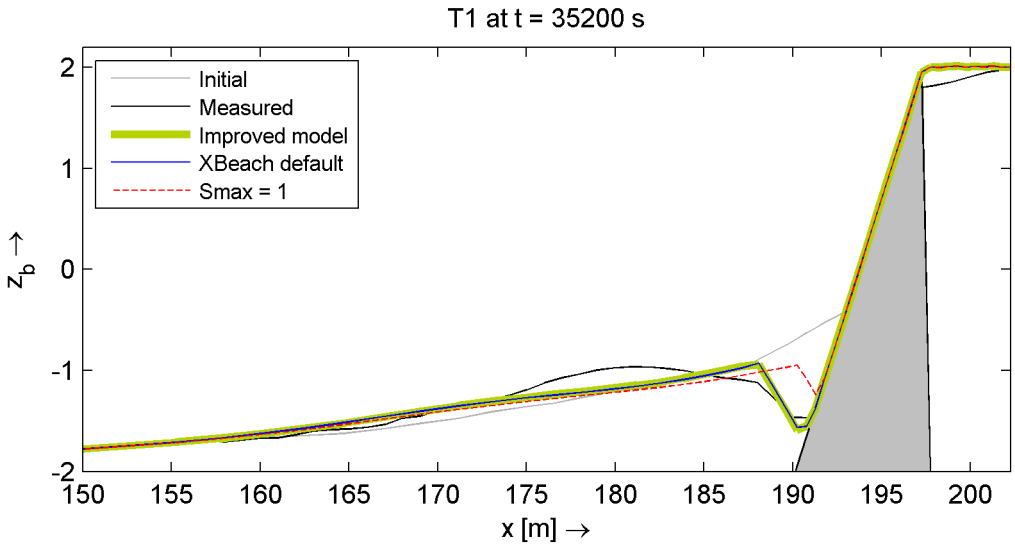

Figure F.8: Model results for T1.

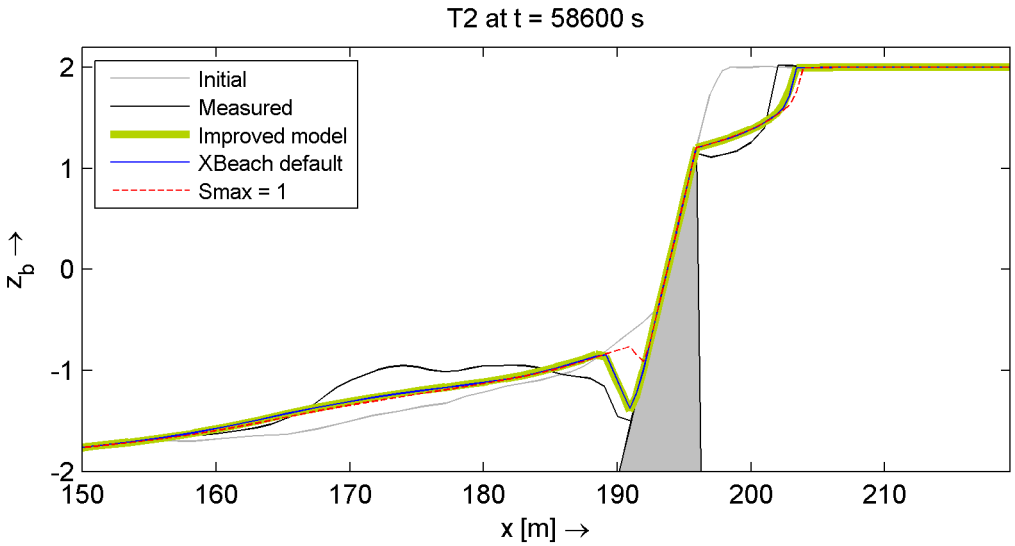

Figure F.9: Model results for T2.

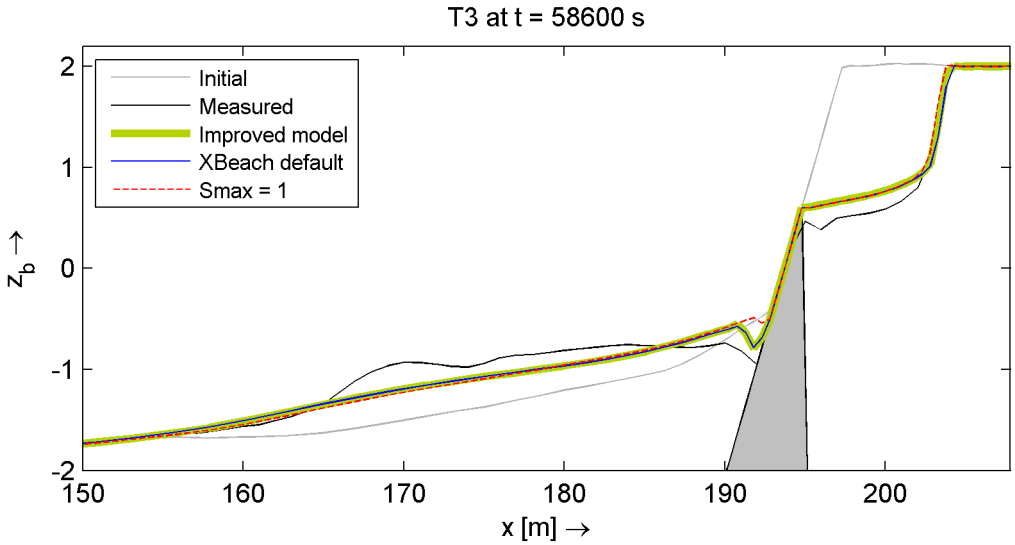

Figure F.10: Model results for T3.

F.2.3 Sensitivity

The Brier Skill Scores and the bias of the erosion hole depth are given in Table F.6. The data shows that the performance of the improved model and the variations to this improved model is very similar to the XBeach default. The visual observation that the θ_{max} limiter has a poor predictive skill is confirmed with the data.

Table F.6: Brier Skill Score and erosion hole depth calculated from x = 150 m till the right side of the domain. Improvements in BSS compared to the base run of more than 0.05 are marked green, decreases in score of more than 0.05 are marked red.

	T1 (35200s)		T2 (58600s)		T3 (58600s)	
Model run	BSS	Erosion hole [m]	BSS	Erosion hole [m]	BSS	Erosion hole [m]
Measurements		0.87		0.88		0.45
XBeach default	0.82	0.93	0.80	0.76	0.95	0.26
Smax = 1	**0.60**	0.66	**0.64**	0.39	0.93	0.08
Soulsby slope effect	0.80	0.92	0.77	0.66	0.95	0.24
Improved model	0.83	0.93	0.81	0.77	0.94	0.27
No dilatancy effect	0.83	0.93	0.81	0.78	0.95	0.27
With A = 1.75 (dilatancy)	0.83	0.93	0.80	0.76	0.94	0.26
No bed slope effect	0.83	0.93	0.80	0.76	0.94	0.25
With 20° internal friction	0.84	0.93	0.81	0.79	0.95	0.29
No fall velocity reduction	0.83	0.93	0.81	0.77	0.95	0.27
With conservative Exner	0.83	0.93	0.80	0.74	0.94	0.25

F.2.4 Conclusions

The improved model has very similar model results compared to the XBeach default settings. This conclusion is also valid for the modifications made to the improvement. There are hence no side effects observed in this case. This conclusion is not valid for the θ_{max} limiter, which results in substantial less erosion.

Appendix G

Overwash and breaching cases

In Chapter 6, the improved model is assessed. This appendix provides the model runs of the improved model related to overwash and breaching conditions. These cases are already introduced in Chapter 3, so only a short introduction to each case will be given.

Table G.1: Overview of the modelled experiments to investigate the performance under overwash and breaching conditions.

Appendix	Page	Name	Dimensions	Waves	Description
G.1	G.2	Scheldt Flume	1D	Yes & No	A one-dimensional flume experiment containing a down-scaled dike profile, a water level gradient causes erosion. A variety of cases is considered of which one includes waves. Cross-sections of the dike profile were made in the experiment frequently.
G.2	G.8	Zwin	2D	No	A full-scale dam breach experiment is modelled in XBeach. Measurement data of the breach width is available and is used to compare the performances of the different model runs.
G.3	G.14	Santa Rosa	2D	Yes	The hindcast model by McCall (2008) is considered. It models the erosion of Santa Rosa Island by hurricane Ivan.

G.1 Scheldt Flume

G.1.1 Model description

As introduced in Section 3.2, the Scheldt Flume experiment consists of a one-dimensional dike breach in a flume. In the comparison of the improved model to this experiment, not only the dike profile without waves is considered but also a variety of other model runs, see Table G.2. The D_{15} value is required in the dilatancy method of Van Rhee (2010). Since this value is not provided in the experimental data, a linear interpolation is made between the measured D_{10} and the D_{50}.

Table G.2: Overview of the characteristics of the experiments. Last three variables are the wave dissipation parameters.

Experiment	Profile	Waves	T_p [s]	H_{m0}	Porosity	$D15$ [μm]	$D50$ [μm]	$D90$ [μm]
T5	Dike	No			0.391	162	220	297
T3	Dune	No			0.426	71	104	166
T4	Dune	Yes	2.3	0.3	0.436	76	106	149
T6	Dune	No			0.375	161	218	295

Table G.3: Adjustments to the default parameter settings of Table D.1

Parameter	Value	Unit	Meaning
morstart	180	s	Start time of the morphology computation.
tstart	180	s	Start time of the output.
swave	$0/1$	–	Short waves module is turned off if no waves are included in the run.
instat	$0/4$	–	If no waves are included, a value of 0 is taken. Otherwise a value of 4 is used in combination with a value for *gammajsp* of 1.0 resulting in a Pierson-Moskowitz-spectrum.

The initial profiles used in the experiments are presented in Figure G.1. As visible, the profiles only differ in the front slope of the profiles. The top of the profiles and the back sides are exactly the same.

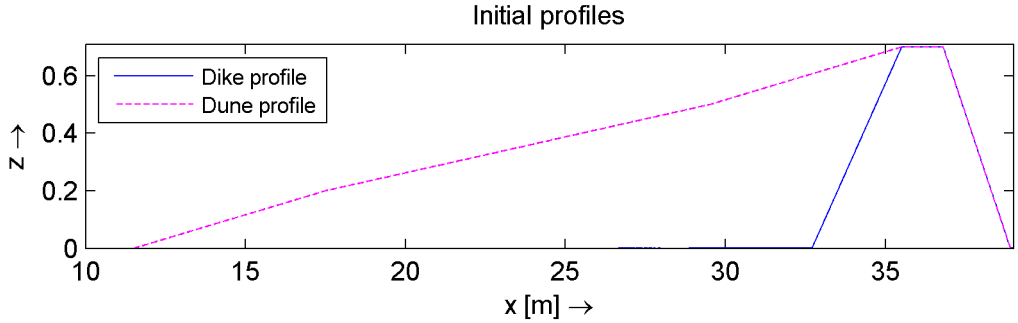

Figure G.1: Initial profiles.

Calculation of the Brier Skill Score

To compare the results of the different improvements in the improved model, the Brier Skill Score (BSS) is applied. The goal of the BSS is to obtain a reasonable representation of an expert judgement. It is important to make a clear definition of the calculation method to prevent undesired effects. In the end, it is not possible to put the judgement of all modelled features into one single number, but it is feasible to focus on the most important features. In this stage, mainly the propagation velocity of the erosion front and the shape/steepness of the eroded dune are considered as important.

If one would simply take the BSS of the bed level elevations, these features are not represented well enough in the score. For example, the first plot of Figure G.2 shows that the XBeach default settings and the improved model do perform approximately equally bad if a vertical BSS is taken. The location and the shape of the eroded dune are not taken into account in this method if located outside of the measurement data range.

A way more representative method of calculating the BSS is by measuring the deviations parallel to the front of the dike/dune. As visible in the two other plots of Figure G.2, the different runs are now rated more in line with the actual performances regarding the propagation velocity and the shape of the erosion front. To neglect the influence of the antidunes on the BSS, the measurement data are restricted such that these do not cover an antidune region in any of the runs, see the right top plot of Figure G.2. The measurement data range for the different parameter settings is taken the same such that a fair comparison can be made.

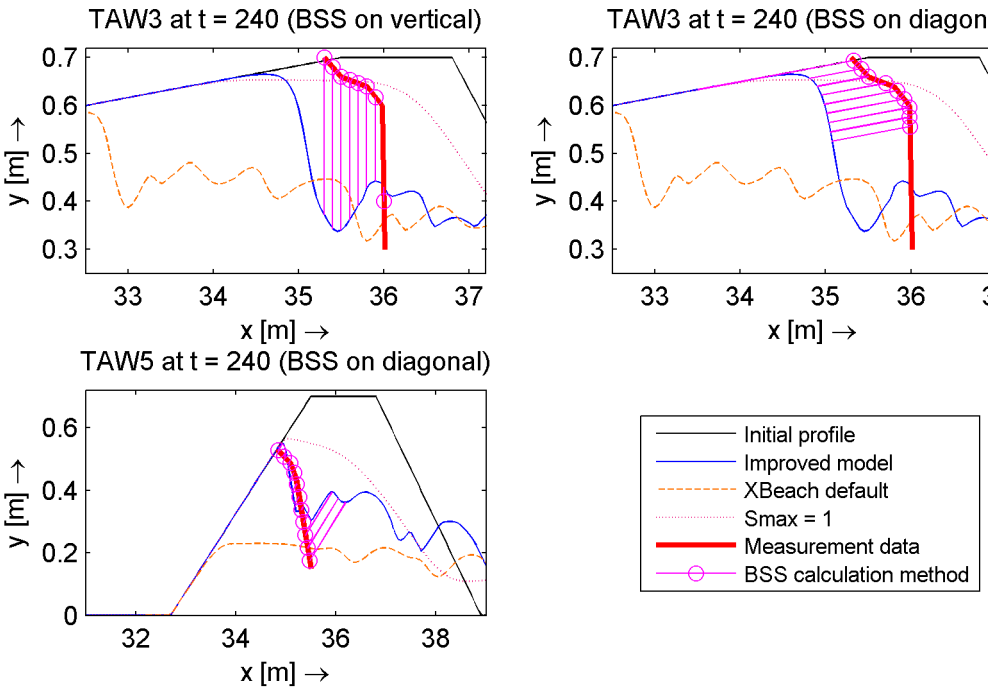

Figure G.2: Calculation methods for the Brier Skill Score.

G.1.2 Results

Evolution of the profiles over time

Figure G.3 shows the cross section of the different model runs at two moments in time. Roughly, the $120\ s$ results are at the end of phase two of the breaching phase, the $320\ s$ results are during the third breaching phase.

As visible, the modelled profiles match almost perfectly for the T5 and T6 experiments at the end of the second phase, just before the crest lowers. Not only the location of the back slope, but also the steepness and the height of the slope fits fine. During the third breaching phase, the differences with respect to the experiment data increase, but the results are substantially better with respect to the XBeach default.

For the T3 and T4 experiments, both with finer grains and the second one with waves, larger differences with respect to the experimental data are found. Still, the improved model shows substantial hindering of erosion causing better results than the XBeach default.

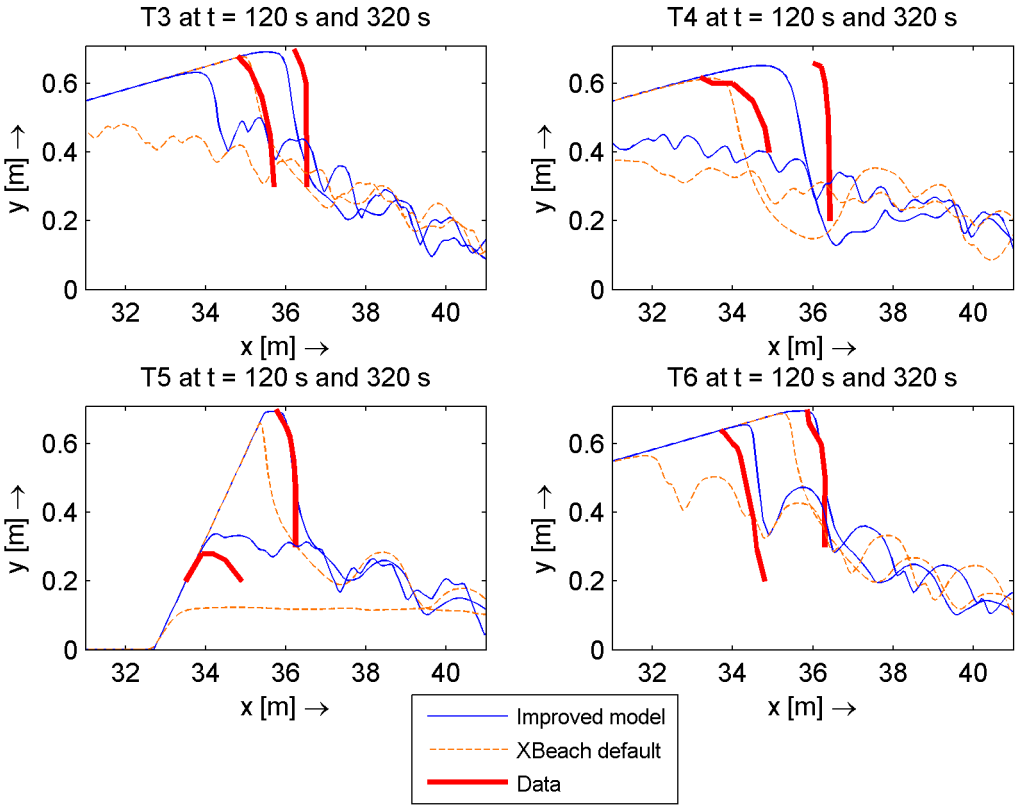

Figure G.3: Cross sections of the improved model and the XBeach default at several moments in time.

Validation of the modelled water levels

Figure G.4 compares the modelled water levels to those observed during the experiment. As visible, the upstream water levels are in line with the measurements. However, the downstream water levels show some substantial differences. These differences can have an influence on the modelled profiles. For now, these differences are thought to be acceptable since the tendency of the improvements is important, not the exact prediction.

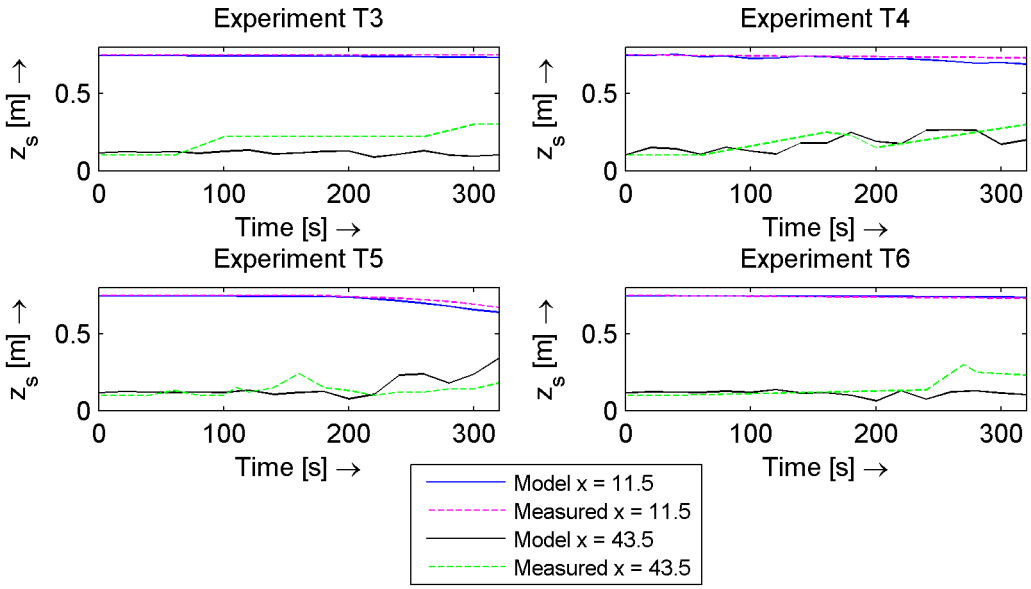

Figure G.4: Comparison of the water levels with experimental data.

G.1.3 Sensitivity

Tables G.4-G.7 present the BSS and bias calculated with the diagonal method, as visualised in Figure G.2, for all the model runs at several times.

The general picture, that the improved model results in substantial better predictions compared to the XBeach default, is also in line with the presented data. Especially for the model runs with course sand (T5 and T6) are the results very good. For the model runs with fine sand (T3 and T4) is still to much erosion modelled, better results are achieved if a stronger dilatancy effect is modelled by a larger value for the A coefficient.

The θ_{max} limiter causes very bad results during the second breaching phase, whereas the performance increases slightly during the third phase.

If no dilatancy is taken into account, the performance of the improved model reduces substantially. Hence, dilatancy is an important driver for the good performance of the improved model.

Also the bed slope effect has a substantial influence on the model results. In the T3 and T4 experiment, a better skill is achieved if no bed slope effect is used. This does not mean that the bed slope effect should not be included. The better performance in the T3 and T4 experiment by not taking the bed slope effect into account is related to the fact that the bed slope effect causes an increase of erosion at the back side of the dune/dike. In these cases, still to much erosion occurs and the additional erosion by the bed slope effect causes a lower skill. This does not mean that the bed slope effect is not working properly.

The fall velocity reduction and the conservative Exner equation modify the predictions only slightly, these improvements don't seem to be important based on this experiment.

Table G.4: T3: Brier Skill Score and bias calculated for the domain of the measurement data. Improvements in skill score compared to the base run of more than 0.05 are marked green, decreases in score of more than 0.05 are marked red. A negative bias means an over-prediction of the erosion rates.

T3	t = 40 s		t = 120 s		t = 160 s		t = 240 s	
Model run	BSS	Bias [m]	BSS	Bias [m]	BSS	Bias [m]	BSS	Bias [m]
XBeach default	0.72	-0.08	-0.26	-0.89	-2.46	-1.62	-8.70	-3.23
Smax = 1	**0.23**	0.29	**0.39**	0.50	**0.56**	0.38	**0.60**	-0.09
Soulsby slope effect	0.75	-0.07	-0.04	-0.80	-1.84	-1.47	-7.05	-2.95
Improved model	**0.85**	0.05	**0.89**	-0.23	**0.69**	-0.49	**0.20**	-0.93
No dilatancy effect	0.68	0.03	**0.42**	-0.47	-0.56	-1.07	-3.59	-2.22
With A = 1.75 (dilatancy)	**0.88**	0.07	**0.98**	-0.08	**0.93**	-0.23	**0.64**	-0.59
No bed slope effect	**0.86**	0.06	**0.93**	-0.17	**0.79**	-0.40	**0.31**	-0.85
With 20° internal friction	**0.85**	0.05	**0.87**	-0.25	**0.64**	-0.53	**0.10**	-0.98
No fall velocity reduction	**0.85**	0.05	**0.89**	-0.23	**0.69**	-0.49	**0.20**	-0.93
With conservative Exner	**0.84**	0.06	**0.89**	-0.24	**0.68**	-0.49	**0.26**	-0.89

Table G.5: T4: Brier Skill Score and bias calculated for the domain of the measurement data. Improvements in skill score compared to the base run of more than 0.05 are marked green, decreases in score of more than 0.05 are marked red. A negative bias means an over-prediction of the erosion rates.

T4	t = 40 s		t = 120 s		t = 160 s		t = 240 s	
Model run	BSS	Bias [m]	BSS	Bias [m]	BSS	Bias [m]	BSS	Bias [m]
XBeach default	0.05	-0.34	-1.91	-1.92	-6.44	-3.27	-7.01	-5.23
Smax = 1	**0.29**	0.29	**0.32**	0.87	**0.49**	0.81	**0.73**	0.88
Soulsby slope effect	**0.12**	-0.33	-1.64	-1.82	-5.87	-3.14	-6.64	-5.12
Improved model	**0.80**	-0.12	**0.70**	-0.59	**-0.00**	-1.20	-0.51	-2.29
No dilatancy effect	**0.49**	-0.20	-0.33	-1.26	-2.68	-2.25	-3.69	-4.02
With A = 1.75 (dilatancy)	**0.88**	-0.08	**0.93**	-0.29	**0.69**	-0.66	**0.44**	-1.40
No bed slope effect	**0.82**	-0.11	**0.78**	-0.50	**0.17**	-1.09	-0.33	-2.15
With 20° internal friction	**0.79**	-0.13	**0.67**	-0.63	-0.10	-1.25	-0.61	-2.36
No fall velocity reduction	**0.80**	-0.12	**0.70**	-0.60	-0.02	-1.21	-0.60	-2.35
With conservative Exner	**0.79**	-0.13	**0.69**	-0.61	-0.06	-1.23	-0.60	-2.36

Table G.6: T5: Brier Skill Score and bias calculated for the domain of the measurement data. Improvements in skill score compared to the base run of more than 0.05 are marked green, decreases in score of more than 0.05 are marked red. A negative bias means an over-prediction of the erosion rates.

T5	t = 40 s		t = 120 s		t = 160 s		t = 240 s	
Model run	BSS	Bias [m]	BSS	Bias [m]	BSS	Bias [m]	BSS	Bias [m]
XBeach default	0.87	-0.00	0.55	-0.36	-1.67	-0.76	0.69	-0.58
Smax = 1	**0.41**	0.20	**0.70**	0.22	**0.91**	0.07	0.72	0.60
Soulsby slope effect	0.87	0.00	**0.63**	-0.32	-1.33	-0.71	0.69	-0.56
Improved model	0.85	0.08	**0.98**	0.03	**0.99**	0.03	**0.94**	0.17
No dilatancy effect	**0.80**	0.06	**0.90**	-0.11	**0.58**	-0.29	**0.90**	-0.11
With A = 1.75 (dilatancy)	0.86	0.09	**0.96**	0.10	**0.92**	0.12	**0.97**	0.21
No bed slope effect	0.85	0.09	**0.97**	0.10	**0.93**	0.12	**0.97**	0.22
With 20° internal friction	0.85	0.08	**0.99**	0.02	**0.99**	0.01	**0.96**	0.11
No fall velocity reduction	0.85	0.08	**0.98**	0.03	**0.99**	0.03	**0.94**	0.17
With conservative Exner	0.85	0.08	**0.99**	0.03	**0.99**	0.03	**0.94**	0.17

Table G.7: T6: Brier Skill Score and bias calculated for the domain of the measurement data. Improvements in skill score compared to the base run of more than 0.05 are marked green, decreases in score of more than 0.05 are marked red. A negative bias means an over-prediction of the erosion rates.

T6	t = 40 s		t = 120 s		t = 160 s		t = 240 s	
Model run	BSS	Bias [m]	BSS	Bias [m]	BSS	Bias [m]	BSS	Bias [m]
XBeach default	0.85	0.04	0.80	-0.40	0.66	-0.75	0.57	-1.33
Smax = 1	**0.34**	0.33	**0.61**	0.49	**0.79**	0.39	**0.84**	0.55
Soulsby slope effect	0.85	0.04	0.83	-0.36	**0.72**	-0.68	**0.63**	-1.23
Improved model	**0.78**	0.16	**0.98**	0.08	**0.99**	0.07	**0.98**	0.20
No dilatancy effect	**0.73**	0.14	**0.93**	-0.09	**0.95**	-0.29	**0.95**	-0.43
With A = 1.75 (dilatancy)	**0.79**	0.17	**0.96**	0.18	**0.95**	0.22	**0.94**	0.42
No bed slope effect	**0.77**	0.17	**0.97**	0.15	**0.97**	0.18	**0.95**	0.37
With 20° internal friction	**0.78**	0.16	**0.98**	0.07	**0.99**	0.04	**0.98**	0.16
No fall velocity reduction	**0.78**	0.16	**0.98**	0.08	**0.99**	0.07	**0.98**	0.20
With conservative Exner	**0.78**	0.16	**0.98**	0.08	**0.99**	0.06	**0.98**	0.19

G.1.4 Conclusions

To conclude, the improved model results in better results with respect to the XBeach default. With the improved model, the erosion rates are less overpredicted. The main driver for this improvement is dilatancy. Also the bed slope effect is a process that is significant. The fall velocity reduction and the conservative Exner equation are of much less importance.

G.2 Zwin

G.2.1 Model description

The Zwin experiment is introduced in section 3.3. In contrast to the Scheldt Flume experiment, now are also the two-dimensional aspects of the breach considered. During the experiment, the width of the breach was measured. This width gives some insight in the breaching process.

The grid file and boundary conditions used for the Zwin model are based on the model published in the XBeach skillbed (Deltares, 2014a). The model grid is designed large enough to enforce the correct boundary conditions. Downstream of the breach, the polder area is described by the following formulation in which z_p represents the water level in the polder above NAP (Visser, 1998):

$$A_p = \begin{cases} 170000 z_p - 100000 \text{ for } \mathrm{z_p} > \mathrm{NAP} + 0.60\mathrm{m} \\ 2100000 z_p - 4540000 \text{ for } \mathrm{z_p} > \mathrm{NAP} + 2.30\mathrm{m} \end{cases} \tag{G.1}$$

Figure G.5 shows the model grid with its bathymetry. Compared to the skillbed model, the grid spacing is somewhat refined to ensure a grid spacing of $0.5\ m$ near the breach. The sloping bathymetry downstream of the dike breach enforces an basin area corresponding to Equation G.1.

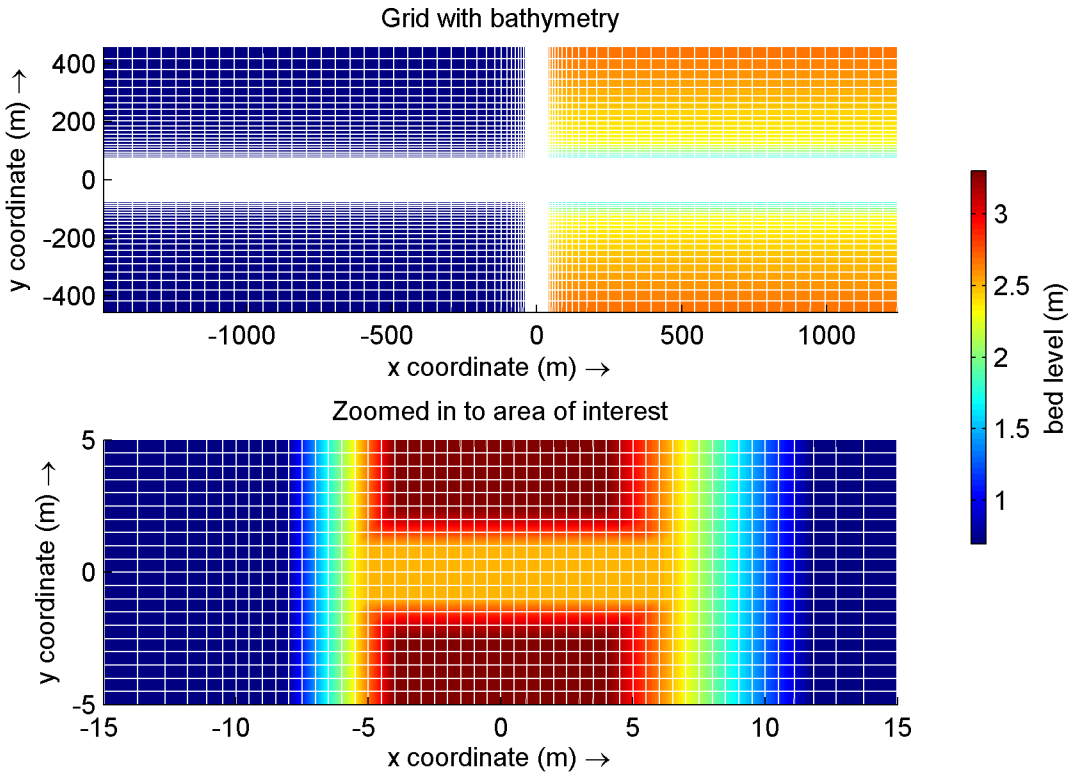

Figure G.5: Initial profile with the grid used for the calculation. Near the area of interest is a grid size of $0.5\ m$ taken. The grid size is increased with a factor of 1.15 up to a grid size of $50\ m$.

At the sea side, a water level elevation is enforced based on measurement data which is plotted in Figure G.6. As visible, the rising tide enlarges the water level elevation during the initial phase of the breach after which a slight fall of the elevation is observed due to the outflow of water through the breach.

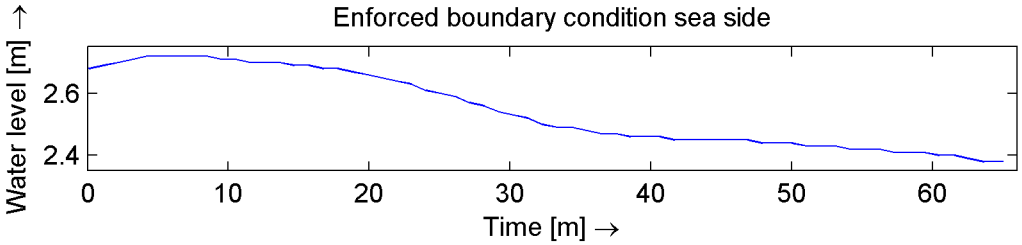

Figure G.6: Water level boundary condition at sea side.

The sand-dam was built with local sand from the Zwin Channel and the beach (Visser, 1998), which differs in grain size substantially, as visible in Table G.8. As a result, the sand is not uniform. More or less in line with the parameters used in the mathematical model of Visser (1998), the grain sizes of Table G.9 are used in the XBeach model.

Table G.8: Grain sizes for the different types of sand.

Sand	D10 $[mm]$	D50 $[mm]$	D90 $[mm]$
'Original' Zwin Sand	0.155	0.185	0.285
Suppletion sand	0.215	0.315	0.600

Table G.9: Adjustments to the default parameter settings of Table D.1

Parameter	Value	Unit	Meaning
C	65	$m^{0.5}/s$	Chézy coefficient.
D_{15}	159	μm	15% percentile sediment grain size.
D_{50}	220	μm	Median sediment grain size.
D_{90}	290	μm	90% percentile sediment grain size.

G.2.2 Results

Breach width

In Figure G.7, the evolution of the breach width over time is presented. The first observation is the substantial difference between the XBeach default and the proper implementation of the engineering Soulsby slope effect. From this, it can be concluded that the XBeach default settings result in a very large overestimation of the breach width. This overestimation can be explained by the steep slopes of which the on-slope directed vector is directed perpendicular to the flow direction. Based on this, it is wise to compare the improvements for this case with respect to the Soulsby slope effect and not to the XBeach default.

Since the improved model contains hindering of erosion, it is not unexpected that it results in a smaller breach width compared to the Soulsby slope effect run. It is not the intention to obtain a perfect fit to the data, the shape of the solution and the sensitivity is more important. From the evolution of the breach width over time, it can be learned that the improved model has a more or less continuous underestimation of the breach width by 20%, whereas the shape of the Soulsby slope effect breach width evolution is not in line with the measurement data; first an over prediction is modelled and after 25 minutes an under prediction occurs. The underestimation of the breach width in the improved model could hence be a calibration issue.

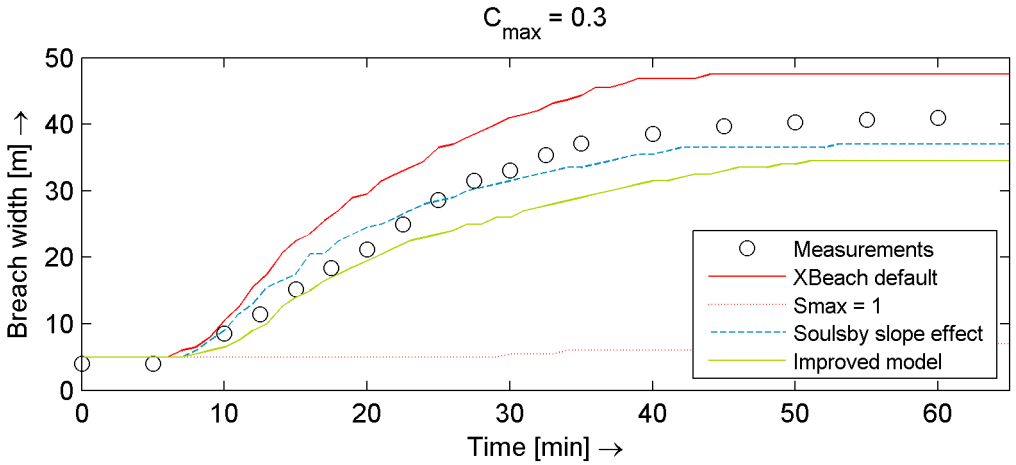

Figure G.7: Evolution of the gap width over time for a maximum sediment concentration of 0.3.

Cross-section

In Figure G.8, cross-sections at several times are given. From this, it is clear why the XBeach default run causes a substantial overestimation of the breach width: the slope effect causes a substantial smoothing of the cross-section profile resulting in a less deep, but wider breach. In contrast, the engineering bed slope effect of Soulsby is a pure modification of the sediment transport rates in the direction of the transport, a very rugged profile is found. Finally, the improved model contains not only a modification of the transport in the transport direction but also a change of direction based on the bed slope, this causes the slightly smoothed profile.

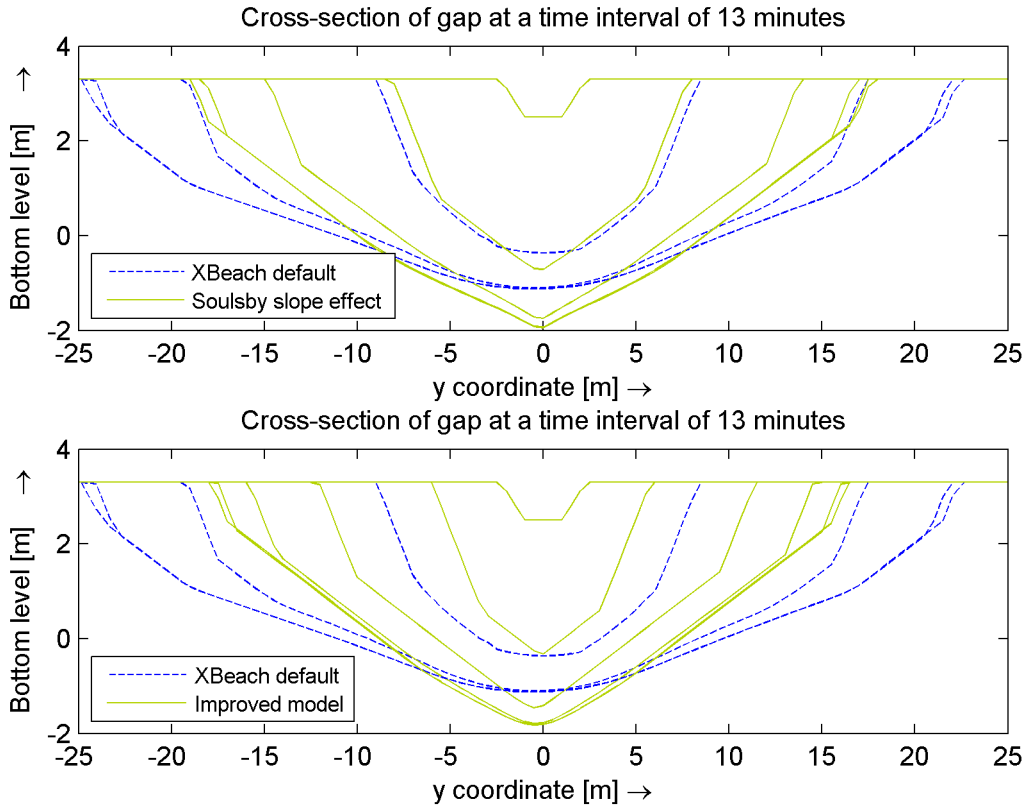

Figure G.8: Evolution of the gap cross-section over time for various model runs.

Validation of the hydrodynamics

Figure G.9 shows a validation of the modelled water levels and flow velocities. Since the initial water level in the basin equals $0.7\ m$, the measurement data suggests a $1\ m$ increase of the water level of the basin in the first 5 minutes of the breaching event. This is not likely to be valid by the small initial gap size and the large area of the basin surface. Visser (1998) mentions that the measurement device at the point downstream of the breach gives erroneous data since it was not continuously under water in the first 35 minutes of the breach (pressure sensor located at NAP+$1.65\ m$). Neglecting these explicable deviations, the modelled hydrodynamics seems to be in quite good accordance to the measurement data. But still, differences in the order of $0.1\ m$ in water level and $0.5\ m/s$ are observed which can result in considerable different results.

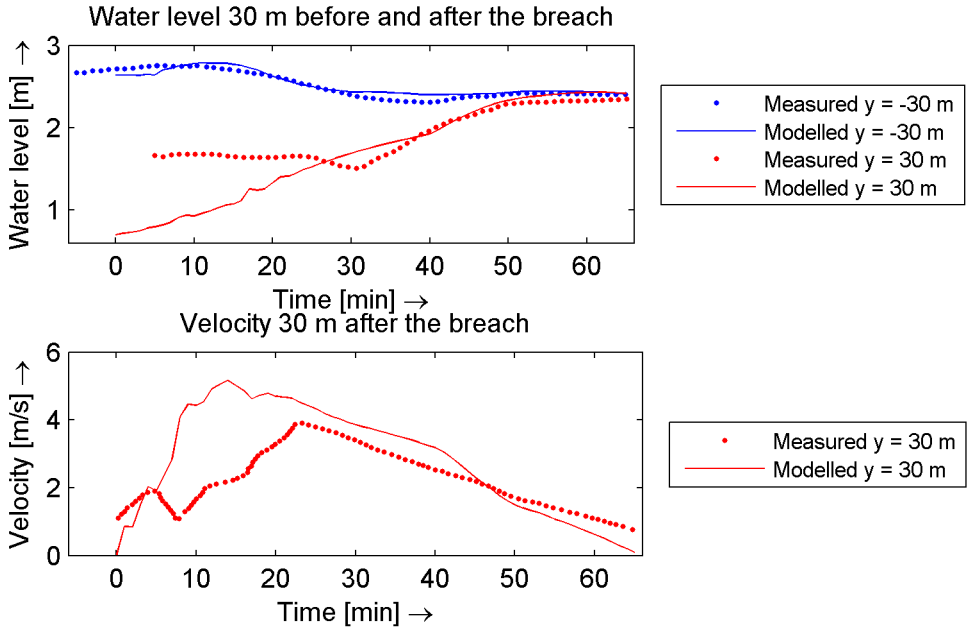

Figure G.9: Model results are of the improved model compared to measurements regarding water levels and velocities.

G.2.3 Sensitivity

A smaller depth averaged concentration

If the depth averaged sediment concentration is limited to 0.1, the resulting breach widths are considerably smaller, see Figure G.10. Further, the breaching process is initiated later; only after 10 minutes is the first increment of the breach width visible whereas the data suggests that this should happen 5 minutes earlier. The limitation to the sediment concentration causes hence a limitation of the erosion rates which is not likely to be physically valid.

Based on this Figure, the XBeach default settings seem to perform fine. However, it is already noted that the small limitation to the concentration and the bed slope effect in the XBeach default are not realistic. The match to the data can thus be qualified as a coincidence.

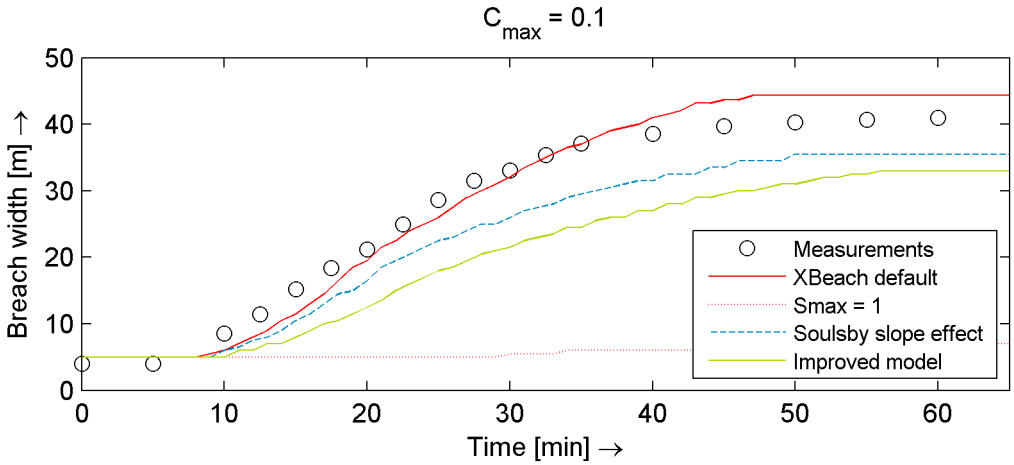

Figure G.10: Evolution of the gap width over time for a maximum sediment concentration of 0.1.

A close look to the individual processes

Table G.10 shows the performance of the different model runs based on the BSS, bias and final width of the breach. To determine the BSS, the reference scenario of a constant breach width is taken.

The earlier observation, regarding the bad performance of the θ_{max} limitation, is confirmed with the data. Just like with the visual observations, the focus is not on the exact results but on the differences between the runs. Based on the bias, it can be concluded that the influence on the breach width by dilatancy is in the order of $2.5\ m$, the bed slope effect in the order of $0.5\ m$, the fall velocity reduction in the order of $0.4\ m$ and the conservative Exner equation in the order of $0.1\ m$.

Table G.10: Brier Skill Score and bias calculated for the domain of the measurement data. The BSS is calculated for the time-width function, the BSS is compared to a do-nothing scenario (constant gap width of 4.0 m over time). Improvements in skill score compared to the base run of more than 0.05 are marked green, decreases in score of more than 0.05 are marked red. Improvements in the modelled gap width compared to the base run of more than 1.0 m are marked green, all deteriorations are marked red.

	$C_{max} = 0.1$			$C_{max} = 0.3$		
Model run	BSS	Bias [m]	Final W [m]	BSS	Bias [m]	Final W [m]
Measurements			41.00			41.00
XBeach default	0.99	-0.13	44.32	0.94	6.36	47.51
Smax = 1	**0.11**	-20.84	**7.00**	**0.11**	-20.84	**7.00**
Soulsby slope effect	0.96	-4.86	**35.50**	**0.99**	-0.64	**37.00**
Improved model	**0.89**	-8.09	**33.00**	0.96	-4.25	34.50
No dilatancy effect	**0.94**	-6.23	**35.00**	**0.99**	-1.78	**36.00**
With A = 1.75 (dilatancy)	**0.86**	-9.12	**32.00**	0.94	-5.58	**33.50**
No bed slope effect	**0.88**	-8.33	**33.00**	0.95	-4.64	**33.50**
With double direction	**0.89**	-8.12	**33.50**	0.96	-4.15	34.50
With 20° internal friction	**0.90**	-7.83	**33.50**	0.96	-3.98	34.50
No fall velocity reduction	**0.90**	-7.71	**33.50**	0.97	-3.83	34.50
With conservative Exner	**0.89**	-8.11	**33.00**	0.96	-4.33	**34.00**

G.2.4 Conclusions

The current implementation of the bed slope effect is different from the engineering bed slope effect by Soulsby. Now, not only the magnitude of the sediment transport direction is affected, but also the direction is modified by the present implementation of the bed slope effect. The result is a very smooth, but broad, breach profile. The final breach with is $13.5\ m$ broader compared to the improved model.

All model runs, except the XBeach default with the invalid implementation of the Soulsby bed slope effect, result in an underestimation of the breach width. This is not directly a malfunctioning of the XBeach model. The uncertainties in the model parameters and measurement data are substantial. With some calibration, results could be obtained which are more in line with the observations. Such a calibration is not the purpose of this research.

More important is to look to the individual sensitivities. Off course, every hindering of the erosion result in less agreement with the observations since there is already an underestimation of the final gap width. As explained, this does not mean that the more physical based approach is less correct. If the focus is on the individual processes, it seems that dilatancy is the most important contribution to the improved model followed by the bed slope effect and the hindered settling velocity. The conservative Exner equation is of no real importance in the achieved results.

Finally, it is observed that the Shields parameter restriction method has a very bad performance. A gap width of only $7\ m$ is modelled whereas $41\ m$ is observed in reality.

G.3 Santa Rosa

G.3.1 Model description

The Santa Rosa model was introduced in Section 3.4. The grid file and boundary conditions used for this model run are based on the model made by Robert McCall (McCall, 2008; McCall et al., 2010). Now the improved model is applied on this case study to test whether the model improvements result in substantial better predictions. With the present XBeach model, very large overestimations of the erosion rates were made.

A morphological acceleration factor of 10 is used to accelerate the model computation. Without the acceleration factor, it would take 10 days to model the 38 hour storm. With the acceleration factor, it takes "only" one day. Otherwise, a thorough sensitivity is not practical.

Table G.11: Adjustments to the default parameter settings of Table D.1

Parameter	Value	Unit	Meaning
morfac	10	–	Morphological acceleration factor.

G.3.2 Results

The initial bed level is presented in the left plot of Figure G.11. As visible, there are several low spots in the dune row where the overwash process will start first.

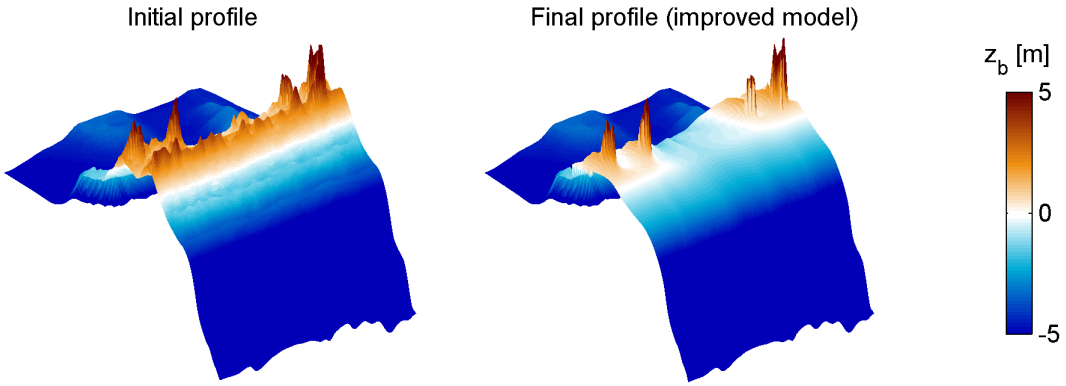

Figure G.11: Initial and modelled profile of the Santa Rosa model.

During the storm, an average erosion of $0.09\ m$ occurred on top of the barrier island, see Figure G.12. With the improved model, the erosion rates are overestimated substantially, comparable to the default XBeach settings. The modelled final profile is presented in the right plot of Figure G.11. The XBeach model predicts hence a huge breaching channel whereas in reality much smaller erosion rates occurred.

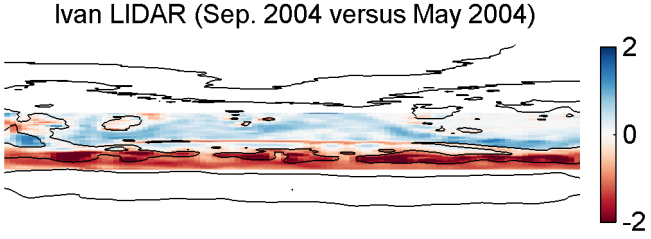

Figure G.12: LIDAR data Santa Rosa, post storm versus pre storm.

G.3.3 Sensitivity

Sensitivity to the processes in the improved model

Table G.12 presents the Brier Skill Score and the bias for the variety of model runs. Only with a limitation of the Shields parameter to 1, a positive skill is achieved with a bias of $-0.18\ m$. Although this bias seems small with respect to the other biasses calculated, the actual average bottom level change on top of the barrier is just 9 centimeters. The bias is hence twice the actual bottom change, which is substantial.

From the other model runs no strong conclusions can be made since the skill of the model is very bad without the Shields parameter limitation. However, the hindering effect of dilatancy is visible in the results.

Table G.12: Brier Skill Score and bias calculated for the domain of the measurement data (on top of the barrier island). A negative bias means an over prediction of the erosion rates.

Model run	BSS	Bias [m]
XBeach default	-5.76	-1.86
Smax = 1	0.75	-0.18
Soulsby slope effect	-5.66	-1.85
Improved model	-4.60	-1.66
No dilatancy effect	-5.27	-1.78
With A = 1.75 (dilatancy)	-4.02	-1.56
No bed slope effect	-4.65	-1.68
With double direction	-4.79	-1.70
With 20° internal friction	-4.63	-1.67
No fall velocity reduction	-4.60	-1.66
With conservative Exner	-4.69	-1.68

Sensitivity to the enforced surge level

To test the importance of the boundary conditions, the surge level is reduced with 20% and 40% at sea side. These modifications are made to the improved model. Figure G.13 shows the default surge level of the Santa Rosa model and the modified ones. For the 40% surge reduction, also a model run with the same reduction on the bay is performed.

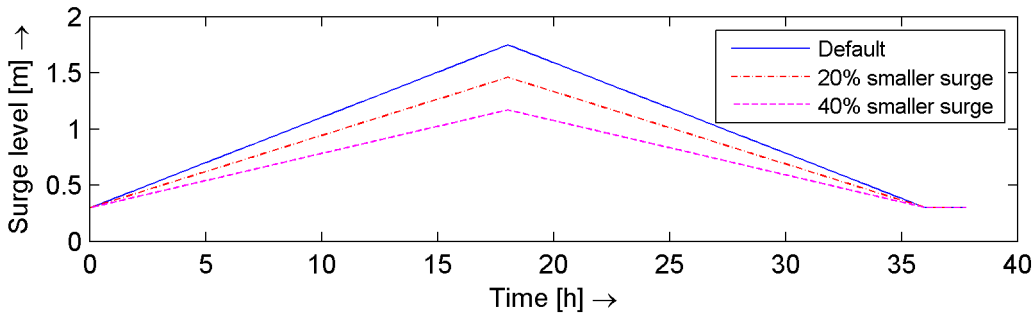

Figure G.13: Visualisation of the reduced surge level.

Table G.13 shows the skill of the improved model with the variety of storm surge levels. The data shows that the skill and bias improve with a decreasing storm surge level. Further, the water level in the bay shows an important influence on the model results. If the bay water level is taken the same as the default surge level and only the sea side water level is decreased, the best results are achieved.

Table G.13: Brier Skill Score and bias calculated for the domain of the measurement data (on top of the barrier island). Presented runs are used to test the sensitivity of the improved model to the surge level. A negative bias means an over prediction of the erosion rates.

Model run	BSS	Bias [m]
Improved model	-4.60	-1.66
40% *lower surge on sea and bay*	-2.20	-1.18
40% *lower surge on sea*	-0.03	-0.59
20% *lower surge on sea*	-1.39	-1.02

Sensitivity to additional model parameters

Besides the surge level, additional model parameters are investigated. By the uncertainty of the grain sizes, a model run is performed with twice as large grain sizes. Further, the permeability is decreased with a factor ten to investigate if the dilatancy method hinders erosion sufficiently if the dilatancy force is increased. Finally the sensitivity of the model to the Chézy value is observed. The Chézy value is changed over the whole model domain, and in two model runs the Chézy value is only decreased on top of the barrier island (with a linear interpolation of the Chézy value to the bay and the sea over several grid cells), See Figure G.14 for more details.

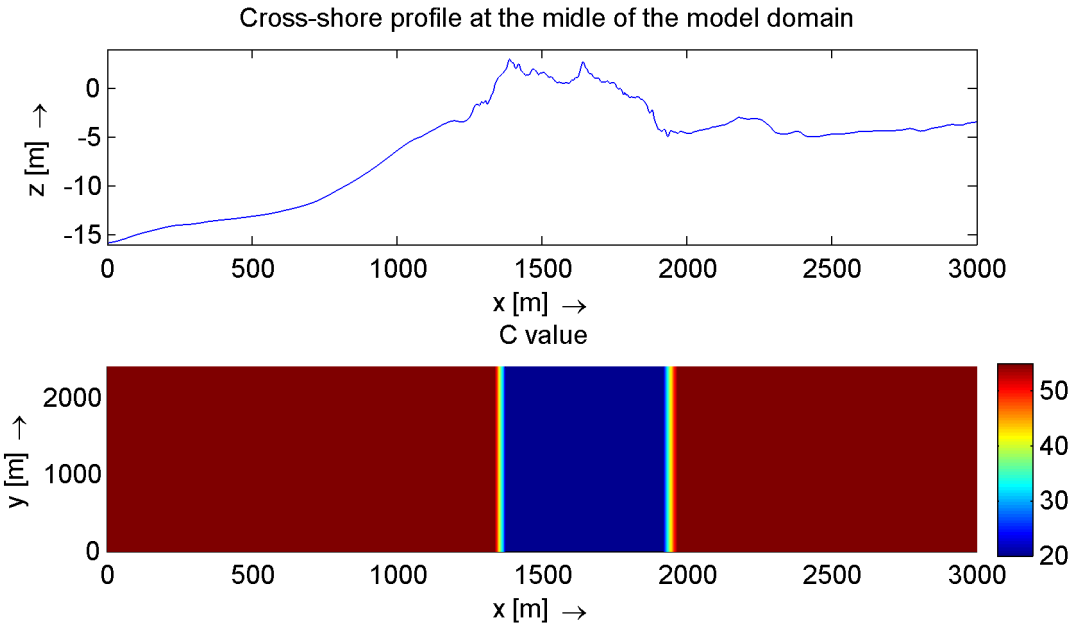

Figure G.14: Visualisation of the location varying Chézy value if the Chézy value reduction is limited to the island. Visualised is a reduction to a Chézy value of 20 on the island, but the method is comparable for a limitation to 35.

Table G.14 present the skill of the different model runs. First, increasing the grain sizes causes substantial less erosion, what can be explained from the lower transport rates for larger grain sizes. Also a ten times smaller permeability causes less erosion, the hindering effect of dilatancy is modelled much stronger. For both cases, the skill of the model did improve, but the improvements are too small to achieve a positive predictive skill.

The modification of the Chézy value causes much more substantial differences. Generally, the larger the Chézy value, the smaller the bed friction for which the data shows far more erosion. Reducing the Chézy value results hence in less erosion. It is questionable whether a low Chézy value in the order of 20 or $35\ m^{0.5}/s$ is reasonable over the whole model domain. Therefore, the model runs with the Chézy value reduction only on top of the barrier island are performed, which show also a substantial improvement of the results. The reduction of the Chézy value on top of the barrier island could be caused by vegetation.

The modification of the Chézy value is also performed without the model improvements. Then, a lower skill is achieved. Also under these conditions does the improved model result in better predictions.

Table G.14: Brier Skill Score and bias calculated for the domain of the measurement data (on top of the barrier island). Presented runs are part of the additional sensitivity to the improved model. A negative bias means an over prediction of the erosion rates.

Model run	BSS	Bias [m]
Improved model	-4.60	-1.66
Doubled grain sizes	-1.68	-1.08
Ten times smaller k value (permeability)	-2.24	-1.19
Chézy = 20	0.69	-0.03
Chézy = 20 on barrier island only	0.59	-0.09
Chézy = 20 without model improvements	0.69	-0.08
Chézy = 35	0.23	-0.40
Chézy = 35 on barrier island only	0.14	-0.44
Chézy = 35 without model improvements	0.07	-0.54
Chézy = 100	-25.39	-3.83

G.3.4 Conclusions

Both the XBeach default settings as the improved model show a very poor skill on the Santa Rosa case study. Whereas the average erosion on the barrier island equals $0.09\ m$, the XBeach model predicts an average decrease in bottom level of more than $1.6\ m$. Reducing the surge level increases the results, especially if the surge level in the bay is not modified. Further, a larger grain size or a ten times smaller permeability result in less erosion, but still a negative skill is achieved. Only by limiting the Chézy value to 20 or $35\ m^{0.5}/s$ on the barrier island or over the whole model domain, reasonable skill scores are achieved.

Appendix H

Fire Island model

This appendix presents the details of the model set-up of the Fire Island model, dealt with in Chapter 7. After the model set-up is presented, the sensitivity of the model to various variations is tested.

H.1 Model set-up

There are several assumptions made with the generation of the XBeach model of Fire Island. Although all the considerations have the purpose of achieving an as accurate representation of reality as possible, it is important to be aware of them. Figure H.1 shows the procedure followed to achieve a robust and accurate model. The grid sizes are a trade-off between accuracy and computational time required to run the model. More details are given in the next sections.

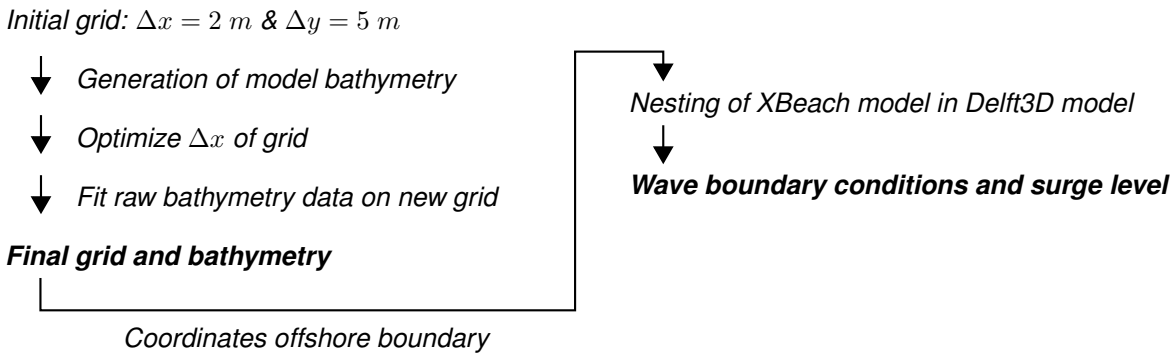

Figure H.1: Procedure of the model set-up.

H.1.1 Bathymetry

Several datasets of the bottom level are available, see Table H.1. None of these datasets has a complete reliable coverage of the model domain and each has its own accuracy and validity. Although the CRM data has a full coverage of the model domain, it is not useful on top on the barrier island (everything has a bottom level of $1\ m$ there) and in shallow water (accuracy of the bottom level is in the order of the water depth at those locations). On top of the barrier Island, LIDAR data has the best accuracy and finest resolution (extracted on a $1\ m$ x $1\ m$ grid). In front of the barrier Island, the LARC data covers the breaker bar which was also visible in the satellite image of Figure 7.2, see Figure H.2. Downside of the LARC data is the accretion in front of the breach channel by the sediment transport through the channel.

Table H.1: Indexation of the available bathymetry data.

Dataset	Date	Vertical accuracy	Coverage	Source
Pre-Sandy LIDAR (LIght Detection And Ranging)	20-01-2012	$0.09\ m$ (RMSE)	$\approx z_b > 0\ m$	NOAA
Post-Sandy LIDAR (LIght Detection And Ranging)	05-11-2012	$0.075\ m$ (RMSE)	$\approx z_b > 0\ m$	NOAA
CRM (Coastal Relief Model)	05-08-2012	Order of $1\ m$	Full	NOAA
LARC (Lighter Amphibious Resupply Cargo)	26-06-2013	$0.26\ m$ (RMSE)	$\approx -8\ m < z_b$	USGS

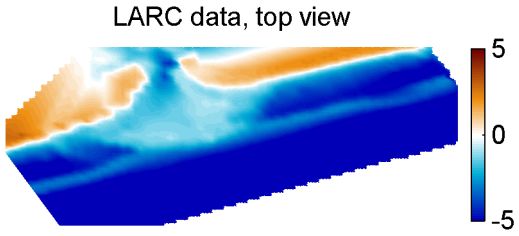

Figure H.2: Post Sandy LARC data. Date of measurement campaign: June 26th, 2013. Source: USGS.

Two bathymetry set-ups are made: one prior to Sandy which will be used as an initial profile of the model, the second one is made to represent the post-Sandy situation based on which the performance of the model is assessed.

Pre-storm

The pre-Sandy bathymetry should cover the full model domain, since a bottom level is required in each computational grid cell. A selection is made between the different data sources of Table H.1.

At depths of more than $6.5\ m$, the CRM data are used to represent the bathymetry. Since the large grid resolution of the CRM data ($90\ m$ x $90\ m$) causes a profile with steps, a smooth profile is interpolated on all the CRM cross-sections. This smooth CRM profile is fitted to the most left cross section (largest y value) of the LARC data, as presented in Figure H.2, such that the influence of the accretion in front of the channel is minimized and a reasonable pre-storm profile with breaker bar is created. This procedure is visualised in Figure H.3. With this procedure, a uniform profile is generated for the bottom level at depths of more than $2.5\ m$.

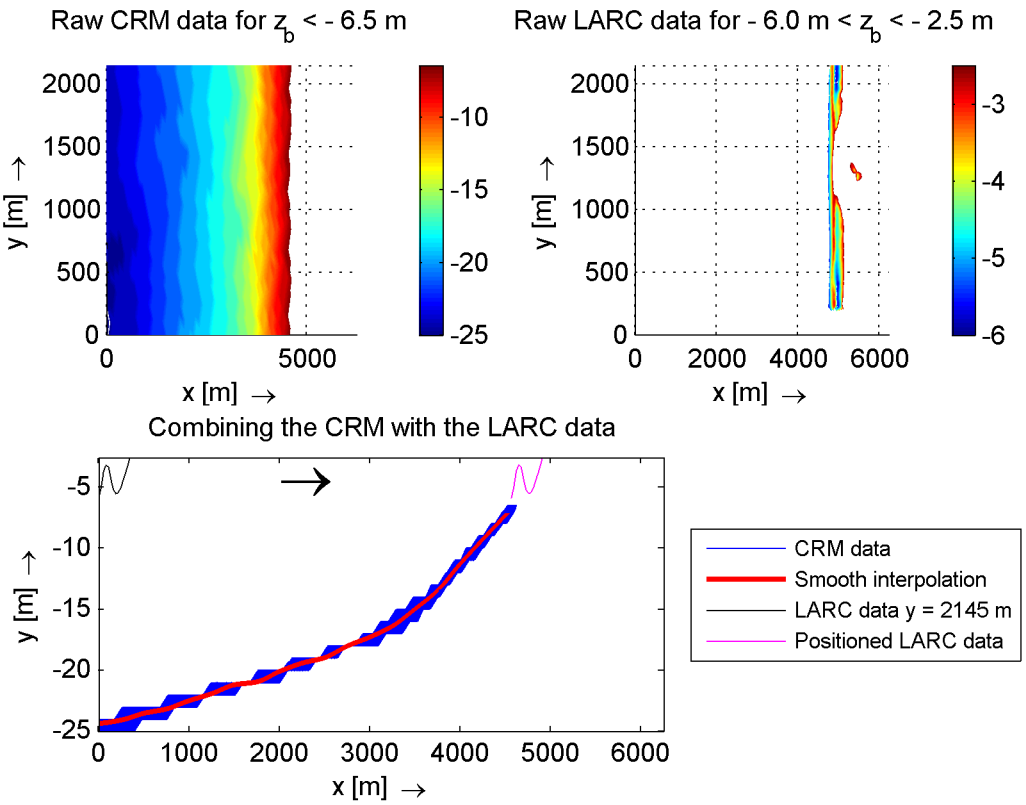

Figure H.3: Combining the CRM data with the LARC data.

Based on the procedure of Figure H.3, a profile is available which can be fitted to the LIDAR data, see Figure H.4. The smooth CRM-LARC profile is translated horizontally in each cross section till the extrapolated line of this profile crosses the LIDAR data.

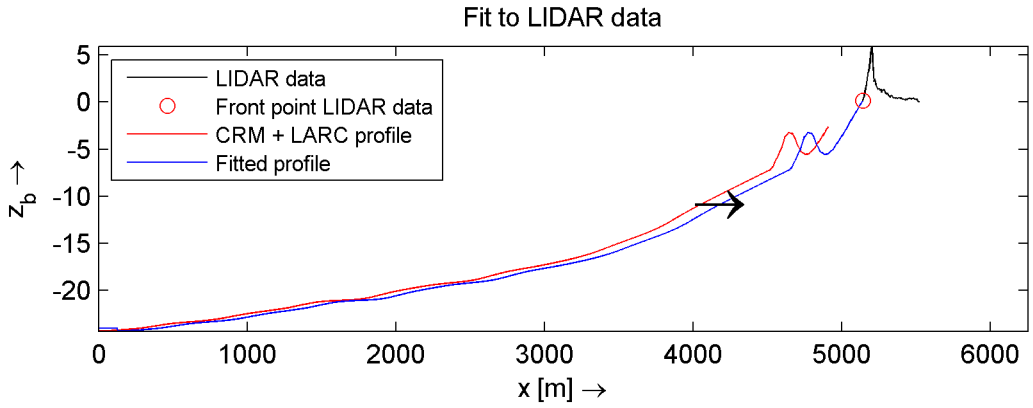

Figure H.4: Combining profile with the LIDAR data.

No accurate data are available to describe the bottom profile in the bay. The CRM data do give estimates for this depth, but the accuracy of that dataset is in the order of one meter, which makes the CRM data unusable for the bay. Therefore, a spatially uniform initial bottom level is assumed with a smooth transition to the LIDAR data on the barrier Island. The initial bottom level in the bay is subject to changes in the sensitivity analysis. For now, a bottom level in the bay of $-1\ m$ is taken based on the CRM data. A smooth transition to the LIDAR data over several grid cells is applied to prevent the occurrence of steep slopes.

Figure H.5 presents the resulting pre-Sandy bathymetry based on the analysis presented in this section. In deep water and near the breaker bar, the bathymetry is not precisely alongshore uniform as it is fitted to the front of the LIDAR data which is not exactly a straight line in longshore direction.

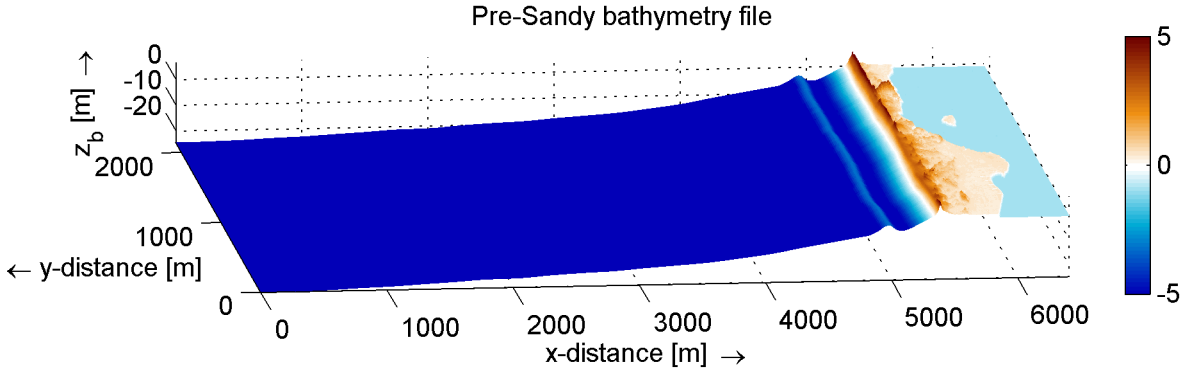

Figure H.5: Pre-Sandy model bathymetry.

Post-storm

To test the model performance, the model results are compared with post-storm bathymetry. Since the CRM model data has a too large inaccuracy compared to the morphological changes, it cannot be used to assess the model performance. Further, the LARC data could be used to approximate the profile of the breaker bar, but the data are achieved after a too large period after the storm to describe the post-storm bathymetry precisely. Therefore, only the post-storm LIDAR data has enough accuracy and is made close enough after the storm to represent the post-storm situation. This data are presented in Figure H.6.

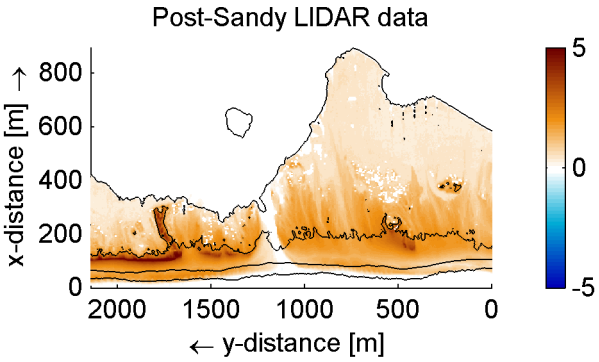

Figure H.6: Post-Sandy LIDAR data. The black depth contours are provided at an elevation of 0 and 2 m relative to NAVD88 of the initial depth profile.

H.1.2 Grain sizes

A short measurement campaign, performed by the USGS at a distance of $1\ km$ from the project location, resulted in the data on the grain sizes of Table H.2. By the spatial variability of grain sizes, it is difficult to get to one representative grain size distribution based on just these three samples. For now, a D_{15} of $290\ \mu m$, a D_{50} of $400\ \mu m$, and a D_{90} of $600\ \mu m$ is taken as representative.

Table H.2: Data on the grain sizes by the USGS.

Location	D16 [$\mu\ m$]	D50 [$\mu\ m$]	D90 [$\mu\ m$]
Swash zone	424	653	1186
Just after the dune	268	378	576
Overwash fan	299	416	611

H.1.3 Model grid

As explained in Figure H.1, initially a grid size of $2\ m$ in x-direction and $5\ m$ in y-direction is used. In deeper water, larger grid cell sizes are reasonable. Based on a minimum of 12 points per wave length, a maximum grid size to depth ratio of 2 and the pre-Sandy bathymetry of section H.1.1, an optimized grid in x-direction is generated.

Because waves are not necessarily perpendicular incident to the coast, the model should be widened at both sides of the area of interest. Otherwise, shadow zones result in regions in which the wave boundary conditions are not fully enforced, see Figure H.7. Therefore, at both sides of the model domain, the grid is extended to cover incident waves under an angle of $45°$, which means a widening of $5\ km$ at both sides. To prevent a too large computational time, grid sizes are extended in y-direction with an increment factor of the size of 1.15 and a maximum grid size of $50\ m$.

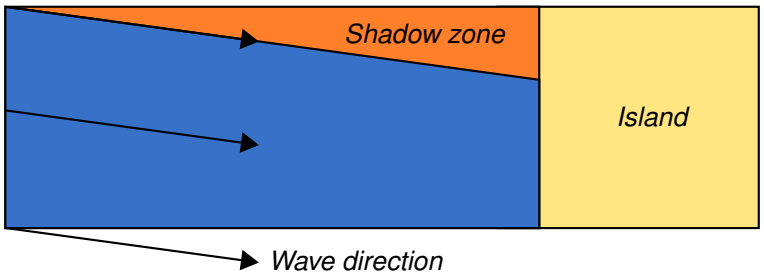

Figure H.7: Explanation of the shadow zone problem.

The optimized grid is presented in Figure H.8. The total grid contains 547 grid cells in x-direction and 654 in y-direction. The area of interest, hence without the shadow zones, consists of 547 grid cells in x-direction and 434 in y-direction. By taking the shadow zones into account, only 51% more grid cells are used which makes this procedure acceptable in view of the computational time required.

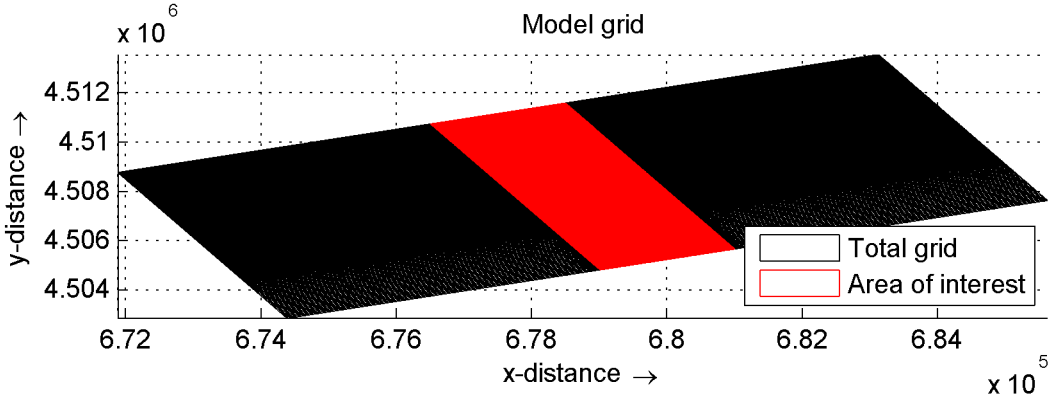

Figure H.8: Model grid coverage.

H.1.4 Boundary conditions

At the lateral boundaries, Neumann conditions are used to achieve zero water level gradients. In the bay, the water level is set equal to the one measured at a measurement station nearby. At the offshore boundary, waves are enforced by water levels and discharges obtained from a nesting procedure in a Delft3D model.

The Delft3D model is currently under development by Deltares. It covers a large enough part of the North Atlantic Ocean to provide reliable predictions of wave parameters and storm surge based on the input of a spatially non-uniform wind field. Since the model is still under development, the results are not yet optimal. However, the model provides better estimates of the local hydrodynamic parameters if compared to simply use measurement data at stations located $100\ km$ away from the location of interest with different coastline characteristics.

Water level in the bay

Based on measurements done by the USGS, the data of two storm-tide sensors is examined to get to a representative water level elevation in the bay over time. Two locations are studied which were located close to the project location: Location I (known as SSS-NY-SUF-021WL) and Location II (SSS-NY-SUF-026WL) of which the locations and data are presented in Figure H.9.

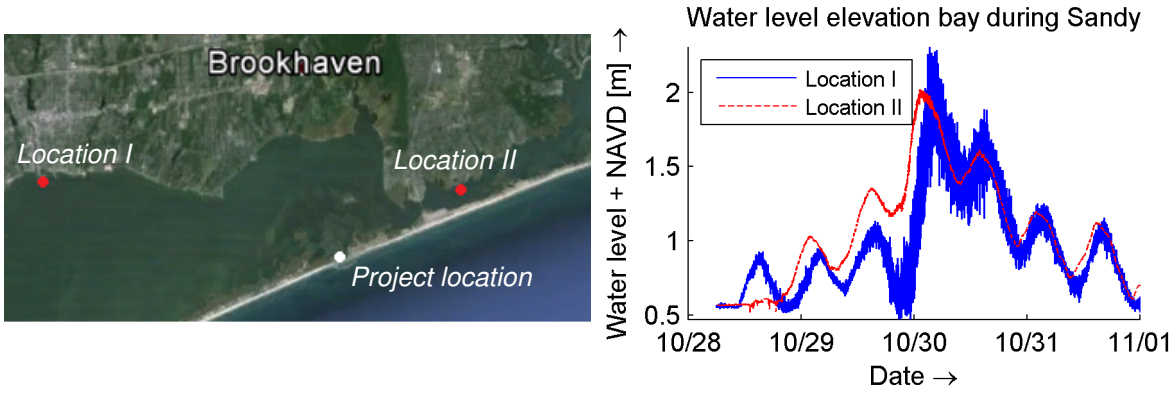

Figure H.9: Left: measurements point of the water level in the bay, source map: Google Earth. Right: measurement data based on storm-tide sensors at these points by the USGS.

Apart from the scatter in the data at Location I, both datasets show similar trends on the evolution of the water level in the bay over time. As Location II is located closer to the project location and less scatter is present in the data, this location is used as model input.

Surge level at sea

The Delft3D model, as introduced in the beginning of this section, is used as the provider of the off-shore boundary condition regarding the water levels. As the model is still under development, the water levels at the closest measurement point (Sandy Hook) are compared with the Delft3D model results. Figure H.10 shows the location of this measurement point with respect to the project location.

Figure H.10: Measurements point of the water level at sea.

In Figure H.11, the water levels are presented. The Delft3D water levels are increased slightly with $0.3\ m$ to deal with the structural underestimation of the surge level in the model. As visible, a relatively good fit on the measurement data is achieved. On the project location, the surge is very similar to the one modelled at Sandy Hook apart from small differences.

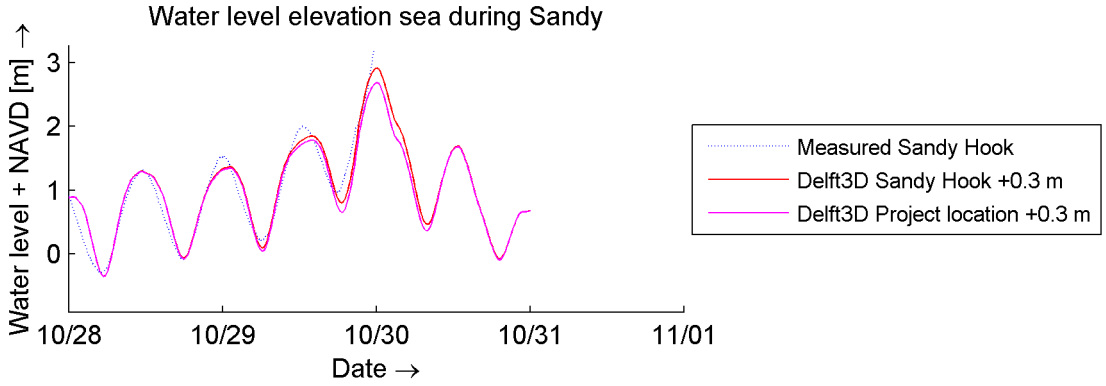

Figure H.11: Water level at sea, data by NOAA.

Waves at sea

From the Delft3D model, SWAN files are extracted containing full spectrum data which can directly be used as input for the XBeach model. The data are validated at the wave buoy of Figure H.12.

Figure H.12: Measurements point of the waves at sea.

Figure H.13 presents the wave data at this buoy together with model results at the same location. The model results are not perfectly in line with the data set as some differences arise. The error of the model seems to be in the order of $1\ m$ regarding the wave height and $1\ s$ regarding the dominant wave period. In the beginning of the storm, errors in the direction of the waves are substantial (in the order of 40 degrees), during the peak of the storm the data is much better represented (with errors in the order of 10 degrees). These errors are not readily fixed as increasing the energy in the spectrum would also affect the directional spreading of the spectrum. These errors are not a real problem as the purpose of the case study is not achieving the exact final solution but more the observation of the general tendency of the model.

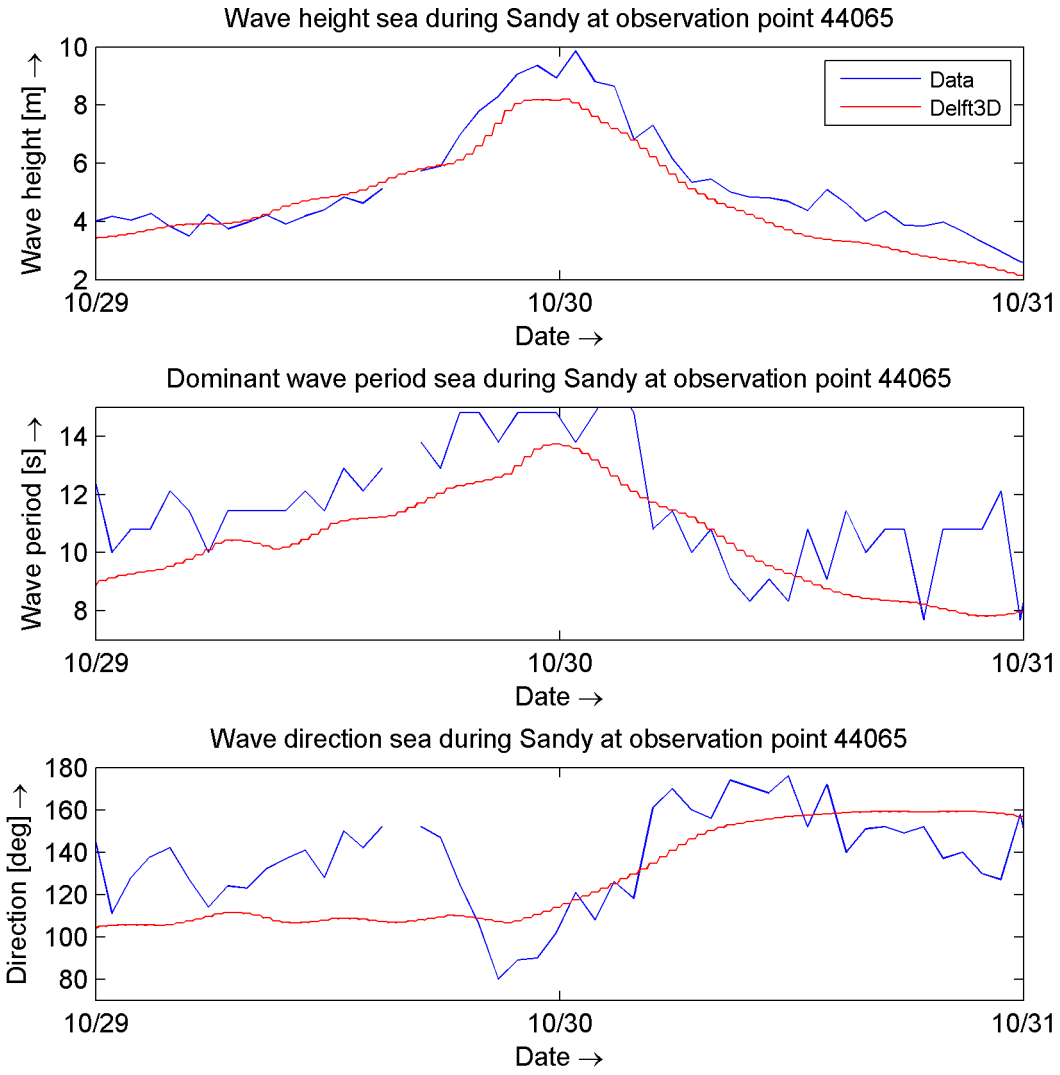

Figure H.13: Validation of the wave characteristics of the Delft3D model at a buoy 44065 with data provided by NOAA.

H.2 Importance improvements in the improved model

In Chapter 7, the improved model is applied on the Fire Island case study. In this section, the importance of the various improvements is assessed. Tables H.3 and H.4 present the performance of the various improvements. The most influential additional physics in the improved model are the dilatancy effect and the bed slope effect. Still, the influence of the additional physics is an order of magnitude less than the magnitude of the overestimations.

Table H.3: BSS and bias for the various improvements.

Model run	BSS					Bias [m]				
Zone:	A	B	C	D	**Total**	A	B	C	D	**Total**
XBeach default	-9.84	-4.06	-2.76	-16.43	**-3.92**	-1.36	-1.98	-1.36	-0.05	**-1.17**
Smax = 1	0.59	0.52	0.71	-3.45	**0.61**	-0.07	0.08	-0.10	0.10	**-0.02**
Improved model	-8.85	-3.73	-2.71	-23.16	**-3.73**	-0.95	-1.83	-1.32	0.03	**-1.05**
No dilatancy effect	-9.28	-4.01	-2.78	-23.92	**-3.90**	-1.06	-1.89	-1.34	0.02	**-1.09**
With A = 1.75 (dilatancy)	-7.73	-3.58	-2.69	-23.04	**-3.56**	-0.74	-1.78	-1.31	0.03	**-1.01**
No bed slope effect	-9.47	-3.91	-2.76	-25.08	**-3.89**	-1.07	-1.87	-1.33	0.01	**-1.08**
With double direction	-9.33	-3.96	-2.76	-23.28	**-3.88**	-1.21	-1.89	-1.34	-0.01	**-1.11**
With 20° internal friction	-8.44	-3.78	-2.72	-23.26	**-3.72**	-0.96	-1.84	-1.32	0.02	**-1.06**
No fall velocity reduction	-8.81	-3.74	-2.71	-23.11	**-3.73**	-0.91	-1.83	-1.32	0.03	**-1.04**
With conservative Exner	-8.81	-3.74	-2.72	-23.41	**-3.74**	-0.94	-1.83	-1.32	0.03	**-1.05**

Table H.4: Model performance indicators for the various improvements. A star ($*$) indicates that the indicator cannot be calculated for the specific model run, e.g. if too much dune lowering took place to be able to calculate the average dune retreat.

Model run	Number of breaches	Dune retreat at $z_b = 4m$ [m]		Δx_{cg} [m]
		$y = 1800\ m$	$y = 2000\ m$	zone C
LIDAR data	1	8.0	14.0	26.7
XBeach default	$>> 1$	*	*	*
Smax = 1	0	12.0	8.0	44.2
Improved model	$>> 1$	*	*	*
No dilatancy effect	$>> 1$	*	*	*
With A = 1.75 (dilatancy)	$>> 1$	*	*	*
No bed slope effect	$>> 1$	*	*	*
With double direction	$>> 1$	*	*	*
With 20° internal friction	$>> 1$	*	*	*
No fall velocity reduction	$>> 1$	*	*	*
With conservative Exner	$>> 1$	*	*	*

H.3 Importance improvements in the improved model with adjustments

As it turned out that the improvements in the improved model were not sufficient to achieve a positive skill in the Fire Island case study, additional modifications were made to the model in Chapter 8. Now it is checked how important the individual improvements are in the adjusted version of the improved model. Tables H.5 and H.6 present the performance of the various improvements. As visible, the model results are not very sensitive to the improvements. The bed slope effect and the dilatancy effect are again the most influential, although the variation in skill and bias is limited.

Table H.5: BSS and bias for the various improvements in the adjusted model.

Model run	BSS					Bias [m]				
Zone:	A	B	C	D	**Total**	A	B	C	D	**Total**
XBeach default	-9.84	-4.06	-2.76	-16.43	**-3.92**	-1.36	-1.98	-1.36	-0.05	**-1.17**
Smax = 1	0.59	0.52	0.71	-3.45	**0.61**	-0.07	0.08	-0.10	0.10	**-0.02**
Combined adjustments	0.44	0.10	0.36	-8.21	**0.23**	-0.05	0.03	0.18	0.14	**0.11**
No dilatancy effect	0.52	0.16	0.36	-8.22	**0.26**	-0.06	0.05	0.18	0.14	**0.11**
With A = 1.75 (dilatancy)	0.54	0.22	0.38	-7.93	**0.29**	-0.05	0.07	0.18	0.14	**0.12**
No bed slope effect	0.52	0.16	0.36	-8.22	**0.26**	-0.06	0.05	0.18	0.14	**0.11**
With double direction	-0.28	-0.01	0.39	-8.24	**0.15**	-0.01	-0.04	0.17	0.14	**0.10**
With 20° internal friction	0.52	0.16	0.36	-8.22	**0.26**	-0.06	0.05	0.18	0.14	**0.11**
No fall velocity reduction	0.52	0.16	0.36	-8.22	**0.26**	-0.06	0.05	0.18	0.14	**0.11**
With conservative Exner	0.52	0.14	0.36	-8.27	**0.25**	-0.06	0.04	0.18	0.14	**0.11**

Table H.6: Model performance indicators for the various improvements in the adjusted model. A star ($*$) indicates that the indicator cannot be calculated for the specific model run, e.g. if too much dune lowering took place to be able to calculate the average dune retreat.

Model run	Number of breaches	Dune retreat at $z_b = 4m$ [m]		Δx_{cg} [m]
		$y = 1800\ m$	$y = 2000\ m$	zone C
LIDAR data	1	8.0	14.0	26.7
XBeach default	$>> 1$	*	*	*
Smax = 1	0	12.0	8.0	44.2
Combined adjustments	1	14.0	12.0	57.2
No dilatancy effect	1	14.0	12.0	57.0
With A = 1.75 (dilatancy)	1	14.0	12.0	56.3
No bed slope effect	1	14.0	12.0	57.0
With double direction	1	*	16.0	56.7
With 20° internal friction	1	14.0	12.0	57.0
No fall velocity reduction	1	14.0	12.0	57.0
With conservative Exner	1	14.0	12.0	57.2

H.4 Changes in the bathymetry of the improved model with adjustments

The bottom level in the bay is not precisely known. Therefore, this section investigates the influence of this unknown on the model results. The bottom level in the bay is heightened half a meter to $NAVD88$-$0.5\ m$ and lowered half a meter to $NAVD88$-$1.5\ m$.

Tables H.7 and H.8 present the skill of the model if the bed level in the bay is modified. As visible, the differences are small if the bed is heightened in the bay slightly. However, some substantial deviations are observed if the bed level is lowered in the bay. In this case, no breaching takes place.

Table H.7: BSS and bias for the modified bay bottom level in the adjusted model.

Model run	BSS					Bias [m]				
Zone:	A	B	C	D	**Total**	A	B	C	D	**Total**
XBeach default	-9.84	-4.06	-2.76	-16.43	**-3.92**	-1.36	-1.98	-1.36	-0.05	**-1.17**
Smax = 1	0.59	0.52	0.71	-3.45	**0.61**	-0.07	0.08	-0.10	0.10	**-0.02**
Combined adjustments	0.44	0.10	0.36	-8.21	**0.23**	-0.05	0.03	0.18	0.14	**0.11**
Bay: $z_b = NAVD88\text{-}0.5m$	0.34	0.14	0.34	-8.72	**0.22**	-0.05	0.07	0.18	0.15	**0.12**
Bay: $z_b = NAVD88\text{-}1.5m$	0.53	0.33	0.41	-8.98	**0.34**	-0.05	0.14	0.27	0.15	**0.18**

Table H.8: Model performance indicators for the modified bay bottom level in the adjusted model. A star ($*$) indicates that the indicator cannot be calculated for the specific model run, e.g. if too much dune lowering took place to be able to calculate the average dune retreat.

Model run	Number of breaches	Dune retreat at $z_b = 4m$ [m]		Δx_{cg} [m]
		$y = 1800\ m$	$y = 2000\ m$	zone C
LIDAR data	1	8.0	14.0	26.7
XBeach default	$>> 1$	*	*	*
Smax = 1	0	12.0	8.0	44.2
Combined adjustments	1	14.0	12.0	57.2
Bay: $z_b = NAVD88\text{-}0.5m$	1	14.0	12.0	56.8
Bay: $z_b = NAVD88\text{-}1.5m$	0	14.0	12.0	49.7

As the bed level in the bay could be a hindering aspect in the breaching process, as accreted sediment restricts the hydrodynamics, it is expected that the depth of the breach channel is depending on the depth in the bay. To test this hypothesis, the evolution of the depth in the breach channel is examined, see Figure H.14. From this figure, it can be learned that the depth in the breach channel depends indeed on the depth in the bay. The deepest location of point B in time is $-0.74\ m$ for the bay bed level of $NAVD88$-$0.5\ m$ whereas it is $-1.14\ m$ with the bay bed level of $NAVD88 - 1\ m$ ($0.4\ m$ deeper). This observation is not confirmed if the bed level in the bay is lowered to $NAVD$-$1.5\ m$ as no more breaching is modelled in that case. It can hence be concluded that the depth in the bay is an important parameter regarding the breaching process. The exact relation of this parameter to the breach evolution cannot be stated based on just these three model runs by the complexity of the process.

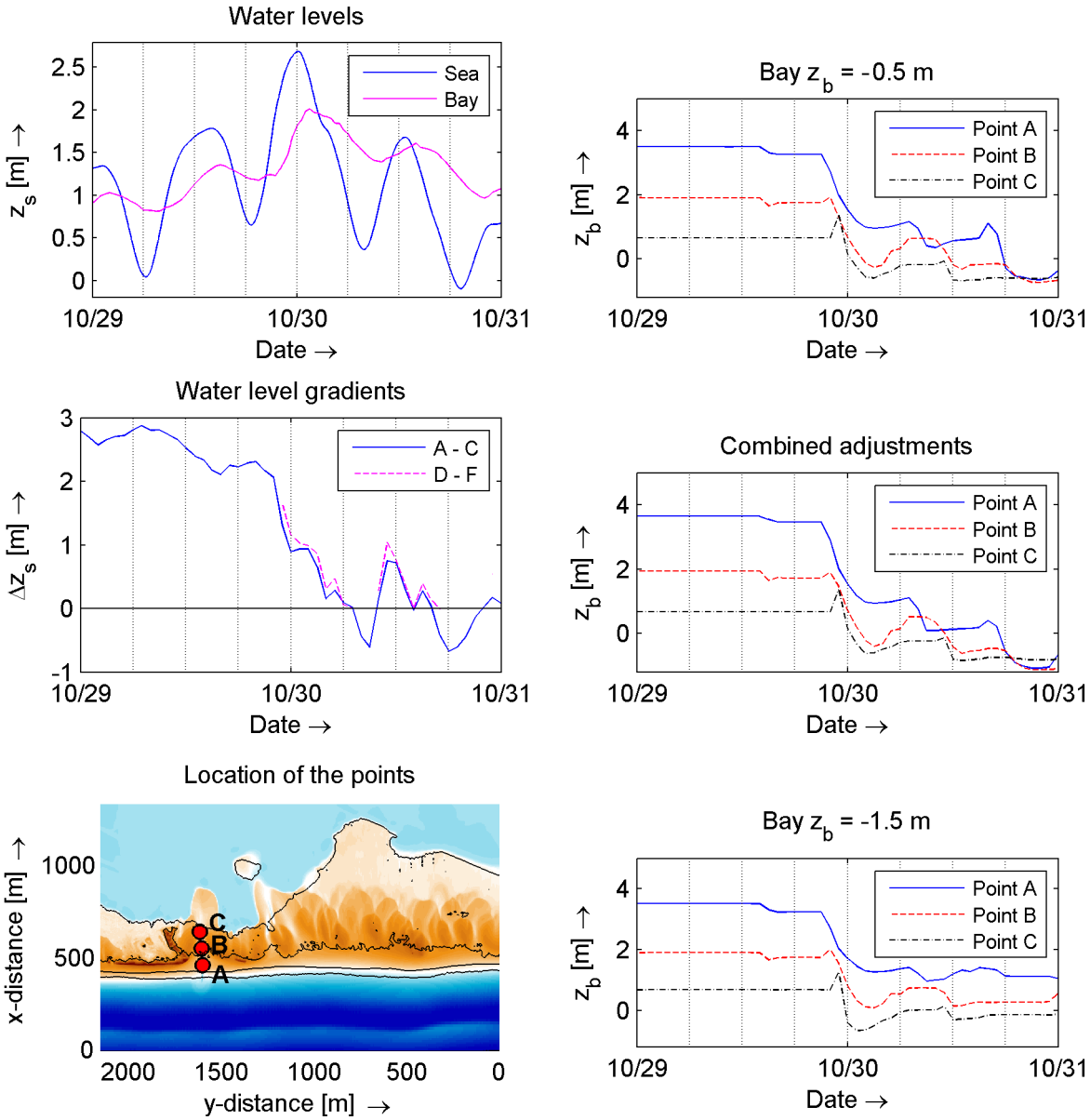

Figure H.14: Bottom level elevation in the breaches over time for several bed levels in the bay. The water level gradients are provided over the two outward points.

H.5 Validity of the morphological acceleration factor

The morphological acceleration factor (known as the *morfac*) reduces the computational time by increasing the morphological changes by a certain factor such that less hydrodynamics has to be computed, see Equation C.6. In this thesis, a morphological acceleration factor of 10 is used. With this factor, the model computation takes over 24 hours on eight computational cores. Without this factor, it would take roughly 10 days for each model run to complete. Using such factor is hence a necessity to perform the research within the available time. On forehand, it is difficult to test if the proposed factor is reasonable as the model results are not yet close to the observations (see Chapter 7). In this section, the final results achieved with the factor of 10 are compared to those with a factor of 1. Figures H.15 to H.17 and Tables H.9 and H.10 present the model performance both for the morphological acceleration factor of 10 as for a value of 1.

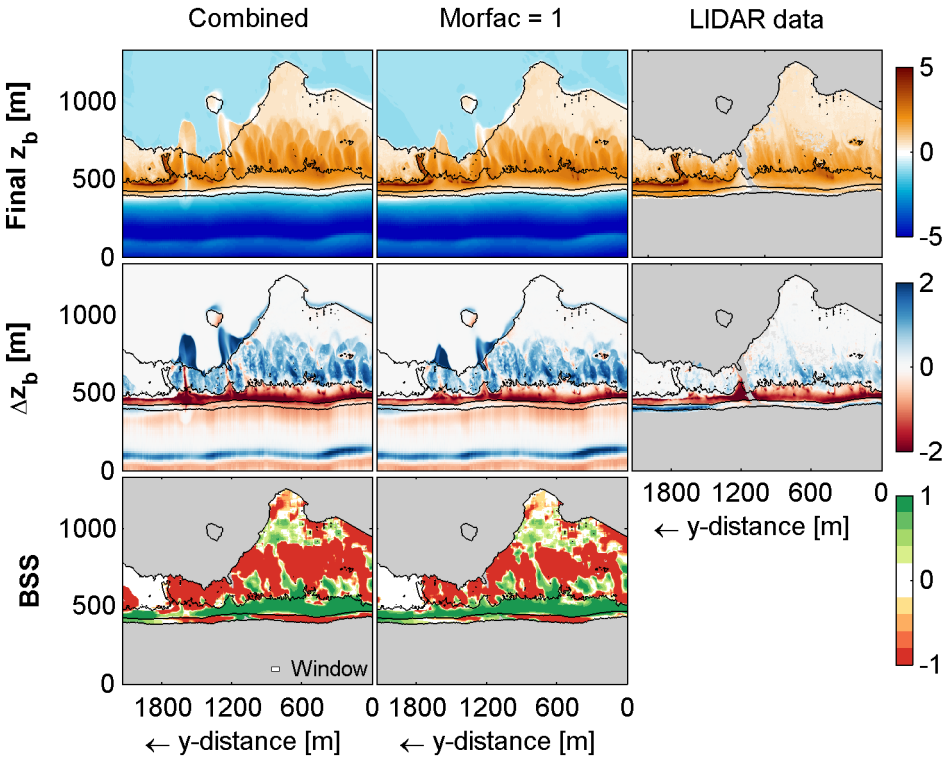

Figure H.15: Performance comparison between the run with a morfac of 10 and without the factor. Shown are the final bed level, the bed level changes by the storm event and the Brier Skill Score with a moving window of 10x10 cells. The black depth contours are provided at an elevation of 0 and 2 m relative to NAVD88 of the initial depth profile. Spots without data are marked gray.

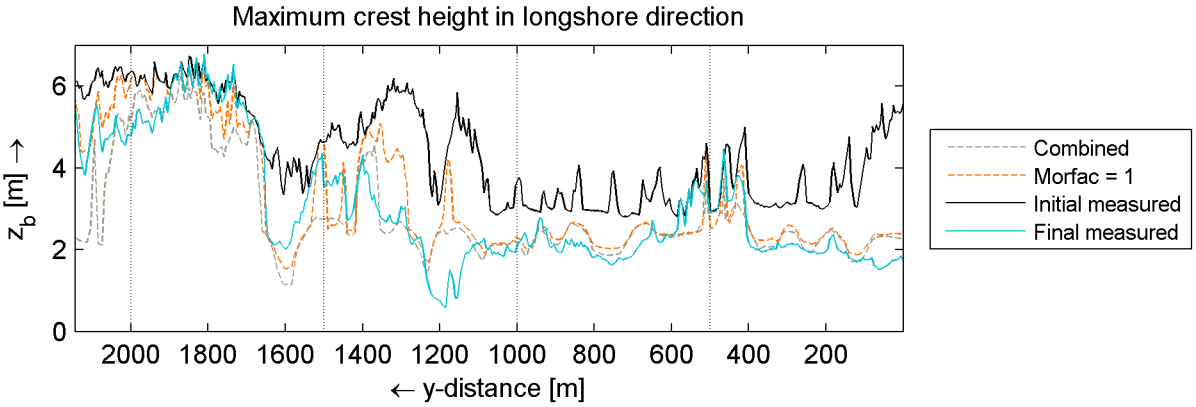

Figure H.16: Maximum crest height in longshore direction of the run with a morfac of 10 and without the factor.

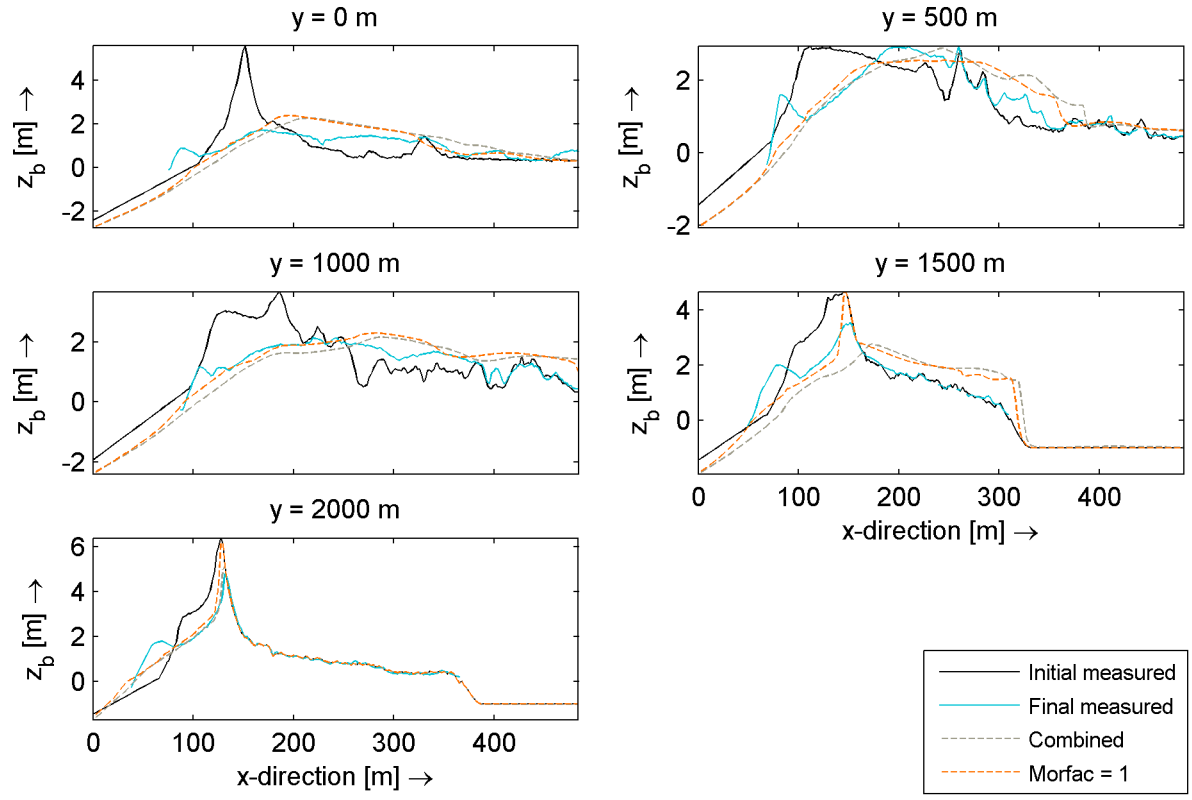

Figure H.17: Cross-sections of the run with a morfac of 10 and without the factor. The cross-sections are provided at certain y-coordinates corresponding to the earlier presented figures.

Table H.9: BSS and bias for the different morphological acceleration factors.

Model run	BSS					Bias $[m]$				
Zone:	A	B	C	D	**Total**	A	B	C	D	**Total**
Combined adjustments	0.44	0.10	0.36	-8.21	**0.23**	-0.05	0.03	0.18	0.14	**0.11**
Morfac = 1	0.75	0.44	0.48	-3.14	**0.47**	-0.04	0.23	0.26	0.06	**0.17**

Table H.10: Model performance indicators for the different morphological acceleration factors.

Model run	Number of breaches	Dune retreat at $z_b = 4m$ $[m]$		Δx_{cg} $[m]$
		$y = 1800\ m$	$y = 2000\ m$	zone C
LIDAR data	1	8.0	14.0	26.7
Combined adjustments	1	14.0	12.0	57.2
Morfac = 1	0	12.0	8.0	46.7

Based on all the information provided in this section, one could conclude that using the morphological acceleration factor causes some notable differences. The most important ones are listed below:

1. The wrongly modelled overwash deposits at $y = 2100\ m$ are not visible if no morphological acceleration is performed. This feature could hence be classified as an error induced by the morphological acceleration.

2. The breach at $y = 1550\ m$, visible in the run with the morphological acceleration factor, did not appear in reality. This feature is also not modelled if no acceleration factor is applied. However, the crest height visualisation of Figure H.16 shows that, in the run without an acceleration, breaching is still initiated but just too less crest lowering is modelled to form a permanent breach channel. As breaching is a very sensitive process, see also the previous section regarding the dependency on the depth in the bay, a slight modification of the parameters could cause a successful breach in the model without the morphological acceleration.

Based on these observations, one could conclude that the morphological acceleration factor induces some deviations but the main tendency of the model is the same. No breaching is modelled if no morphological acceleration is applied. However, with slightly different parameters comparable results are likely to be found as breaching is thought to be a very sensitive process. As discussed, using a morphological acceleration factor for these kind of researches is necessary to be able to perform a large variety of model runs.

Appendix I

Depth-averaging breaching cases

To test whether it is justifiable to average flow and transport over depth, a more detailed analysis is made. It is suggested that depth-averaging might especially be a problem for breaching cases in which the flow velocity can vary strongly over depth. As no experimental data on the spatial variability of flow and sediment transport is available, the Delft3D model is used to test what the influence is of depth-averaging on the results in the Zwin model. It is not possible to do this with XBeach as it supports no multi-layer computations.

I.1 Model set-up

Four Delft3D models are created, each with a different bottom level file and boundary conditions. As an input to the models, the bottom level and water level elevation at the boundaries of the XBeach model at four different times (1 minute, 5 minutes, 20 minutes and 30 minutes) are used. The morphology module is turned off, to prevent changes in the bottom profile, but sediment transport is still enabled. The model duration is taken long enough to achieve a stationary situation. With this model set-up, four different moments in the breaching process are examined. Figure I.1 presents the four bottom profiles used in this analysis.

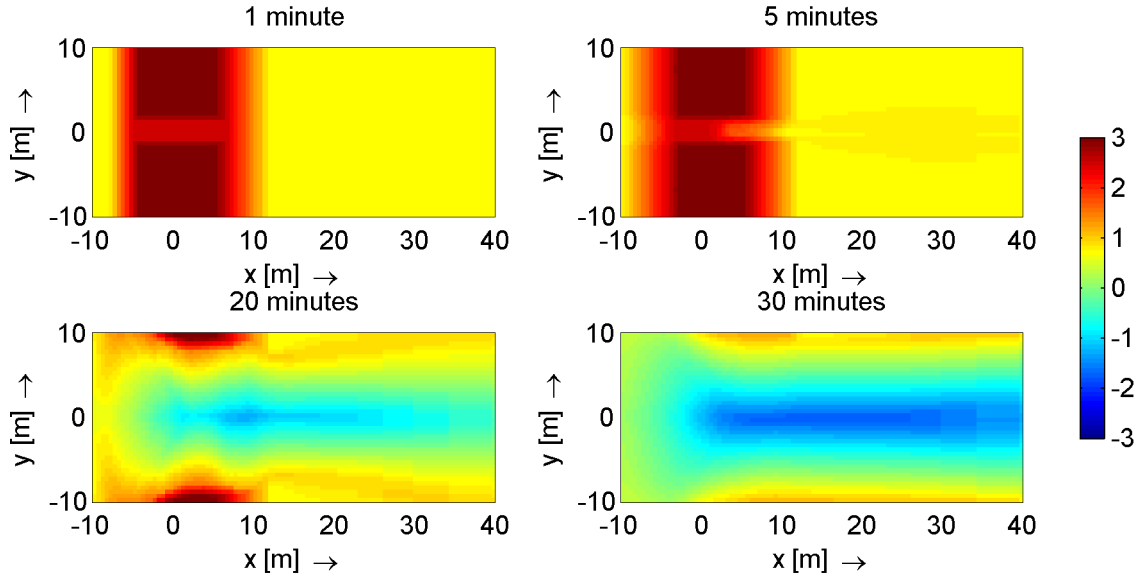

Figure I.1: Delft 3D model of Zwin, bottom levels.

All these four Delft3D models are calculated with one layer (depth-averaging) and with twenty layers to make a comparison possible. The 20 layers are defined such that a high vertical resolution of 0.536% of the water depth is obtained in the lowest layer which increases gradually with a factor 1.2 per layer to 17.11% of the water depth at the top layer.

I.2 Results

The results of the models are given in Figures I.2 to I.5. First, the sediment concentrations are presented for both the depth-averaged model as the model with 20 layers. Further, a plot is provided on the direction of the transport vectors at several locations and the contours of the sediment concentrations are plotted together for both runs in one plot.

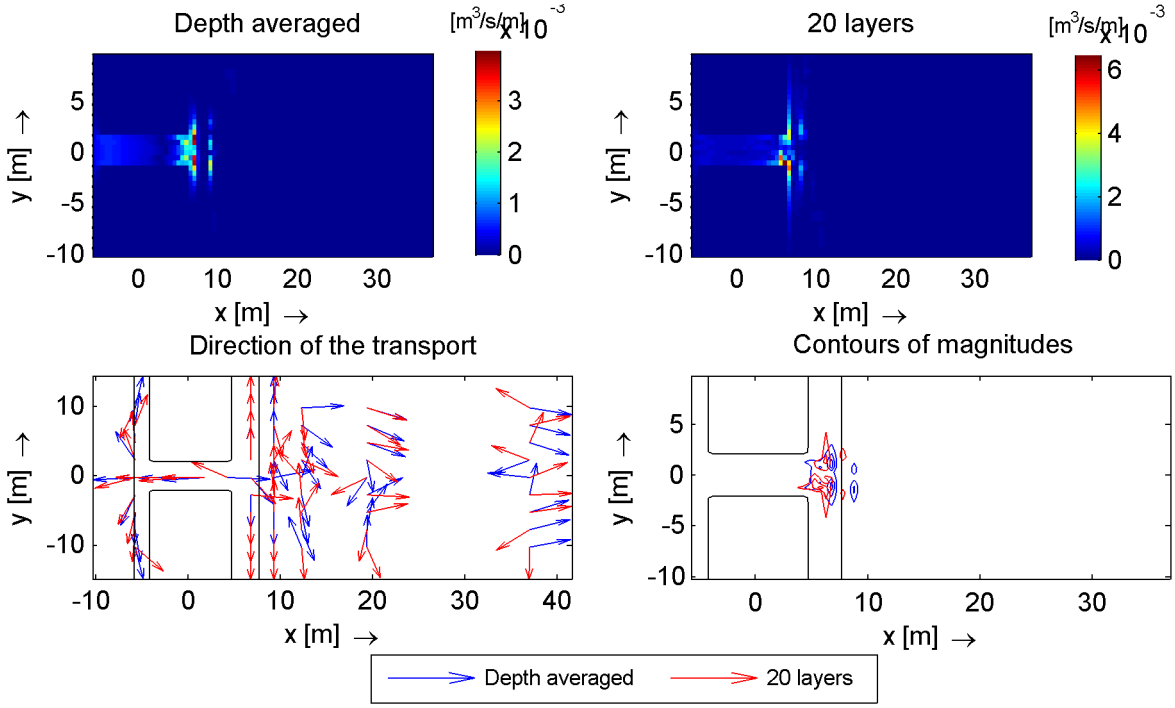

Figure I.2: Delft 3D model of Zwin after 1 minute. The black lines are the $2\ m$ and $3\ m$ depth contours.

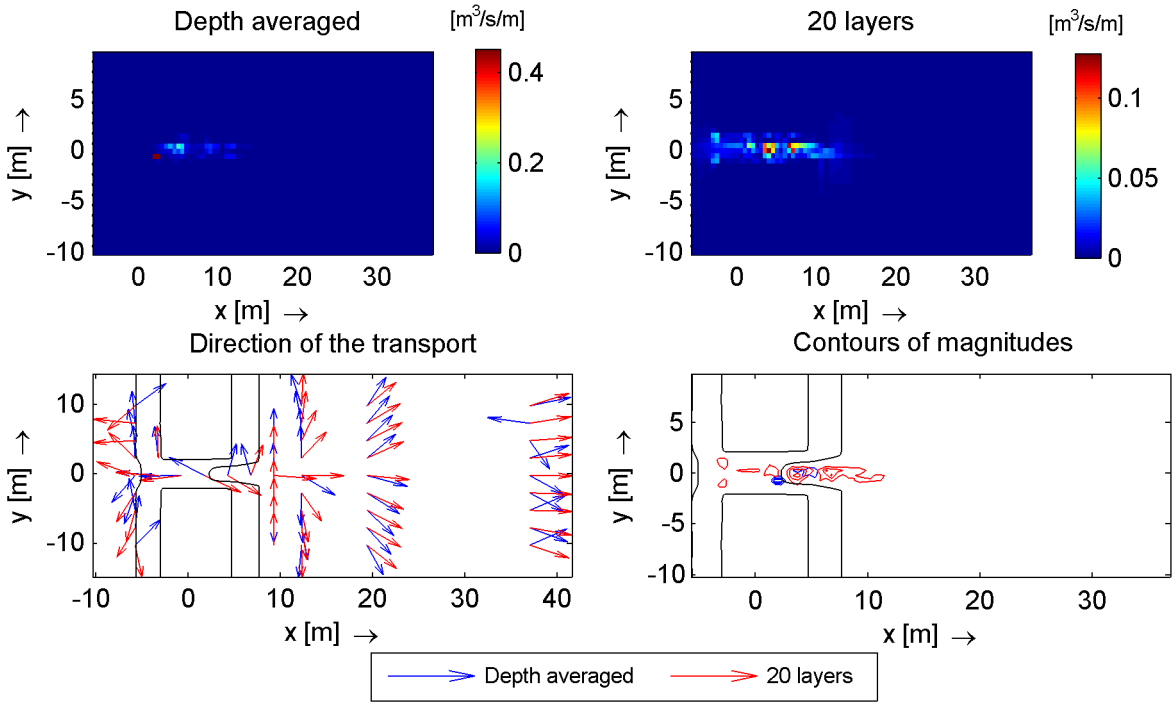

Figure I.3: Delft 3D model of Zwin after 5 minutes. The black lines are the $2\ m$ and $3\ m$ depth contours.

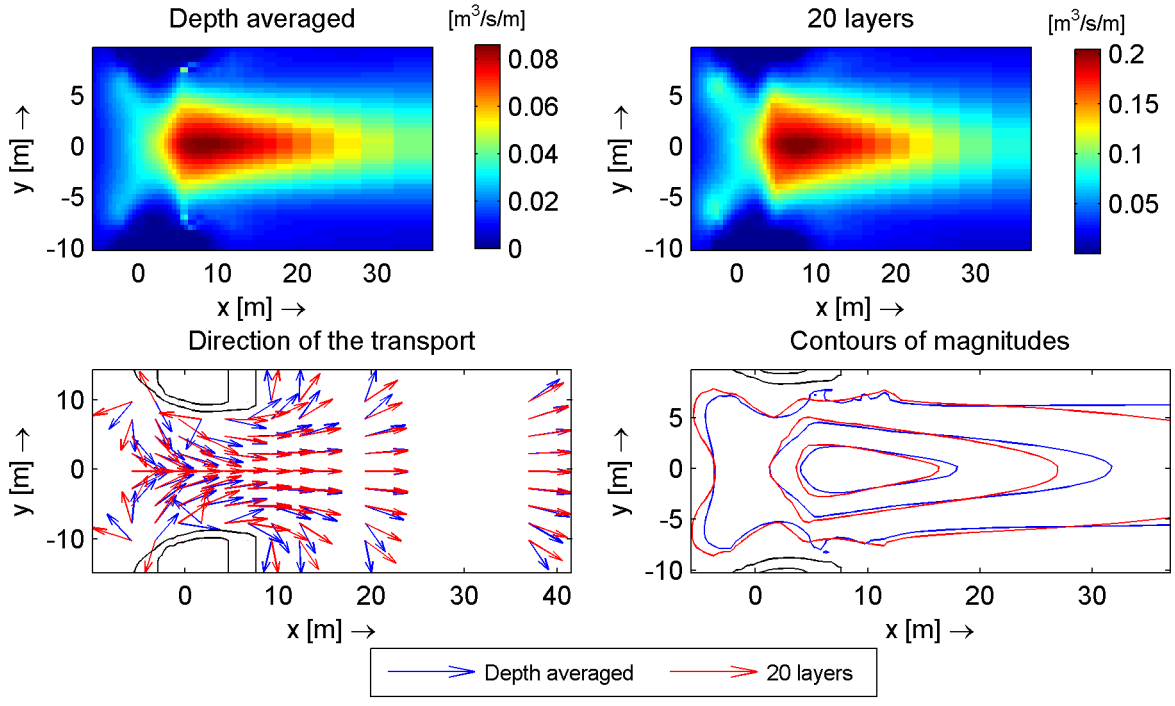

Figure I.4: Delft 3D model of Zwin after 20 minutes. The black lines are the $2\ m$ and $3\ m$ depth contours.

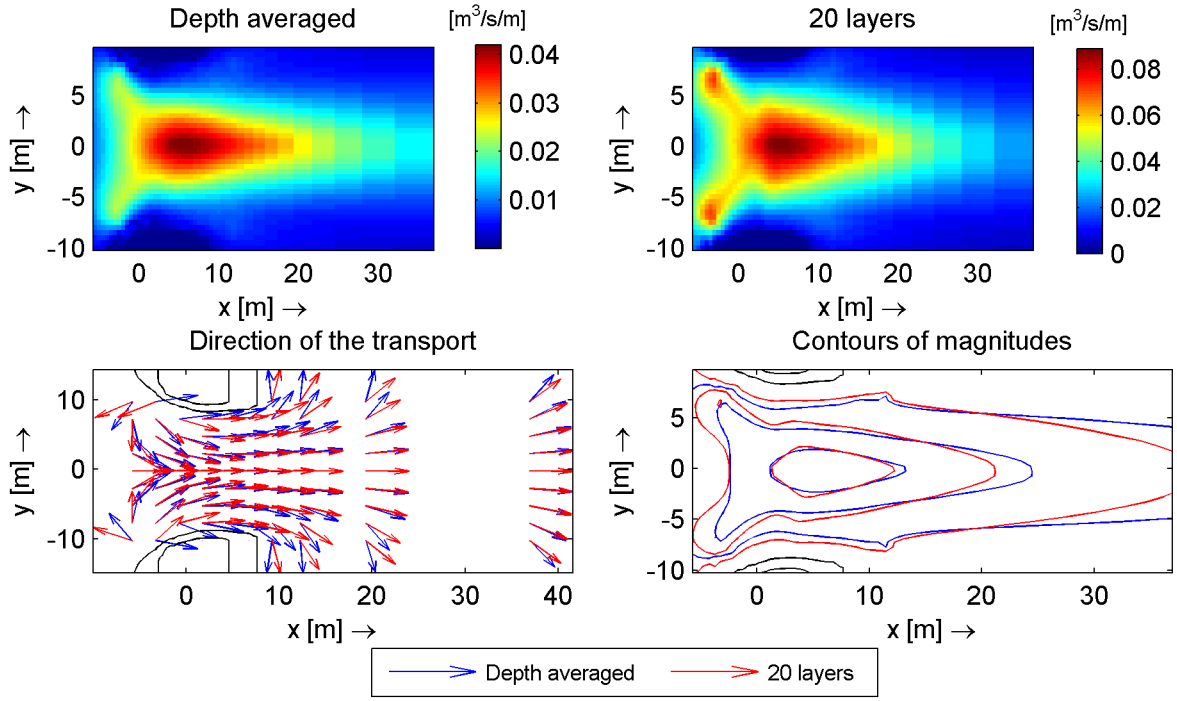

Figure I.5: Delft 3D model of Zwin after 30 minutes. The black lines are the $2\ m$ and $3\ m$ depth contours.

It stands out that the maximum magnitude of the sediment concentration in the depth-averaged model is substantially different compared to the one in the multi-layer model. This is the case for all the Delft3D model results. This could be explained by the fact that the depth-averaged model requires a slightly different calibration factor with respect to the multi-layer model.

For the model representing the situation after 1 minute and the model regarding the bottom level after 5 minutes, the differences are substantial. In these phases, the breach is not yet fully developed and only a thin layer of water flows over the dike surface. As the bathymetry is extracted from the XBeach model, the bottom level is not really smooth at these two times.

For now, the analysis is focussed on the situation in the Zwin model after 20 and 30 minutes. Overall, the depth-averaged model shows comparable results with respect to the multi-layer model, despite a magnitude difference which was suggested to be a calibration issue. As it is not the magnitude of the transport rates but the gradients in the transport rates which are determining the bed level changes, the gradients of the models representing the situation after 20 and 30 minutes are presented in Figure I.6. As visible, the gradients for the depth averaged model are very comparable to the multi-layer model if a multiplication factor of 2.5 is considered, which is based on the magnitude difference in the earlier presented figures.

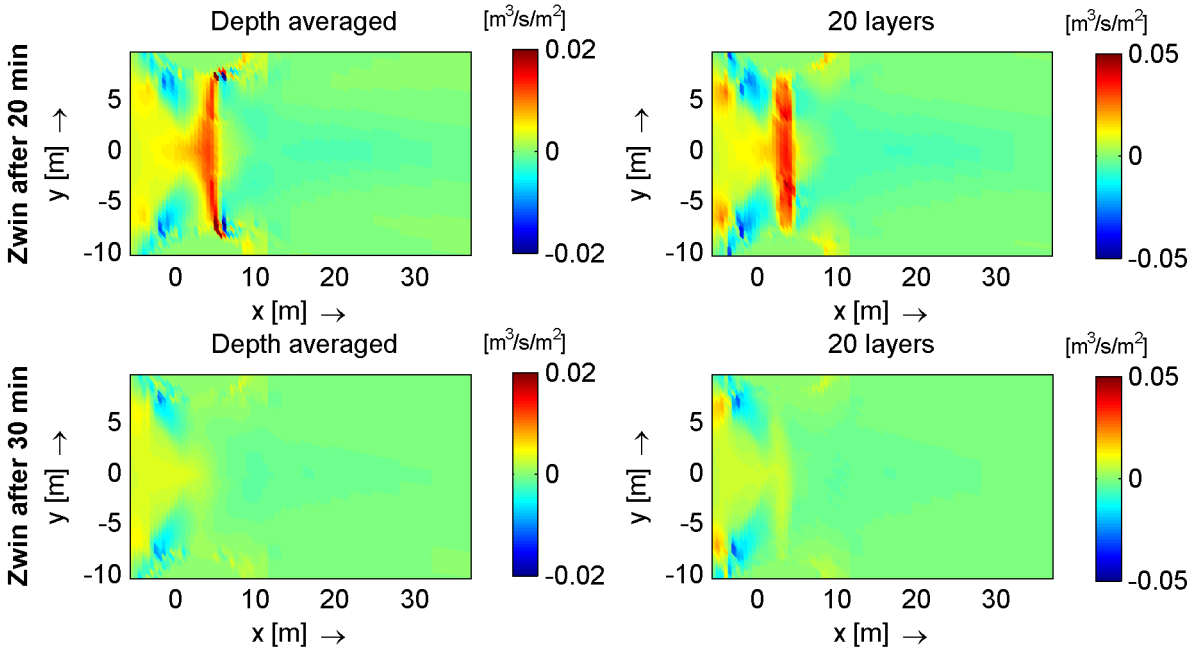

Figure I.6: Gradients in the Delft 3D model of Zwin after 30 minutes. The black lines are the $2\ m$ and $3\ m$ depth contours.

Especially near the boundaries of the breach channel, deviations in the direction of the transport are observed between the depth-averaged and the 20 layers model. The differences seem to be zero in the channel axis and increase with the distance from the axis of the breach channel. Some relation could be found to parametrize this effect. However, first a proper calibration is required such that at least the magnitudes are more in line with the multi-layer model. Further, this difference is not very substantial in the region with the largest gradients in sediment transport rates.

I.2.1 Conclusion

Based on this analysis, it could be reasonable to use a depth-averaged model as XBeach to describe the breaching process. By depth-averaging, some errors are introduced. This is not necessarily a problem as long as one is aware of the fact that by depth-averaging some processes, as non-uniform spiral flow, can simply not be modelled. To account for the three-dimensional effects in a breach, one could fit a relation on the model results, to correct for the difference in direction induced by averaging over the depth. Finding this relation is not subject of this thesis as it would require a more thorough study before a widely usable correction factor can be determined.

A comparison of the sediment transport results with the XBeach results is not readily made. As the purpose of this appendix is not the comparison of XBeach with Delft3D, but more on the depth-averaging assumption in general, the comparison with XBeach is not treated.

Finally, it is noted that the multi-layer approach requires a proper definition of the layers by the user. For example, a constant layer thickness results in a too thick layer near the bed if not a sufficient amount of layers is used.